Western&Graduate&PostdoctoralStudies

Western University
Scholarship@Western

Electronic Thesis and Dissertation Repository

4-5-2023 1:00 PM

Building a Magnetosome-like Nanoparticle for Magnetic Resonance Imaging

Qin Sun, *The University of Western Ontario*

Supervisor: Goldhawk, Donna E., *The University of Western Ontario*
Co-Supervisor: Prato, Frank S., *The University of Western Ontario*
A thesis submitted in partial fulfillment of the requirements for the Doctor of Philosophy degree in Medical Biophysics
© Qin Sun 2023

Follow this and additional works at: https://ir.lib.uwo.ca/etd

Part of the Medical Biophysics Commons

Abstract

With its superb spatial and temporal resolution, magnetic resonance imaging (MRI) has great potential to track cellular activities that define early stages of disease. To improve molecular imaging techniques, we are developing MRI reporter gene expression based on the magnetosome. In magnetotactic bacteria (MTB), magnetosome formation compartmentalizes iron biominerals in membrane-enclosed vesicles. We hypothesize that essential magnetosome proteins interact in any cell type to form rudimentary magnetosome-like nanoparticles, providing a genetically-controlled contrast agent for molecular MRI.

MTB genes *mamE*, *mamB*, *mamI*, and *mamL* were cloned from *M. magneticum* sp. AMB-1 genomic DNA by PCR and inserted into fluorescent vectors to create Mam fusion proteins then stably expressed in human MDA-MB-435 melanoma cells. Cines of fluorescent elements detected in intact cells were captured with confocal microscopy (Nikon A1R) and analyzed using both ImageJ and Mathematica for Brownian motion and velocity. To obtain longitudinal and transverse relaxation rates, cells stably expressing magnetosome proteins were supplemented with 250 µM ferric nitrate, harvested, mounted in a gelatin phantom, and scanned at 3 Tesla (Biograph mMR).

Tomato-MamL, Tomato-MamL/GFP-MamI, and Tomato-MamB all express punctate, mobile fluorescence, while GFP-MamE expresses punctate but stationary fluorescence. Analysis of motility revealed that magnetosome proteins have variable diffusion coefficients due to their variable sizes, but all magnetosome proteins travel at a velocity of around 0.2 µm/s. Relaxation rates of iron-supplemented cells expressing Tomato-MamB, GFP-MamI, or Tomato-MamL have significantly higher R2 and R2* than non-supplemented cells. Interestingly, iron-supplemented cells expressing GFP-MamE or co-expressing FLAG-MamL/GFP-MamI had relaxation rates comparable to unsupplemented cell types.

This is the first report characterizing essential magnetosome proteins MamE, MamB, MamI, and MamL in mammalian cells. Analysis of motion shows that magnetosome proteins travel at velocities comparable to the mammalian motor protein myosin. Expression of either MamB, MamI or MamL increases transverse relaxation rates; however, co-expression of

MamI and MamL reduces them again, suggesting a regulatory effect of magnetosome gene combinations. Biosynthesis of magnetosome-like nanoparticles in mammalian cells would provide an endogenous magnetic resonance (MR) contrast agent under genetic control. This patented technology would provide long-term molecular imaging for tracking cellular and molecular activities throughout the cell's life cycle.

Keywords

Molecular imaging, Magnetic resonance imaging, Magnetotactic bacteria, Magnetosome, Gene-based iron contrast, Nanoparticle, Reporter gene, Fluorescence imaging, Particle tracking, Protein-protein interaction

Summary for Lay Audience

Magnetic Resonance Imaging (MRI) is a medical imaging technology that is used worldwide to diagnose disease. It is very useful as it can show subtle differences in the soft tissues of the body. However, in its present form it is limited to detection of about one million cells. Special contrast agents are being developed with the goal of reducing the minimally detected cells to about one thousand. We have been developing such a contrast agent and our theoretical calculations suggest that if we are successful MRI will be able to detect as few as 3,000 cells.

We have been molecular engineering such a contrast agent that when introduced into a human cell will become MRI visible when the cell performs a specific function. This required us to find genes as raw material for this process. We isolated four genes from a special kind of bacteria that produces a form of iron that is the greatest MRI contrast agent known.

We have successfully shown that each of these four genes can be introduced into human cells. But for this to work, all four protein products from these genes must find each other and co-operate in making a special iron particle within the cell. Currently, we have introduced two genes in the cell and found that these proteins can find each other. What remains now is to first introduce three genes and evaluate their interactions, then finally introduce all four genes to reach our ultimate goal of MRI detection of about 1,000 cells.

Co-Authorship Statement

This dissertation contains information from one published book chapter, one article not yet accepted but under revision, and two articles that will be submitted to scientific journals. As the first author of all written content, I have contributed significantly to the proposal of projects, experimental designs, data acquisition and analysis, and manuscript writing and revisions. All authors have or will contribute to suggestions and feedback prior to submission of respective articles. Dissertation chapters including specific articles are described below.

Chapter 1 contains text from the book chapter titled "Optimizing Reporter Gene Expression for Molecular Magnetic Resonance Imaging", which is chapter 9 in the book "Bioimaging: Imaging by Light and Electromagnetics in Medicine and Biology" edited by Shoogo Ueno. This book was published in 2020 by CRC Press Taylor & Francis Group in Japan. The chapter was co-authored by Sun Q, Prato FS, and Goldhawk DE. Sun Q contributed to creation of figures and chapter revising while Prato FS and Goldhawk DE contributed to chapter writing, editing, and revising.

Chapter 2 is an original research article titled "Essential Magnetosome Proteins MamI and MamL from Magnetotactic Bacteria Interact in Mammalian Cells" which was submitted to *Journal of Biological Chemistry*, peer-reviewed, and returned in 2022. The manuscript author list is: Sun Q, Yu L, Donnelly SC, Fradin C, Thompson RT, Prato FS, and Goldhawk DE. Sun Q contributed to experimental design, data collection and analysis, creation of figures and tables, manuscript writing, editing, and revising. Yu L contributed to data collection and analysis and creation of figures and tables. Donnelly SC and Fradin C contributed to experimental design, data collection and analysis, creation of figures and tables, and manuscript writing, editing, and revising. Thompson RT contributed to experimental funding and manuscript revising. Prato FS contributed to experimental funding and to manuscript editing and revising. Goldhawk DE contributed to experimental design and manuscript writing, editing, and revising. This manuscript has been revised and will be resubmitted to *Journal of Biological Chemistry* in early 2023.

Chapter 3 is an original research article titled "Cellular Distribution and Motion of Essential Magnetosome Proteins Expressed in Mammalian Cells". The manuscript author list is: Sun Q, Fradin C, Thompson RT, Prato FS, and Goldhawk DE. Sun Q contributed to experimental design, data collection and analysis, creation of figures and tables, manuscript writing, editing, and revising. Fradin C contributed to experimental design, development of image analysis code, data collection and analysis, creation of figures and tables, and manuscript writing, editing, and revising. Thompson RT contributed to experimental funding and will contribute to manuscript revising. Prato FS contributed to experimental funding and to manuscript editing and revising. Goldhawk DE contributed to experimental design and manuscript writing, editing, and revising. This manuscript will be submitted for publication in 2023.

Chapter 4 is an original research article titled "Magnetic Resonance Parameters and Cellular Iron Content of Magnetosome Proteins Expressed in Mammalian Cells". The manuscript author list is: Sun Q, Vivekanantha P, Gelman N, Thompson RT, Prato FS, and Goldhawk DE. Sun Q contributed to experimental design, data collection and analysis, creation of figures and tables, manuscript writing, editing, and revising. Vivekanantha P contributed to data collection and analysis. Gelman N contributed to manuscript editing and revising. Thompson RT contributed to experimental funding and will contribute to manuscript revising. Prato FS contributed to experimental funding and to manuscript editing and revising. Goldhawk DE contributed to experimental design and manuscript writing, editing, and revising. This manuscript will be submitted for publication in 2023.

Acknowledgments

First and foremost, I would like to thank my mom, Lian Xue, for her immense love and dedication in raising me as a single mother. I would like to thank my dad, Hexi Sun, for always making the most out of the limited time we spend together due to us being miles and miles apart. I can always count on you both, whether it rains or shines.

I would like to thank my supervisors Dr. Donna Goldhawk and Dr. Frank Prato for always making time for me, whether it be to talk about my project or just to lend a listening ear to my ups and downs in life. Thank you both so much for being such patient, caring, and supportive supervisors.

I would like to thank my advisory committee (Dr. Mamadou Diop and Dr. Jeremy Burton) for giving me constructive feedback and much needed advice. I would like to thank Dr. Cécile Fradin for being a fantastic collaborator, for working with me during crazy hours of the day and night, for teaching me new techniques and theories, and for being supportive throughout my studies. I would like to thank Dr. Neil Gelman for coaching me through MR theory, data analysis, and discussion. I would like to thank Dr. Savita Dhanvantari and Dr. Paula Foster for running a fantastic molecular imaging group and for being understanding and supportive faculty members. I would like to thank John Butler, Heather Biernaski, Lynn Keenliside, and Marcus Flamminio for their technical assistance during this project.

I would like to thank Dr. Aaron Ward and Dr. Charles McKenzie for being excellent graduate chairs during my period of study. They have always made time for the students in the department, and their dedication to the success of their students and appreciation and understanding of mental health means everything to me.

I would like to thank the members of the Goldhawk lab for being excellent helpers and team players, and for always brightening up my day at the lab. Thanks to Sarah Donnelly for working excellently alongside me, for bringing me snacks, for making me laugh with jokes and conversation, and for being the best lab buddy ever. Thanks to Selinia Hong for riding the ups and downs of molecular cloning protocols with me. Thanks to Jonathan Yohans, Moeiz Ahmed, and Moayyad Nassar for being great friends and lab members.

I would like to thank my closest friends Shiny Yang, Rachel Champion, and Talek Julian for finding time in their busy lives to spend time with me when I need a moment to relax and to cheer me up when I am feeling stressed or feeling down. You are the best friends anyone could ever ask for.

I would like to thank my partner, Enrique Alvarado, for being with me and loving me throughout the ups and downs of my academic career and of my day-to-day life. Thank you for supporting me and comforting me through difficult times, for cooking my favourite meals when I am busy, for laughing at my lame jokes, and for always being there when I need a hug or a shoulder to cry on.

Last but not least, I would like to thank my cats:

Nellie, who always loved food and treats, who was sassy and snappy to everyone but always was kind to me, and who I miss so, so dearly.

Moonie, who loves cuddles and is the friendliest cat ever, and who loves helping me write by sitting on my keyboard.

Posy, who loves having the zoomies and loves to take much-needed naps with me.

Table of Contents

List of Tables

List of Figures

List of Abbreviations

ANOVA	Analysis of Variance
BCA	Bicinchoninic Acid
BSA	Bovine Serum Albumin
CALB-AM	Calcein Blue and Aceto-Methoxies
CDF	Cation Diffusion Facilitator
CNR	Contrast to Noise Ratio
CPP	Cell Penetrating Pepetide
DMEM	Dulbecco's Modified Eagle Medium
DMT1	Divalent Metal Transporter 1
DTT	Dithiothreitol
EDTA	Ethylenediamine Tetraacetic Acid
EGFP	Enhanced Green Fluorescence Protein
ER	Endoplasmic Reticulum
FBS	Fetal Bovine Serum
FCS	Fluorescence Correlation Spectroscopy
FCCS	Fluorescence Cross-Correlation Spectroscopy
FIESTA	Fast Imaging Employing Steady-state Acquisition
FPN	Ferroportin
GAPDH	Glyceraldehyde 3-Phosphate Dehydrogenase
GFP	Green Fluorescent Protein
GRE	Gradient Echo
HRP	Horseradish Peroxidase
ICP-MS	Inductively-Coupled Plasma Mass Spectrometry
IR	Inversion Recovery
MAI	Magnetosome Gene Island
ME	Magneto-Endosymbionts
MR	Magnetic Resonance
MRI	Magnetic Resonance Imaging
mRNA	Messenger Ribonucleic Acid
MSD	Mean-Squared Displacement
MTB	Magnetotactic Bacteria
MW	Molecular Weight
PBS	Phosphate Buffered Saline
PET	Positron Emission Tomography
$R1 = 1/T1$	
$R2 = 1/T2$	
$R2' = R2* - R2$	
RF	Radiofrequency
RFP	Red Fluorescent Protein
RIPA	Radioimmunoprecipitation Assay
ROI	Region of Interest
SDS	Sodium Dodecyl Sulfate
SDS-PAGE	SDS Polyacrylamide Gel Electrophoresis
SE	Single Echo

SEM	Standard Error of the Mean
SPIO	Superparamagnetic Iron Oxide
SNP	Single Nucleotide Polymorphism
T	Tesla
TBS	Tris-Buffered Saline
TE	Echo Time
Tf	Transferrin
TF	Transcription Factor
TfRc	Transferrin Receptor
TR	Repetition Time
tRNA	Transfer Ribonucleic Acid
YFP	Yellow Fluorescent Protein

Chapter 1

1   Introduction

In magnetic resonance imaging (MRI), methods for the non-invasive detection of cells and their activities often rely on the manipulation of cellular iron. In many aspects, this is ideal. Iron perturbs the magnetic resonance (MR) signal and thus influences measurable MR parameters. All cells, and therefore tissues, require an iron cofactor for various functions, thus iron-related MR measures inherently target integral cellular activities. In addition, differential regulation of iron enhances the distinction between tissue and cell type(s), which enables MRI to non-invasively monitor changes in iron-related organ function. For example, after a hemorrhagic heart attack, cardiac MR can quantitate the iron that often accumulates in infarcted tissue and predisposes a patient to heart failure (1, 2, 3). In addition, the inflammatory component of heart disease involves immune cell responses that target the iron export activity of monocytes (4) and macrophages (5, 6).

One of the great challenges in MRI is development of sensitive, iron-related measures that complement the exquisite spatial resolution of this modality. There has been short-term success with a variety of superparamagnetic iron oxide (SPIO) nanoparticles that temporarily boost the cellular MR signal (7). These advancements in exogenously-introduced iron contrast have demonstrated the power and feasibility of tracking cells. However, reporting cellular activity throughout the cell's life cycle means tapping into the endogenous workings of the cell. New approaches are required for this type of molecular imaging. The use of molecular cloning techniques, to overexpress iron-

handling protein(s) that amplify MR contrast (8), has opened new avenues in gene-based iron-labelling (9). These genetically engineered cells clearly possess the ability to express a long-lived signal, suitable for preclinical imaging.

While the search continues for the most efficient expression system(s), the utility of reporter genes for *in vivo* imaging by MRI and other modalities is increasingly recognized. With this type of endogenous contrast, we can examine the regulation of cellular activities that predict disease and offer therapeutic solutions. To realize the full potential of this technology for MRI, we have drawn on the best-known example of efficient, gene-based iron-labelling in single cells: the magnetosome found in magnetotactic bacteria (MTB) (10). The manner of iron compartmentalization in the magnetosome not only reflects fine-tuned regulation of iron, which is a necessary feature of iron metabolism in virtually every cell type (11) but also provides the means by which a cell's magnetic properties may be altered and potentially exploited to provide unique MRI signatures. For example, iron-containing abdominal pathologies are often detected using MRI (12).

In this chapter, we introduce the magnetotactic bacteria and their magnetosomes (1.1), specifically the genes involved in their stepwise assembly. An introduction of proteins and their synthesis, modification, degradation, function, and interactions are covered in section 1.2. To understand the protein environment and the potential interactions with cellular components, the cytoskeleton and molecular motors are reviewed in section 1.3. To appreciate the potential of a rudimentary magnetosome-like nanoparticle as an MRI contrast agent, MRI concepts are reviewed in section 1.4. Finally, concepts in reporter gene expression for molecular MRI are reviewed in section 1.5. A

brief chapter summary is provided in section 1.6, and the overall thesis objectives and outline are listed in chapter 1.7.

1.1. Magnetotactic bacteria and the magnetosome

Magnetosome synthesis is a protein-directed process, beginning with expression of structural genes that encode the required magnetosome components. While the nature of these components is still incompletely understood, progress has been made in many areas. The genomes of numerous MTB have now been sequenced, permitting comparison of conserved gene sequences and synteny (13, 14). Despite the breadth of MTB species, there are common genes that specify the main magnetosome structure and approximately two thirds of these are clustered on a magnetosome genomic island (15). Removal of this cluster of DNA prevents magnetotaxis in the microorganism but is not lethal, demonstrating that magnetosomes likely confer selective advantage(s) rather than compulsory function(s).

Studies examining specific gene deletions have further categorized which magnetosome gene products are essential to the structure versus auxiliary (14, 16). That is, some proteins regulate critical steps in magnetosome formation while others control optional features like subcellular arrangement and crystal morphology. These findings raise the possibility that certain magnetosome genes may be used as regulatory agents in the design and synthesis of MR contrast for reporter gene expression. As the magnetosome compartment becomes more fully understood, it should also be feasible to genetically program various features of the magnetosome, including variations in the degree and type of biomineralization and strength of magnetism, all of which impinge on

the MR signal (17). Manipulation of these features is thus compatible with the notion that magnetosome-like nanoparticles in any cell type may be tailored for a desired purpose and not restricted to magnetotaxis.

1.1.1. Stepwise assembly of the magnetosome

The current body of magnetosome knowledge supports a model of biosynthesis in which there is a hierarchy of protein expression dictating which components create the framework upon which the iron biomineral is compartmentalized, shaped and localized within the cell. This also implies that no one protein recapitulates the entire structure; rather, its assembly depends on multiple protein-protein interactions (18, 19). Although this design is more complex than previously acknowledged (20), the elaborate nature of magnetosome nanoparticles provides a wealth of information about how to program a vesicle for any purpose, including iron biomineralization for MRI reporter gene expression. Complexity in design also explains why single gene expression systems have fallen short of the robust MR signals obtained with intact MTB or isolated magnetosomes and their variants (21). It is the sum of individual steps in magnetosome formation that creates a compartment housing a well-defined crystal. Understanding how these steps work together to produce the magnetosome will enhance how we utilize this structure for molecular MRI.

Magnetosome biosynthesis begins with vesicle formation, followed by the initiation of iron biomineralization and then maturation of the crystal (22). The molecular instructions that prescribe vesicle formation must subsequently be linked to biomineralization and candidate proteins involved in rendering these activities are

steadily being described (15). We propose that a subset of these may be sufficient for the formation of a rudimentary magnetosome-like nanoparticle in mammalian cells. For this, we envision that designation of the vesicle membrane involves establishing the point of contact for initiation of iron biomineralization. This docking site would then constitute the critical protein-protein interactions required for the first step(s) in magnetosome formation. The schematic in Figure 1.1 predicts one potential sequence of interactions based on the essential roles of magnetosome membrane (Mam) proteins I, L, B and E (16).
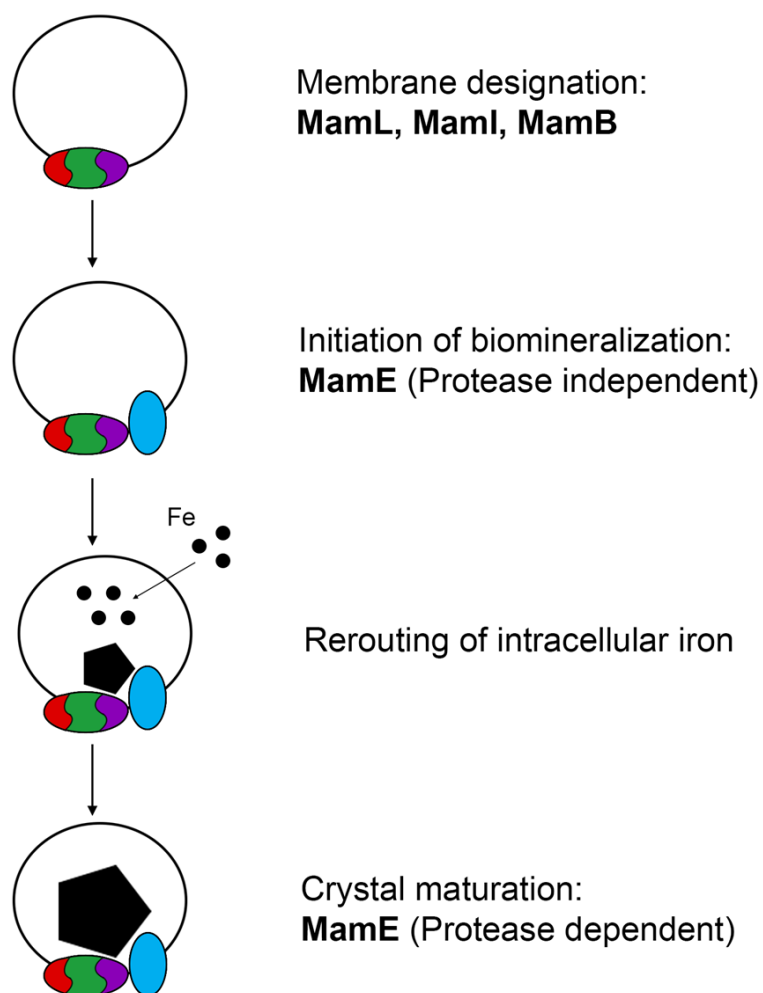
Figure 1.1 Modelling the roles of essential magnetosome proteins in a step-wise formation of the magnetosome.

First, the proteins MamL (red), MamI (green), and MamB (purple) assemble at the membrane, designating the site for magnetosome formation (solid black circle). Subsequently, MamE (blue) is recruited to the nascent magnetosome vesicle to initiate iron biomineralization. This step proceeds independent of MamE protease activity. Then, intracellular iron is rerouted to the rudimentary magnetosome compartment, permitting

magnetite crystal formation. This enables maturation of the iron biomineral in a step that requires the proteolytic activity of MamE.

1.1.2.   Protein structure of magnetosome proteins

Bioinformatics predictions (14) of the magnetosome proteins MamI, MamL, MamB, and MamE give us insights on their protein structure. These predicted structures can give us information on how the proteins interact with each other and with the environment in which they are expressed.

1.1.2.1. Predicted structure of MamI

MamI is a small, 69 amino acid long protein. The protein has two predicted transmembrane domains from amino acids 3 to 23 and 32 to 52. MamI has two very short cytoplasmic ends that range from amino acids 1 to 2 and 53 to 69, and has a luminal loop from amino acids 24 to 31 (23). This loop region is thought to have iron binding capabilities and to be able to purify forms of magnetite (24). Figure 1.2 shows the AlphaFold predicted structure of MamI (25, 26).
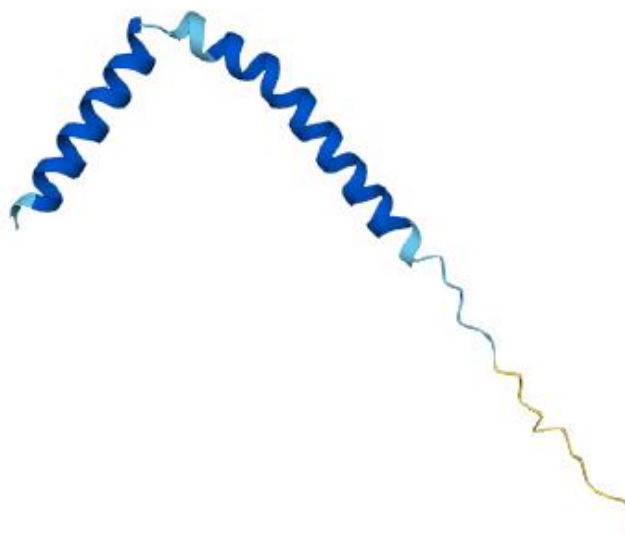
Figure 1.2 AlphaFold structure prediction of the AMB-1 magnetosome protein MamI.

Colours reflect the structure confidence in which dark blue regions represent areas of very high structure confidence, light blue regions represent areas of good structure confidence, yellow regions represent areas of low structure confidence, and orange regions represent areas of very low confidence.

1.1.2.2. Predicted structure of MamL

MamL is a small, 78 amino-acid long protein. Similar to MamI, the protein has two transmembrane domains that range from amino acids 1 to 22 and 39 to 59. MamL has a short, luminal domain that ranges from amino acids 23 to 38 and has a cytoplasmic tail that ranges from amino acids 60 to 78 (21). Figure 1.3 shows the AlphaFold predicted structure of MamL (23, 24).
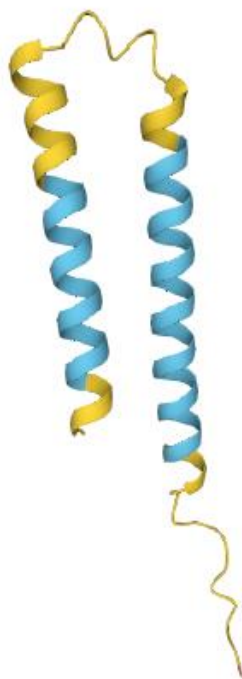
Figure 1.3 AlphaFold structure prediction of the AMB-1 magnetosome protein MamL.

Colours reflect the structure confidence in which light blue regions represent areas of good structure confidence, yellow regions represent areas of low structure confidence, and orange regions represent areas of very low confidence.

Previous reports have indicated the possibility of interaction between MamL and cytoskeletal components (27, 28). Specifically, the C terminus of MamL has been compared to cell-penetrating peptides (CPPs) and arginine-rich peptides (ARPs) due to the abundance of positively-charged amino acids (29). These positive charges interact with negatively-charged cytoskeletal components. To evaluate the potential of the cytoplasmic tail of MamL to interact with the mammalian cytoplasmic environment, the

15 amino acids from the C-terminal was analyzed for positively-charged amino acids.

The cytoplasmic domain of MamL has 7 positively charged amino acids (Figure 1.4).
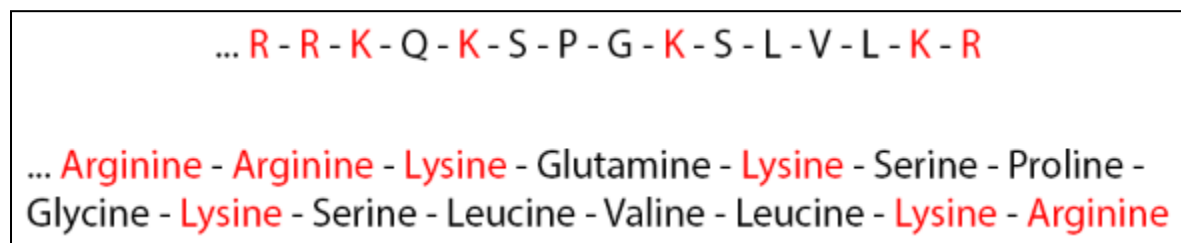
Figure 1.4 The amino acid sequence of the MamL C-terminal tail.

The positively charged amino acids are displayed in red font.

1.1.2.3. Predicted structure of MamB

MamB is a 296 amino-acid long protein with two domains. The protein has a transmembrane domain ranging from amino acids 1 to 214, and a C-terminal cytosolic domain ranging from amino acids 215 to 296. Based on similar protein structure comparison in the UniProt database, the C-terminal domain of MamB is likely responsible for hetero- and homodimerization and assumes a V-shaped fold to bind one iron cation per subunit (21). Figure 1.5 shows the AlphaFold predicted structure of MamB (23, 24).

Figure 1.5 AlphaFold structure prediction of the AMB-1 magnetosome protein MamB.

Colours reflect the structure confidence in which dark blue regions represent areas of very high structure confidence, light blue regions represent areas of good structure confidence, yellow regions represent areas of low structure confidence, and orange regions represent areas of very low confidence.

MamB is present in various species of magnetotactic bacteria, and the protein is not identical in each of these species. Variations between species are visually represented in Figure 1.6. There exists a large portion of MamB, approximately from amino acids 30 to 245, which is conserved between various MTB species. Unlike for MamE proteins, the transmembrane domain of MamB does not have strong homology between species. MamB is also variable in length, with its two most common lengths being 296 or 209 amino acids.
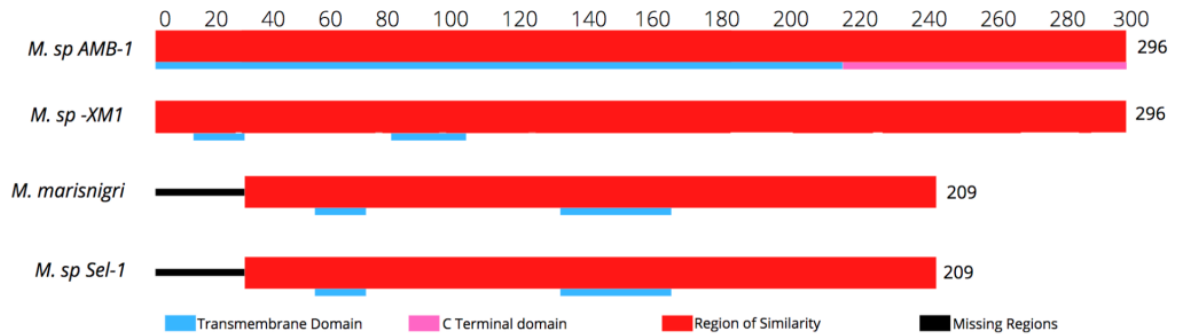
Figure 1.6 Bioinformatics analysis of the homology of magnetosome protein MamB across several magnetotactic bacterial species

Regions of similarity across species are highlighted in red, while regions of the protein that are not present in AMB-1 are in black. The topological and transmembrane domains of the protein are indicated in light blue or pink, respectively.

To evaluate the potential of the cytoplasmic domain of MamB to interact with the mammalian cytoplasmic environment, the 81 amino acids region from the C-terminal was analyzed for positively-charged amino acids. The cytoplasmic domain of MamB has 15 positively charged amino acids (Figure 1.7).
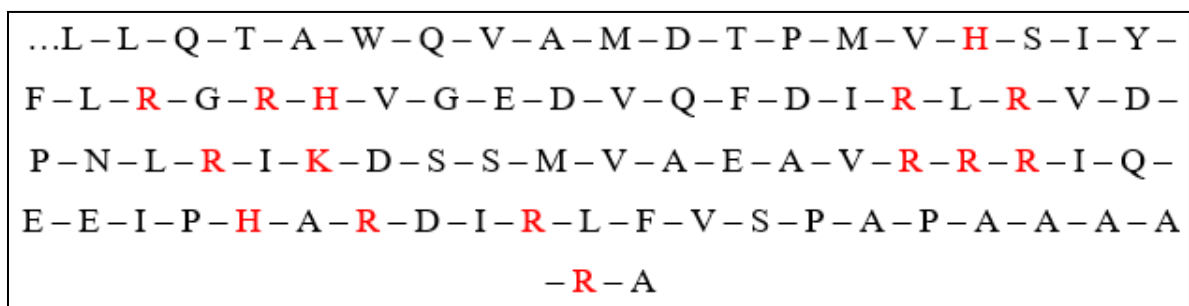
Figure 1.7 Sequence analysis of the cytoplasmic domain of MamB.

Positively-charged amino acids are shown in red.

1.1.2.4.Predicted structure of MamE

MamE is a 728 amino-acid long protein with multiple domains. The protein has a short cytoplasmic domain ranging from amino acids 1 to 21, a short, alpha-helical transmembrane domain ranging from amino acids 22 to 42, and a large luminal domain from amino acids 42 to 728. The luminal domain is the protein's most functional domain and has roles in iron binding and proteolysis (30). Figure 1.8 shows the AlphaFold predicted structure of MamE (23, 24).
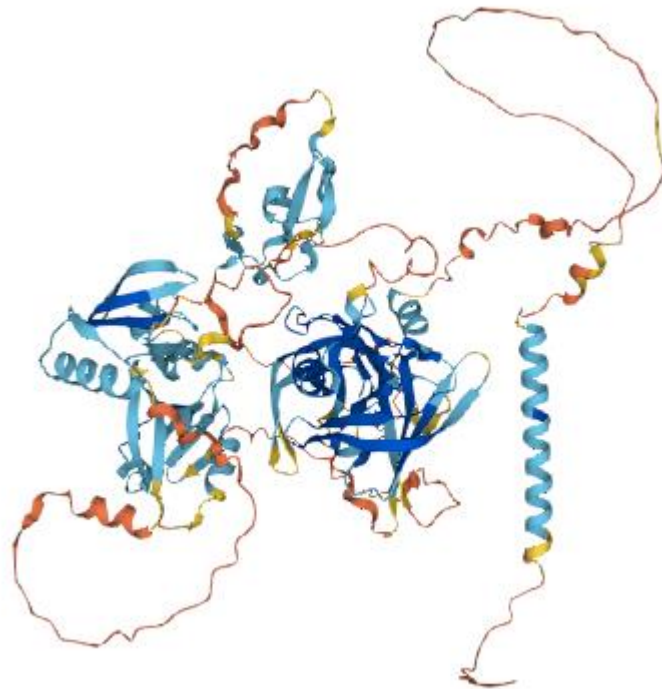
Figure 1.8 AlphaFold structure prediction of the AMB-1 magnetosome protein MamE.

Colours reflect the structure confidence in which dark blue regions represent areas of very high structure confidence, light blue regions represent areas of good structure

confidence, yellow regions represent areas of low structure confidence, and orange

regions represent areas of very low confidence.

MamE is a large protein that is present in other species of magnetotactic bacteria.

The protein is not identical in each of these species. Variations between species are

visually represented in Figure 1.9. The transmembrane domain of MamE is located in a

region of the protein which has strong homology between species. Each species has an

area of variability within MamE from around amino acids 425 to 470. MamE also differs

in length amongst species, with the most common length being 728 amino acids.
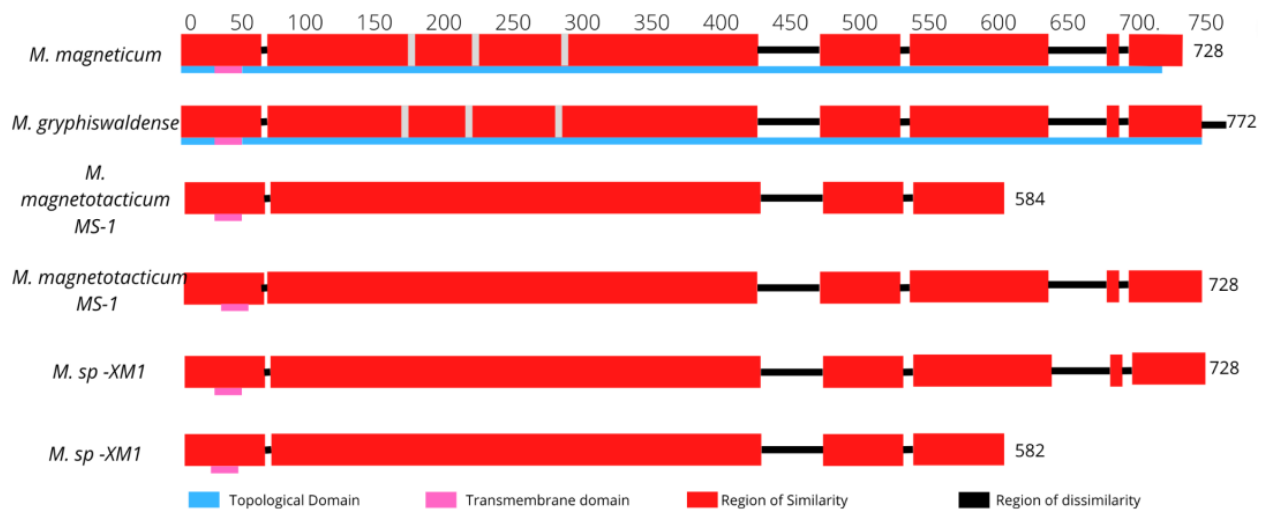
Figure 1.9 Bioinformatics analysis of the homology of magnetosome protein MamE across several magnetotactic bacterial species.

Regions of similarity across species are highlighted in red, while regions of dissimilarity

are in black, and single nucleotide polymorphisms (SNPs) are in grey. The topological and

transmembrane domains of the protein are indicated in light blue or pink, respectively.

To evaluate the potential of the cytoplasmic tail of MamE to interact with the

mammalian cytoplasmic environment, the 21 amino acids from the C-terminal was

analyzed for positively-charged amino acids. The tail of MamE has two positively charged amino acids, arginine, and lysine (Fig. 1.10).

...M - A - M - F - N - G - D - V - E - D - G - G - R - G - D - A - S - C -

G - K - D

Methionine – Alanine – Methionine – Phenylalanine – Asparagine –

Glycine – Aspartic acid – Valine – Glutamine – Aspartic acid – Glycine

– Glycine – Arginine – Glycine – Aspartic acid – Alanine – Serine –

Cysteine – Glycine – Lysine – Aspartic acid
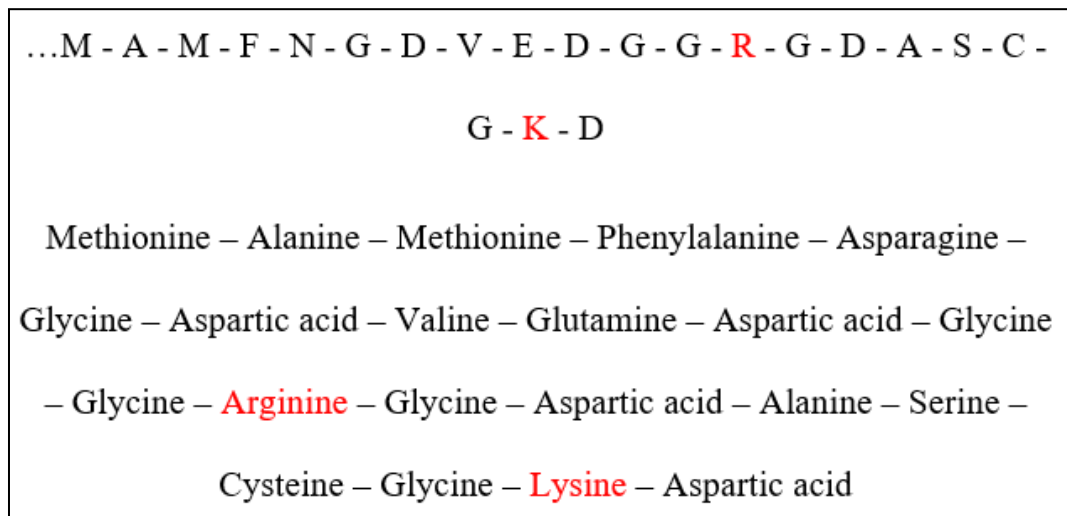
Figure 1.10 Sequence analysis of the cytoplasmic tail of MamE.

Positively-charged amino acids are shown in red.

1.1.3.   Designating the vesicle

Since most magnetosome proteins are membrane-bound (16), their expression in any cell type involves a lipid bilayer. In prokaryotes, this implicates the cell membrane; however, in eukaryotes, integral membrane proteins are routed through vesicles emanating from the Golgi apparatus and will remain within the cytoplasmic compartment (31) unless directed otherwise by specific membrane localization signals. Regardless of cell type, iron biomineralization is confined to a membrane-enclosed compartment and this is an important protective mechanism, built into the magnetosome blueprint, for avoiding iron cytotoxicity. In species of *Magnetospirillum*, neither magnetosome vesicle nor iron biomineral are produced in the absence of MamI, MamL or MamB (14),

establishing the importance of these proteins in key steps of magnetosome synthesis. In contrast, deletion of MamE interferes with biomineralization but still permits vesicle formation. Based on these results, magnetosome proteins that assemble at the membrane are probably not all directly involved in iron-handling. A no less important, regulatory role is held by proteins that designate the membrane location for initiation and elaboration of the iron biomineral. This notion is consistent with cryotomographic images of MTB, revealing both empty magnetosome vesicles as well as those containing biominerals of varying sizes within a single magnetosome chain (22, 32). Figure 1.1 therefore is a working hypothesis that implicates MamI, MamL and MamB in the initial designation of a magnetosome membrane.

In MTB, these 3 genes are not likely to be sufficient for vesicle formation. Raschdorf *et al.* reported that MTB mutants expressing 7 Mam proteins, including MamI, MamL and MamB, will form vesicular structures identified by cryoelectron tomography (33). However, in mammalian cells, fewer genes may be necessary. Since eukaryotic cells are already equipped with intracellular vesicles, then presumably, only those magnetosome proteins that attract iron biomineralization function(s) to an existing vesicle would be necessary (Fig. 1.11). In support of this, Chapter 2 report the interaction of MamI and MamL in a mammalian cell line (28). While encouraging, it remains to be seen whether MamB and/or MamE will co-localize with MamI and MamL as predicted in MTB (15). Nevertheless, this work infers that essential magnetosome protein-protein interactions are specific, irrespective of cellular environment. For the development of MRI reporter gene expression, such specificity is ideal and paves the way for genetically encoding a reproducible magnetosome-like structure in any cell type (34, 35).
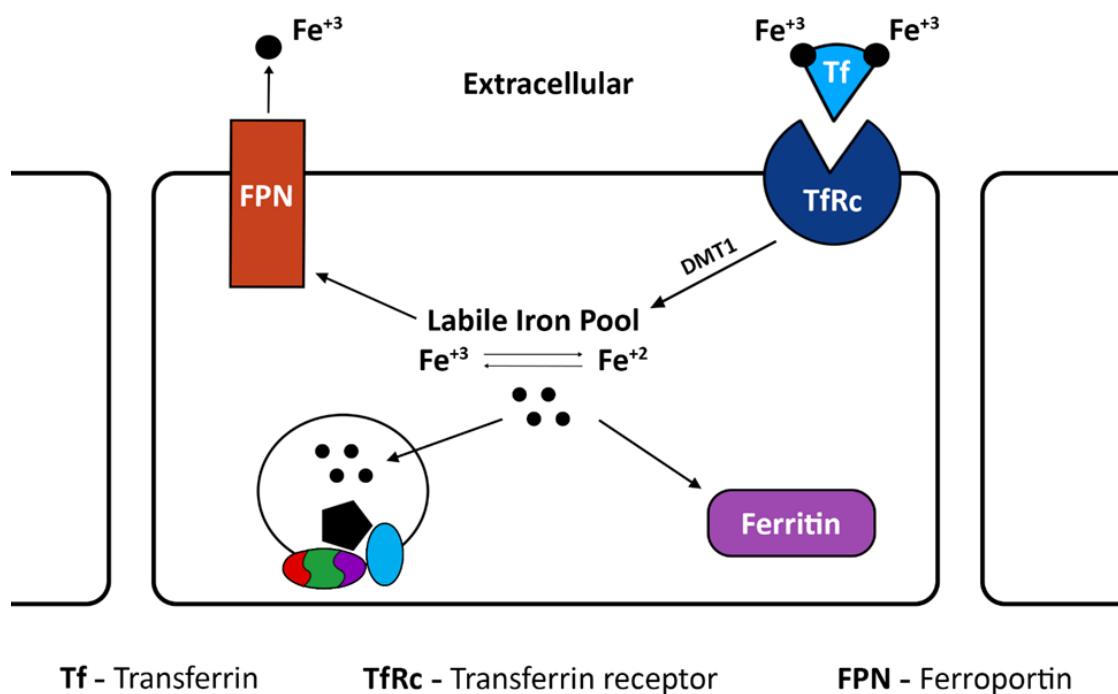
Figure 1.11 Modelling key features of mammalian iron regulation in cells producing magnetosome-like nanoparticles.

Serum iron in its ferric state (Fe^{+3}) is mainly bound to transferrin (Tf) and taken up by cells through transferrin receptor-mediated endocytosis (TfRc). Within the intracellular compartment, ferric iron is reduced to its ferrous state (Fe^{+2}) and delivered to a redox-active, labile iron pool by divalent metal transporter 1 (DMT1 (36)). From there, surplus iron is stored in ferritin when not needed for immediate cellular activities. In cells expressing magnetosome-like particles, iron is rerouted to this compartment by magnetosome proteins (Fig. 1.1). Only select cells, including monocytes and macrophages, export iron through ferroportin (FPN).

1.1.4.   Building the iron biomineral

The contribution of individual MTB genes to the process of magnetosome formation has been examined in both prokaryotes and eukaryotes. With the exception of *mamB*, *mamE*, *mamI* and *mamL*, single deletion of many magnetosome genes in MTB produces irregularities in the biomineral crystal structure or its arrangement within the cell but does not destroy the compartment. There may be redundant functions among magnetosome proteins or subtle changes in magnetosome function that are not readily detected using common microbiology measures, like C_{mag} (37, 38) or a simple lab magnet (39). If instead of responding to the geomagnetic field (25-65 µTesla (40)), the objective is an *in vivo* response to MRI at clinical field strengths on the order of 3 Tesla (3T), then cells bearing the same type of iron biomineral would respond differently to the change in external field strength. The interaction of iron biomineral with magnetic field in turn has an effect on relaxation rates of the proton, which is observed with MRI. This influence of iron will vary depending on the oxidation state, size and shape of the crystal. Hence, diverse MR signals could be genetically programmed by taking advantage of the remarkable number of magnetosome sizes and shapes evident in diverse species of MTB.

An early report of magnetosomes in *Anisonema* algae indicated that eukaryotic cells are capable of magnetosome synthesis (41). Since then, expression of select MTB genes in mammalian cells has demonstrated compatibility of such transgene expression systems and enhancement of cellular iron stores, leading to MR contrast improvements (31, 42, 43, 44, 45). Figure 1.11 depicts key steps in the regulation of iron metabolism to provide some context for the biosynthesis of magnetosome-like nanoparticles in

mammalian cells. Just like other iron-requiring cellular activities, the magnetosome-like compartment is shown drawing iron from the labile iron pool. In this way, iron homeostasis is maintained while a new magnetosome-like iron storage compartment is being synthesized. Using single MTB expression systems, the response of various features of mammalian iron homeostasis have been examined. In the iron-exporting P19 cell line, MagA expression augments total cellular iron content without altering its iron export function (31). However, Guan et al. showed that the level of transferrin receptor (TfRc) decreases and the level of ferritin increases in MagA-expressing A549 lung cancer cells (46). Even though further studies are needed to understand the full effect of MTB iron-handling protein on mammalian cell systems, these early findings suggest that mammalian iron metabolism is compatible with MTB protein expression and any influence it may have on (re)routing intracellular iron. Even the magnetosome-associated, magnetic particle membrane specific (Mms) protein, Mms6 has a measurable effect on the MR signal (45, 47).

1.2. Understanding proteins

In order to appreciate the potential of magnetosome proteins as gene-based contrast agents, we must understand the processes of protein synthesis, folding, sorting, and degradation.

1.2.1. Protein synthesis

Protein synthesis begins in the nucleus of the cell, where DNA is used as a template and transcribed into messenger ribonucleic acid (mRNA). In prokaryotes, such as in MTB, the mRNA is immediately able to undergo translation. In contrast, eukaryotic

cells produce pre-mRNA, and this molecule must undergo post-transcriptional

modifications in order to become mature mRNA (48). This step occurs in the nucleus of

the eukaryotic cell and include protective modifications such as 5′ capping and 3′ poly(A)

tail addition to the pre-mRNA molecule and other modifications such as RNA splicing to

remove introns (noncoding regions) of the pre-mRNA. The mature mRNA molecule can

then exit the nucleus into the cytoplasm, in which translation occurs.

Both prokaryotic and eukaryotic cells use ribosomes to synthesis polypeptide

chains by using mature mRNA molecules as templates (49). However, in prokaryotes,

this process can start simultaneously with transcription whereas translation and

transcription are two separate, discontinuous processes in eukaryotes (50). Ribosomes

attach to the mRNA at the start codon (nucleotide sequence AUG) and reads the molecule

in triplet nucleotides. Transfer ribonucleic acid (tRNA) molecules deliver the correct

amino acid by binding to the triple nucleotide reading frame with its complimentary

nucleotide sequence (anticodon). In eukaryotes, this process produces one polypeptide

chain per mature mRNA molecule, and thus the mRNA is deemed monocistronic. In

prokaryotes, mRNA molecules are polycistronic, meaning one mRNA can have multiple

translation start sites and produce multiple different polypeptides. This difference is

attributed to differences in the arrangement of DNA that code for proteins between

eukaryotes and prokaryotes. In prokaryotic cells, genes that are functionally-related

assemble in groups, called operons, and are located adjacent to each other. In eukaryotic

cells, genes that encode proteins are translated into separate mRNA molecules, which in

turn will be translated into separate, individual proteins (51).

1.2.2. Protein folding

Once the polypeptide chain is formed, the molecule will fold into a specific, three-dimensional structure in which the protein gains stability and can perform its biological function. All proteins start with their primary structure, which is simply its linear amino-acid sequence, and then form secondary, tertiary, and/or quaternary structure (52). The secondary structure of proteins are the formation of alpha helices and beta sheets through intramolecular hydrogen bonding (Fig. 1.12). Proteins then form tertiary structure by folding into orientations that face hydrophilic amino acids towards aqueous environments and hydrophobic amino acids towards hydrophobic cores of the protein (Fig 1.12). The tertiary structure can be further stabilized by the formation of disulfide bridges. Finally, quaternary protein structure includes the assembly of subunits, or multiple polypeptide chains, into a fully functional group of proteins, or includes the arrangement of multiple domains of a single polypeptide chain into one functional protein (Fig. 1.12).

Primary Structure
(amino acid chain)
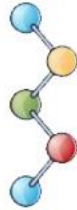
Secondary Structure

Alpha Helix   Beta Sheet

Hydrogen
Bond

Tertiary Structure

🟠 Hydrophobic
🟢 Hydrophilic
Ⓢ Disulfide Bond

Quaternary Structure

Domain 1   Domain 2

Domain 3   Domain 4

Polypeptide 1   Polypeptide 2

Polypeptide 3   Polypeptide 4
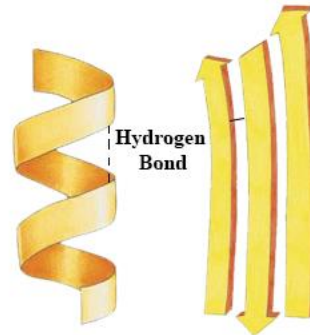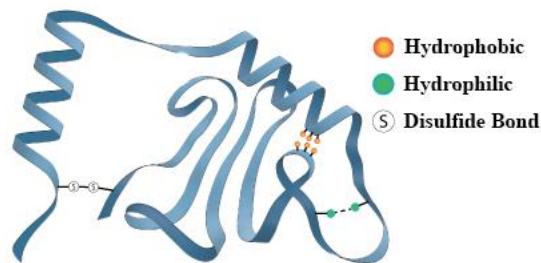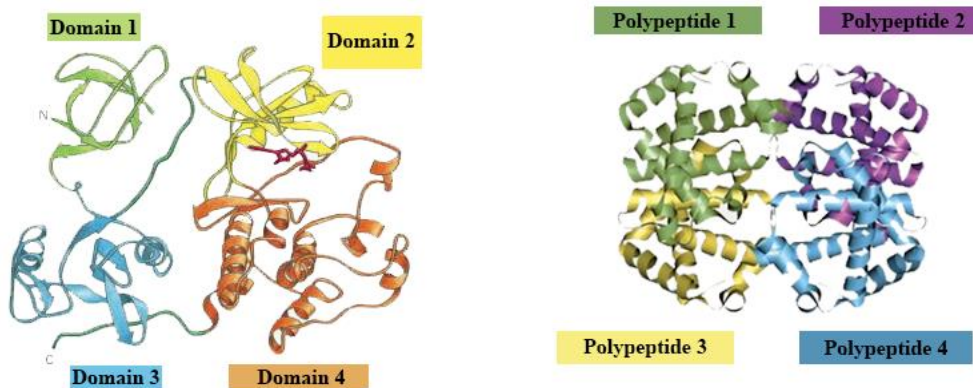
Figure 1.12 Protein folding starts with primary structure and proceeds through secondary, tertiary, and finally quaternary structure.

Adapted from Alberts 2002 (45).

1.2.3.   Protein modifications

After the proteins have obtained their three-dimensional structure, they can still undergo further modifications that can alter protein function, protein localization, and protein interaction (53). This process occurs in both eukaryotic and prokaryotic cells. There are four categories of post-translational modifications: protein cleavage, addition of chemical groups, addition of molecules, and formation of intramolecular bonds. Some proteins, including the magnetosome protein MamE, require cleavage by proteases in order to become active. These proteases are commonly site-specific and hydrolyze the peptide bonds between amino acids to create shorter polypeptide chains. Chemical groups such as methyl, acetyl, or most commonly phosphate groups can be added onto amino acids of mature proteins (48). These chemical groups can alter the level of protein activity by changing protein-protein or protein-substrate interactions. One common example of the addition of complex molecules to mature proteins is glycosylation (54). Glycosylation involves the covalent bonding of polysaccharides to target proteins, and this process can have a critical role in the correct folding of the final protein structure. This process occurs both in the endoplasmic reticulum and Golgi apparatus of eukaryotic cells. In prokaryotes, oligosaccharides are transferred from a lipid carrier to the target protein (55). Proteins that are to be secreted outside of the cells to function as extracellular proteins often undergo post-translational modifications that include covalent bonding of quaternary structures. These bonds stabilize the protein further so that it can withstand a wide variety of extracellular conditions (46).

1.2.4.   Protein sorting

In order to carry out their function, mature proteins need to be transported to their appropriate locations within or outside the cell. Proteins are transported using information that is present within their amino acid sequence (56). These sequences, also known as signal peptides, have a small positively charged, hydrophilic N-terminal region, 10-15 hydrophobic amino acids in the middle, and a small polar C-terminal region (57). Once the protein has reached its functional location, the signal peptide is generally cleaved from the protein.

In eukaryotes, the Golgi apparatus is primarily responsible for protein and lipid transport. After proteins are synthesized in the endoplasmic reticulum (ER), they enter the Golgi and undergo many post-translational modifications, including glycosylation, as they move through the Golgi (Fig. 1.13). Proteins then leave by being transported in vesicles that bud off the trans side of the Golgi, that is, the side facing away from the ER. Depending on the signal peptide of the protein, the vesicle can be directed to intracellular locations such as the mitochondria, the nucleus, peroxisomes, or the cytosol, or can be transported out of the cell in secretory vesicles.

In prokaryotes, proteins may function in the cytoplasm; be sorted to the plasma membrane, periplasm (in gram-negative bacteria) or cell wall (in gram-positive bacteria); or be secreted (58). Bacterial proteins contain signal peptides within their protein sequences to allow for proper sorting. These peptides can be simple tags such as N-terminal signal peptides for translocation across the cytoplasmic membrane (58). These tags are recognized by the bacterial co-translation pathway proteins SecA or SecB and

are similar to eukaryotic protein sorting mechanisms involved in targeting proteins to the

endoplasmic reticulum. In gram-negative bacteria, more complex protein targeting

mechanisms exist to translocate proteins across the outer membrane. These proteins have

targeting signals such as noncleavable C-terminal sequences and are recognized by

secretory machinery proteins T1SS to T6SS (58). Although prokaryotes lack intracellular

organelles, proteins may assemble onto cytosolic structures such as gas vesicles or, in the

case of MTB, magnetosomes.
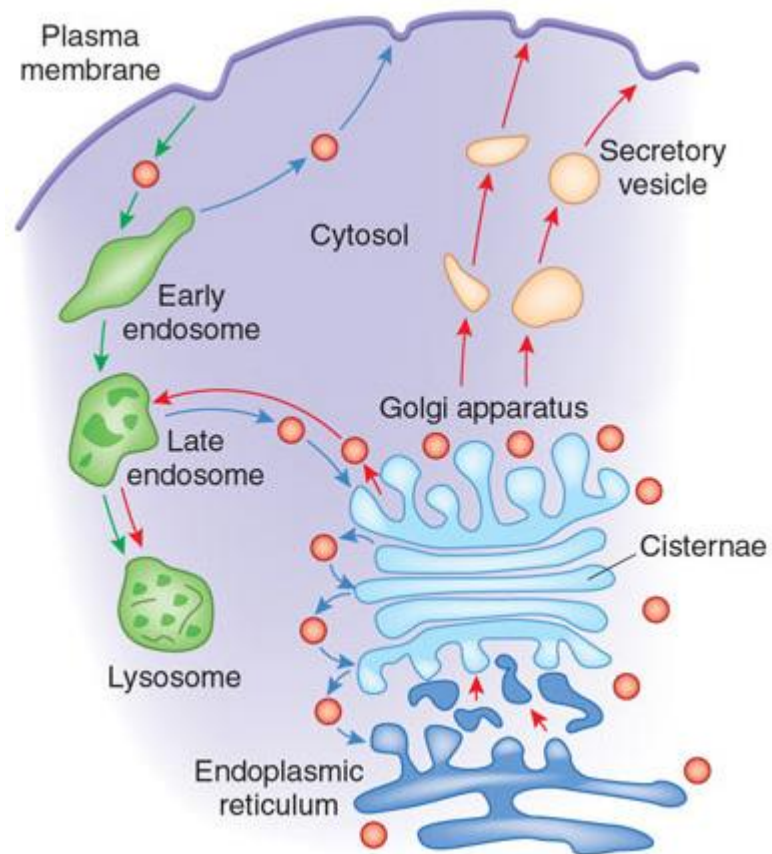
Figure 1.13 The Golgi apparatus is in charge of modifying and sorting of proteins for transport throughout the eukaryotic cell.

Red balls represent vesicles being transported throughout the cell.

1.2.5.   Protein degradation

Proteins can remain active in the cell as short as a few minutes to as long as several days (59). In eukaryotes, there are two major protein degradation pathways: the ubiquitin-proteasome pathway and the lysosomal proteolysis pathway. The ubiquitin-proteasome pathway uses chains of multiple ubiquitin polypeptides to tag proteins via lysine residues for rapid degradation (52). Polyubiquinated proteins are recognized by proteasomes, which are large, multisubunit protease complexes. In lysosomal proteolysis, lysosomes uptake proteins and break them down using digestive enzymes such as proteases. One pathway that leads to lysosomal proteolysis is the formation of autophagosomes through budding of the ER (52). These autophagosomes, which contain proteins to be degraded, will fuse with lysosomes. This uptake can be nonselective, although some cytosolic proteins are taken up in a selective manner through recognition of a specific amino acid sequence.

In prokaryotes, cells do not have lysosomes, autophagosomes, or ubiquitin; however, protein degradation is still selective and highly regulated. Protein degradation is mediated by ATP-dependent proteases, which use ATP hydrolysis to recognize, unfold, translocate, and degrade protein substrates (60). These proteases recognize both misfolded proteins and proteins that have specific degradation tags.

1.2.6.   Protein-protein interactions

Proteins rarely function alone. Such as in the stepwise assembly of the magnetosome, proteins frequently rely on other proteins to perform their functions. Protein-protein interactions are highly-specific contacts between two or more proteins

that render the protein(s) functional, as proteins often regulate one another. The main forces involved in protein-protein interactions are steric and hydrophobic interactions, electrostatic forces and hydrogen bonding (61).

1.2.6.1. Steric complementarity

Proteins that interact with each other usually have interface surfaces that are complementary to each other (62). The proteins may interact and form a flat protein-protein interface or a twisted interface (55). The majority of protein-protein interfaces also contain cavities which complement the shape and electrostatic forces of the two proteins.

1.2.6.2. Hydrophobic interactions

Proteins that interact will often have their hydrophobic domains facing each other. This conformation is energetically favourable as it keeps both proteins' hydrophobic (domains) away from the aqueous environment. The hydrophobic regions on the protein-protein contact interfaces are organized in patches, with the number of patches varying from 1 to 15 and the size mostly in the range of 200 to 400 Angstroms (61).

1.2.6.3. Electrostatic forces

Electrostatic potential energy is decreased by the interaction between charged atoms of two interacting proteins (63). It is a type of non-covalent interaction that occur between positively- and negatively-charged atoms. These charges are localized in clusters on the protein-protein interface and each interface can hold up to 12 charged groups (54). Salt bridges favourably form across these interfaces due to the distribution of opposite charges on these interfaces.

1.2.6.4. Hydrogen bonding

Another possible noncovalent protein-protein interaction are hydrogen bonds, which are dipole-dipole attractions between molecules. These interactions arise between hydrogen atoms that are covalently bonded to a highly electronegative atom such as nitrogen, oxygen, fluorine, etc. The number of hydrogen bonds on a protein-protein interface is proportional to the size of the interface, with an average of 10 bonds per interface (54). The majority of hydrogen bonds are formed between amino acid side chains, with the exception being β-sheet interfaces or protein complexes with substrates capable of forming hydrogen bonds.

1.2.6.5. Aqueous interfaces

Water molecules surround contacting protein surfaces and are within cavities of the protein-protein interface. These water molecules form hydrogen bonds with protein groups and other water molecules to form an aqueous network along the interface (54). The aqueous network helps stabilize the protein complexes by increasing the shape and charge complementarity of the interface.

1.2.6.6. Conformational changes

Some proteins that interact undergo structural changes when they come together and form complexes. When the proteins interact, they induce changes in the positions of their amino acid side chains and thereby move the main protein chain. These rearrangements are energetically favourable because they enable additional hydrogen bond formation and packing of amino acid residues (54).

1.2.7. Fluorescent proteins

Fluorescent molecules, or fluorophores, are chemical compounds that can emit light when excited at a specific wavelength. Different fluorophores have distinct characteristics and structure, and typically contain several large aromatic groups (64). Fluorophores can be classified generally into four categories: fluorescent proteins, small organic compounds, synthetic polymers, or multi-component systems. In the context of this dissertation, the focus will be placed on fluorescent proteins.

Many types of fluorescent proteins that emit different colours are used as fluorescent tags for optical bioimaging (65). The earliest fluorescent protein that was isolated and developed was the green fluorescent protein (GFP), which was derived from aequorin protein purified from *Aequorea victoria* jellyfish in the 1960s and 1970s. Since then, many fluorescent proteins have been developed, notably the yellow fluorescent protein (YFP) and the red fluorescent protein (RFP), from which the tandem Tomato (tdTomato) fluorescent protein was modified. These proteins are very useful in the field of cellular and molecular biology and can be applied in the monitoring of gene activation, or the selective labeling and tracking of proteins, of organelles, and cells (66).

GFP is the most common fluorescent protein used in imaging. The protein emits green light when stimulated with ultraviolet or blue light (59). It is relatively small (28 kDa), compact, and chemically inert (ie. it tends not to interact with the environment in which it is expressed). In this dissertation, GFP was used as a reporter gene where it was directly attached to a protein of interest (magnetosome protein).

tdTomato is a fluorescent protein introduced in 2004 as a variant of the RFP DsRed (67). The protein emits red light when stimulated with green light. It is a 54 kDa tandem protein (contains two fluorescent proteins) and is reported to be 6 times brighter than GFP. It is also used as a reporter gene in this dissertation and is also directly attached to magnetosome proteins to form fusion fluorescent-magnetosome proteins.

1.3. The cytoskeleton and molecular motors

The cytoskeleton is a dynamic network of proteins that form filaments and interlink throughout the cytoplasm of both eukaryotic and prokaryotic cells. It performs many roles, primarily to provide and maintain the cell's shape (68). The cytoskeleton also allows cells to migrate, moderates cell signaling pathways, allows for uptake of extracellular materials and their transport, plays a crucial part in cellular division, and holds and organizes intracellular components (61).

1.3.1.　The eukaryotic cytoskeleton

The eukaryotic cytoskeleton is made up of three main groups of filaments: microfilaments, intermediate filaments, and microtubules. Each filament is made up of the polymerization of protein subunits, with microfilaments containing actin subunit and microtubules containing tubulin subunits (69). Intermediate filaments are made up of different protein subunits depending on the cell type and can contain keratin, lamin, desmin, etc.

Microfilaments, or actin filaments, are the main filaments responsible for cell shape and movement. They also form the tracks on which myosin molecules walk on for intracellular transport (70). Intermediate filaments also function to hold the cell's shape

through tension of the filaments. These filaments organize the intracellular structure of the cell, and anchor organelles and structure the cytoplasm (71). Intermediate filaments also enable cell signaling and communication by forming cell-cell connections and cell-matrix junctions. Microtubules are responsible for structural components of the cell, for cell division, and have a major role in intracellular transport. Cilia and flagella, which function in receiving sensory information, processing extracellular signals, and cell motility, are made up of microtubules. Microtubules are responsible for the movement and separation of chromosomes during mitosis. They also act as tracks for the molecular motors dyneins and kinesins, which transport organelles and vesicles in the cell (72).

1.3.2.   The prokaryotic cytoskeleton

Until 1992 it was thought that the cytoskeleton was exclusive to eukaryotes; however, it was discovered that bacteria have proteins that are homologous to tubulin and actin (73). The cytoskeleton in bacteria play essential roles in cell division, function to determine and maintain cell shape, and determine cell polarity (74).

In bacteria, the protein MreB is a homologue of eukaryotic actin. Non-spherical bacteria rely on MreB to maintain cell shape. This protein assembles into a rigid, helical network that lies under the cytoplasmic membrane and covers the entire length of the bacterial cell (75). MreB also aids in cell division and is responsible for determining bacterial polarity by moderating the positioning of bacterial polar proteins (76).

The bacterial proteins ParM and SopA are structurally similar to actin, but have functions similar to eukaryotic microtubules (77). These proteins polymerize bidirectionally and thus are dynamic molecules, a characteristic of tubulin molecules.

These proteins are involved in plasmid separation, a form of DNA replication in the

bacteria. The role ParM has in plasmid separation is akin to the role of tubulin in

chromosome separation in the eukaryotic cell (78).

The bacterial protein crescentin is homologous to eukaryotic intermediate

filaments. It organizes into helical filament structures and supports crescent- and helical-

shaped bacteria by associating with the cell membrane on one lateral side of the cell (79).

The protein has domains similar to eukaryotic keratin and lamin proteins (79).

1.3.3.   The cytoskeleton in magnetotactic bacteria

Magnetotactic bacteria are unique in that they contain organelles in the form of

magnetosomes. The initial formation of these magnetosomes require the invagination of

the bacterial plasma membrane. In the MTB species AMB-1, it is reported that a group of

at least 5 proteins, MamI, L, B, Q, and Y, are responsible for the bending and shaping of

the plasma membrane into the magnetosome membrane (80). These proteins function to

bend and sustain plasma membrane curvature through membrane scaffolding much

similar to dynamin (13). Additionally, they remodel and stabilize the membrane by the

insertion transmembrane helices.

Once formed, these magnetosomes are organized in chains and require the

organization of MamK, an actin-like protein that polymerizes and forms filaments

throughout the bacteria (13). MamK also localizes alongside MreB, another actin-like

protein present in MTB species. Together, these two proteins form filamentous branches

that function in cell morphology and organization (81). MamK is also suggested to

function similar to the bacterial actin-like protein ParM, in which they both generate

mechanical forces through polymerization and depolymerization (13, 82, 83). MamJ, another protein that is part of the *mamAB* operon, interacts with MamK and is suggested to attach magnetosomes to MamK filaments. Altogether, these MTB proteins suggest that different types of bacteria develop specific cytoskeletal proteins to accommodate their specific functions.

1.3.4. Active transport

1.3.4.1.Molecular motors in vesicle transport

Molecular motors are molecules that are capable of producing mechanical work. These molecules perform active transport of intracellular cargo or organelles, and are responsible for muscle contraction or cellular movement, by consuming energy typically in the form of ATP (84). Eukaryotic cells have several different types of cytoskeletal motors (meaning that they operate by interacting with cytoskeletal filaments) such as myosin, kinesin, and dynein (Fig 1.14).
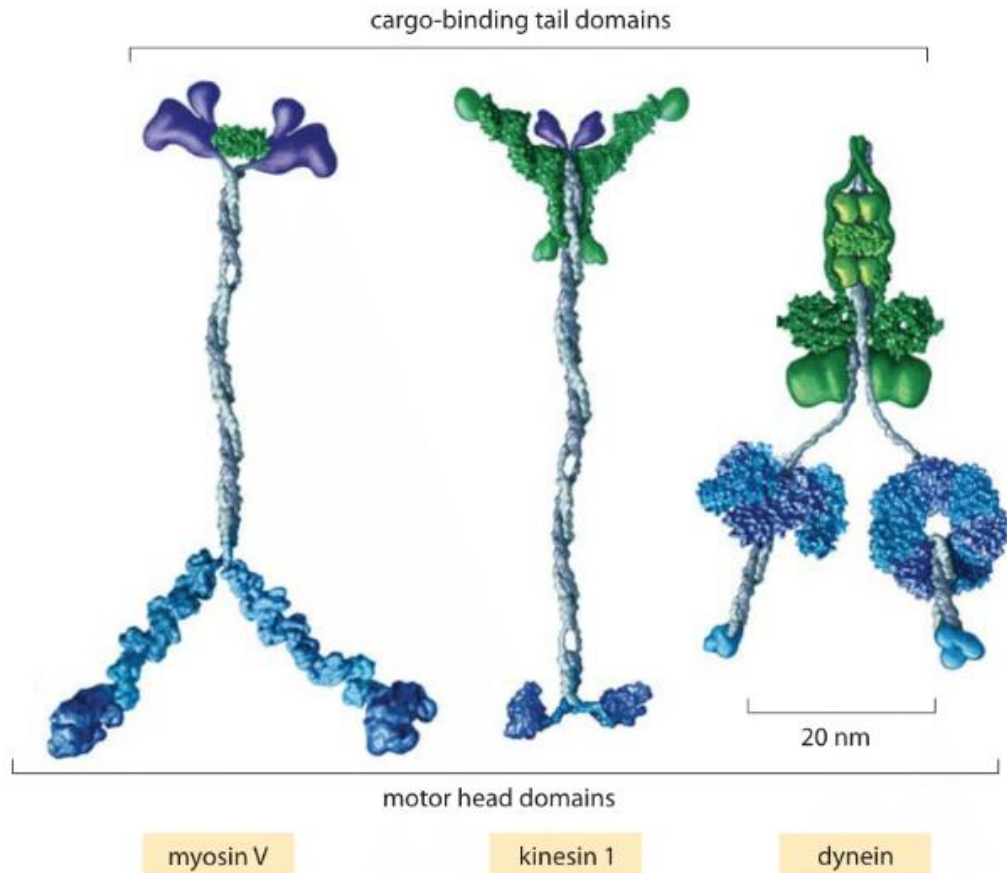
Figure 1.14 The three classes of cytoskeletal molecular motors in eukaryotic cells.

Myosin molecules bind to actin filaments, kinesin molecules bind to microtubules, and

dynein molecules bind to filaments specific to their cell type. The top of the figure shows

the cargo-binding tail domain on which various vesicles or organelles can bind. The

bottom of the figure shows the head domain that interacts with the filament on which

they walk. Figure adapted from Howard 2001 (85).

Myosin molecules have a major role in muscle contraction, although they are

responsible for a multitude of other cellular motor functions such as intracellular cargo

transport, cytoplasmic streaming, cell division, cell motility, etc (85, 86). Myosins are a

large family of molecular motors, and humans have over 40 different myosin genes. Due

to their variety, myosin molecules move at a wide range of speeds along actin filaments, from myosin VI moving at 60 nm/s to Myosin XI moving at 60,000 nm/s (78).

Kinesin molecules have roles in mitosis, meiosis, intracellular cargo transport, and axonal and intraflagellar transport (50). These proteins walk on microtubules and specialize in anterograde transport, in which they transport cargo from the center of the cell towards the periphery. Kinesins that take part in mitosis and meiosis move at speeds ranging from 20 to 90 nm/s, those that aid in vesicle transport move at 700-800 nm/s, and those that aid in flagellar or axonal transport move at 2000 nm/s (78).

Dynein molecules transport cargo, aid in the movement of cells through cilia and flagellar beating, and aid in mitosis (87). These molecules travel on microtubules and specialize in retrograde transport, in which they transport cargo from the periphery or exterior of the cell towards the center. There are two types of dynein; axonemal dynein that are responsible for the movement of cilia and flagella and cytoplasmic dynein that are responsible for cargo transport and centrosome assembly in mitosis. Axonemal dynein moves at speeds up to 7000 nm/s, while cytoplasmic dynein move much slower at 1000 nm/s (78).

1.3.5. Molecular diffusion

At the scale of molecules and organelles, collisions with solvent molecules result in molecular and organelle diffusion, and this ubiquitous random type of motion exists alongside to the directed motions provided by molecule motors. Molecular diffusion, or particle diffusion, is the thermal movement of all molecules and is affected by temperature, viscosity of the medium in which the particle resides, and the size of the

particle (88). It is characterized by the diffusion coefficient, a quantity that represents to which extent the particle can spread by diffusion in a certain amount of time. As temperature increases, so does the kinetic energy of the particles, and thus particles will diffuse at a faster rate (the diffusion coefficient increases). As the medium becomes more viscous, particles are more restricted in their movement and thus diffuse at a slower rate (the diffusion coefficient decreases). The larger a particle is, the more mass and inertia it contains and thus it will diffuse at a slower rate (smaller diffusion coefficient) than smaller particles. The random diffusive motion of particles in a medium is called Brownian motion (89). Because of the random nature of Brownian motion, particles will diffuse about until they are evenly spread within the medium. Diffusing particles only change direction when they bump into another particle or solvent molecule or bump into the solid confinement of the medium (90).

1.4. Principles of the MRI signal

In order to appreciate the potential of magnetosome proteins as gene-based MR contrast agents, we must understand the source and principles of the MRI signal. The MRI signal comes from protons (hydrogen nuclei) in the subject being imaged. As there are many protons in biological samples, the signal is strong and allows resolution of structures in small animals (*e.g.* rodents) at fractions of a mm and in larger animals (*e.g.* dogs, pigs) and humans at approximately 1 mm^3. However, discrimination of different tissues by proton density alone is poor since the concentration of protons in soft biological tissues does not vary greatly. Instead, since protons in different tissues often have different spin relaxation behaviours, detection of these can improve tissue discrimination. Both the application of radiofrequency (RF) pulses at specific frequencies

and the switching of magnetic field gradients can be used to distinguish different proton

relaxation rates in a biological sample. In principle, there are two main classes of

relaxation effects which are called spin-lattice or longitudinal relaxation time (T1) and

spin-spin or transverse relaxation time (T2), with the units of time usually expressed in

seconds or milli-seconds (s or ms). Often these relaxation times are converted to

relaxation rates (R1 and R2) by inverting T1 and T2, resulting in units of inverse time,

e.g. s^{-1}. Furthermore, spin-spin relaxation is represented by two quantities: R2 and R2*,

where R2* ≥ R2. While R2 is measured by using spin echoes, R2* is measured with

gradient echoes. In addition, while R2 represents an intrinsic property of the tissue, R2*

is affected not only by tissue properties but also by non-uniformities in the local magnetic

field. As such, R2* is very sensitive to the presence of iron, particularly in the form of

magnetite. The difference between R2* and R2 is represented by R2$'$ and is often referred

to as the non-recoverable spin-spin relaxation.

1.4.1. Paramagnetic contrast agents

Innate relaxation behaviours of different tissues are often not sufficient to

discriminate diseased from normal states within a given organ system (*e.g.* liver, heart);

hence, paramagnetic MRI contrast agents have been developed. These agents provide

additional discrimination where they accumulate differentially in a particular tissue.

Paramagnetic agents primarily shorten the T1 relaxation time of the protons (*i.e.* increase

R1), with extent of shortening dependent on tissue concentration of the paramagnetic

contrast agent. It is important to note that paramagnetic contrast agents, in general, do not

alter the magnetic field at the tissue level. Rather, through dipole-dipole interactions, they

directly increase the R1 relaxation rate of those water molecules that come in close

contact with the paramagnetic centers (91). In addition, paramagnetic agents have little effect on spin-spin relaxation; at all times, $T2 \leq T1$. Although, when concentration of the paramagnetic contrast agent becomes high enough, T1 can be reduced to less than the tissue T2 value, at which point T2 will approximate T1. The relaxivity (R1) of paramagnetic contrast agents for a typical MRI in medical imaging (on 1.5T and 3T systems) is about 4 $(mM\ sec)^{-1}$ (92) and the sensitivity of detection is approximately 0.1 mM. To achieve this requires injection of approximately 0.1 mmole contrast agent per kg body weight, which is a very large amount of contrast agent to be incorporated by the cell. Tracking cells labelled with paramagnetic contrast agents is thus limited.

1.4.2.   Ferromagnetic contrast agents

Ferromagnetic contrast agents primarily affect spin-spin relaxation times and their T2 relaxivity is generally much greater than the T1 relaxivity of paramagnetic agents. For example, SPIO particles were one of the first iron particles to be introduced. Their R2 relaxivity is so high, they can be loaded into cells and tracked after transplantation with MRI. For example, if mammalian cells labeled with approximately 60 pg Fe/cell are injected in a mouse brain, then individual cells can be detected using 1.5T MRI with a specialized RF coil and an enhanced magnetic field gradient for small animal imaging (93). In this work, Heyn *et al.* used a 3D Fast Imaging Employing Steady-state Acquisition (FIESTA) pulse sequence to emphasize the difference in spin-spin relaxation times.

SPIO particles have an iron core (magnetite, also called iron (II, III) oxide) of approximately 30 nm in diameter. The reported T2 relaxivity of SPIO particles is 180

$(mM s)^{-1}$ at 7T (21, 94). However, when they are incorporated into cells, the T2 relaxivity is considerably reduced (94). In addition, tracking cells with SPIO labels has the following limitations: a) release of SPIO through apoptosis or exocytosis can label interstitial tissue or phagocytic cells and falsely report the targeted cellular activity, and b) in proliferating cells, the number of SPIO particles per cell drops leading to loss of signal in longitudinal studies (95).

1.4.3. MRI of magnetosomes

Although SPIO labeled cells give the needed contrast-to-noise ratio (CNR) to follow cells immediately after transplantation, one needs an MRI reporter gene to follow the fate of transplanted cells over days and weeks. Meriaux *et al.* have shown that individual magnetosomes particles have a relaxivity similar to SPIO particles (96). Brewer *et al*. went a step further and imaged the equivalent of MTB, obtaining an R2 value of 250 $(mM s)^{-1}$, comparable to 178 $(mM s)^{-1}$ for SPIO (21). However, when particles derived from MTB, called magneto-endosymbionts (ME), were introduced into mammalian cells, the R2 values were reduced to 35 $(mM s)^{-1}$. Similar incorporation of SPIO also reduced relaxivity to approximately the same degree: 62 $(mM s)^{-1}$. Brewer *et al.* went on to investigate the minimum number of eukaryotic cells that could be observed if ME labeled cells were injected into the mouse brain and imaged by MRI at 7T. They labeled each cell with approximately 400 ME; injected mice with either 100 or 1000 cells; were able to detect both; and concluded that as few as 100 such cells could be tracked. Interestingly, Goldhawk *et al.* took a different approach (10). Taking values reported by Benoit *et al.* (97), in which MTB were imaged within mouse tumours, and using the amount of iron per MTB as well as R2 values measured *in vivo*, a calculation

was performed determining the minimum number of eukaryotic cells needed to change

R2 by 1 s^{-1}. That gave the minimum number of cells that could be detected if each cell

contained 100 times the amount of iron in MTB. This was based on the diameter of a

bacterium, which is about one-tenth the diameter of a mammalian cell. Hence, the

volume of a mammalian cell would be approximately 1000 times greater than that of a

bacterium. Using this approach, they estimated that a minimum of 3 cells could be

detected in small animals and a minimum of 2,600 cells in large animals/humans (10).

These very different approaches give somewhat different results, with incorporation of

400 ME per cell providing a lower sensitivity (approximately 50 cells) than the

equivalent number of magnetosomes in 100 ME (approximately 3 cells) and suggesting

that reporter gene expression based on the magnetosome may be more sensitive by a

factor of approximately 70 (50 times 4 all divided by 3). Of course, this outcome depends

on generating sufficient magnetosome-like particles per cell using key magnetosome

genes with essential roles in iron biomineralization to achieve the proposed iron per cell.

Lee *et al.* (98) investigated the dependence of R2 on interecho time in mammalian

cells expressing a single MTB gene: *magA*. Compared to control cells they found that

MagA-expressing cells had greater iron content and that increases in R2 with increasing

interecho times. As it is known that R2 relaxivity of iron oxide particles depends on echo

spacing (99, 100), this strongly suggests that iron particles were formed from a single

MTB iron-handling gene. Lee *et al.* further suggested how these interecho effects could

be used to uniquely image magnetosome-like particles, by acquiring image-based R2

measurements with two different interecho times and, from the difference, assessing the

iron-related contribution to R2 (98).

Cho *et al.* further demonstrated that mammalian cells expressing MagA from an inducible promoter could be successfully implemented as an MRI genetic reporter (20). While significant effects on T2- and T2*-weighted images were reported, the technology has not been widely adapted probably because the contrast was low and relatively large amounts of tissue had to be selected to get sufficient signal to noise.

1.5. Defining reporter gene expression

Genetic encoding of reporter genes enables the tracking of several features of cellular activity, regardless of platform used to detect the encoded proteins. For example, although all somatic cells contain the full complement of an organism's DNA (the genotype), not all of these genes are expressed at once. Each cell type regulates the expression of individual genes to obtain specific cell functionality (the phenotype). The transcription factors that regulate gene expression thus perform a key role in determining what function a cell has. The same transcription factor (TF) regulation applies to reporter genes that are introduced for the purpose of monitoring cellular activity.

Broadly-speaking, there are two types of TF regulation: constitutive and selective. On the one hand, genes that are expressed constitutively are generally required for cell functions that operate continuously, like glycolysis or oxidative phosphorylation. The "housekeeping" factors that control these genes are virtually always present and ready to drive the required gene expression, to preserve baseline functioning in most any cell type. On the other hand, selective TF activity regulates specific gene expression that distinguishes one cell type from another. This category of TF is therefore characteristic of

specific cell type(s), microenvironment, stage of development, health, and disease. Every

cell contains both types of TF.

Simply-stated, a reporter gene encodes a protein that can be reliably detected by

some method of choice. If the reporter gene is constitutively-expressed, it generates a

constant label that can theoretically be monitored through all phases of the cell, including

its proliferation and differentiation. If the reporter gene is selectively-expressed, it

imparts a signal that will only be detected when specific TF activity is present, including

those that trigger a disease process like inflammation, fibrosis, or metastasis.

Traditionally, "reporter gene expression" is a term coined to describe this type of

selective gene expression. It is a powerful tool for understanding cellular phenotype and

identifying what factors contribute to function and malfunction.

1.5.1. Imaging reporter

Most cells do not have sufficient, inherent contrast to enable *in vivo* molecular

imaging by any modality. With little exception, an imaging reporter is needed to

distinguish background signal from cellular target. Reporter gene technology not only

serves this purpose but will outperform exogenous contrast with respect to duration of

signal and relationship to cellular molecular activity (101, 102, 103). What remains is the

challenge of developing imaging reporter genes with high enough contrast to noise ratio

(CNR) for satisfactory molecular imaging in living subjects.

This challenge has been met with varying levels of success, depending on the

imaging modality (10, 104, 105). Toward applications in cell therapy, several methods

are available to quantitatively image transplanted cells using reporter genes like

thymidine kinase for nuclear medicine or luciferase for optical imaging. However, the use of reporter genes in nuclear medicine requires injection of radioactive substrate and creates a massive background signal, often obscuring the desired signal. In optical techniques, poor depth of penetration requires either the insertion of invasive light detectors and/or surgical exposure of the targeted area.

Although transforming cells with foreign DNA for imaging with reporter genes is not yet readily accepted by regulatory bodies for human use, the preclinical market for this technology is huge and will inform medical practices. For example, gas vesicles (bacterial structures that provide buoyancy) have been expressed in both human cells and *E. coli* to develop ultrasound acoustic reporter gene imaging (106, 107). Similarly, to develop reporter gene imaging for MRI, various MTB transgene expression systems have been developed (20, 31, 43, 45, 46).

1.5.2. The search for an MRI reporter

Of all the medical imaging platforms, MRI provides the best resolution of soft tissues at any imaging depth using non-ionizing radiation. Already a mainstream clinical imaging platform, what MRI lacks in sensitivity can be compensated for by contrast agents that either amplify the MR signal, like hyperpolarized compounds, or modify the signal, like iron, which amplifies differences in MR signals. In addition, many MRI sequences are available to capture different aspects of the biophysical properties that govern a cell's response to magnetism. Beyond the standard longitudinal (T1) and transverse (T2, T2*) relaxation times of water protons, methods have been developed to monitor changes in sodium, pH, oxygenation of hemoglobin (allowing detection of

neuronal activity in the brain (108) and tissue oxygenation in the heart (109)), blood flow

in the brain (110) and diffusion (111), to name a few. More specifically,

neurotransmitters such as glutamate have been used as endogenous functional MRI

contrast agents to detect synaptic activity and evaluate energy demands in different

regions of the brain (108). Arterial spin labelling, an MRI technique that uses blood-

water for endogenous flow contrast in the brain, provides diagnostic information for

pathologies such as Alzheimer's disease and frontotemporal dementia (110). In the heart,

a technique termed cardiac functional MRI uses carbon dioxide as a contrast agent to

assess myocardial oxygenation and help detect ischemic heart disease (109). Diffusion

MRI, which takes advantage of the movement of water molecules through tissue

structures, has applications in a variety of diseases. It is becoming a popular method of

imaging cancer since tumors have decreased water diffusion due to increased cell mass

and density (111).

Extensive opportunities for multi-parametric imaging, with or without the

addition of contrast agents, mean that scientific breakthroughs facilitated by using MRI

afford excellent value for the investment in MR research, including technical

improvements in hardware and software by imaging scientists and engineers. Moreover,

the movement toward hybrid MR scanners, like positron emission tomography

(PET)/MRI, creates further options for comprehensive imaging with complete

registration of signals from multiple organ systems, reducing the negative impact of

motion on image interpretation, adding sensitivity of a radiolabel to the MR image, and

supporting the acquisition of multiple signals within a single imaging session. In addition,

because MR image acquisition is a relatively slow process, when imaging with PET/MRI

over longer times, the concentration of radioisotope can be reduced, and the average PET signal collected over that longer time.

In view of these MRI attributes, a reporter gene expression system that enhances T1- or T2-weighted contrast for molecular MRI opens another phase in the evolution of this modality. For example, gene-based MRI reporters that generate contrast in cell grafts are ideal tools to aid long-term cell tracking (112). Several of these reporter systems have been investigated for monitoring of metastatic cancer and include creatine kinase (113), divalent metal transporter (DMT1) (114), β-galactosidase (115), and tyrosinase (116). Ferritin has been reported for long-term monitoring of stem cell grafts in mice (117, 118, 119, 120). By drawing on examples in nature of cells that generate their own endogenous magnetism, we have developed a template for further exploration of MRI reporter gene technology. MTB have the potential to synthesize and regulate iron biominerals with superparamagnetic qualities but no cytotoxicity. To date, the magnetosome protein MagA has been investigated as an MRI gene-based contrast agent (43, 44).

1.5.3. Magnetotactic bacteria and their magnetic properties

While iron is a required co-factor in all cells, few if any generate as refined an iron biomineral as found in MTB. These prokaryotes synthesize particles of magnetite (Fe_3O_4) or greigite (Fe_3S_4) within a membrane-enclosed vesicle called a magnetosome (121). Protected from iron toxicity by the lipid bilayer, MTB use their magnetosomes to respond to the earth's magnetic field and display magnetotaxis appropriate to Northern and Southern hemispheres (122, 123). A growing body of literature has examined

multiple applications of MTB and magnetosomes (124, 125, 126), taking advantage of their navigational properties in response to magnetic fields (127, 128), their ability to deliver thermal therapy (129, 130, 131), and their precise synthesis of crystalline particles (132, 133, 134, 135) which, for example, could be useful as a reporter probe in magnetic particle imaging (10).

1.6. Summary

Prospects for future development of molecular MRI place the spotlight on synthetic biology, to build magnetosome-like nanoparticles in mammalian cells that enhance gene-based iron-labelling and MRI contrast for reporter gene expression. Results obtained from the expression of single MTB genes in mammalian hosts indicate the compatibility of these bacterial iron-handling proteins in a variety of cell types. However, no one MTB or magnetosome gene alone has provided optimal iron contrast for non-invasive imaging. A more faithful adaptation of MTB strategy for iron biomineral formation requires assembling multiple magnetosome proteins on a designated membrane. This role of biomineral compartmentalization in the design and regulation of biogenic iron nanoparticles has generally been under appreciated, perhaps because it adds complexity to the structure. Nevertheless, with such complexity comes multiple opportunities for regulating the magnetosome-like compartment, offering versatility in the genetic programming of reporter gene expression and in specification of the resulting iron biomineral. For MRI, there is potential for creating distinct MR signatures based on the complement of magnetosome genes expressed, the nature of their regulation by transcription factors, and the morphology of the encoded iron biomineral.

1.7. Thesis objectives and outline

The central objective of this research is to develop a rudimentary magnetosome-like nanoparticle to enable the control of a gene-based MRI contrast agent. The goal is to provide an endogenous MR label for long-term molecular imaging throughout a cell's life cycle. This technology has many applications, such as enabling the tracking of early disease activities and monitoring transcriptional activation. These can greatly improve current molecular imaging techniques. This objective is also motivated by novel observations that will be made about magnetosome protein expression in a mammalian cell system. The proteins of interest MamI, MamL, MamB, and MamE have not been expressed in a mammalian system prior to this study. Thus, the purpose of this study is also to investigate the compatibility, behaviour, localization, and interaction of these proteins with the mammalian intracellular environment. We hypothesize that the magnetosome proteins MamI, MamL, MamB, and MamE will co-localize on an intracellular membrane to form a rudimentary magnetosome-like nanoparticle in mammalian cells, and that the proteins will work together synergistically to be able to sequester iron into the magnetosome-like structure to increase cellular MR parameters.

The specific objectives of this study are to:

1.   Express magnetosome genes *mamI, mamL, mamB,* and *mamE* in a mammalian cell line.

2.   Characterize behavior of mammalian cells individually expressing magnetosome genes.

3.   Investigate potential protein-protein interactions of mammalian cells co-

expressing magnetosome genes.

4.   Evaluate the influence of magnetosome proteins MamI, MamL, MamB, and MamE on the MR signal of mammalian cells.

These specific objectives are addressed in three manuscripts (Chapters 2 to 4), which are briefly described in the following outline.

Chapter 2: Essential magnetosome proteins MamI and MamL from magnetotactic bacteria interact in mammalian cells

The project started with the expression of the two smallest magnetosome proteins, MamI and MamL, in the mammalian melanoma cell line MDA-MB-435. Protein expression was verified using immunoblotting and fluorescence microscopy. Fluorescence microscopy also revealed protein localization, interaction, and expression pattern in the cell. To further understand the behaviour of these magnetosome proteins, fluorescence correlation spectroscopy (FCS; a collaborative technique with Dr. Cécile Fradin from McMaster University) was used to determine protein diffusion coefficient and apparent radius in a cell-free system. Finally, a co-immunoprecipitation assay was conducted to investigate protein-protein interaction between MamI and MamL.

Chapter 3: Cellular distribution and motion of essential magnetosome proteins expressed in mammalian cells

This chapter details trajectory analysis of the motion of the fluorescent particles described in the previous chapter. With fluorescence microscopy, it was determined that MamL, MamI+L, and MamB had punctate, mobile expression within the cells. These particles were tracked using ImageJ, and their trajectories were analyzed using

Mathematica. Particle movement was further described by determining their velocity and diffusion coefficient. These values were compared within each magnetosome protein expression, and with molecular motors in the literature. Furthermore, connections between protein mobility and protein structure were discussed for each expression system. This chapter is a collaborative work with Dr. Cécile Fradin from McMaster University.

Chapter 4: Magnetic resonance parameters and cellular iron content of magnetosome proteins expressed in mammalian cells

After expression of magnetosome proteins MamI, MamL, MamB, and MamE in mammalian cells, their effect(s) on cellular MR signal and cellular MR content were investigated. Cells expressing magnetosome proteins were placed in wells inside of a spherical gelatin phantom, and the phantom is scanned at 3 Tesla on a Biograph mMR to obtain both longitudinal and transverse relaxation rates. To determine the effects of the magnetosome proteins on total cellular iron content, lysed cell samples were sent for elemental iron analysis using inductively-coupled plasma mass spectrometry (ICP-MS). The obtained iron concentration values were normalized to total cellular protein and compared within magnetosome protein expression systems.

Chapter 5: Conclusions, Limitations, and Future Work

This chapter summarizes the overall conclusions of this research and outlines future work that this project leads to.

1.8. References

1.   Kali A, Cokic I, Tang R, Dohnalkova A, Kovarik L, Yang HJ, et al. Persistent Microvascular Obstruction After Myocardial Infarction Culminates in the Confluence of Ferric Iron Oxide Crystals, Proinflammatory Burden, and Adverse Remodeling. Circ Cardiovasc Imaging. 2016;9(11).

2.   Kali A, Cokic I, Tang R, Dohnalkova A, Kovarik L, Yang H, et al. Persistent Microvascular Obstruction After Myocardial Infarction Culminates in the Confluence of Ferric Iron Oxide Crystals, Proinflammatory Burden, and Adverse Remodeling. Circ Cardiovasc Imaging. 2016;9:e004996.

3.   Cokic I, Chan SF, Guan X, Nair AR, Yang HJ, Liu T, et al. Intramyocardial hemorrhage drives fatty degeneration of infarcted myocardium. Nat Commun. 2022;13(1):6394.

4.   Dassanayake P. Monocyte MRI Relaxation Rates are Regulated by Extracellular Iron and Hepcidin. Scholarship@Western Electronic Thesis and Dissertation Repository: Western University, London, Canada; 2019.

5.   Delaby C, Pilard N, Goncalves A, Beaumont C, Canonne-Hergaux F. Presence of the iron exporter ferroportin at the plasma membrane of macrophages is enhanced by iron loading and down-regulated by hepcidin. Blood. 2005;106:3979-84.

6.   Wilk B, Wisenberg G, Dharmakumar R, Thiessen J, Goldhawk D, Prato F. Hybrid PET/MR Imaging in Myocardial Inflammation Post-Myocardial Infarction. J Nucl Cardiol. 2019:In press.

7.   Wang YX. Superparamagnetic iron oxide based MRI contrast agents: Current status of clinical application. Quant Imaging Med Surg. 2011;1(1):35-40.

8.   Nyström N, Hamilton A, Xia W, Liu S, Scholl T, Ronald J. Longitudinal Visualization of Viable Cancer Cell Intratumoral Distribution in Mouse Models Using Oatp1a1-Enhanced Magnetic Resonance Imaging. Invest Radiol. 2019;54:302-11.

9.   Goldhawk D, Rohani R, Sengupta A, Gelman N, Prato F. Using the magnetosome to model effective gene-based contrast for magnetic resonance imaging. WIRES Nanomed Nanobiotechnol. 2012;4:378-88.

10.   Goldhawk D, Gelman N, Thompson R, Prato F. Forming magnetosome-like nanoparticles in mammalian cells for molecular MRI. In: Bulte J, Modo M, editors. Design and Applications of Nanoparticles in Biomedical Imaging. Switzerland: Springer International Publishing; 2017. p. 187-203.

11.   Hentze M, Muckenthaler M, Galy B, Camaschella C. Two to tango: regulation of mammalian iron metabolism. Cell. 2010;142:24-38.

12.   Thomas A, Morani A, Liu P, Weadock W, Hussain H, Elsayes K. Iron-Containing Abdominal Pathologies: Exploiting Magnetic Susceptibility Artifact on Dual-Echo Gradient-Echo Magnetic Resonance Imaging. J Comput Assist Tomogr. 2019;43:165-75.

13.   Lefevre CT, Trubitsyn D, Abreu F, Kolinko S, Jogler C, de Almeida LG, et al. Comparative genomic analysis of magnetotactic bacteria from the Deltaproteobacteria provides new insights into magnetite and greigite magnetosome genes required for magnetotaxis. Environmental microbiology. 2013;15(10):2712-35.

14.   Murat D, Quinlan A, Vali H, Komeili A. Comprehensive genetic dissection of the magnetosome gene island reveals the step-wise assembly of a prokaryotic organelle. Proc

Natl Acad Sci USA 2010;107:5593–8.

15. Uebe R, Schuler D. Magnetosome biogenesis in magnetotactic bacteria. Nat Rev Microbiol. 2016;14:621-37.

16. Nudelman H, Zarivach R. Structure prediction of magnetosome-associated proteins. Front Microbiol. 2014;5:article 9.

17. Ramanujan R. Magnetic Particles for Biomedical Applications. In: Narayan R, editor. Biomedical Materials2009. p. 477-91.

18. Quinlan A, Murat D, Vali H, Komeili A. The HtrA/DegP family protease MamE is a bifunctional protein with roles in magnetosome protein localization and magnetite biomineralization. Molecular Microbiology. 2011;80(4):1075-87.

19. Uebe R, Keren-Khadmy N, Zeytuni N, Katzmann E, Navon Y, Davidov G, et al. The dual role of MamB in magnetosome membrane assembly and magnetite biomineralization. Molecular Microbiology. 2018;107(4):542-57.

20. Cho I, Moran S, Paudya R, Piotrowska-Nitsche K, Cheng P-H, Zhang X, et al. Longitudinal Monitoring of Stem Cell Grafts In Vivo Using Magnetic Resonance Imaging with Inducible Maga as a Genetic Reporter. Theranostics. 2014;4:972-89.

21. Brewer K, Spitler R, Lee K, Chan A, Barrozo J, Wakeel A, et al. Characterization of Magneto-Endosymbionts as MRI Cell Labeling and Tracking Agents. Mol Imaging Biol. 2018;20:65-73.

22. Komeili A. Molecular mechanisms of compartmentalization and biomineralization in magnetotactic bacteria. FEMS Microbiol Rev. 2012;36:232-55.

23. The UniProt C. UniProt: the Universal Protein Knowledgebase in 2023. Nucleic Acids Research. 2022:gkac1052.

24. Bereczk-Tompa E, Posfai M, Toth B, Vonderviszt F. Magnetite-Binding Flagellar Filaments Displaying the MamI Loop Motif. Chembiochem. 2016;17(21):2075-82.

25. Jumper J, Evans R, Pritzel A, Green T, Figurnov M, Ronneberger O, et al. Highly accurate protein structure prediction with AlphaFold. Nature. 2021;596(7873):583-9.

26. Varadi M, Anyango S, Deshpande M, Nair S, Natassia C, Yordanova G, et al. AlphaFold Protein Structure Database: massively expanding the structural coverage of protein-sequence space with high-accuracy models. Nucleic Acids Res. 2022;50(D1):D439-D44.

27. Komeili A. Molecular mechanisms of compartmentalization and biomineralization in magnetotactic bacteria. FEMS Microbiol Rev. 2012;36(1):232-55.

28. Sun Q, Fradin C, Thompson R, Prato F, Goldhawk D, editors. Developing Magnetic Resonance Reporter Gene Imaging: Co-Expression of Magnetotactic Bacteria Genes *mamI* and *mamL*. World Molecular Imaging Congress; 2019; Montreal, Canada.

29. Schmidt N, Mishra A, Lai GH, Wong GC. Arginine-rich cell-penetrating peptides. FEBS Lett. 2010;584(9):1806-13.

30. Hershey DM, Browne PJ, Iavarone AT, Teyra J, Lee EH, Sidhu SS, et al. Magnetite Biomineralization in Magnetospirillum magneticum Is Regulated by a Switch-like Behavior in the HtrA Protease MamE. J Biol Chem. 2016;291(34):17941-52.

31. Liu L, Alizadeh K, Donnelly S, Dassanayake P, Hou T, McGirr R, et al. MagA expression attenuates iron export activity in undifferentiated multipotent P19 cells. PLOS ONE. 2019;14:e0217842.

32. Schüler D. Genetics and cell biology of magnetosome formation in magnetotactic bacteria. FEMS Microbiology Reviews. 2008;32(4):654-72.

33.   Raschdorf O, Forstner Y, Kolinko I, Uebe R, Plitzko J, Schüler D. Genetic and Ultrastructural Analysis Reveals the Key Players and Initial Steps of Bacterial Magnetosome Membrane Biogenesis. PLoS Genet. 2016;126:e1006101.

34.   Goldhawk D, Koropatnick D, Figueredo R, Prato F, Thompson R, Gelman N, inventors; European Patent # 3110952, assignee. Combined expression of contrast genes in eukaryotic cells2019.

35.   Prato F, Goldhawk D, McCreary C, McGirr R, Dhanvantari S, Thompson R, et al., inventors; USPTO Patent # US 9,556,238 B2; MMI., assignee. Magnetosome Gene Expression in Eukaryotic Cells patent US 9,556,238 B2. 2017.

36.   Yanatori I, Kishi F. DMT1 and iron transport. Free Radical Biology and Medicine. 2019;133:55-63.

37.   Kolinko I, Lohße A, Borg S, Raschdorf O, Jogler C, Tu Q, et al. Biosynthesis of magnetic nanostructures in a foreign organism by transfer of bacterial magnetosome gene clusters. Nature Nanotechnology. 2014;9:193-7.

38.   Schuler D, Uhl R, Bauerlein E. A simple light scattering method to assay magnetism in Magnetospirillum gryphiswaldense. FEMS Microbiol Ecol. 1995;132:139-45.

39.   Le Nagard L, Morillo-Lopez V, Fradin C, Bzylinski D. Growing magnetotactic bacteria of the genus *Magnetospirillum*: strains MSR-1, AMB-1 and MS-1. JOVE. 2018;140:e58536.

40.   Martel S, Mohammadi M. Switching between Magnetotactic and Aerotactic Displacement Controls to Enhance the Efficacy of MC-1 Magneto-Aerotactic Bacteria as Cancer-Fighting Nanorobots. Micromachines. 2016;7:97.

41.   Torres de Araujo F, Pires M, Frankel R, Bicudo C. Magnetite and magnetotaxis in algae. Biophys J. 1986;50:375-8.

42.   Sengupta A, Quiaoit K, Thompson RT, Prato FS, Gelman N, Goldhawk DE. Biophysical features of MagA expression in mammalian cells: implications for MRI contrast. Front Microbiol. 2014;5:29.

43.   Rohani R, Figueredo R, Bureau Y, Koropatnick J, Foster P, Thompson RT, et al. Imaging tumor growth non-invasively using expression of MagA or modified ferritin subunits to augment intracellular contrast for repetitive MRI. Mol Imaging Biol. 2014;16(1):63-73.

44.   Goldhawk DE, Lemaire C, McCreary CR, McGirr R, Dhanvantari S, Thompson RT, et al. Magnetic Resonance Imaging of Cells Overexpressing MagA, an Endogenous Contrast Agent for Live Cell Imaging. Molecular Imaging. 2009;8(3):129.

45.   Zhang X-Y, Robledo B, Harris S, Hu X. A Bacterial Gene, mms6, as a New Reporter Gene for Magnetic Resonance Imaging of Mammalian Cells. Mol Imaging. 2014:1-12.

46.   Guan X, Yang B, Xie M, Kumar Ban D, Zhao X, Lal R, et al. MRI reporter gene MagA suppresses transferrin receptor and maps Fe2+ dependent lung cancer. Nanomed. 2019;21:102064.

47.   Elfick A, Rischitor G, Mouras R, Azfer A, Lungaro L, Uhlarz M, et al. Biosynthesis of magnetic nanoparticles by human mesenchymal stem cells following transfection with the magnetotactic bacterial gene mms6. Scientific Reports. 2017;7:39755.

48.   B A. Molecular biology of the cell. 6 ed. Group TaF, editor. Abingdon, UK:

W.W. Norton & Company; 2015.

49.   Toole G, Toole S. AQA biology A level. Student book. 2 ed. Great Clarendon Street, Oxford, UK: Oxford University Press; 2015.

50.   Berg J, JL T, L S. Biochemistry. 5 ed. New York, USA: NCBI Bookshelf; 2002.

51.   Lodish H. Processing of Eukaryotic mRNA. U.S. National Library of Medicine1970.

52.   Alberts B, Johnson A, Lewis J, Raff M, Roberts K, Walters P. Molecular Biology of the Cell. 2 ed. New York and London: Garland Science; 2002.

53.   Duan G, Walther D. The roles of post-translational modifications in the context of protein interaction networks. PLoS Comput Biol. 2015;11(2):e1004049.

54.   Schubert M, Walczak MJ, Aebi M, Wider G. Posttranslational modifications of intact proteins detected by NMR spectroscopy: application to glycosylation. Angew Chem Int Ed Engl. 2015;54(24):7096-100.

55.   Li H, Debowski AW, Liao T, Tang H, Nilsson HO, Marshall BJ, et al. Understanding protein glycosylation pathways in bacteria. Future Microbiol. 2017;12:59-72.

56.   Lodish H, Berk A, Kaiser C, Krieger M, Bretscher A, Ploegh H, et al. Molecular Cell Biology. 9 ed. New York, USA: W.H. Freeman and Company; 2021.

57.   Nelson D. Principles of biochemistry. 7 ed. New York, USA: Lehninger 2017.

58.   Filloux A. Secretion signal and protein targeting in bacteria: a biological puzzle. J Bacteriol. 2010;192(15):3847-9.

59.   Cooper G. The Cell: A Molecular Approach. 2 ed. Sunderland, MA, USA: Sinauer Associates; 2000.

60.   Mahmoud SA, Chien P. Regulated Proteolysis in Bacteria. Annu Rev Biochem. 2018;87:677-96.

61.   Veselovsky AV, Ivanov YD, Ivanov AS, Archakov AI, Lewi P, Janssen P. Protein-protein interactions: mechanisms and modification by drugs. J Mol Recognit. 2002;15(6):405-22.

62.   Jones S, Thornton JM. Principles of protein-protein interactions. Proc Natl Acad Sci U S A. 1996;93(1):13-20.

63.   Maleki M, Vasudev G, Rueda L. The role of electrostatic energy in prediction of obligate protein-protein interactions. Proteome Sci. 2013;11(Suppl 1):S11.

64.   Stockert JC, Blázquez-Castro A. Fluorescence Microscopy in Life Sciences: Bentham Science Publishers; 2017.

65.   Stepanenko OV, Shcherbakova DM, Kuznetsova IM, Turoverov KK, Verkhusha VV. Modern fluorescent proteins: from chromophore formation to novel intracellular applications. Biotechniques. 2011;51(5):313-4, 6, 8 passim.

66.   Jensen EC. Use of fluorescent probes: their effect on cell biology and limitations. Anat Rec (Hoboken). 2012;295(12):2031-6.

67.   Shaner NC, Campbell RE, Steinbach PA, Giepmans BN, Palmer AE, Tsien RY. Improved monomeric red, orange and yellow fluorescent proteins derived from Discosoma sp. red fluorescent protein. Nat Biotechnol. 2004;22(12):1567-72.

68.   Alberts B. Molecular Biology of the Cell. 5 ed. New York, USA: Garland Science; 2008.

69.   Hardin J, Bertoni G, Kleinsmith L. Becker's World of the Cell. 8 ed. New York, USA: Pearson; 2015.

70.   Gunning PW, Ghoshdastider U, Whitaker S, Popp D, Robinson RC. The evolution of compositionally and functionally distinct actin filaments. J Cell Sci. 2015;128(11):2009-19.

71.   Herrmann H, Bär H, Kreplak L, Strelkov SV, Aebi U. Intermediate filaments: from cell architecture to nanomechanics. Nat Rev Mol Cell Biol. 2007;8(7):562-73.

72.   Vale RD. The molecular motor toolbox for intracellular transport. Cell. 2003;112(4):467-80.

73.   Wickstead B, Gull K. The evolution of the cytoskeleton. J Cell Biol. 2011;194(4):513-25.

74.   Shih YL, Rothfield L. The bacterial cytoskeleton. Microbiol Mol Biol Rev. 2006;70(3):729-54.

75.   Kürner J, Medalia O, Linaroudis AA, Baumeister W. New insights into the structural organization of eukaryotic and prokaryotic cytoskeletons using cryo-electron tomography. Exp Cell Res. 2004;301(1):38-42.

76.   Gitai Z, Dye N, Shapiro L. An actin-like gene can determine cell polarity in bacteria. Proc Natl Acad Sci U S A. 2004;101(23):8643-8.

77.   Popp D, Narita A, Lee LJ, Ghoshdastider U, Xue B, Srinivasan R, et al. Novel actin-like filament structure from Clostridium tetani. J Biol Chem. 2012;287(25):21121-9.

78.   Gitai Z. Plasmid segregation: a new class of cytoskeletal proteins emerges. Curr Biol. 2006;16(4):R133-6.

79.   Charbon G, Cabeen MT, Jacobs-Wagner C. Bacterial intermediate filaments: in vivo assembly, organization, and dynamics of crescentin. Genes Dev. 2009;23(9):1131-44.

80.   Barber-Zucker S, Keren-Khadmy N, Zarivach R. From invagination to navigation: The story of magnetosome-associated proteins in magnetotactic bacteria. Protein Sci. 2016;25(2):338-51.

81.   Ozyamak E, Kollman J, Agard DA, Komeili A. The bacterial actin MamK: in vitro assembly behavior and filament architecture. Journal of Biological Chemistry. 2013;288(6):4265-77.

82.   Katzmann E, Muller FD, Lang C, Messerer M, Winklhofer M, Plitzko JM, et al. Magnetosome chains are recruited to cellular division sites and split by asymmetric septation. Mol Microbiol. 2011;82(6):1316-29.

83.   Löwe J, Amos LA. Evolution of cytomotive filaments: the cytoskeleton from prokaryotes to eukaryotes. Int J Biochem Cell Biol. 2009;41(2):323-9.

84.   Bustamante C, Chemla YR, Forde NR, Izhaky D. Mechanical processes in biochemistry. Annu Rev Biochem. 2004;73:705-48.

85.   Howard J. Mechanics of Motor Proteins and the Cytoskeleton Sunderland. 552001.

86.   Hartman MA, Spudich JA. The myosin superfamily at a glance. J Cell Sci. 2012;125(Pt 7):1627-32.

87.   Lee WL, Kaiser MA, Cooper JA. The offloading model for dynein function: differential function of motor subunits. J Cell Biol. 2005;168(2):201-7.

88.   Adamczyk Z. Diffusion of Particles. In: Tadros T, editor. Encyclopedia of Colloid and Interface Science. Berlin, Heidelberg: Springer Berlin Heidelberg; 2013. p. 247-.

89.   Feynman R. The Feynman Lectures of Physics1964.

90.   Tsekov R. Brownian motion of molecules: the classical theory. Annuals of the University of Sofia, Faculty of Chemistry; 1995. p. 57-66.

91.   Moran G, Prato F. Modeling (1H) exchange: an estimate of the error introduced in MRI by assuming the fast exchange limit in bolus tracking. Magn Reson Med. 2004;51:816-27.

92.   Szomolanyi P, Rohrer M, Frenzel T, Noebauer-Huhmann I, Jost G, Endrikat J, et al. Comparison of the Relaxivities of Macrocyclic Gadolinium-Based Contrast Agents in Human Plasma at 1.5, 3, and 7 T, and Blood at 3 T. Invest Radiol. 2019;54:559-64.

93.   Heyn C, Ronald J, Mackenzie L, MacDonald I, Chambers A, Rutt B, et al. In vivo magnetic resonance imaging of single cells in mouse brain with optical validation. Magn Reson Med. 2006;55:23-9.

94.   Taylor A, Herrmann A, Moss D, Sée V, Davies K, Williams S, et al. Assessing the efficacy of nano- and micro-sized magnetic particles as contrast agents for MRI cell tracking. PLoS One. 2014;9:e100259.

95.   Bernau K, Lewis C, Petelinsek A, Reagan M, Niles D, Mattis V, et al. In Vivo Tracking of Human Neural Progenitor Cells in the Rat Brain Using Magnetic Resonance Imaging Is Not Enhanced by Ferritin Expression. Cell Transplant. 2016;25:575-92.

96.   Mériaux S, Boucher M, Marty B, Lalatonne Y, Prévéral S, Motte L, et al. Magnetosomes, biogenic magnetic nanomaterials for brain molecular imaging with 17.2 T MRI scanner. Adv Healthc Mater. 2015;4:1076-83.

97.   Benoit M, Mayer D, Barak Y, Chen I, Hu W, Cheng Z, et al. Visualizing implanted tumors in mice with magnetic resonance imaging using magnetotactic bacteria. Clin Cancer Res. 2009;15:5170-7.

98.   Lee C, Thompson R, Prato F, Goldhawk D, Gelman N. Investigating the Relationship between Transverse Relaxation Rate (R2) and Interecho Time in MagA-expressing Iron-labeled Cells. Mol Imaging. 2015;14:551-60.

99.   Ghugre N, Coates T, Nelson M, Wood J. Mechanisms of tissue-iron relaxivity: nuclear magnetic resonance studies of human liver biopsy specimens. Magn Reson Med. 2005;54:1185-93.

100.   Rozenman Y, Zou X, Kantor H. Cardiovascular MR imaging with iron oxide particles: utility of a superparamagnetic contrast agent and the role of diffusion in signal loss. Radiology. 1990;175:655-9.

101.   Kim JA, Åberg C, Salvati A, Dawson KA. Role of cell cycle on the cellular uptake and dilution of nanoparticles in a cell population. Nature Nanotechnology. 2012;7(1):62-8.

102.   Li M, Wang Y, Liu M, Lan X. Multimodality reporter gene imaging: Construction strategies and application. Theranostics. 2018;8(11):2954-73.

103.   Terrovitis J, Stuber M, Youssef A, Preece S, Leppo M, Kizana E, et al. Magnetic resonance imaging overestimates ferumoxide-labeled stem cell survival after transplantation in the heart. Circulation. 2008;117(12):1555-62.

104.   Meikle SR, Kench P, Kassiou M, Banati RB. Small animal SPECT and its place in the matrix of molecular imaging technologies. Physics in Medicine and Biology. 2005;50(22):R45-R61.

105.   Youn H, Chung JK. Reporter Gene Imaging. American Journal of Roentgenology. 2013;201(2):W206-W14.

106.   Bourdeau RW, Lee-Gosselin A, Lakshmanan A, Farhadi A, Kumar SR, Nety SP,

et al. Acoustic reporter genes for noninvasive imaging of microorganisms in mammalian hosts. Nature. 2018;553(7686):86-90.

107.   Farhadi A, Ho GH, Sawyer DP, Bourdeau RW, Shapiro MG. Ultrasound imaging of gene expression in mammalian cells. Science. 2019;365(6460):1469-75.

108.   Magistretti P, Allaman I. A cellular perspective on brain energy metabolism and functional imaging. Neuron. 2015;86:883-901.

109.   Yang H, Oksuz I, Dey D, Sykes J, Klein M, Butler J, et al. Accurate needle-free assessment of myocardial oxygenation for ischemic heart disease in canines using magnetic resonance imaging. Sci Transl Med. 2019;11:eaat4407.

110.   Anazodo U, Finger E, Kwan B, Pavlosky W, Warrington J, Günther M, et al. Using simultaneous PET/MRI to compare the accuracy of diagnosing frontotemporal dementia by arterial spin labelling MRI and FDG-PET. Neuroimage Clin. 2017;17:405-14.

111.   Le Bihan D, Iima M. Diffusion Magnetic Resonance Imaging: What Water Tells Us about Biological Tissues. PLOS Biol. 2015;13(9).

112.   Cho K, Moran SP, Paudyal R, Piotrowska-Nitsche K, Cheng P, Zhang X, et al. Longitudinal Monitoring of Stem Cell Grafts In Vivo Using Magnetic Resonance Imaging with Inducible MagA as a Genetic Reporter. Theranos. 2014;4(10):972-989.

113.   Koretsky AP, Brosnan MJ, Chen LH, Van Dyke T. NMR detection of creatine kinase expressed in liver of transgenic mice: determination of free ADP levels. Proc Natl Acad Sci USA. 1990;87:3112-3116.

114.   Bartelle BB, Szulc KU, Suero-Abreu GA, Rodriguez JJ, Turnbull DH. Divalent metal transporter, DMT1: A novel MRI reporter protein. Magn Reson Med. 2013;70(3):842-850.

115.   Louie AY, Huber MM, Ahrens ET, Rothbacher U, Moats R, Jacobs RE, et al. In vivo visualization of gene expression using magnetic resonance imaging. Nat Biotechnol. 2000;18:321-325.

116.   Alfke H, Stoppler H, Nocken F, Heverhagen JT, Kleb B, Czubayko F, et al. In vitro MR imaging of regulated gene expression. Radiol. 2003;228:488-492.

117.   Vandsburger MH, Radoul M, Addadi Y, Mpofu S, Cohen B, Eilam R, et al. Ovarian carcinoma: quantitative biexponential MR imaging relaxometry reveals the dynamic recruitment of ferritin-expressing fibroblasts to the angiogenic rim of tumors. Radiol. 2013;268:790-801.

118.   Cohen B, Dafni H, Meir G, Harmelin A, Neeman M. Ferritin as an endogenous MRI reporter for noninvasive imaging of gene expression in C6 glioma tumors. Neoplasia. 2005;7:109-117.

119.   Vande Velde G, Rangarajan JR, Toelen J, Dresselaers T, Ibrahimi A, Krylychkina O, et al. Evaluation of the specificity and sensitivity of ferritin as an MRI reporter gene in the mouse brain using lentiviral and adeno-associated viral vectors. Gene therapy. 2011;18:594-605.

120.   Kim HS, Cho HR, Choi SH, Woo JS, Moon WK. In vivo imaging of tumor transduced with bimodal lentiviral vector encoding human ferritin and green fluorescent protein on a 1.5T clinical magnetic resonance scanner. Cancer Res. 2010;70:7315-7324.

121.   Araujo A, Abreu F, Tavares Silva K, Bazylinski D, Ulysses Lins U. Magnetotactic Bacteria as Potential Sources of Bioproducts. Mar Drugs. 2015;13:389-430.

122.   Blakemore RP, Frankel RB, Kalmijn AJ. South-seeking magnetotactic bacteria in the Southern Hemisphere. Nature. 1980;286(5771):384-5.

123.   Leão P, Teixeira LCRS, Cypriano J, Farina M, Abreu F, Bazylinski DA, et al. North-Seeking Magnetotactic Gammaproteobacteria in the Southern Hemisphere. Applied and Environmental Microbiology. 2016;82(18):5595-602.

124.   Alphandéry E. Applications of magnetosomes synthesized by magnetotactic bacteria in medicine. Frontiers in bioengineering and biotechnology. 2014;2:5.

125.   Bazylinski DA, Schübbe S. Controlled Biomineralization by and Applications of Magnetotactic Bacteria. Advances in Applied Microbiology. 62: Academic Press; 2007. p. 21-62.

126.   Vargas G, Cypriano J, Correa T, Leao P, Bazylinski DA, Abreu F. Applications of Magnetotactic Bacteria, Magnetosomes and Magnetosome Crystals in Biotechnology and Nanotechnology: Mini-Review. Molecules (Basel, Switzerland). 2018;23(10).

127.   Faivre D. Formation of magnetic nanoparticle chains in bacterial systems. MRS Bulletin. 2015;40(6):509-15.

128.   Klumpp S, Lefèvre C, Bennet M, Faivre D. Swimming with magnets: From biological organisms to synthetic devices. Physics Reports. 2018;789.

129.   Chen C, Chen L, Yi Y, Chen C, Wu L-F, Song T. Killing of *Staphylococcus aureus* via Magnetic Hyperthermia Mediated by Magnetotactic Bacteria. Applied and Environmental Microbiology. 2016;82(7):2219-26.

130.   Martel S. Targeting active cancer cells with smart bullets. Therapeutic Delivery. 2017;8(5):301-12.

131.   Yoshino T, Matsunaga T, Tanaka T. Bioengineering and Biotechnological Applications of Bacterial Magnetic Particles. In: Matsunaga T, Tanaka T, Kisailus D, editors. Biological Magnetic Materials and Applications. Singapore: Springer Singapore; 2018. p. 77-93.

132.   Bain J, Legge CJ, Beattie DL, Sahota A, Dirks C, Lovett JR, et al. A biomimetic magnetosome: formation of iron oxide within carboxylic acid terminated polymersomes. Nanoscale. 2019;11(24):11617-25.

133.   Bakhshi PK, Bain J, Gul MO, Stride E, Edirisinghe M, Staniland SS. Manufacturing Man-Made Magnetosomes: High-Throughput In Situ Synthesis of Biomimetic Magnetite Loaded Nanovesicles. Macromolecular Bioscience. 2016;16(11):1555-61.

134.   Le Nagard L, Zhu X, Yuan H, Benzerara K, Bazylinski DA, Fradin C, et al. Magnetite magnetosome biomineralization in Magnetospirillum magneticum strain AMB-1: A time course study. Chemical Geology. 2019;530:119348.

135.   Yoshino T, Shimada T, Ito Y, Honda T, Maeda Y, Matsunaga T, et al. Biosynthesis of Thermoresponsive Magnetic Nanoparticles by Magnetosome Display System. Bioconjugate Chemistry. 2018;29(5):1756-62.

Chapter 2

2   Essential magnetosome proteins MamI and MamL from magnetotactic bacteria interact in mammalian cells

To optimize the development of a magnetosome-like nanoparticle, selected magnetosome genes *mamI, mamL, mamB,* and/or *mamE* were expressed in mammalian cells to evaluate their behaviour and interaction. Chapter 2 describes the behaviour of magnetosome proteins MamI and MamL when individually expressed in mammalian cells, and the interaction between these two proteins when co-expressed.

Data obtained with fluorescence correlation spectroscopy (FCS) was done in collaboration with Dr. Cécile Fradin from McMaster University. FCS data was analyzed by Liu Yu, a Masters student from the Fradin lab. Collaborative data are presented in Tables 2.4 and 2.5 and Figure 2.16.

This chapter has been submitted for publication: Sun Q, Yu L, Donnelly SC, Fradin C, Thompson RT, Prato FS, and Goldhawk DE. *Journal of Biological Chemistry.* 2022.

2.1   Introduction

As advancements in non-invasive imaging technology continue to shape medical practice (1), there is a pressing need for greater *in vivo* molecular detail, not only to better understand the location and migration of disease processes but also temporal changes in specific gene expression (2, 3). For this type of molecular imaging, endogenous contrast agents offer huge advantages, tracking cellular activities throughout their life cycle and

responding to *in vivo* cues. Magnetic resonance imaging (MRI) has the needed soft tissue resolution and depth of penetration in a non-ionizing platform; nevertheless, cellular imaging relies heavily on exogenous contrast agents (4). To expand the capabilities of molecular MRI in mammalian cells, we are using magnetosome genes to program the synthesis of iron particles. Since this form of iron contrast can be genetically regulated, it may be suitable for magnetic resonance (MR) detection of reporter gene expression (5). Magnetotactic bacteria (MTB) synthesize magnetosomes, which consist of an iron biomineral (often magnetite, Fe_3O_4) sequestered within a membrane-bound compartment (6, 7). This form of superparamagnetic iron oxide constitutes an ideal MR contrast agent (8, 9) and if mammalian cells could replicate the program of magnetosome synthesis, then MRI at clinical field strength could theoretically detect as few as 3 cells in small animals and approximately 1000 cells in large animals or humans (5).

Magnetosome biosynthesis is under the control of approximately 30 genes, many of which are clustered on a magnetosome genomic island (7, 10, 11). While the proposed functions of these bacterial genes have been divided into vesicle formation and crystal formation (12), most genes are non-essential, as deletion of only a select few genes completely abrogates magnetosome biosynthesis (13). In addition, these essential genes are among those required for vesicle formation in MTB (14), which is the first step in magnetosome formation and ensures a compartment where iron can be safely concentrated for biomineralization, without introducing cytotoxicity. We further propose that essential magnetosome genes constitute the scaffold upon which the fuller magnetosome structure relies (5). This hypothesis implicates select magnetosome proteins in designating where the structure will assemble and therefore anchoring the

nanoparticle in a given membrane. If correct, this also suggests that a rudimentary

magnetosome-like particle could be genetically programmed in a variety of cell types and

for a variety of applications, dependent on the final crystal structure (15).

In the last decade, several groups have reported MR contrast enhancement using

single transgene expression systems like *magA*, encoding a putative iron transporter in

species of *Magnetospirillum* (16, 17) or *mms6*, encoding an iron crystallizing protein (18,

19). On the one hand, no one iron-handling protein can recreate the full magnetosome

structure while on the other hand most can be individually deleted without compromising

the entire structure (13, 20). The number and function of essential magnetosome genes,

upon which the entire magnetosome structure relies, is still poorly understood. In general,

these genes are widely conserved across species of MTB, are found on the *mamAB*

operon, and frequently display preserved gene synteny (7). Moreover, their presence

defines the magnetosome as a hierarchical protein structure, containing a common base

upon which assembly of the final magnetosome form depends.

Since forming the vesicle that will protect the cell from iron toxicity has been

established as a first step in magnetosome synthesis (21), we speculate that less genetic

information may be required to initiate magnetosome synthesis in eukaryotes than in

prokaryotes, the former of which inherently direct vesicle formation through the Golgi

apparatus (22). In this case, replicating a magnetosome-like particle in eukaryotic cells

will only rely on the expression of genes required for designating the compartment and,

using specific protein-protein interactions, directing subsequent iron biomineralization.

We have tested this hypothesis using *mamI* and *mamL*, two magnetosome genes which

are conserved among magnetite-producing MTB (20), are essential to vesicle formation,

and when deleted, prevent magnetosome formation (11, 20). We therefore expressed

fluorescent fusion proteins of MamI and MamL, alone and together, in a mammalian cell

line. Using confocal microscopy and fluorescence correlation spectroscopy (FCS), we

then demonstrated the nature of their intracellular membrane localization in a foreign cell

environment and provided evidence of their co-localization and potential for interaction.

2.2   Materials and Methods

2.2.1   Molecular Cloning

2.2.1.1 *mamI* and *mamL*

Magnetosome genes *mamI* and *mamL* were amplified by PCR from the genomic

DNA of *Magnetospirillum magneticum* strain AMB-1 (ATCC 700264) using custom

primers (Table 2.1). The *mamI* and *mamL* amplicons were purified using a PCR clean-up

kit (Invitrogen, Life Technologies, Burlington, Canada); digested with appropriate

restriction enzymes (Table 2.1); and purified once more, prior to insertion in the

molecular cloning vectors pEGFP-C1 (Clontech; Fig. 2.1) and ptdTomato-C1 (Clontech;

Fig. 2.2), respectively. Sequencing information for *mamI* and *mamL* is shown in

Appendix A.1 and A.2. After propagation in *Escherichia coli* strain XL10GOLD, the

vector-insert plasmid constructs were purified and used for mammalian cell transfection,

as outlined below.

Table 2.1 Primer design for the cloning of MTB genes *mamI* and *mamL* into pEGFP-C1 and ptdTomato-C1, respectively.

Gene		Primer (5' – 3')	Restriction Site*	Vector
mamI	Forward	GCATCAAGA**CTGCAG**TAACG	*PstI*	pEGFP-C1
	Reverse	CTACGTCACCAT**TGATCA**TGGCCATC	*BclI*	
mamL	Forward	CGCGGC**AGATCT**AGGACAGTGGC	*BglII*	ptdTomato-C1
	Reverse	TCACTCCA**AAGCTT**CCCGACC	*HindIII*	

*Restriction enzyme sites appear in bold in the primer sequence.
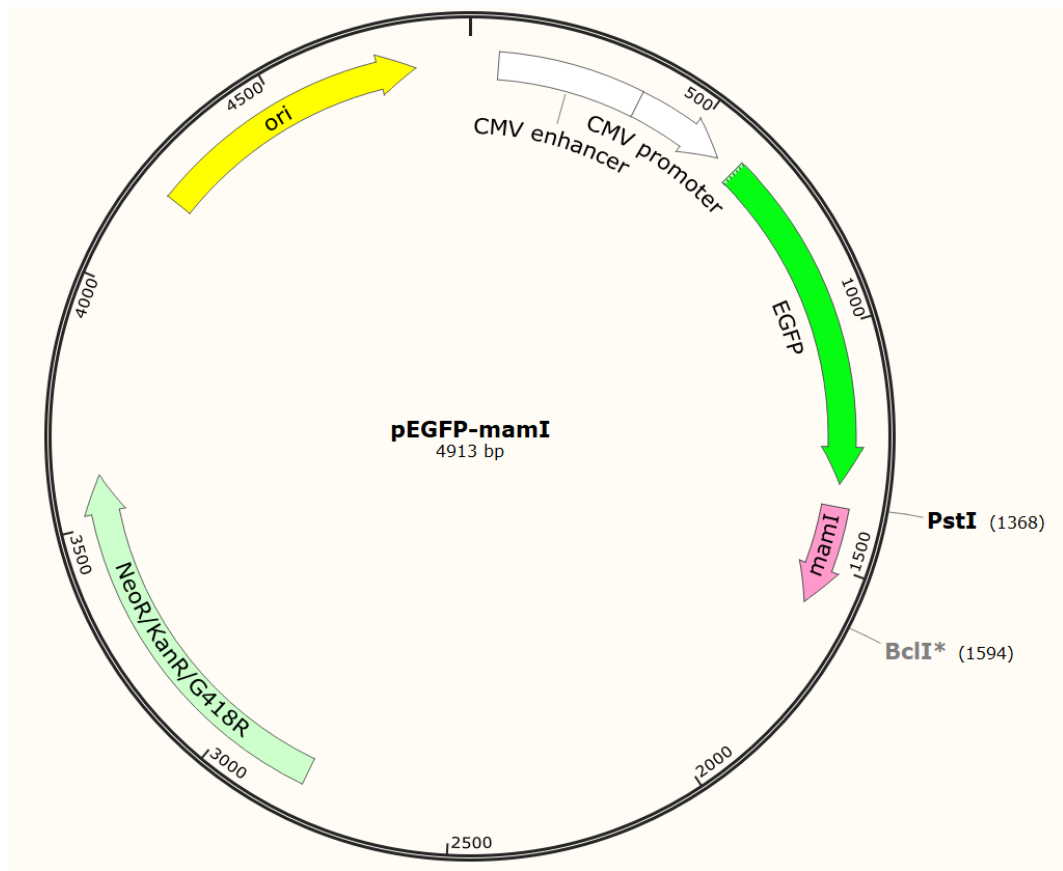
Figure 2.1 Vector-insert map of the cloning strategy of magnetosome gene *mamI*.

Vector-insert map of pEGFP-mamI shows *mamI* (pink) cloned in downstream of EGFP

(bright green) between restriction sites PstI and BclI. The bacterial origin of replication

(ori) is shown in yellow. The mammalian cytomegalovirus (CMV) enhancer and

promoter, which allow for constitutive gene expression, is shown in white. The

NeoR/KanR/G418R gene (light green) provides kanamycin antibiotic resistance in

bacterial cells and G418 antibiotic resistance in mammalian cells.
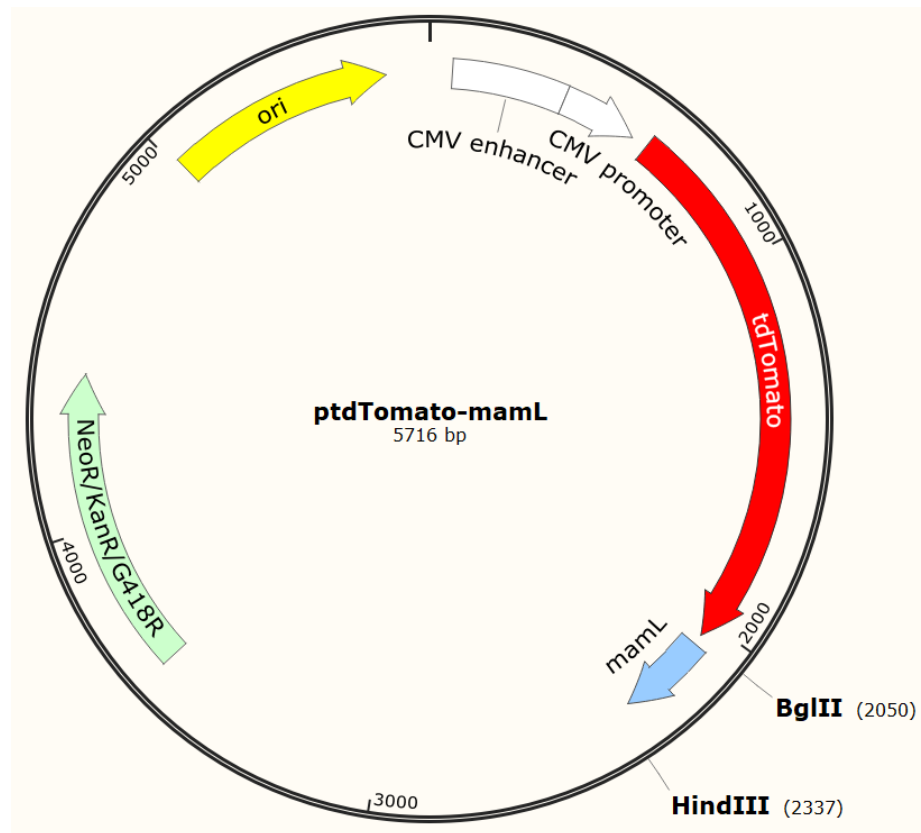
Figure 2.2 Vector-insert map of the cloning strategy of magnetosome gene *mamL*.

Vector-insert map of ptdTomato-mamL shows *mamL* (blue) cloned in downstream of

tdTomato (red) between restriction sites BglII and HindIII. The bacterial origin of

replication (ori) is shown in yellow. The mammalian CMV enhancer and promoter,

which allow for constitutive gene expression, is shown in white. The NeoR/KanR/G418R

gene (light green) provides kanamycin antibiotic resistance in bacterial cells and G418

antibiotic resistance in mammalian cells.

2.2.1.2 *mamL* truncation

To investigate the function of different regions of the MamL protein, the last 15 amino acids from the C-terminal end of MamL were removed by introducing an early stop codon. Primers were designed were designed that included a stop codon 45 nucleotides upstream from the end of *mamL* (Table 2.2). These primers were then used in PCR amplification of the truncated *mamL* gene, and the gene was then inserted into the ptdTomato-C1 vector with restriction enzymes EcoRI and BglII (Fig. 2.3). Sequencing information is shown in Appendix A.3.

Table 2.2 Primer design for the cloning of MTB gene *mamL_{trunc}* into the ptdTomato-C1 vector.

Gene	Primer (5' – 3')		Restriction Site*	Vector
mamL_{trunc}	Forward	CGCGGC**AGATCT**AGGACAGTGGC	*BglII*	ptdTomato-C1
	Reverse	TCTGCTT**GAATTC**TCACATGACG	*EcoRI*	

*Restriction enzyme sites appear in bold in the primer sequence.
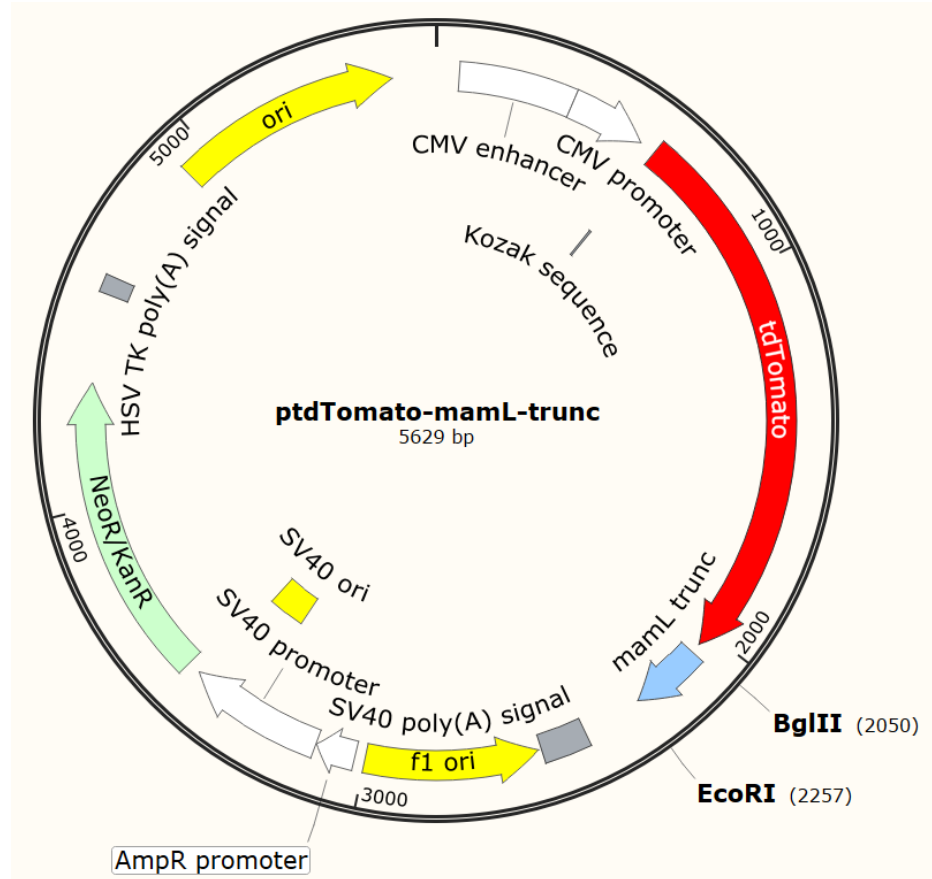
Figure 2.3 Vector-insert map of the cloning strategy of magnetosome gene
mamL_{trunc}.

Vector-insert map of ptdTomato-mamL$_{trunc}$ shows *mamL$_{trunc}$* (blue) cloned in after

tdTomato (red) between restriction sites BglII and EcoRI. The bacterial origin of

replication (ori) is shown in yellow. The mammalian CMV enhancer and promoter,

which allow for constitutive gene expression, is shown in white. The NeoR/KanR/G418R

gene (light green) provides kanamycin antibiotic resistance in bacterial cells and G418

antibiotic resistance in mammalian cells.

2.2.1.2 *mamL*trunc and *mamI*

To evaluate the interaction of MamL$_{trunc}$ with MamI, transient transfections were performed. EGFP-MamI-expressing cells were plated on 35 mm glass-bottom cell culture dishes and transfected with 1 µg of Tomato-*mamL$_{trunc}$* DNA and 2 µg of Lipofectamine 2000. Cells were imaged 72-hours post-transfection with the confocal microscope, as described below in section 2.2.8.

2.2.1.2 pSF-FLAG-*mamL*-EMCV-*FLuc*

To refine the co-expression of MamI and MamL, the pSF-EMCV-*FLuc* vector was used to generate FLAG-tagged MamL under Puromycin selection. Interaction between MamI and MamL can then be identified using the green fluorescence of EGFP. Primers flanking *mamL* in ptdTomato construct were designed to include a FLAG tag (DYKDDDDK) for immunodetection (Table 2.3). The FLAG-*mamL* insert was amplified using PCR, purified using a PCR clean-up kit (Invitrogen, Life Technologies, Burlington, Canada), and digested using SacI and EcoRI (Table 2.3). FLAG-*mamL* was then inserted into the pSF-EMCV-FLuc vector and propagated in *Escherichia coli* strain XL10GOLD (Fig. 2.4). Sequencing information is shown in Appendix A.4.

Table 2.3 Primer design for the cloning of FLAG-*mamL* into the pSF-EMCV-FLuc vector.

Gene	Primer (5' – 3')		Restriction Site*	Vector
FLAG-*mamL*	Forward	GACTCA**GAGCTC**ATG<u>GACT</u> <u>ACAAAGACGATGACGACAA</u> <u>G</u>AGTGGC	*SacI*	pSF-EMCV-FLuc
	Reverse	GACTGCA**GAATTC**GAAAGC TTC	*EcoRI*	

*Restriction enzyme sites appear in bold in the primer sequence. FLAG tag sequence is underlined in the forward primer.
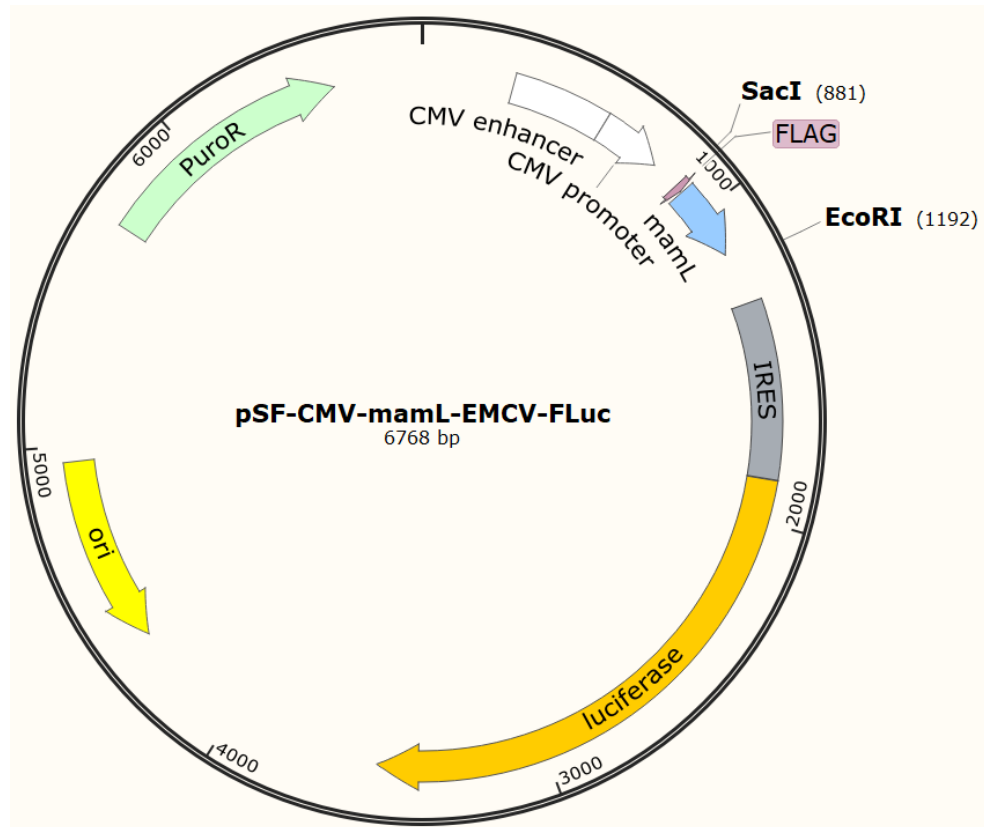
Figure 2.4 Vector-insert map of the cloning strategy of magnetosome gene *FLAG-mamL*.

Vector-insert map of pSF-CMV-FLAG-*mamL*-EMCV-*FLuc* shows *mamL* (blue) with a

FLAG tag (pink) directionally cloned at SacI and EcoRI restriction sites. The

bioluminescence gene *luciferase* (orange) is also present in this construct. The bacterial

origin of replication (ori) is shown in bright yellow. The mammalian CMV enhancer and

promoter, which allow for constitutive gene expression, is shown in white. The PuroR

gene (light green) provides puromycin antibiotic resistance in mammalian cells.

2.2.2   Cell Culture and Transfection

MDA-MB-435 cells (ATCC HTB-129; derived from an adult female and characterized as a melanoma cell line) are a model of aggressive tumorigenesis (23). Cells were cultured in 100 mm polystyrene cell culture dishes (CELLSTAR, VWR International, Mississauga, Canada) with Dulbecco's Modified Eagle Medium (DMEM) containing 1 g/L glucose (Gibco, Life Technologies, Burlington, Canada), 10% fetal bovine serum (FBS; Gibco), 4 U/mL penicillin, and 4 µg/mL streptomycin at 37°C with 5% CO_2. To create cell lines expressing the enhanced green fluorescent protein (EGFP)-MamI fusion protein or the red fluorescent protein tdTomato (Tomato)-MamL fusion protein, cells were grown to 60-70% confluency on a 100 mm dish and transfected using Lipofectamine 2000 (Invitrogen), according to company protocol, using 8 µg of pEGFP-*mamI* or ptdTomato-*mamL*, respectively. For co-expression of both pEGFP-*mamI* and ptdTomato-*mamL,* cells stably expressing Tomato-MamL were transfected with 8 µg of pEGFP-*mamI*. For expression of Tomato-MamL$_{trunc,}$ parental MDA-MB-435 cells were transfected with 4 µg of Tomato-*mamL$_{trunc}$* DNA and 12 µg of Lipofectamine 2000. For expression of FLAG-MamL, parental MDA-MB-435 cells were transfected with 4 µg of pSF-FLAG-*mamL*-EMCV-*FLuc* DNA. For expression of FLAG-MamL/EGFP-MamI, EGFP-MamI-expressing cells were transfected with 8 µg of pSF-FLAG-*mamL*-EMCV-*FLuc* DNA. After 16 hours transfections were stopped, and cells were placed in full medium for 48 hours before commencing antibiotic selection.

2.2.3   Selection of Stable Cell Lines

To select cells stably expressing EGFP-MamI and/or Tomato-MamL fusion proteins, transfected cells were grown in the presence of 500 µg/mL of Geneticin (G418; Gibco). To enrich the populations of fluorescing cells, we used fluorescence activated cell sorting (FACS; Robarts Research Institute, London, Canada). For each expression system, two cell populations were obtained, with either high or medium fluorescent intensity. Western blots and confocal fluorescence microscopy were performed on cells displaying high fluorescence while medium fluorescence was adequate for FCS.

For selection of cells stably expressing Tomato-MamL$_{trunc}$, transfected cells were grown in the presence of 500 µg/mL of G418. For selection of cells stably expressing FLAG-MamL, transfected cells were grown in the presence of 0.4 µg/mL Puromycin (Gibco). For selection of cells stably expressing FLAG-MamL/EGFP-MamI, transfected cells were grown in the presence of 500 µg/mL G418 and 0.5 µg/mL Puromycin. These expression systems were not sorted with FACS due to adequate level of fluorescence intensity.

2.2.4   Protein Sample Preparation

Stably transfected cells were cultured to 70% confluency on a 100 mm dish, then washed twice using 10 mL phosphate buffered saline pH 7.4 (PBS, 137 mM NaCl/2.7 mM KCl/10 mM Na$_2$HPO$_4$). Four to five dishes of cells were then collected into a 1 mL lysis solution containing 850 µL of radioimmunoprecipitation assay buffer (RIPA, 10 mM Tris-HCl pH 7.5/140 mM NaCl/1% NP-40/1% sodium deoxycholate/0.1% sodium

dodecyl sulfate [SDS]) and 150 µL of Complete Mini protease inhibitor cocktail (Roche Diagnostic Systems, Laval, Canada). Cells were then sonicated using three 12-second bursts of a Sonic Dismembrator (model 500, Thermo Fischer Scientific, Ottawa, Canada) at an amplitude of 30%. Total amount of protein was quantified using the BCA assay (24).

2.2.5   Western Blot

Protein samples of MDA-MB-435 cells stably expressing EGFP (40 µg), Tomato (40 µg), EGFP-MamI (20 µg), or Tomato-MamL (20 µg), or stably co-expressing Tomato-MamL/EGFP-MamI (80 µg) were reduced with 100 mM dithiothreitol (DTT) in sample preparation buffer (1 M Tris-HCl pH 6.8/10% SDS/0.1% Bromophenol Blue/43% glycerol) and heated at 85°C for at least 5 min. Reduced samples were then subjected to discontinuous SDS polyacrylamide gel electrophoresis (SDS-PAGE) using a 10% running gel (14% running gel for FLAG-MamL detection). Protein was transferred onto a nitrocellulose blot using the Original iBlot Gel Transfer Device (Life Technologies, Burlington, Canada).

For EGFP detection, nonspecific protein binding was blocked in 5% bovine serum albumin (BSA)/Tris-buffered saline pH 7.4 (TBS) for 3 h at room temperature. Blots were then incubated for 15 h in 1:1000 mouse α-GFP (Invitrogen)/3% BSA/TBS/0.02 % sodium azide (TBSA); then washed using TBS/0.1% Tween 20 (TBST; Sigma-Aldrich, Oakville, Canada) for 30 min with 4 changes of buffer; and incubated for 2 h in 1:20,000 horseradish peroxidase (HRP)-conjugated goat α-mouse IgG (Sigma-Aldrich)/1% BSA/TBS. All incubations were performed at room temperature. Blots were then washed

with 0.1% TBST for 30 min with 4 changes of buffer and imaged using the Chemigenius Gel Doc (Syngene). A chemiluminescent signal was detected using SuperSignal West Pico Chemiluminescent Substrate (Thermo Fischer Scientific), according to the manufacturer's instructions.

For Tomato detection, blots were blocked in 3% BSA/TBSA for approximately 18 h at room temperature and then incubated for 18 h in 1:1000 primary goat α-tdTomato (MyBioSource, San Diego, USA)/3% BSA/TBSA at 4°C. After washing in 0.1% TBST as described above, blots were incubated for 1 h in 1:20,000 HRP-conjugated rabbit α-goat IgG (Sigma-Aldrich)/1% BSA/TBS at room temperature.

For FLAG detection, blots were blocked in 3% BSA/TBS overnight and then incubated for 18 h in 1:1000 primary mouse α-FLAG (Thermo Fisher Scientific)/3% BSA/TBSA. After washing in 0.1% TBST as described above, blots were incubated for 2 h in 1:20,000 HRP-conjugated goat α-mouse IgG (Sigma-Aldrich)/1% BSA/TBS. All incubations were done at room temperature.

Glyceraldehyde 3-phosphate dehydrogenase (GAPDH) was used as a loading control. For GAPDH detection, blots were placed in stripping solution (1 M Tris-HCl pH 6.8/10% SDS/0.016% β-mercaptoethanol) and agitated in a 37°C water bath for 30 min prior to washing in 0.1% TBST and blocking in 5% BSA/TBS. The primary and secondary antibodies were 1:2000 rabbit α-GAPDH (Sigma-Aldrich)/3% BSA/TBSA and 1:20,000 HRP-conjugated goat α-rabbit IgG (Sigma-Aldrich)/1% BSA/TBS, respectively.

2.2.6   Co-immunoprecipitation

Co-immunoprecipitation was adapted from a published procedure (23). Protein samples were prepared and quantified as described above. For immunoprecipitation, 5 mg of GFP-MamI or FLAG-MamL protein sample was mixed with 5 µL of α-GFP and incubated for 1h at 4°C. Prior to binding the antibody, Protein-G Sepharose beads (Cytiva, Vancouver, BC, Canada) were washed and added to each protein-antibody mixture and then incubated 1h at 4°C. Unbound protein was washed away with RIPA buffer and 10 mM Tris-HCl. Protein associated with Protein-G Sepharose was resuspended in 40 µL of sample buffer (125 mM Tris-HCl pH 6.8/3.3% SDS/100 mM DTT) and heated to 80°C for 15min to dissociate protein from beads. Glycerol (10% v/v) and bromophenol blue (~0.1% w/v) were added to each sample prior to storing at -20°C until SDS-PAGE.

The co-immunoprecipitation blot was blocked in 4% BSA/TBSA for approximately 5 h then incubated for 18 h in 1:2000 primary goat α-FLAG (Thermo Fisher Scientific)/3% BSA/TBSA at room temperature. After washing in 0.1% TBST as described above, blots were incubated for 1 h in 1:20,000 HRP-conjugated rabbit α-goat IgG (Sigma-Aldrich)/1% BSA/TBS.

2.2.7   Confocal Imaging

Stably transfected cell lines were examined with confocal fluorescence microscopy (Nikon A1R Confocal Microscope). In preparation for confocal microscopy, approximately 100,000 cells were cultured in a 35 mm glass-bottom dish (MatTek Corporation, Cedarlane, Burlington, Canada) for 48 hours. On the day of imaging, the dish was placed in a stage-top incubator to maintain 37°C and 5% CO_2. Images and timelapses were captured using a Galvano scanner with NIS-Elements AR 5.11.01 (Nikon Instruments Inc.), using a 20X objective with 0.75 numerical aperture. To capture images of cells expressing a single fluorophore, the FITC microscope filter (495 nm excitation/519 nm emission) was used for cells expressing the EGFP fluorophore and the TRITC microscope filter (557 nm excitation/576 nm emission) was used for cells expressing the Tomato fluorophore. To capture images of cells co-expressing both fluorophores (EGFP and Tomato), the FITC and TRITC filters were turned on simultaneously. Captured images of cells in both channels were then merged in Adobe Photoshop CS7.

Timelapses were acquired with the time lapse function in NIS-Elements AR 5.11.01, which acquires a picture every 2 s for a total of 60 s. Timelapses were captured in either channel or both channels simultaneously, as described above. The NIS-Elements software automatically generated a time lapse video with single or merged channels. This video was then edited in Adobe Photoshop CS7 and exported as a GIF file.

2.2.8   Fluorescence Correlation Spectroscopy

Fluorescence correlation spectroscopy (FCS, Fig. 2.5) analyzes the concentration and movement of labeled particles by examining fluorescence fluctuations during their diffusion (24). This technique can be applied to characterize the behaviour of fluorescent fusion proteins extracted from cells. Fluorescence cross-correlation spectroscopy (FCCS), a dual-colour version of FCS, has additional applications in the analysis of enzymatic reactions and co-diffusion of two particles (24). While this chapter only presents FCS data, we hope to investigate the interaction between MamI and MamL using FCCS in the future. By attaching distinct fluorophores to two specific proteins (ie. EGFP-MamI, tdTomato-MamL), their protein-protein interactions can be investigated.
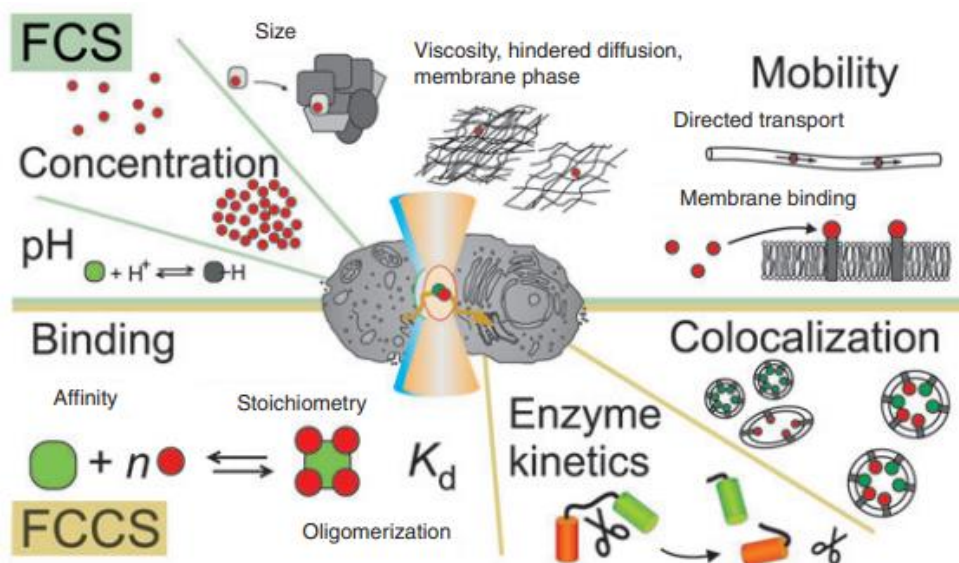
Figure 2.5 Parameters assessed by FCS and FCCS.

FCS analyses the diffusion pattern, the mobility, and the direct transport of single particles. FCCS analyses the binding, enzyme kinetics, and co-localization of two particles. Figure adapted from Bacia et al., 2006 (24).

FSC uses a modified confocal microscope to measure fluctuations in fluorescence signal from the diffusion of fluorescently-labeled particles across a focal point (24). This signal is then auto-correlated and estimation of parameters like apparent radius and diffusion coefficient are obtained (25).

Lysed samples of the parental MDA-MB-435 cell line, those expressing either EGFP-MamI or Tomato-MamL, and those co-expressing Tomato-MamL and EGFP-MamI cells were collected following the protein sample preparation described above and stored at -20°C. FCS data was acquired using an Evotec Insight confocal instrument (Evotech Technologies, Hamburg, Germany, now Perkin-Elmer, Waltham, USA) equipped with a 40X water immersion objective (Olympus, Tokyo, Japan) and a 40 µm confocal pinhole. A 488 nm excitation source (power 20 µW) was used for samples containing EGFP fluorescence and a 532 nm excitation source (power 10 µW) was used for samples containing Tomato fluorescence. A calibration step was first performed with fluorescent dyes to determine the dimensions of the detection volume in EGFP and Tomato channels. The viscosity and background fluorescence of the cell extract was obtained from parental cells. Solubilized samples of total cellular protein (2 mg/ml) were then loaded into the wells of a glass-bottom 96-well plate (Greiner Sensoplate, Sigma-Aldrich) and FCS measurements acquired for each sample (3 to 5 repeats of 20 to 60 s measurements, acquired approximately 5 µm above the glass coverslip to avoid mismatch in the refractive index between immersion water and cell extract).

Both autocorrelation functions and photon counting histograms were generated and analyzed, using either a one-component or two-component model, and taking into account the photophysics of the fluorescent proteins. The diffusion coefficient (*D*) and

intrinsic brightness (B) of the fluorescent particles detected in each sample were then calculated according to standard protocols (25). The apparent radius of the fluorescent species detected (R) was calculated using the Stokes-Einstein relationship:

$$D = kT/(6\pi\eta R)$$

where k is Boltzmann's constant, $T = 300$ K is the absolute temperature, and viscosity of the cell extract, $\eta = 1.29\ \eta_{water} = 1.15 \times 10^{-3}$ Pa·s, was measured in a separate experiment.

2.2.9   Statistical Analysis

All statistical tests were performed using GraphPad Prism version 8. An unpaired t-test was used to identify any significant difference between the FCS intrinsic brightness of Tomato and Tomato-MamL particles, and that of EGFP and EGFP-MamI particles. Significant differences between the FCS parameters of EGFP, EGFP-MamI, and EGFP-MamI/Tomato-MamL structures were determined using one-way analysis of variance (ANOVA). Similarly, significant differences between FCS parameters of Tomato, Tomato-MamL, and Tomato-MamL/EGFP-MamI structures were determined using one-way ANOVA.

2.3   Results

2.3.1   Magnetosome gene expression in a mammalian system

Like other MTB (23, 26, 27) and magnetosome (19) proteins expressed in mammalian cell lines, MamI and/or MamL were stable in long-term cell culture, with little or no effect on cell viability. Cells were transfected with pEGFP-*mamI* and ptdTomato-*mamL* constructs, either alone or in combination, to obtain stable expression of N-terminal fluorescent fusion proteins. Compared to cells expressing EGFP alone, western blots revealed an increase in the size of α-EGFP immuno-stained bands in samples from EGFP-MamI-expressing cells (Fig. 2.6, A and C). The size shift was consistent with the expected molecular weight (MW) of MamI (approximately 8 KDa). Similarly, compared to cells expressing Tomato from the empty vector, western blots revealed an increase in the size of α-tdTomato immuno-stained bands in samples from Tomato-MamL-expressing cells (Fig. 2.7, B and C). This size shift was likewise commensurate with the reported MW of MamL (approximately 13 KDa). Full blots are available in Appendix B.1.
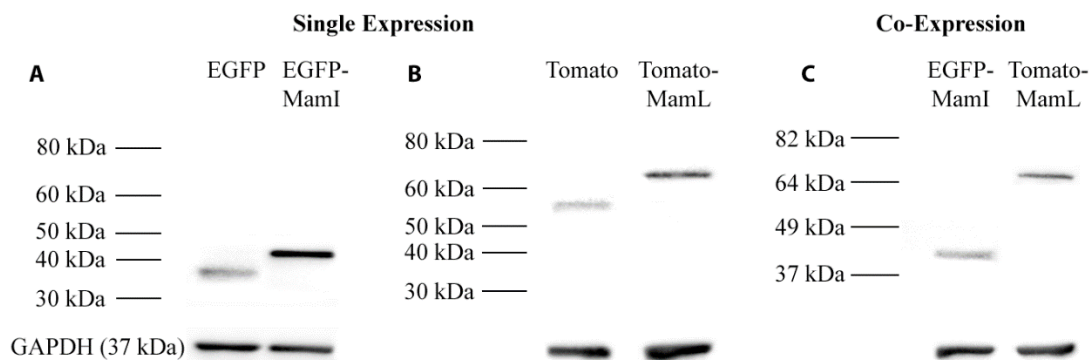
Figure 2.6 Immunoblots of mammalian cells expressing fluorescent magnetosome fusion proteins.

Total cellular protein from MDA-MB-435 cells stably expressing either EGFP or EGFP-MamI (*A*), Tomato or Tomato-MamL (*B*), or both magnetosome fusion proteins (*C*) was examined by western blot, using mouse α-EGFP (*A*, *C*) and/or rabbit α-Tomato (*B*, *C*) as the primary antibodies. Type of fluorescent protein expressed by the cells is indicated above each lane. In panel C, the same cell sample was probed for each magnetosome fusion protein. Approximate MW is shown in the left margin. The loading control was GAPDH (bottom panels).

The pattern of intracellular fluorescence was examined in living cells using confocal fluorescence microscopy. Cells expressing EGFP-MamI produced a net-like pattern of green fluorescence (Fig. 2.8), distinct from the diffuse fluorescence of EGFP alone (Fig. 2.7, A and B). The atypical pattern of EGFP-MamI fluorescence neither circumscribes the plasma membrane nor outlines the standard shape of intracellular vesicle (Fig. 2.8, C and D).
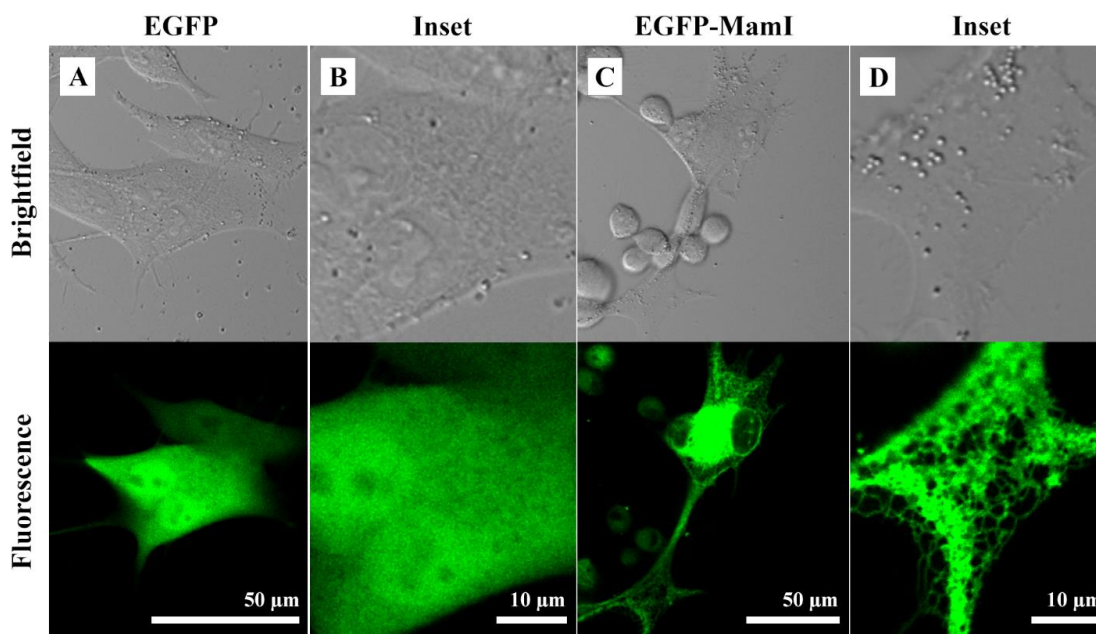
Figure 2.7 Confocal fluorescence microscopy of mammalian cells stably expressing EGFP-MamI fusion protein.

Transfected cells were placed under selection and enriched using FACS to obtain populations expressing EGFP alone (*A* and *B*) or fused to MamI (*C* and *D*). Compared to the uniform fluorescence pattern of EGFP in the cytosol, EGFP-MamI fusion protein displays a net-like pattern of intracellular fluorescence.

In contrast, cells expressing Tomato-MamL displayed punctate red fluorescence throughout the cell (Fig. 2.8). Unlike the uniformly diffuse fluorescence of Tomato alone (Fig. 2.8, A and B), Tomato-MamL fusion protein appeared in discrete intracellular points, with little or no labelling of the plasma membrane (Fig. 2.8, C and D).
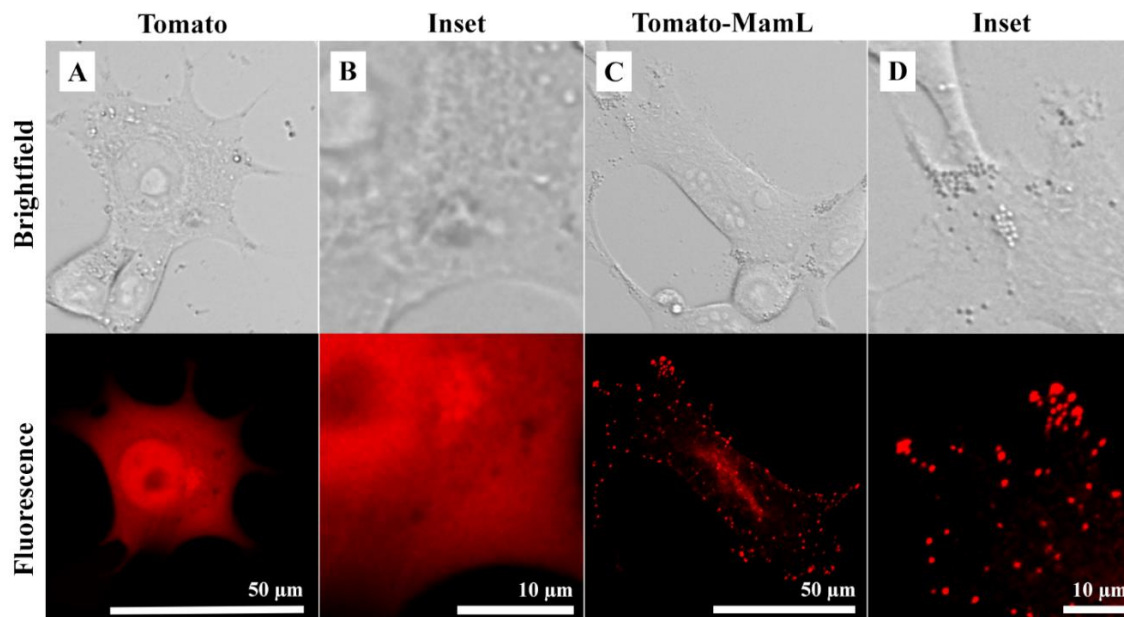
Figure 2.8 Confocal fluorescence microscopy of mammalian cells stably expressing Tomato-MamL fusion protein.

Transfected cells were placed under selection and enriched using FACS to obtain populations expressing Tomato alone (*A* and *B*) or fused to MamL (*C* and *D*). Compared to the uniform fluorescence pattern of Tomato in the cytosol, Tomato-MamL fusion protein displays a punctate intracellular fluorescence pattern. These punctate structures are dispersed throughout the cell.

2.3.2   Mobility of MamL in mammalian cells

Interestingly, Tomato-MamL expression in mammalian cells produced mobile structures. Compared to the green, fluorescent structures of EGFP-MamI, whose location remained relatively stable, some of the Tomato-MamL red fluorescent particles exhibited considerable displacement. In addition to movement within the x-y plane of focus, the

pattern of red fluorescence appeared to dip in and out of the focal plane, indicating

potential movement of Tomato-MamL along the z-axis.

2.3.3   Mobility of truncated MamL

Structural modeling of MamL predicts that a cationic C-terminal peptide lies

outside the transmembrane domain (12). To assess the influence of this putative

extramembrane domain on Tomato-MamL localization and mobility, the C-terminal 15

amino acids were removed, permitting expression of Tomato-MamL$_{trunc}$ fusion protein.

Western blotting confirmed the size difference between full-length (67 kDa) and Tomato-

MamL$_{trunc}$ (65 kDa) (Fig. 2.9). Full blots are available in Appendix B.2.
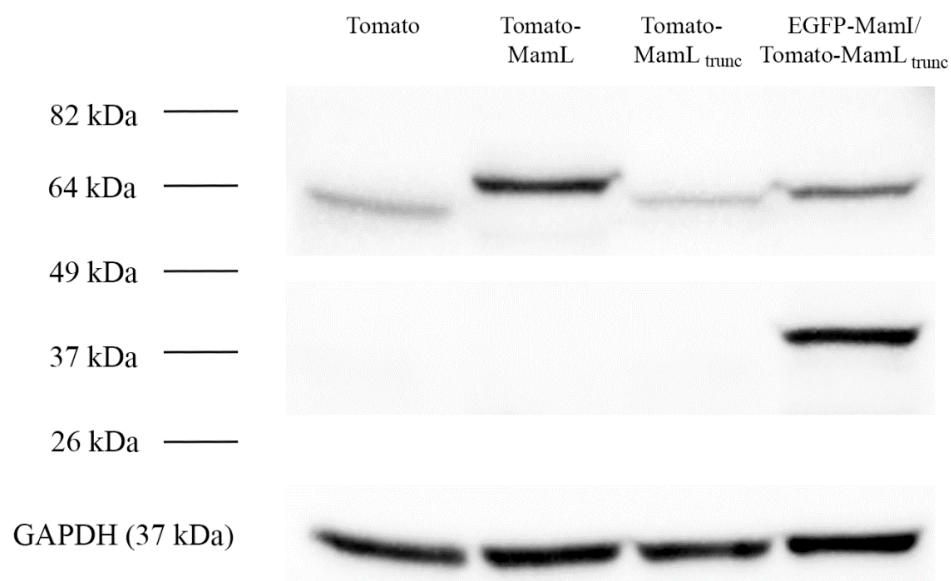
Figure 2.9 Validation of Tomato-MamLtrunc expression in mammalian cells.

Total cellular protein from MDA-MB-435 cells stably expressing either Tomato,

Tomato-MamL, Tomato-MamL$_{trunc}$, or both EGFP-MamI and Tomato-MamL$_{trunc}$ was

examined by western blot. Type of fluorescent protein expressed by the cells is indicated above each lane. For EGFP-MamI/Tomato-MamL$_{trunc}$ extracts, the same cell sample was probed for each magnetosome fusion protein. Approximate MW is shown in the left margin. The loading control was GAPDH (bottom panel).

Confocal fluorescence microscopy confirmed the presence of punctate, mobile Tomato-MamL$_{trunc}$ particles in mammalian cells (Fig. 2.10A) However, over half of the cell population displayed a diffuse pattern of red fluorescence (Fig. 2.10B).
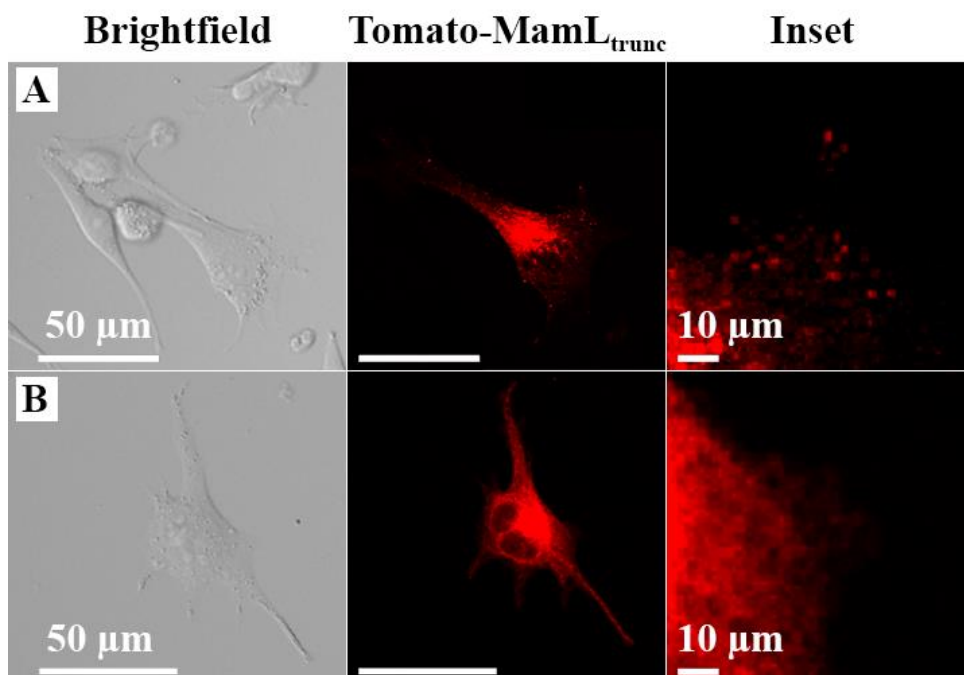
Figure 2.10 Confocal fluorescence microscopy of mammalian cells stably expressing Tomato-MamL$_{trunc}$ fusion protein.

The population of cells expressing Tomato-MamL$_{trunc}$ displayed a punctate pattern (A) in approximately 40% of cells and a diffuse pattern (B) in the remaining 60% of cells. Punctate structures were dispersed throughout the cell, similar to full-length Tomato-MamL.

2.3.4   Co-localization of MamI and MamL

Stable co-expression of EGFP-MamI and full-length Tomato-MamL yielded a

population of cells that was enriched for both red and green fluorescence by FACS (Fig.

2.11). When co-expressed with Tomato-MamL, the pattern of EGFP-MamI fluorescence

was no longer net-like. Instead, green fluorescence was now punctate (Fig. 2.11B),

similar to the pattern of Tomato-MamL (Fig. 2.11C). Moreover, when both red and green

channels were superimposed, yellow punctate fluorescence was observed throughout the

cells (Fig. 2.11D), indicating co-localization of EGFP-MamI and Tomato-MamL.

Remarkably, the same pattern of mobility was displayed by both EGFP-MamI and

Tomato-MamL when co-expressed in the same cells.
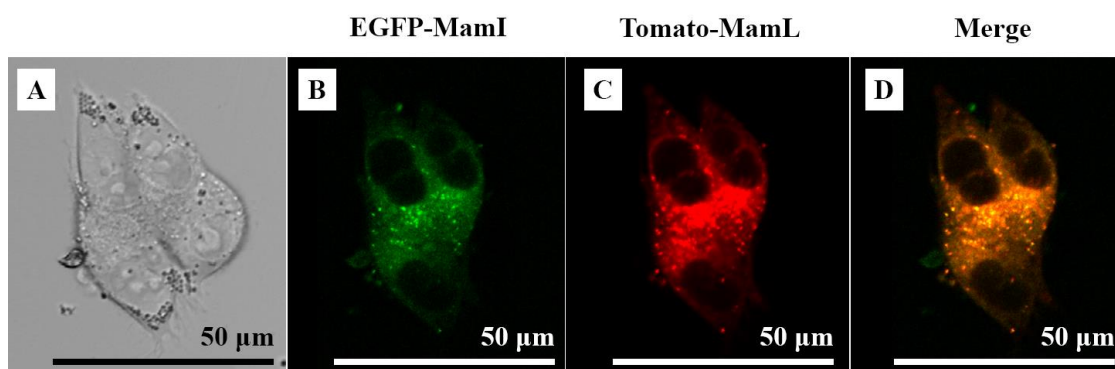
Figure 2.11 Confocal fluorescence microscopy of mammalian cells stably co-expressing Tomato-MamL and EGFP-MamI fusion proteins.

Transfected cells were placed under selection and enriched using FACS to obtain a

population co-expressing Tomato-MamL and EGFP-MamI. Dividing cells shown in

brightfield (*A*) are displayed under green (*B*) and red (*C*) fluorescence, highlighting the

expression of EGFP-MamI and Tomato-MamL, respectively. Merging green and red

fluorescence (*D*) indicates colocalization of fusion proteins in a yellow, punctate intracellular fluorescent pattern. These punctate structures are dispersed throughout the cell.

2.3.5   Effect of MamL truncation on co-localization with MamI

Compared to the punctate fluorescence of full-length MamL, cells expressing MamL$_{trunc}$ displayed both diffuse (~60%) and punctate (~ 40%) red fluorescence (Fig. 2.10). When Tomato-MamL$_{trunc}$ was co-expressed with EGFP-MamI, three different patterns of fluorescence were observed: diffuse green and red (~45%), diffuse green and punctate red (~45%), and punctate green and red (~10%) (Fig. 2.12). Removal of the MamL C-terminal peptide partially disrupted the co-localization and interaction of these two proteins. Cells co-expressing EGFP-MamI and Tomato-MamL$_{trunc}$ that have red and green punctate fluorescent pattern retain the mobility observed in full length MamL-MamI complexes. However, mobility of the fluorescent particles is not always present in MamL$_{trunc}$ co-expression systems. In approximately 45% of cells, Tomato-MamL$_{trunc}$ structures are mobile while the EGFP-MamI is diffuse throughout the cell, suggesting that removal of the MamL C-terminal peptide reduced the efficiency of the interaction between MamI and MamL.

| Brightfield | EGFP-MamI | Tomato-MamL$_{trunc}$ | Merge | Inset |
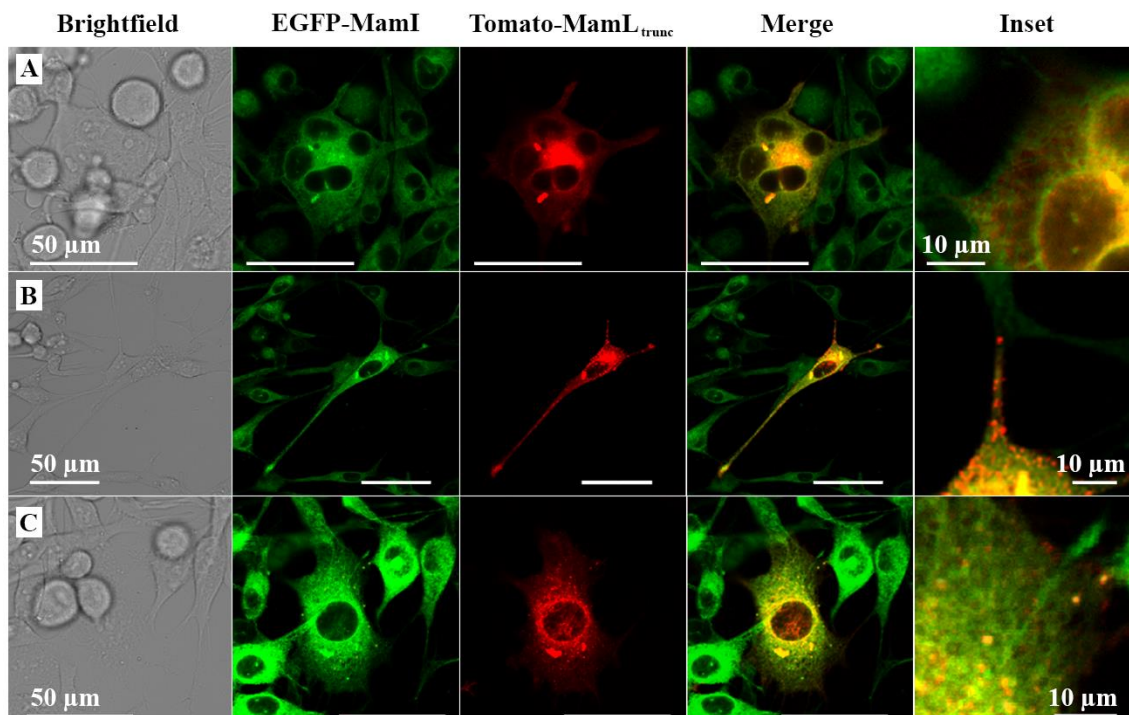
Figure 2.12 Confocal fluorescence microscopy of mammalian cells co-expressing Tomato-MamL$_{trunc}$ and EGFP-MamI fusion proteins.

Cells shown in brightfield are displayed under green (EGFP-MamI) and red (Tomato-MamL$_{trunc}$) fluorescence. Merging green and red fluorescence (Merge) indicates colocalization of fusion proteins in yellow. Co-expression of EGFP-MamI/Tomato-MamL$_{trunc}$ displays diffuse green and red fluorescence (A), diffuse green and punctate red fluorescence (B), and punctate green and red fluorescence (C). All punctate structures are dispersed throughout the cell and mobile. Scale bars indicate 50 µm unless otherwise noted.

2.3.6   Co-localization of FLAG-MamL and EGFP-MamI

When EGFP-MamI is co-expressed with FLAG-MamL, the net-like green-fluorescent pattern of EGFP-MamI (when expressed alone) changes to a green punctate mobile pattern (Fig. 2.13), consistent with an interaction between these magnetosome proteins and little or no interference from the fluorescent moiety. Western blots (Fig. 2.14) confirm the presence of both EGFP-MamI and full-length FLAG-MamL. Full blots are available in Appendix B.3.
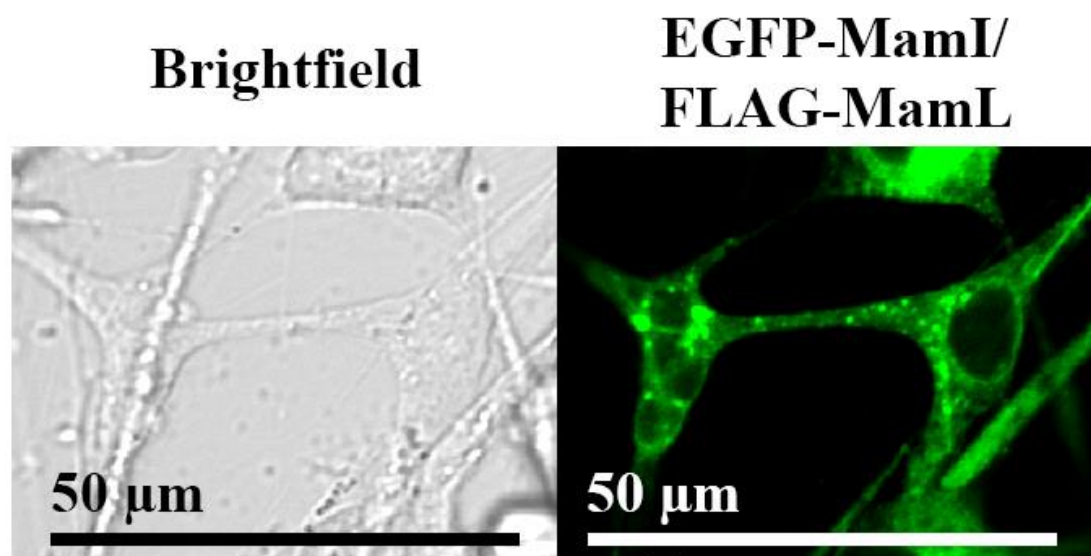
Figure 2.13 Confocal fluorescence microscopy of mammalian cells stably co-expressing FLAG-MamL and EGFP-MamI.

Micrographs display a population of MDA-MB-435 cells co-expressing FLAG-tagged MamL and EGFP-MamI fusion protein. The punctate intracellular fluorescent pattern is identical to that obtained with Tomato-MamL and GFP-MamI co-expression (Fig. 2.11), with mobile punctate structures dispersed throughout the cell.
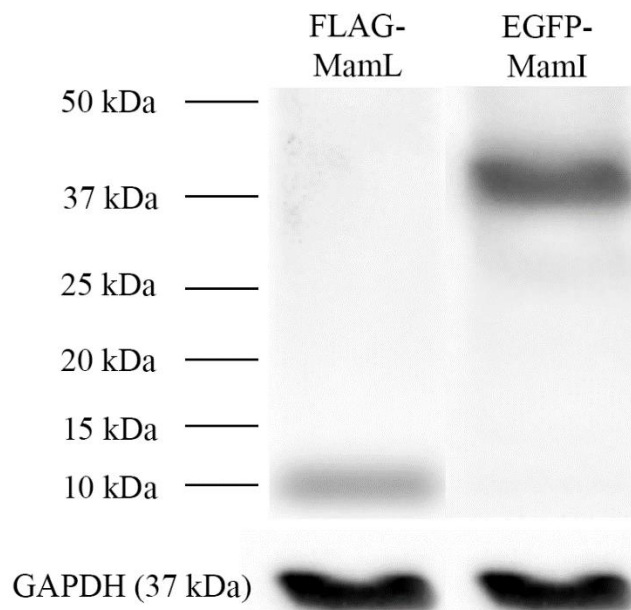
Figure 2.14 Immunoblots of mammalian cells co-expressing magnetosome fusion proteins.

Total cellular protein from MDA-MB-435 cells stably expressing both FLAG-MamL and EGFP-MamI was examined by western blot using mouse α-FLAG and mouse α-EGFP as the primary antibodies. The two lanes indicate the same sample probed for each protein. Approximate size of FLAG-MamL is 11 kDa. Approximate MW is shown in the left margin. The loading control was GAPDH (bottom panels).

2.3.7   Interactions between MamI and MamL

Apparent MamI-MamL interactions were further examined by FCS in lysed cell

samples containing total cellular protein (Fig. 2.15).
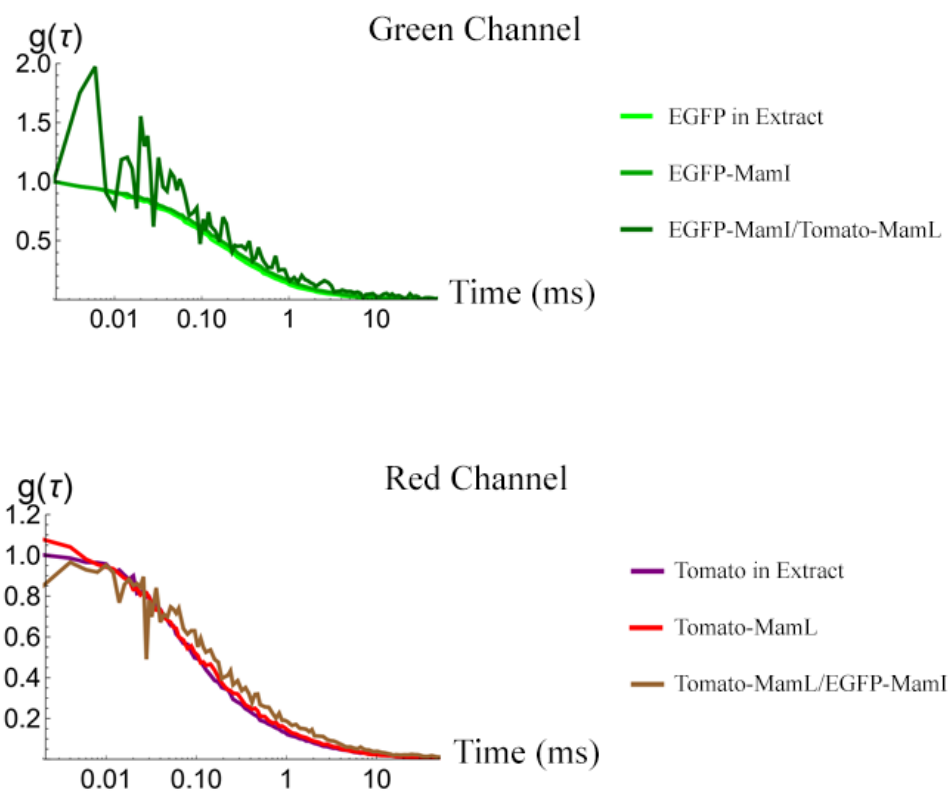
Figure 2.15 Autocorrelation curves obtained from fluorescence correlation spectroscopy of mammalian cells.

Curves in the green channel (top) are signals collected from EGFP (light green), EGFP-

MamI (green), or EGFP-MamI/Tomato-MamL (dark green) in lysed samples containing

total cellular protein. Curves in the red channel (bottom) are signals collected from

Tomato (purple), Tomato-MamL (red), or Tomato-MamL/EGFP-MamI (brown). Curves

are semi-log plots with autocorrelation function ($g(\tau)$) on the y-axis and lag time (ms) on

the x-axis.

Using this technique, the diffusion coefficient of fluorescent species present in the sample was measured and their apparent radius (R) was calculated. The diffusion of EGFP-MamI (in the absence of Tomato-MamL) was not significantly different from that of EGFP alone ($D = 90$ $\mu m^2/s \pm 3\%$ vs 108 $\mu m^2/s \pm 4\%$), as might be expected if EGFP-MamI exists as a monomer or dimer in the cell extract (Table 2.4). The specific brightness of the EGFP-MamI species detected (10.5 x 10^3 photon/s) was approximately double that of EGFP (4.9 x 10^3 photon/s), further suggesting that the fusion protein might be a dimer. On the other hand, in extracts from cells co-expressing both proteins, EGFP-MamI/Tomato-MamL diffused significantly slower than when EGFP-MamI was expressed alone ($D = 43.2$ $\mu m^2/s \pm 50\%$ vs 90 $\mu m^2/s \pm 3\%$, $p < 0.01$), as expected of a larger particle (Table 2.4). The intrinsic brightness of the fusion protein in the context of co-expression could not be determined in this case, because of heterogeneity in the population of detected particles. The apparent radius of EGFP-MamI when co-expressed with Tomato-MamL (4.4 nm, calculated from the value of the measured diffusion coefficient) was significantly larger ($p < 0.05$) than when EGFP-MamI was expressed alone (2.1 nm).

Table 2.4 FCS parameters in mammalian cell extracts of EGFP, EGFP-MamI or EGFP-MamI/Tomato-MamL.

	EGFP	EGFP-MamI	EGFP-MamI / Tomato-MamL
Diffusion coefficient [*] (μm^2/s)	108 ± 4% [†]	90 ± 3% [‡]	43.2 ± 50% [†, ‡]
Apparent radius [*] (nm)	1.7 ± 4% [§]	2.1 ± 3% [¶]	4.4 ± 50% [§, ¶]
Intrinsic brightness (10^3 photon/s)	4.9 ± 1% [#]	10.5 ± 1% [#]	ND

[*] Data are median +/- standard deviation expressed as percentage of the median (n = 5).

[†, ‡, #] $p < 0.001$ [§, ¶] $p < 0.05$ ND, not detectable

In the red channel, a similar pattern was observed for the diffusion of Tomato-MamL (Table 2.5). Its diffusion coefficient (49 μm^2/s ± 3%) is very close to that of Tomato (51 μm^2/s ± 56%), as expected if Tomato-MamL in the cellular extract exists as a monomer. This is confirmed by the very similar intrinsic brightness of Tomato-MamL and Tomato (2.5 x 10^3 vs. 2.6 x 10^3 photons/s, respectively). In extracts of cells co-expressing Tomato-MamL and EGFP-MamI, the particle is diffusing more slowly (D = 29 μm^2/s ± 38%) than either Tomato or Tomato-MamL alone, indicating that a larger structure is formed upon co-expression of these fluorescent magnetosome fusion proteins (again, with population heterogeneity precluding the measurement of intrinsic

brightness). Based on the value of its diffusion coefficient, the average apparent radius of the Tomato-MamL/EGFP-MamI particle is 6.6 nm (Table 2.5), comparable to the size measured in the green fluorescence channel (4.4. nm, Table 2.5).

Table 2.5 FCS parameters of mammalian cell extracts expressing Tomato, Tomato-MamL, or Tomato-MamL/EGFP-MamI.

	Tomato	**Tomato-MamL**	**Tomato-MamL/ EGFP-MamI**
Diffusion coefficient [*] (μm^2/s)	$51 \pm 56\%$	$49 \pm 3\%$	$29 \pm 38\%$
Apparent radius [*] (nm)	$3.7 \pm 56\%$	$3.8 \pm 3\%$	$6.6 \pm 38\%$
Intrinsic brightness (10^3 photon/s)	$2.6 \pm 1\%$	$2.5 \pm 1\%$	ND

[*] Data are median +/- standard deviation expressed as percentage of the median (n = 5).

ND, not detectable

Protein-protein interactions between EGFP-MamI and FLAG-MamL were further examined by co-immunoprecipitation (Fig. 2.16). When immunoprecipitated samples of cells co-expressing GFP-MamI and FLAG-MamL are probed with anti-GFP antibody, both GFP-MamI and FLAG-MamL are detected on the blot. The presence of FLAG-MamL protein following an anti-GFP pull-down provides evidence that MamI and MamL proteins are physically interacting.
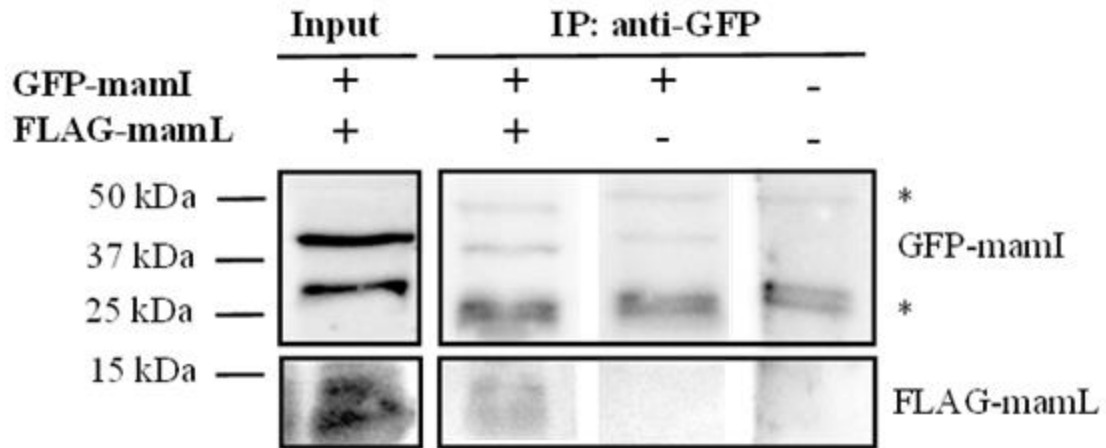
Figure 2.16 FLAG-MamL co-immunoprecipitates with EGFP-MamI.

Western blots detect EGFP-MamI and FLAG-MamL immunoprecipitated from extracts

of cells expressing both proteins. Co-immunoprecipitation was performed with mouse

anti-GFP antibody. Input = 2% of IP. Protein bands for EGFP-mamI and FLAG-mamL

are seen ~41 kDa and ~11 kDa, respectively. Asterisks indicate antibody heavy and light

chains from the immunoprecipitation.

2.4   Discussion

This report describes the expression of fluorescently tagged, magnetosome-associated membrane proteins MamI and MamL in a mammalian cell system and demonstrates their ability to co-localize and interact in a foreign environment. The specificity of this magnetosome protein interaction was characterized by fluorescence confocal microscopy and correlation spectroscopy, showing co-localization of fluorescent fusion proteins, specific recruitment of MamI to MamL particles, as well as interactions between MamL and mobile element(s) within the mammalian intracellular compartment. The bifunctional nature of MamL in intact cells, indicating associations with both MamI and mammalian molecular motors, was revealed by the recruitment of MamI to the mobile MamL structures when both magnetosome proteins were colocalized. At the same time, cell extracts of co-expressed protein demonstrated a decrease in molecular diffusion coefficients, consistent with the formation of species of increasing macromolecular radius, as expected from the interaction of MamI and MamL.

2.4.1   Combined magnetosome gene expression in mammalian cells

When co-expressed, the proximity of green and red fluorescence from MamI and MamL fusion proteins, respectively, resulted in yellow particles. This evidence of co-localization is strengthened by additional measures documenting changes in the subcellular localization, diffusion coefficient, apparent radius of co-expressed fusion proteins, and co-immunoprecipitation of magnetosome fusion proteins.

Confocal microscopy of live cells expressing EGFP-MamI alone reveals a net-like pattern of green fluorescence, while Tomato-MamL exhibits punctate, red fluorescent structures in the presence and absence of EGFP-MamI. The net-like structure of MamI alone may be related to dimerization of the EGFP fusion protein, whose intrinsic brightness in cellular extracts was twice that of EGFP (10,500 vs 4,500 photons/s). In contrast, Tomato-MamL appears to exist as a monomer in cellular extracts, with intrinsic brightness that is only modestly quenched compared to Tomato (2,500 vs 2,600 photons/s). Although intrinsic brightness values were obtained from FCS measurements in cell extracts (*i.e.* actual cellular structures not preserved), these measurements still give information on the elementary units of protein structures.

The characteristics of singly expressed MamI may be related to the endoplasmic reticulum (ER) which displays a similar net-like pattern in peripheral ER tubules (29). Although biological relevance of this structure within the context of magnetosome assembly is unclear, potentially the interaction between MamI and MamL has features shared with ER-shaping proteins. Regardless, the net-like pattern of MamI was replaced by punctate green fluorescence in the presence of full-length MamL, whether fused to Tomato or FLAG. Moreover, there was no residual net-like pattern, suggesting that the association of MamI and MamL is the dominant interaction, producing an intracellular structure, as expected, during initiation of a magnetosome-like structure in a mammalian cell system.

The apparent diffusion coefficient observed for fluorescent MamI and MamL fusion protein structures in mammalian cells, $D = 2.2 \ \mu m^2/s$, corresponds to that of a particle with a hydrodynamic radius of about 20 nm (assuming a cellular viscosity 5

times that of water). This size is comparable to that of transport vesicles in eukaryotic

cells (radius 15 to 50 nm) and to that of magnetosome crystals (average radius 21 nm in

M. magneticum AMB-1 (28) and between 17 to 60 nm (29) for other MTB species).

While there is no expectation of biomineral formation in the present work, in MTB where

the full complement of magnetosome genes is expressed, divergent roles for MamI have

been reported in different species of *Magnetospirillum*, suggesting that cellular milieu

may influence function. While MamI is essential to vesicle formation in *M. magneticum*,

the same role has not been assigned in *M. gryphiswaldense* (30). In the latter MTB, a role

for MamI in magnetite nucleation has been reported (31). For future applications in

molecular MRI, both roles of MamI will be important and may yet be validated as

mammalian expression systems are developed to incorporate additional, essential

magnetosome genes that optimize the rudimentary magnetosome-like nanoparticle (34).

MamI and MamL are small integral membrane proteins (77 and 123 amino acids,

respectively) with predicted alpha helices that span the (magnetosome) membrane twice

(13). In extracts where cellular structure is removed, correlation spectroscopy indicated

that particles expressing both green and red fluorescence (co-expression of MamI and

MamL) diffused more slowly than either fluorescent protein (EGFP or Tomato) or

fluorescent fusion protein (EGFP-MamI or Tomato-MamL) alone. As expected, if these

two fusion proteins directly interact or localize to the same structure, regardless of which

fluorescent channel is used to generate autocorrelation curves (Fig. 2.16), the diffusion

coefficients of co-expressed fusion proteins are similar (approximately 30 to 40 μm^2/s for

red and green fluorescence, respectively). From these measurements, the radius of the

structure to which MamI and MamL belong in the extract was estimated to be on the

order of 4 to 7 nm. Future work using fluorescence cross correlation spectroscopy will confirm whether or not these fusion proteins are indeed moving together, as strongly suggested by co-immunoprecipitation and changes in their subcellular localization and mobility (discussed below).

2.4.2 MamL mobility and association with MamI

The mobility of MamL particles in mammalian cells is an unexpected finding, offering new insights into magnetosome substructure and the potential roles of individual magnetosome genes. The presence of yellow fluorescent particles not only confirms the association between EGFP-MamI and Tomato-MamL, but also distinguishes this interaction from that occurring between MamL and cellular mobile elements. If MamI binds directly to MamL, then the interaction between these magnetosome proteins may occur primarily in the membrane compartment, leaving the ionic C-terminal tail of MamL available for alternative functions. However, as shown in this chapter, the C-terminus of MamL seems to contribute to the co-localization and interaction of MamI an MamL.

2.4.3 Truncation of the MamL C-terminal tail

Whether expressed alone or in conjunction with EGFP-MamI, Tomato-MamL structures were mobile. Analysis of the amino acid sequence of MamL reveals a C-terminal tail of 15 amino acids that is rich in positively-charged amino acids and bears sequence homology to cell-penetrating peptides (CPP) (12). This class of cationic peptides can traverse the plasma membrane by interacting with negatively charged

phospholipids (32). Although any such role for MamL awaits further characterization, here we describe the mobility of Tomato-MamL structures in terms of plausible interactions between the MamL C-terminal tail and anionic components of the cytoskeleton. This is consistent with structure predictions of MamL, suggesting that its C-terminal cationic residues lie outside the membrane, theoretically exposed to the cytosolic face of an intracellular vesicle (13) . CPP have also been reported to interact with cytoskeletal components; for example, the synthetic arginine-rich peptide R_8W strongly interacts with the anionic proteins actin and tubulin (32, 33). Our analysis of confocal videos is likewise consistent with the notion of MamL C-terminal interactions with mammalian molecular motors (Chapter 3).

We have further investigated the role of the MamL C-terminal tail with the Tomato-MamL$_{trunc}$ mutant. When expressed alone in mammalian cells, MamL$_{trunc}$ displays both diffuse and punctate fluorescence, the former more commonly than the latter. The punctate particles in cells that express MamL$_{trunc}$ retain their mobile nature, suggesting that removal of the C-terminal peptide affected the interaction between MamL and relevant cellular structure. When Tomato-MamL$_{trunc}$ is co-expressed with EGFP-MamI, three different expression patterns were observed: diffuse MamI and MamL$_{trunc}$ (yellow diffuse), diffuse MamI but punctate MamL$_{trunc}$ (green diffuse but red punctate), or punctate MamI and MamL$_{trunc}$ (yellow punctate). Since colocalization (yellow fluorescence) of the two proteins is not always observed, as shown in cells that had diffuse MamI expression but punctate MamL$_{trunc}$ expression, it is likely that the C-terminus of MamL also has a role in the interaction between the two proteins. It is also a possibility that cells displaying green diffuse but red punctate fluorescence are in a

transitional state of MamI/MamL$_{trunc}$ expression in which the MamI protein are in the process of reorganizing into the punctate MamL$_{trunc}$ expression. This transitional state; however, is not seen in cells co-expressing full-length MamL and MamI.

Whether or not the mobility of Tomato-MamL can be attributed to interactions with eukaryotic kinesins remains uncertain. Nevertheless, the three major groups of eukaryotic cytoskeletal proteins - actin, tubulin and intermediate filament proteins - are represented in prokaryotes (34) and evolutionarily conserved in MTB (11, 35), as is the magnetosome structure, which has been likened to a bacterial organelle (12). Potentially, MamL has an underlying role in subcellular movement of the magnetosome, known to be linked by MamK (a non-essential magnetosome protein) to actin-like filaments of the bacterial cytoskeleton (36). In support of bacterial-mammalian protein interactions, a functional role for MamM, a magnetosome-associated cation diffusion facilitator (CDF) protein, in modelling structural and regulatory changes in mammalian CDF homologues, has been previously reported (37).

When expressed as a transgene in the mammalian environment, without the full complement of (essential) magnetosome genes, the orientation of Tomato-MamL is not necessarily predetermined. If its C-terminal is equally exposed to cytoplasmic and luminal faces of the membrane, this will limit the number of particles engaged in directed motion with cytoskeletal partners. In fact, we observed a pattern of directed motion in approximately half of the MamL particles.

Both MamI and MamL have been implicated in membrane invagination in MTB (38) and thus could both strongly influence membrane curvature and liposome size. A

second possible explanation is that, in the absence of MamI, the detected particles

strongly associate with larger structures, like the cytoskeleton, resulting in constrained

(rather than free) Brownian motion and a very small apparent diffusion coefficient.

Alternatively, partial expression of the magnetosome structure may lead to promiscuous

interactions with mammalian components (*i.e.,* molecular motors) that would not exist in

the presence of the full complement of magnetosome gene products. In any case, the data

presented here point to a notable interaction between MamI and MamL, with

consequences related to intracellular mobility of the resulting particle. Conceivably, the

rudimentary magnetosome structure has built-in motility, in part to facilitate

magnetotaxis (39). The nature of additional potential magnetosome protein-protein

interactions is currently under investigation (2, 5) and may rely on ionic interactions

characteristic of CPP.

2.5   Conclusion

We have previously hypothesized that essential magnetosome proteins form a rudimentary structure upon which the membrane-enclosed biomineral is synthesized (5). The data herein support this hypothesis and provide the first confirmation that MamI and MamL interact, even in the complex intracellular compartment of the mammalian cell. This finding is consistent with their proposed role in providing a docking site on the vesicle membrane for additional magnetosome protein interactions. Moreover, the unique patterns of cellular localization observed with MamI and MamL fluorescent fusion proteins suggest that these magnetosome proteins may have additional functionality not previously recognized. Among these is the possibility of creating a scaffold on which a rudimentary magnetosome-like nanoparticle may be assembled for molecular imaging with MRI. Once the relationship between essential magnetosome elements is more fully understood, the regulation of this structure will be possible and permit the selective use of discrete steps in iron biomineralization. This includes regulation of its subcellular localization, timing of assembly or disassembly, and ultimately, control of the size, shape and composition of the crystal. Cellular MRI may be influenced by all these factors, permitting *in vivo* detection of genetically-regulated iron contrast in cells of all kinds, from bacteria (40) to human.

2.6 References

1.   McRobbie D, Moore E, Graves M, Prince M. MRI from proton to picture: Cambridge University Press; 2017.
2.   Sun Q, Prato F, Goldhawk D. Optimizing Reporter Gene Expression for Molecular Magnetic Resonance Imaging: Lessons from the Magnetosome. In: Ueno S, editor. Bioimaging: Imaging by Light and Electromagnetics in Medicine and Biology: CRC Press Taylor & Francis Group; 2020.
3.   Sun Q, Prato FS, Goldhawk DE. Optimizing Reporter Gene Expression for Molecular Magnetic Resonance Imaging: Lessons from the Magnetosome. In: Ueno S, editor. Bioimaging: Imaging by Light and Electromagnetics in Medicine and Biology: CRC Press Taylor & Francis Group; 2020.
4.   Thakor A, Jokerst J, Ghanouni P, Campbell J, Mittra E, Gambhir S. Clinically Approved Nanoparticle Imaging Agents. J Nucl Med. 2016;57:1833–7.
5.   Goldhawk D, Gelman N, Thompson R, Prato F. Forming magnetosome-like nanoparticles in mammalian cells for molecular MRI. In: Bulte J, Modo M, editors. Design and Applications of Nanoparticles in Biomedical Imaging. Switzerland: Springer International Publishing; 2017. p. 187-203.
6.   Araujo A, Abreu F, Tavares Silva K, Bazylinski D, Ulysses Lins U. Magnetotactic Bacteria as Potential Sources of Bioproducts. Mar Drugs. 2015;13:389-430.
7.   Uebe R, Schuler D. Magnetosome biogenesis in magnetotactic bacteria. Nat Rev Microbiol. 2016;14:621-37.
8.   Boucher M, Geffroy F, Preveral S, Bellanger L, Selingue E, Adryanczyk-Perrier G, et al. Genetically tailored magnetosomes used as MRI probe for molecular imaging of brain tumor. Biomaterials. 2017;121:167-78.
9.   Brown R, Cheng Y-C, Haacke E, Thompson M, Venkatesan R. Magnetic Resonance Imaging: Physical Principles and Sequence Design: Wiley-Blackwell; 2014.
10.   Matsunaga T, Okamura Y, Fukuda Y, Wahyudi A, Murase Y, Takeyama H. Complete Genome Sequence of the Facultative Anaerobic Magnetotactic Bacterium Magnetospirillum sp. strain AMB-1. DNA Res. 2005;12:157-66.
11.   Murat D, Quinlan A, Vali H, Komeili A. Comprehensive genetic dissection of the magnetosome gene island reveals the step-wise assembly of a prokaryotic organelle. Proc Natl Acad Sci USA. 2010;107:5593–8.
12.   Komeili A. Molecular mechanisms of compartmentalization and biomineralization in magnetotactic bacteria. FEMS Microbiol Rev. 2012;36:232-55.
13.   Nudelman H, Zarivach R. Structure prediction of magnetosome-associated proteins. Front Microbiol. 2014;5:article 9.
14.   Raschdorf O, Forstner Y, Kolinko I, Uebe R, Plitzko J, Schüler D. Genetic and Ultrastructural Analysis Reveals the Key Players and Initial Steps of Bacterial Magnetosome Membrane Biogenesis. PLoS Genet. 2016;126:e1006101.
15.   Staniland S, Williams W, Harrison A, Ward B, Telling N, Van Der Laan G. Controlled cobalt doping of magnetosomes in vivo. Nat Nanotech. Nat Nanotech. 2008;3:158-62.
16.   Goldhawk D, Lemaire C, McCreary C, McGirr R, Dhanvantari S, Thompson R, et al. Magnetic resonance imaging of cells overexpressing MagA, an endogenous contrast agent for live cell imaging. Mol Imaging. 2009;8:129-39.

17.   Zurkiya O, Chan AW, Hu X. MagA is sufficient for producing magnetic nanoparticles in mammalian cells, making it an MRI reporter. Magn Reson Med. 2008;59(6):1225-31.

18.   Elfick A, Rischitor G, Mouras R, Azfer A, Lungaro L, Uhlarz M, et al. Biosynthesis of magnetic nanoparticles by human mesenchymal stem cells following transfection with the magnetotactic bacterial gene mms6. Scientific Reports. 2017;7:39755.

19.   Zhang X-Y, Robledo B, Harris S, Hu X. A Bacterial Gene, mms6, as a New Reporter Gene for Magnetic Resonance Imaging of Mammalian Cells. Mol Imaging. 2014:1-12.

20.   Lefevre C, Trubitsyn D, Abreu F, Kolinko S, Jogler C, Gonzaga Paula de Almeida L, et al. Comparative genomic analysis of magnetotactic bacteria from the Deltaproteobacteria provides new insights into magnetite and greigite magnetosome genes required for magnetotaxis. Env Microbiol. 2013;15:2712-35.

21.   Komeili A, Li Z, Newman DK, Jensen GJ. Magnetosomes are cell membrane invaginations organized by the actin-like protein MamK. Science. 2006;311(5758):242-5.

22.   Donna EG. Molecular Imaging with Genetically Programmed Nanoparticles. In: Farid AB, editor. Radiopharmaceuticals. Rijeka: IntechOpen; 2021. p. Ch. 10.

23.   Rohani R, Figueredo R, Bureau Y, Koropatnick J, Foster P, Thompson R, et al. Imaging tumor growth non-invasively using expression of MagA or modified ferritin subunits to augment intracellular contrast for repetitive MRI. Mol Imaging Biol. 2014;16:63-73.

24.   Smith P, Krohn R, Hermanson G, Mallia A, Gartner F, Provenzano M, et al. Measurement of protein using bicinchoninic acid. Anal Biochem. 1985;150:76-85.

25.   Kask P, Palo K, Ullmann D, Gall K. Fluorescence-intensity distribution analysis and its application in biomolecular detection technology. Proc Natl Acad Sci USA. 1999;96:13756-61.

26.   Liu L, Alizadeh K, Donnelly S, Dassanayake P, Hou T, McGirr R, et al. MagA expression attenuates iron export activity in undifferentiated multipotent P19 cells. PLOS ONE. 2019;14:e0217842.

27.   Sengupta A, Quiaoit K, Thompson R, Prato F, Gelman N, Goldhawk D. Biophysical features of MagA expression in mammalian cells: implications for MRI contrast. Front Microbiol. 2014;5:29.

28.   Nadkarni R, Barkley S, Fradin C. A Comparison of Methods to Measure the Magnetic Moment of Magnetotactic Bacteria through Analysis of Their Trajectories in External Magnetic Fields. PLOS ONE. 2013;8:e82064.

29.   Bazylinski D, Garratt-Reed A, Frankel R. Electron microscopic studies of magnetosomes in magnetotactic bacteria. Microsc Res Tech. 1994;27:389–401.

30.   Lohße A, Borg S, Raschdorf O, Kolinko I, Tompa E, Pósfai M, et al. Genetic Dissection of the mamAB and mms6 Operons Reveals a Gene Set Essential for Magnetosome Biogenesis in Magnetospirillum gryphiswaldense. J Bacteriol. 2014;196:2658–69.

31.   Bereczk-Tompa E, Posfai M, Toth B, Vonderviszt F. Magnetite-Binding Flagellar Filaments Displaying the MamI Loop Motif. ChemBioChem. 2016;17:2075-82.

32.   Schmidt N, Mishra A, Lai G, Wong G. Arginine-rich cell-penetrating peptides. FEBS Lett. 2010;584:1806-13.

33.   Jones L, Yazzie B, Middaugh C. Polyanions and the proteome. Mol Cell Proteomics. 2004;3:746-69.

34.   Shih Y-L, Rothfield L. The Bacterial Cytoskeleton. Microbiology and Molecular Biology Reviews. 2006;70:729-54.

35.   Lin W, Paterson G, Zhu Q, Wang Y, Kopylova E, Li Y, et al. Origin of microbial biomineralization and magnetotaxis during the Archean. Proc Natl Acad Sci USA 2017;114:2171-6.

36.   Pradel N, Santini C-L, Bernadac A, Fukumori Y, Wu L-F. Biogenesis of actin-like bacterial cytoskeletal filaments destined for positioning prokaryotic magnetic organelles. Proc Natl Acad Sci USA. 2006;103:17485.

37.   Zeytuni N, Uebe R, Maes M, Davidov G, Baram M, Raschdorf O, et al. Bacterial Magnetosome Biomineralization - A Novel Platform to Study Molecular Mechanisms of Human CDF-Related Type-II Diabetes. PLoS ONE. 2014;9:e97154.

38.   Barber-Zucker S, Zarivach R. A Look into the Biochemistry of Magnetosome Biosynthesis in Magnetotactic Bacteria. ACS Chem Biol. 2017;12:13-22.

39.   Howard J. Mechanics of Motor Proteins and the Cytoskeleton. Sunderland, MA: Sinauer Associates; 2001.

40.   Kowalski K, Mulak A. Brain-gut-microbiota axis in Alzheimer's disease. J Neurogastroenterol Motil. 2019;25:48-60.

Chapter 3

3 Cellular distribution and motion of essential magnetosome proteins expressed in mammalian cells

In a mammalian cell line, the fluorescent magnetosome fusion protein Tomato-MamL forms a punctate pattern, and the puncta are mobile. To evaluate their mobility relative to the mobility of Tomato-MamB puncta and in contrast to the immobile puncta formed by EGFP-MamE, the trajectories of the puncta formed by these different fusion proteins were identified in confocal microscopy image sequences with the ImageJ plugin Mosaic Particle Tracker 2D/3D (version 1.0.1) and classified then analyzed with a custom software written for Mathematica. The resulting mobility parameters, including velocities and apparent diffusion coefficients, of MamL, MamL$_{trunc}$, MamB, and MamE when individually expressed in mammalian cells, are described in this chapter. The MamI+MamL co-expression system was also studied in the same way.

The analysis of confocal movies was done in collaboration with Dr. Cécile Fradin at McMaster University. Dr. Fradin guided the development of methods in section 3.2.6.3 to refine the analysis of particle trajectories initially identified using open software. The results presented in Tables 3.3 to 3.15 as well as in Figures 3.8 to 3.20 were obtained using the customized Mathematic analysis tool developed in collaboration with Dr. Fradin.

I would like to thank Sarah Donnelly and Peggy Zhou for contributing to data collection for Figure 3.7.

Contents from this chapter will be submitted for publication with the tentative author list: Sun Q, Fradin C, Thompson RT, Prato FS, and Goldhawk DE.

3.1   Introduction

In magnetotactic bacteria (MTB), magnetosome formation allows the cell to compartmentalize and concentrate iron biominerals in membrane-enclosed vesicles (1). Magnetosome formation is a stepwise, protein-directed process that begins with vesicle formation and culminates with iron biomineralization. This entire process is regulated by approximately 30 genes, the majority of which are located on the magnetosome genomic island (2, 3). Many of these genes encode membrane proteins which are involved in different steps of bacterial magnetosome formation: inner membrane invagination leading to vesicle formation, recruitment of proteins to the vesicle membrane, alignment of vesicles along a protein filament, concentration of iron inside the vesicle and finally magnetic crystal nucleation and growth.

To stimulate formation of a rudimentary magnetosome-like particle in mammalian cells, we are introducing select genes (alone or in combination) deemed essential for the initial stages of magnetosome formation, namely *mamI*, *mamL*, *mamB* and *mamE*. These four genes are clustered on the *mamAB* operon and are highly conserved in most species of MTB (4). The gene products of *mamI*, *mamL*, and *mamB* are believed to play an essential role in the first steps of magnetosome vesicle formation (2, 5, 6), including designation of the vesicle and, in the case of MamB, recruitment of other magnetosome-associated proteins like MamE (7, 8), which also plays a dual role in recruitment of additional magnetosome-associated proteins and the initiation of iron

biomineralization (9). We hypothesize that these four magnetosome proteins will interact in the membranous compartment of mammalian cells.

Sequence analysis of the MamL protein indicates the presence of a positively-charged peptide (2) (Figure 1.4) in the C-terminal 15 amino acids. Cationic peptides, also referred to as cell-penetrating peptides, have been implicated in endocytotic pathways (10). We have previously shown that when individually expressed, Tomato-MamL proteins assemble into punctate structures that move intracellularly. We have also shown that MamL recruits EGFP-MamI to these structures via magnetosome protein-protein interactions (Chapter 2).

Here, we describe the mobility of MamL when expressed as red fluorescent fusion proteins in a mammalian cell line in more details and compare it to that of MamB. Comparison(s) are also drawn to the immobile structures formed by MamE, expressed as a green fluorescent fusion protein. In addition, a green fluorescent MamI fusion protein was studied in cells co-expressing MamL. Here we perform an in-depth analysis of the motion of these punctate intracellular structures and demonstrate that they can be classified into three types of trajectories corresponding to confined, diffusing and actively transported particles. The motion detected for MamL (and for MamI when interacting with MamL) shows that a significant fraction of punctate particles display directed motion. This demonstrates the capacity of magnetosome proteins to spontaneously interact with elements of the eukaryotic transport machinery.

3.2   Materials and Methods

3.2.1   Molecular Cloning

Magnetosome genes *mamI* and *mamL* were amplified by PCR from the genomic DNA of *Magnetospirillum magneticum* strain AMB-1 (ATCC 700264) using custom primers (Table 2.1). The *mamI* and *mamL* amplicons were purified using a PCR clean-up kit (Invitrogen, Life Technologies, Burlington, Canada); digested with appropriate restriction enzymes (Table 2.1); and purified once more, prior to insertion in the molecular cloning vectors pEGFP-C1 (Clontech; Fig. 2.1) and ptdTomato-C1 (Clontech; Fig. 2.2), respectively. Sequencing information for *mamI* and *mamL* is provided in Appendix A.1 and A.2, respectively. After propagation in *Escherichia coli* strain XL10GOLD, the vector-insert plasmid constructs were purified and used for mammalian cell transfection.

For cloning of Tomato-MamL$_{trunc}$, the last 15 amino acids from the C-terminus of MamL were removed by PCR site-directed mutagenesis. Briefly, primers were designed that included a stop codon 45 nucleotides upstream from the end of *mamL* (Table 2.2). These primers were used in PCR amplification of the *mamL$_{trunc}$* gene, which was then inserted into the ptdTomato-C1 vector with restriction enzymes EcoRI and BglII (Fig. 2.3). Sequencing information is provided in Appendix A.3.

For cloning of FLAG-MamL, primers flanking *mamL* in ptdTomato-*mamL* were designed to include a FLAG tag for immunodetection. The *FLAG-mamL* insert was amplified using PCR, purified using a PCR clean-up kit (Invitrogen, Life Technologies, Burlington, Canada), and restriction digested using SacI and EcoRI (Table 2.3). *FLAG-*

mamL was then inserted into the pSF-EMCV-*FLuc* vector and propagated in *Escherichia*

coli strain XL10GOLD (Fig. 2.4). Sequencing information is provided in Appendix A.4.

For cloning of Tomato-MamB, the *mamB* gene was amplified by PCR from

AMB-1 genomic DNA using custom primers (Table 3.1). The amplicon was purified

with a PCR clean-up kit, digested with restriction enzymes (Table 3.1), purified once

more, and inserted into the ptdTomato-C1 vector (Clontech; Fig 3.1). The vector-insert

construct was propagated in *E. coli* strain XL10GOLD, purified, and then used for

mammalian cell transfection. Sequencing information is provided in Appendix A.5.

Table 3.1 Primer design for the cloning of MTB genes *mamB* and *mamE* into ptdTomato-C1 and pEGFP-C1, respectively.

Gene	Primer (5' – 3')		Restriction Site*	Vector
mamB	Forward	CAATCTTGTG**GAATTC**AGAACCG	*EcoRI*	ptdTomato-C1
	Reverse	ACGCTCTGG**CCCGGG**ATGTCC	*SmaI*	
mamE	Forward	ACCCTG**AGATCT**GGATGGTTG	*BglII*	pEGFP-C1
	Reverse	GCCATTATCC**GAGCTC**CACCA	*SacI*	

*Restriction enzyme sites appear in bold in the primer sequence.

Figure 3.1 Vector-insert map of the cloning strategy of magnetosome gene *mamB*.

The vector-insert map of ptdTomato-mamB shows *mamB* (in blue) cloned in downstream

of tdTomato (red) between restriction sites EcoRI and SmaI. The bacterial origin of

replication (ori) is shown in yellow. The mammalian CMV enhancer and promoter,

which allow for constitutive gene expression, is shown in white. The NeoR/KanR/G418R

gene (light green) provides kanamycin antibiotic resistance in bacterial cells and G418

antibiotic resistance in mammalian cells.

For cloning of EGFP-MamE, the *mamE* gene was amplified by PCR from the AMB-1 genomic DNA using custom primers (Table 3.1). The amplicon was purified with a PCR clean-up kit, digested with restriction enzymes (Table 3.1), purified once more, and inserted into the pEGFP-C1 vector (Clontech; Fig 3.2). The vector-insert construct was propagated in *E. coli* strain XL10GOLD, purified, then used for mammalian cell transfection.

When sequencing EGFP-*mamE*, there were two mutations (at amino acids 49 (Gly → Ser) and 641 (Thr → Ser) present in the gene sequence (Appendix A.6). These mutations were not found in the column-purified EGFP-*mamE* DNA but were present in the MaxiPrep EGFP-*mamE* DNA; therefore, some downstream work with the mutated EGFP-*mamE* was done (ie. confocal fluorescence, MRI phantoms, elemental iron analysis). After another attempt at cloning *mamE*, the new EGFP-*mamE* was sequenced and there was one mutation found at amino acid 317 (Thr → Ala) (Appendix A.6). The first *mamE* will be referred to as EGFP-*mamE* (G49S, T641S) and the second *mamE* will be referred to as EGFP-*mamE* (T317A). Sequencing information of both constructs is provided in Appendix A.6.
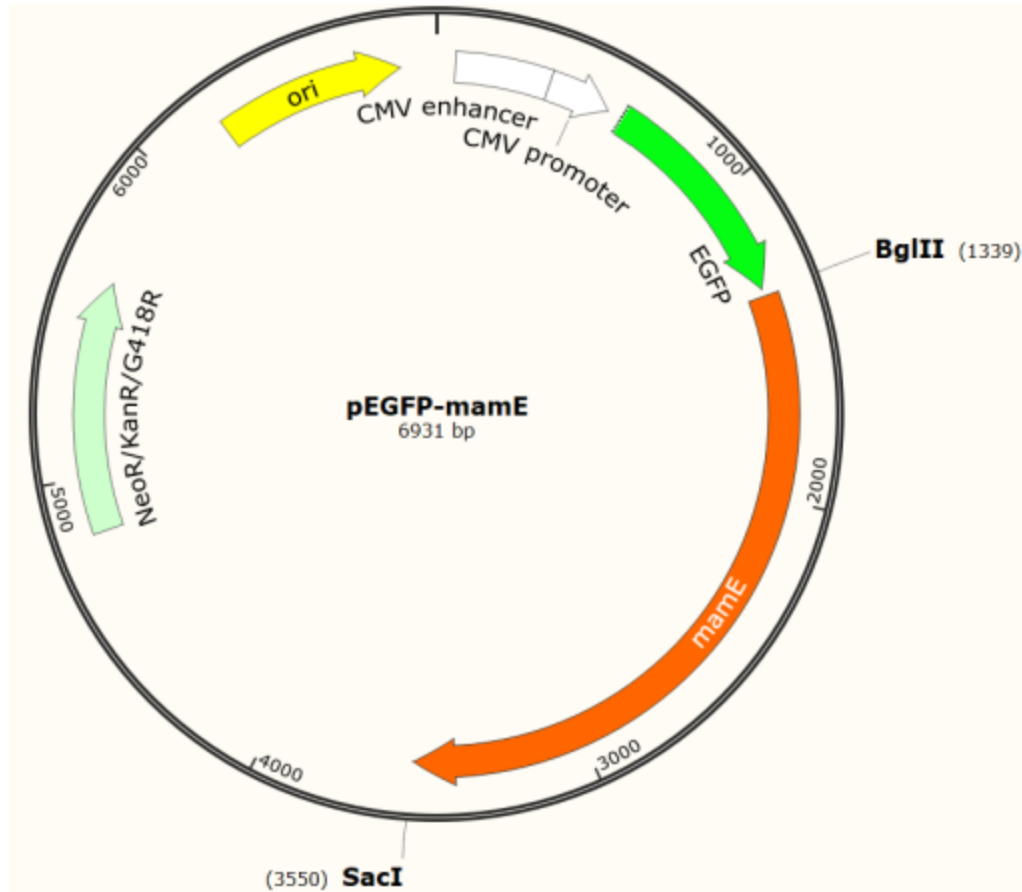
Figure 3.2 Vector-insert map of the cloning strategy of magnetosome gene *mamE*.

The vector-insert map of pEGFP-mamE shows *mamE* (orange) cloned in downstream of

EGFP (bright green) between restriction sites BglII and SacI. The bacterial origin of

replication (ori) is shown in yellow. The mammalian CMV enhancer and promoter,

which allows for constitutive gene expression, is shown in white. The

NeoR/KanR/G418R gene (light green) provides kanamycin antibiotic resistance in

bacterial cells and G418 antibiotic resistance in mammalian cells.

3.2.2   Cell Culture

MDA-MB-435 cells (ATCC HTB-129; derived from an adult female and characterized as a melanoma cell line) are a model of aggressive tumorigenesis (11). Cells were cultured in 100 mm cell culture dishes (CELLSTAR, VWR International, Mississauga, Canada) with Dulbecco's Modified Eagle Medium (DMEM) containing 1 g/L glucose (Gibco, Life Technologies, Burlington, Canada), 10% fetal bovine serum (FBS; Gibco), 4 U/mL penicillin, and 4 µg/mL streptomycin at 37°C with 5% CO_2.

To create cell lines expressing the enhanced green fluorescent protein (EGFP)-MamI fusion protein or the red fluorescent protein tdTomato (Tomato)-MamL fusion protein, cells were grown to 60-70% confluency on a 100 mm dish and transfected using Lipofectamine 2000 (Invitrogen), according to company protocol, using 8 µg of pEGFP-*mamI* or ptdTomato-*mamL*, respectively.

For co-expression of both pEGFP-*mamI* and ptdTomato-*mamL,* cells stably expressing Tomato-MamL were transfected with 8 µg of pEGFP-*mamI*. After 16 hours, cells were placed in full medium for 48 hours before commencing antibiotic selection. For co-expression with the pSF-FLAG-*mamL*-EMCV-FLuc construct, MDA-MB-435/EGFP-MamI cells were grown to 60-70% confluency on a 100 mm dish and transfected using Lipofectamine 2000 (Invitrogen), according to company protocol, using 8 µg of pSF-FLAG-*mamL*-EMCV-FLuc. After 16 hours, cells were placed in full medium for 48 hours before commencing antibiotic selection. To select stable cell lines, cells were grown in the presence of 500 µg/mL Geneticin (G418; Gibco) and 500 ng/mL Puromycin (Gibco).

To create the tdTomato-MamB or the EGFP-MamE cell lines, cells were grown to 60-70% confluency on a 100 mm dish and transfected using Lipofectamine 2000 (Invitrogen), according to company protocol, using 8 µg of ptdTomato-*mamB* or 4 µg of pEGFP-*mamE*, respectively. After 16 hours transfections were stopped, and cells were placed in full medium for 48 hours before commencing antibiotic selection. To select stable cell lines, transfected cells were grown in the presence of 500 µg/mL Geneticin (G418; Gibco).

3.2.3 Protein Sample Preparation

Stably transfected cells were cultured to 70% confluency on a 100 mm dish, then washed twice using 10 mL phosphate buffered saline pH 7.4 (PBS, 137 mM NaCl/2.7 mM KCl/10 mM Na_2HPO_4). Four to five dishes of cells were then collected into a 1 mL lysis solution containing 850 µL of radioimmunoprecipitation assay buffer (RIPA, 10 mM Tris-HCl pH 7.5/140 mM NaCl/1% NP-40/1% sodium deoxycholate/0.1% sodium dodecyl sulfate (SDS)) and 150 µL of Complete Mini protease inhibitor cocktail (Roche Diagnostic Systems, Laval, Canada). Harvested cells were sonicated using three 12-second bursts of a Sonic Dismembrator (model 500, Thermo Fischer Scientific, Ottawa, Canada) at an amplitude of 30%. Total amount of protein was quantified using the BCA assay (12).

3.2.4 Western Blot

Protein samples of MDA-MB-435 cells stably expressing EGFP (40 µg), Tomato (40 µg), EGFP-MamE (40 µg), or Tomato-MamB (40 µg) were reduced with 100 mM dithiothreitol in sample preparation buffer (1 M Tris-HCl pH 6.8/10% SDS/0.1% Bromophenol Blue/43% glycerol) and heated at 85˚C for at least 5 min. Reduced samples

were then subjected to discontinuous SDS polyacrylamide gel electrophoresis (SDS-PAGE) using a 10% running gel. Protein was transferred onto a nitrocellulose blot using the Original iBlot Gel Transfer Device (Life Technologies, Burlington, Canada).

For EGFP detection, nonspecific protein binding was blocked in 5% bovine serum albumin (BSA)/Tris-buffered saline pH 7.4 (TBS) for 3 h at room temperature. Blots were then incubated for 15 h in 1:1000 mouse α-GFP (Invitrogen)/3% BSA/TBS/0.02 % sodium azide (TBSA); then washed using TBS/0.1% Tween 20 (TBST; Sigma-Aldrich, Oakville, Canada) for 30 min with 4 changes of buffer; and incubated for 2 h in 1:20,000 horseradish peroxidase (HRP)-conjugated goat α-mouse IgG (Sigma-Aldrich)/1% BSA/TBS. All incubations were performed at room temperature. Blots were then washed with 0.1% TBST for 30 min with 4 changes of buffer and imaged using the Chemigenius Gel Doc (Syngene). A chemiluminescent signal was detected using SuperSignal West Pico Chemiluminescent Substrate (Thermo Fischer Scientific), according to the manufacturer's instructions.

For Tomato detection, blots were blocked in 3% BSA/TBSA for approximately 18 h at room temperature and then incubated for 18 h in 1:1000 primary goat α-tdTomato (MyBioSource, San Diego, USA)/3% BSA/TBSA at 4°C. After washing in 0.1% TBST as described above, blots were incubated for 1 h in 1:20,000 HRP-conjugated rabbit α-goat IgG (Sigma-Aldrich)/1% BSA/TBS at room temperature.

Glyceraldehyde 3-phosphate dehydrogenase (GAPDH) was used as a loading control. For GAPDH detection, blots were placed in stripping solution (1 M Tris-HCl pH 6.8/10% SDS/0.016% β-mercaptoethanol) and agitated in a 37°C water bath for 30 min

prior to washing in 0.1% TBST and blocking in 5% BSA/TBS. The primary and secondary antibodies were 1:2000 rabbit α-GAPDH (Sigma-Aldrich)/3% BSA/TBSA and 1:20,000 HRP-conjugated goat α-rabbit IgG (Sigma-Aldrich)/1% BSA/TBS, respectively.

3.2.5   Confocal Imaging

Stably transfected cell lines were examined with confocal fluorescence microscopy (using a Nikon A1R confocal microscope) to confirm expression and characterize the intracellular localization of EGFP-MamI, Tomato-MamL, EGFP-MamE (T317A), and Tomato-MamB fusion proteins. In preparation for confocal microscopy, approximately 100 thousand cells were cultured in a 35 mm glass-bottom dish (MatTek Corporation, Cedarlane, Burlington, Canada) for 48 hours. On the day of imaging, the dish was placed in a stage-top incubator to maintain 37°C and 5% CO_2. Images and cines were captured using a Galvano scanner with NIS-Elements AR 5.11.01 (Nikon Instruments Inc.), using a 20X objective with 0.75 numerical aperture. To capture images of cells expressing a single fluorophore, the FITC microscope filter (495 nm excitation/519 nm emission) was used for cells expressing the EGFP fluorophore and the TRITC microscope filter (557 nm excitation/576 nm emission) was used for cells expressing the Tomato fluorophore. To capture images of cells co-expressing both fluorophores (EGFP and Tomato), the FITC and TRITC filters were turned on simultaneously. Captured images of cells in both channels were then merged in Adobe Photoshop CS7.

Time-lapses were acquired with the time lapse function in NIS-Elements AR 5.11.01, recording an image every 1 s for a total of 60 s. Cines were captured in either

channel or both channels simultaneously, as described above. The NIS-Elements software automatically generated a time lapse video in nd2 format with single or merged channels. This video was then edited in Adobe Photoshop CS7 (each frame of the video was cropped and pasted into a single file to create a GIF) and exported as a GIF file.

3.2.6   Particle Trajectory Analysis

3.2.6.1   Particle Tracking

Using a plugin called Mosaic Particle Tracker 2D/3D (version 1.0.1) (13) in the software ImageJ version 1.8.0 (14), the trajectories of particles observed in cells expressing either Tomato-MamL, Tomato-MamL/EGFP-MamI, Tomato-MamL$_{trunc}$, Tomato-MamB, or EGFP-MamE (T317A) were determined from confocal cines, and analyzed.

GIFs of cines were loaded into ImageJ and prepared for analysis by converting them to greyscale, cropping to reduce their size and retaining only the portion of the movie with a single cell, and then optimizing brightness and contrast. This last step does not affect the particle tracking but makes it easier for the user to visualize trajectories. For accurate estimation of diffusion coefficients and velocities, the pixel width (calculated as $d = L/N$, where L is the length of the scale bar in μm added by the image capture software NIS-Elements, and N is the length of the scale bar in pixels) and time interval between two consecutive frames ($\tau = T/(F-1)$, where T is the total duration of the video and F is the total number of frames) were calculated and added to the image properties in ImageJ.

After launching Mosaic Particle Tracker, the parameters used for particle detection were optimized for each cine: values of the radius (size of the tracked particles),

cutoff (threshold intensity value below which detected particles are rejected), and

percentile (range of intensities below the maximum intensity in the image for which

fluorescent spots are considered to be particles) were manually adjusted to allow the

software to detect the most manifest particles in the first image of the movie while not

picking up lower-intensity noise speckle. For particle linking properties, the link range

was set to 3 for all cines. In this way, the software would stop tracking a specific particle

if it was absent for 3 consecutive frames. The displacement (maximum displacement

allowed for a particle between two consecutive frames), which should be set to at least

twice the average displacement of a particle between two frames, was left at the default

setting of 10 pixels. Using these settings for particle trajectory analysis, the software

provided the total number of trajectories detected, a file containing the information

relative to each detected trajectory (i.e., the position of the particle in each frame for

which it was detected) and the possibility of plotting the mean-squared displacement,

$\langle r^2(t) \rangle$, of each detected particle as a log plot.

3.2.6.2   Simple Trajectory Analysis

The mobility of each particle was first assessed by fitting the mean-squared

displacement (MSD) for each trajectory using Mosaic Particle Tracker with a simple

power-law function:

$$\langle r^2(t) \rangle = a \, t^{\alpha}$$

A particle undergoing free Brownian motion should have an MSD close to linear

in time - that is, with an exponent α close to 1. Constrained Brownian motion would

result in $\alpha < 1$. In contrast, a particle undergoing directed motion should be characterized

by α close to 2. If the motion is mixed, with alternate periods of Brownian and directed motion, then one would expect α to be somewhere between 1 and 2. The results of the fit of the MSD was therefore used (along with other information) for differentiation between direct and Brownian motion, as explained below. For the first group of particles, an estimate of the diffusion coefficient was obtained by considering D = a/4 (note that when $\alpha \neq 1$, the diffusion coefficient is estimated from the fitted value of the MSD at t = 1 s, and it is thus more accurate to speak of an apparent diffusion coefficient). Results from simple trajectory analysis are shown in Appendix C.

3.2.6.3   In-depth Trajectory Analysis

Starting from the position and intensity of the tracked particle in each frame returned by Mosaic Particle Tracker, trajectories were further categorized and analyzed using an algorithm written for Mathematica. The main steps of this algorithm are as follows.

Trajectories were first evaluated for inclusion or exclusion based on the following criteria. Rejected trajectories were either too short (less than 8 frames) or had a frame-to-frame displacement that was too large: that is, more than about 1 micron between successive frames or more than about 3 pixels between non successive frames, if the particle was not detected for one frame (these numbers were adjusted for each cell depending on the imaging parameters). Trajectories were also rejected if they had an average intensity that was too low (less than one standard deviation below the mean intensity for all particles) or were detected for less than 70% of the trajectory duration.

For each of the remaining trajectories, the MSD was calculated and fitted (for lag times between 1 and 10 s) using the simple function $\langle r^2(t) \rangle = 4D_a t^{\alpha}$, where D_a is the

particle apparent diffusion coefficient. An estimate of the particle maximum velocity was obtained by identifying the maximum value of the correlation between two successive measurements of the particle apparent velocity:

$$\sqrt{(\vec{v}(t) \cdot \vec{v}(t + \tau))},$$

in which τ is the time interval between consecutive frames

For all trajectories in a given cell, the distribution of single-step displacements (i.e., displacements between two successive frames, corresponding to a time interval $\tau = 1$ s) was generated and fitted with the expression below, which accounts for the existence of two diffusive populations (i.e., the sum of two Rayleigh's distributions):

$$p(r) = \frac{f_1}{s_1{}^2} * r * e^{\frac{-r^2}{2s_1{}^2}} + \frac{f_2}{s_2{}^2} * r * e^{\frac{-r^2}{2s_2{}^2}}$$

Each of these two populations was characterized by an average step size (s_1 and s_2 in order of increasing length), which became the basis for sorting each trajectory into either an immobile, directed, or diffusive trajectory. For immobile trajectories, the total displacement and largest step are both less than $12 \times s_1$. For a directed trajectory, the total displacement is more than $1.5 \times s_2 \times \sqrt{(n)}$, where n is the number of steps in the trajectory, or the trajectory MSD is characterized by an exponent $\alpha > 1.1$, as explained in section 3.2.6.2. The diffusive trajectories are trajectories that are neither immobile nor directed.

3.3 Results

3.3.1 Confocal Images of EGFP-MamE

Figure 3.4 shows the confocal fluorescence image of a cell expressing the EGFP-*mamE* (G49S, T641S) construct. EGFP-MamE shows intracellular fluorescence (Figure 3.3) in a punctate pattern with diffuse fluorescence background. These EGFP-MamE structures are numerous and appear to cluster near the nucleus. Protein expression was confirmed by immunoblot (Figure 3.4; full blot available in Appendix B.4).
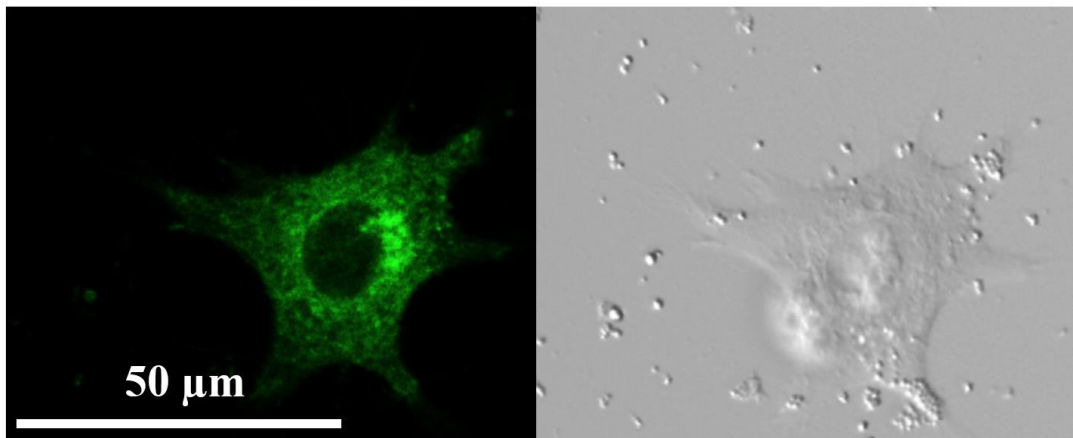
Figure 3.3 Confocal fluorescence microscopy of a mammalian cell stably expressing EGFP-MamE (G49S, T641S).

The EGFP-MamE fusion protein displays a punctate intracellular fluorescence pattern. These structures are more numerous around the nucleus.
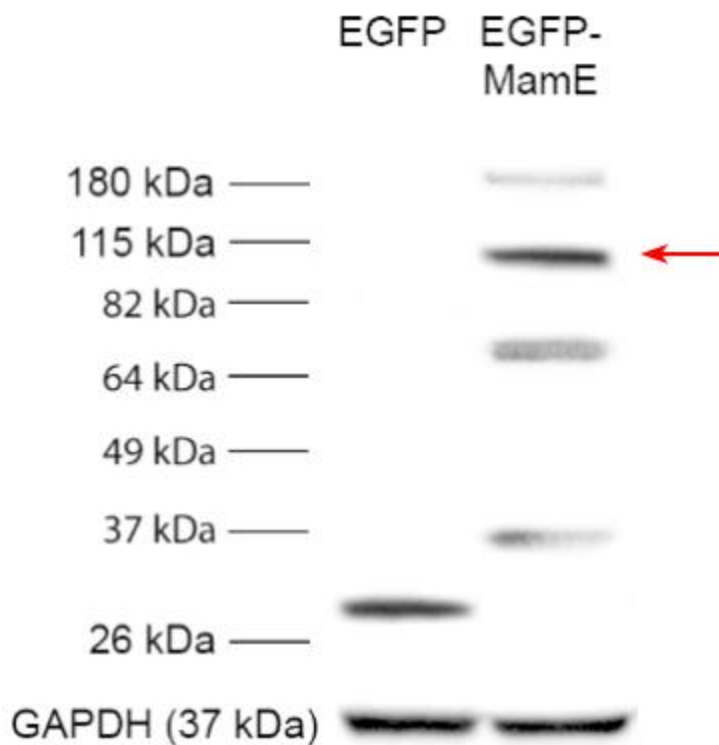
Figure 3.4 Expression of fluorescent EGFP-MamE fusion protein in mammalian cells.

Total cellular protein contents from MDA-MB-435 cells stably expressing EGFP or EGFP-MamE (G49S, T641S) were examined by western blot using mouse α-EGFP as the primary antibody. The approximate size of EGFP-MamE is 110 kDa (red arrow). Bands at lower molecular weights are products of MamE proteolysis (15). Approximate MW is shown in the left margin. The loading control was GAPDH and appears in the bottom panels.

Cells expressing the EGFP-*mamE* (T317A) construct were imaged to confirm whether the two MamE expression systems show similar expression patterns. Figure 3.5 shows the confocal fluorescence image of a cell expressing the EGFP-*mamE* (T317A) construct. Similar to EGFP-MamE (G49S, T641S), EGFP-MamE (T317A) has an

intracellular, punctate expression (Figure 3.5). These punctate structures also cluster near the nucleus and do not appear to be mobile. However, EGFP-MamE (G49S, T641S) appears to express more punctate structures than EGFP-MamE (T317A).
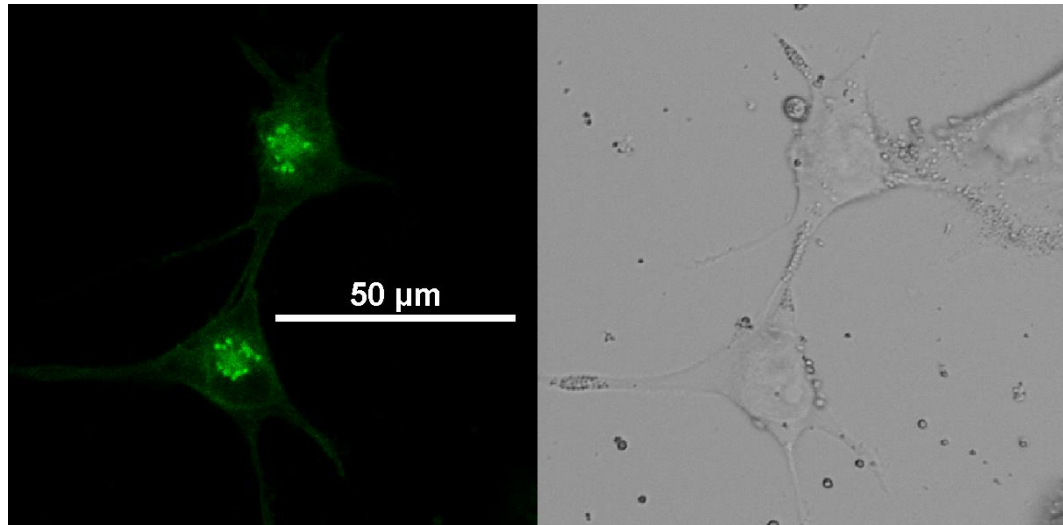
Figure 3.5 Confocal fluorescence microscopy of mammalian cells stably expressing EGFP-MamE (T317A).

Transfected cells were placed under selection to obtain populations expressing EGFP fused to MamE. EGFP-MamE (T317A) fusion protein displays a punctate intracellular fluorescence pattern.

3.3.2   Confocal Images of Tomato-MamB

When Tomato-MamB is stably expressed in MDA-MB-435 cells, the protein is expressed in a punctate pattern similar to Tomato-MamL (Figure 2.9) in the majority of the population (~70%; Figure 3.6A) and in a diffuse pattern in about 30% of the population (Figure 3.6B). The punctate MamB structures are mobile. Protein expression was confirmed by immunoblot (Figure 3.7; full blot available in Appendix B.5).
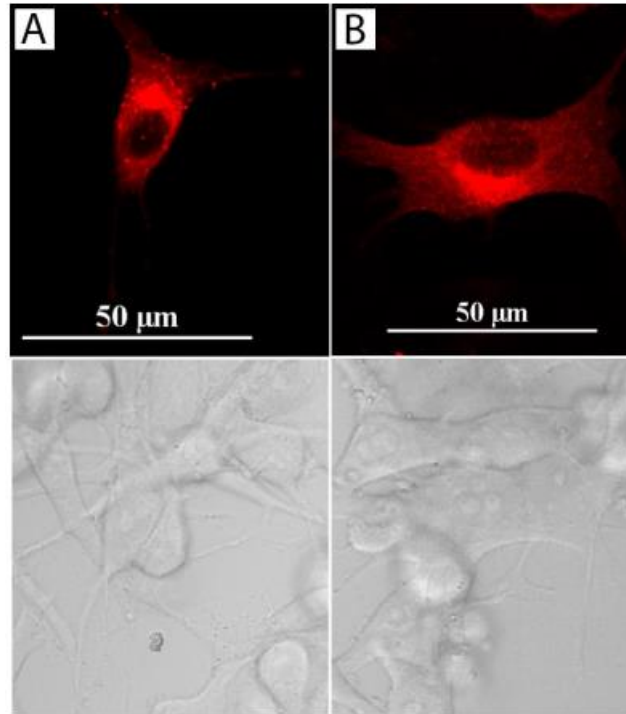
Figure 3.6 Confocal fluorescence microscopy of mammalian cells stably expressing Tomato-MamB fusion protein.

Transfected cells were placed under selection to obtain populations expressing Tomato fused to MamB. Tomato-MamB fusion protein displays either a punctate intracellular fluorescence pattern (A) or a diffuse pattern (B). The punctate structures in (A) are dispersed throughout the cell.
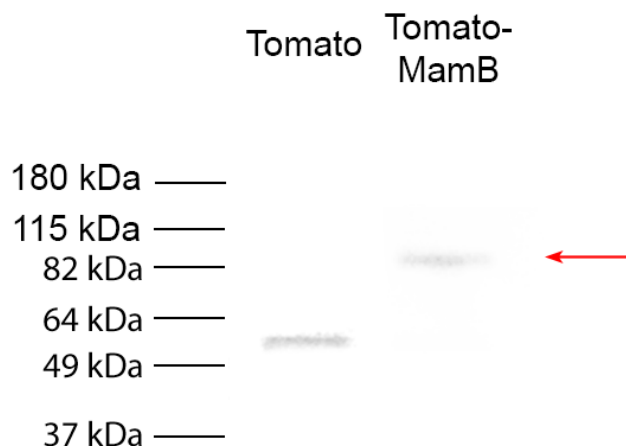
Figure 3.7 Expression of fluorescent Tomato-MamB fusion protein in mammalian cells.

Total cellular protein content from MDA-MB-435 cells stably expressing Tomato or Tomato-MamB were examined by western blot using rabbit α-Tomato as the primary antibody. The approximate size of Tomato-MamB is 91 kDa (red arrow). Approximate MW is shown in the left margin.

3.3.3   Analysis of EGFP-MamE trajectories

Although no evident motion of the puncta formed by MamE was observed in confocal movies, EGFP-MamE (T317A) cells were analyzed for Brownian motion and any directed motion in order to act as an immobile control for other expression systems. A visual representation of the detected MamE trajectories is shown in Figure 3.8, and their displacement distribution is shown in Figure 3.9. It is apparent from these distributions of displacements that the motion of the MamE particles is very highly constrained, since almost no single displacement after t = 1s is larger than 0.2 µm, and since the displacements after 20 s are almost exactly the same as after 1 s. The in-depth trajectory analysis of MamE fluorescent structures showed that 26% of MamE particles

were immobile while 62% were undergoing Brownian motion and only 13% underwent

directed motion at some point in their trajectories (Table 3.2). According to this analysis,

the average apparent diffusion coefficient of MamE particles undergoing Brownian

motion is 1.9 ± 0.4 x 10^{-3} $\mu m^2/s$. The average velocity of the very few MamE particles

undergoing directed motion is 0.17 ± 0.03 $\mu m/s$.

Figure 3.8 Representative cell expressing MamE particle trajectories.

A confocal image of the analyzed cell is shown on the left. Analyzed trajectories are

shown on the right, with stationary particles shown in dark blue, and Brownian motion

and directed motion trajectories represented in green and orange, respectively.

Figure 3.9 Representative distributions of displacements obtained for MamE trajectories of a single cell.

In the main panel the probability density of displacements after t = 1s is shown (black symbols) and fitted assuming two diffusive populations and one directed population (the blue and green shaded peaks represent the contributions of the slow and fast diffusing populations, the orange shaded peak - barely visible in this case - that of the directed population and the black curve shows the sum of these three contributions). The inset shows a comparison between the distribution of displacements after t = 1s (black symbols) and after t = 20 s (grey symbols).

Table 3.2 Summary of MamE trajectory analysis.

	Number of cells	Number of analyzed trajectories	Percent immobile	Percent Brownian	Percent directed	*Apparent diffusion coefficient (10^{-3} µm²/s)	*Velocity (µm/s)
EGFP-MamE	4	47	26	62	13	1.9 ± 0.4	0.17 ± 0.03

*The apparent diffusion coefficient is measured from particles undergoing Brownian motion. The velocity is measured from particles undergoing directed motion.

3.3.4   Mobility of Tomato-MamB

Analyses of Tomato-MamB particle trajectories also reveal both directed and Brownian motion in each cell, with the occurrence of directed trajectories markedly larger than MamE. A visual representation of the detected MamB particles is shown in Figure 3.10, and their displacement distribution is shown in Figure 3.11 - the difference with MamE is clearly visible here, with a significant number of displacements after $t = 1$ s in the 0.2 to 0.4 µm range, and with the distribution of displacements after 20s significantly broader than after 1s, as expected for mobile particles. In-depth analysis of MamB trajectories showed that only 15% of MamB particles were immobile, while 57% were undergoing Brownian motion, and 28% underwent directed motion at some point in their trajectories (Table 3.3). The average apparent diffusion coefficient of MamB

particles undergoing Brownian motion is $4.0 \pm 1.0 \times 10^{-3}\,\mu m^2/s$. The average velocity of MamB particles undergoing directed motion is $0.24 \pm 0.01\,\mu m/s$.

Figure 3.10 Representative cell expressing MamB particle trajectories.

A confocal image of the analyzed cell is shown on the left. Analyzed trajectories are shown on the right, with stationary particles shown in black, and Brownian motion and directed motion trajectories represented in green and orange, respectively.

Figure 3.11 Representative distributions of displacements obtained for MamB trajectories of a single cell.

In the main panel the probability density of displacements after t = 1s is shown (black symbols) and fitted assuming two diffusive populations and one directed population (the blue and green shaded peaks represent the contributions of the slow and fast diffusing populations, the orange shaded peak that of the directed population and the black curve shows the sum of these three contributions). The inset shows a comparison between the distribution of displacements after t = 1s (black symbols) and after t = 20 s (grey symbols).

Table 3.3 Summary table of MamB trajectory analysis.

	Number of cells	Number of analyzed trajectories	Percent immobile	Percent Brownian	Percent directed	*Apparent diffusion coefficient (10^{-3} μm^2/s)	*Velocity (μm/s)
Tomato-MamB	5	571	15	57	28	4.0 ± 1.0	0.24 ± 0.01

*The apparent diffusion coefficient is measured from particles undergoing Brownian motion. The velocity is measured from particles undergoing directed motion.

3.3.5   Mobility of Tomato-MamL

As for Tomato-MamB, analyses of Tomato-MamL particle trajectories reveal a significant number of directed motion, in addition to Brownian motion in each cell. A visual representation of the detected MamL particles is shown in Figure 3.12, and their displacement distribution is shown in Figure 3.13, where a broad distribution after 20 s is apparent. An in-depth analysis of these results showed that 18% of MamL particles were immobile, 56% were undergoing Brownian motion, and 25% underwent directed motion at some point in their trajectories (Table 3.4). The average apparent diffusion coefficient of MamL particles undergoing Brownian motion is 5.1 ± 1.7 x 10^{-3} μm^2/s. The average velocity of MamL particles undergoing directed motion is 0.19 ± 0.05 μm/s.
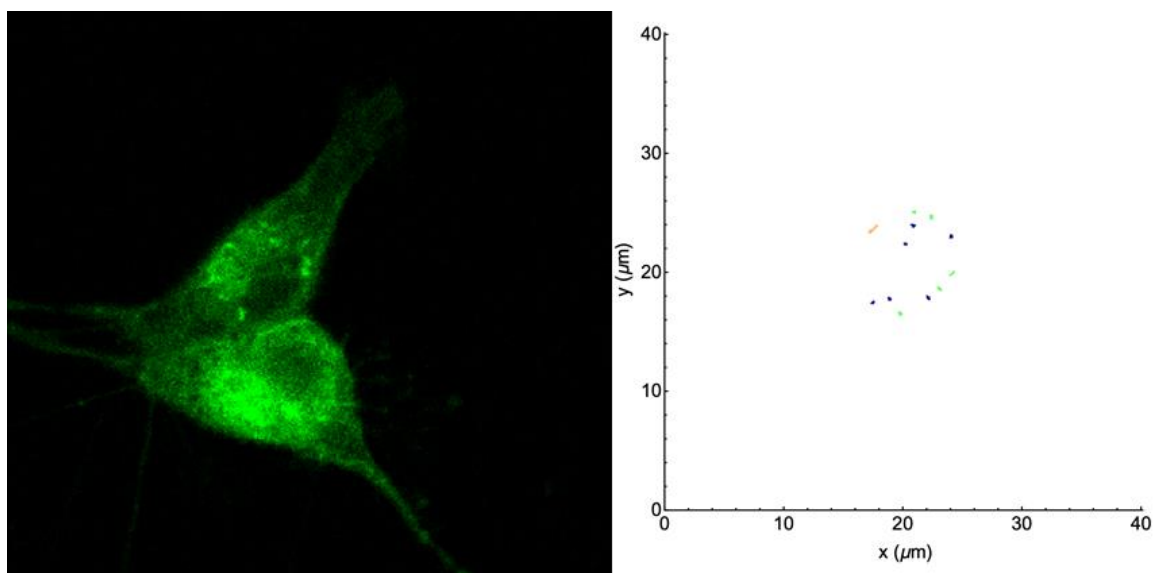
Figure 3.12 Representative cell expressing MamL particle trajectories.

A confocal image of the analyzed cell is shown on the left. Analyzed trajectories are

shown on the right, with stationary particles shown in dark blue, and Brownian motion

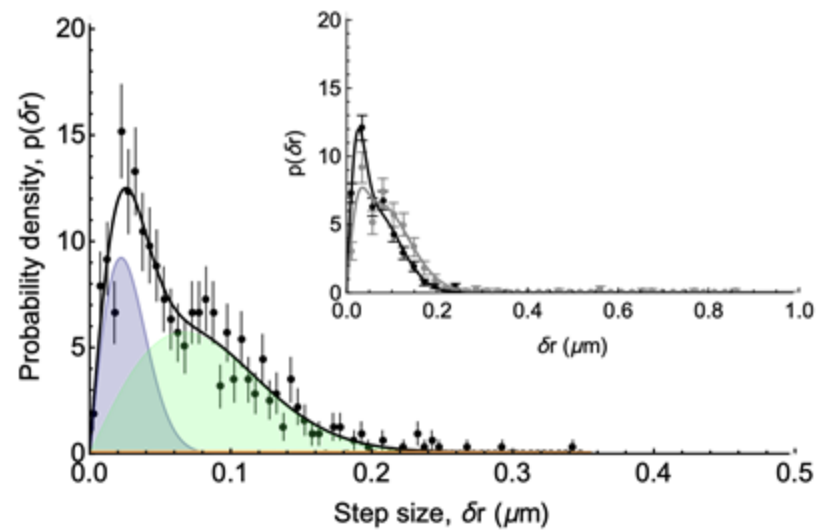and directed motion trajectories represented in green and orange, respectively.

Figure 3.13 Representative distributions of displacements obtained for MamL

trajectories of a single cell.

In the main panel the probability density of displacements after t = 1s is shown (black

symbols) and fitted assuming two diffusive populations and one directed population (the

blue and green shaded peaks represent the contributions of the slow and fast diffusing

populations, the orange shaded peak that of the directed population and the black curve

shows the sum of these three contributions). The inset shows a comparison between the

distribution of displacements after t = 1s (black symbols) and after t = 20 s (grey

symbols).

Table 3.4 Summary of MamL trajectory analysis.

	Number of cells	Number of analyzed trajectories	Percent immobile	Percent Brownian	Percent directed	*Apparent diffusion coefficient (10^{-3} μm^2/s)	*Velocity (μm/s)
Tomato-MamL	7	461	18	56	25	5.1 ± 1.7	0.19 ± 0.05

*The apparent diffusion coefficient is measured from particles undergoing Brownian
motion. The velocity is measured from particles undergoing directed motion.

3.3.6   Mobility of Tomato-MamL$_{trunc}$

To better understand the mobility of MamL, we introduced an early stop codon to

remove 15 amino acids from the C terminus of the MamL protein and examined this

truncated form of MamL. These 15 amino acids are thought to interact with mobile

cytoskeletal elements due to their similarity to cell-penetrating peptides (2), as described

more thoroughly in chapter 1.1.2.2. A visual representation of the detected MamL$_{trunc}$

particles is shown in Figure 3.14, and their displacement distribution is shown in Figure

3.15. Further in-depth analysis of the MamL$_{trunc}$ trajectories showed that 14% of

MamL$_{trunc}$ particles were immobile, 60% were undergoing Brownian motion, and 26%

underwent directed motion at some point in their trajectories (Table 3.5). The average

apparent diffusion coefficient of MamL$_{trunc}$ particles undergoing Brownian motion is 1.9

$\pm$ 1.1 x 10^{-3} µm^2/s. The average velocity of MamL$_{trunc}$ particles undergoing directed

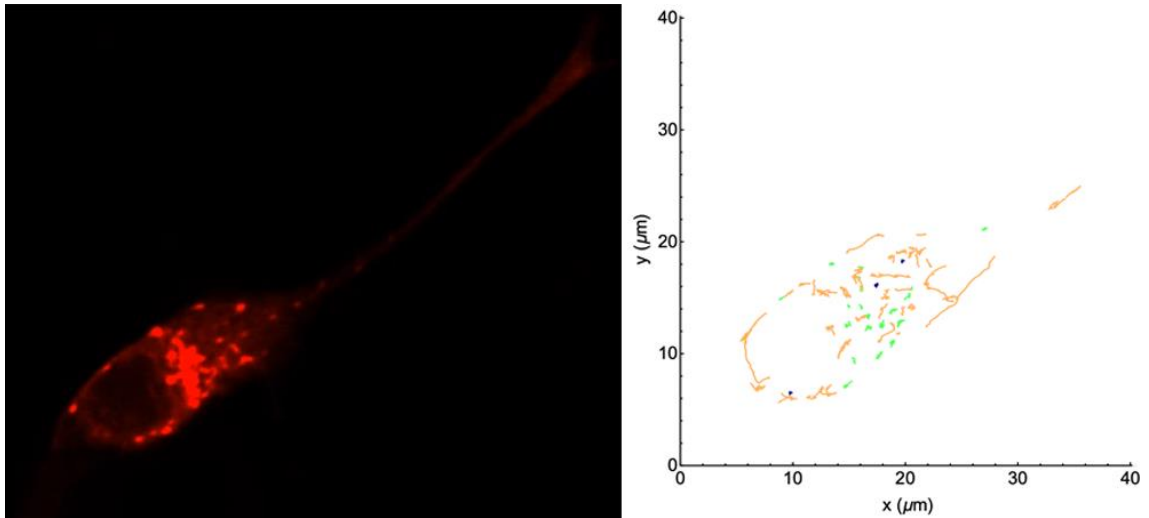motion is 0.14 $\pm$ 0.06 µm/s.
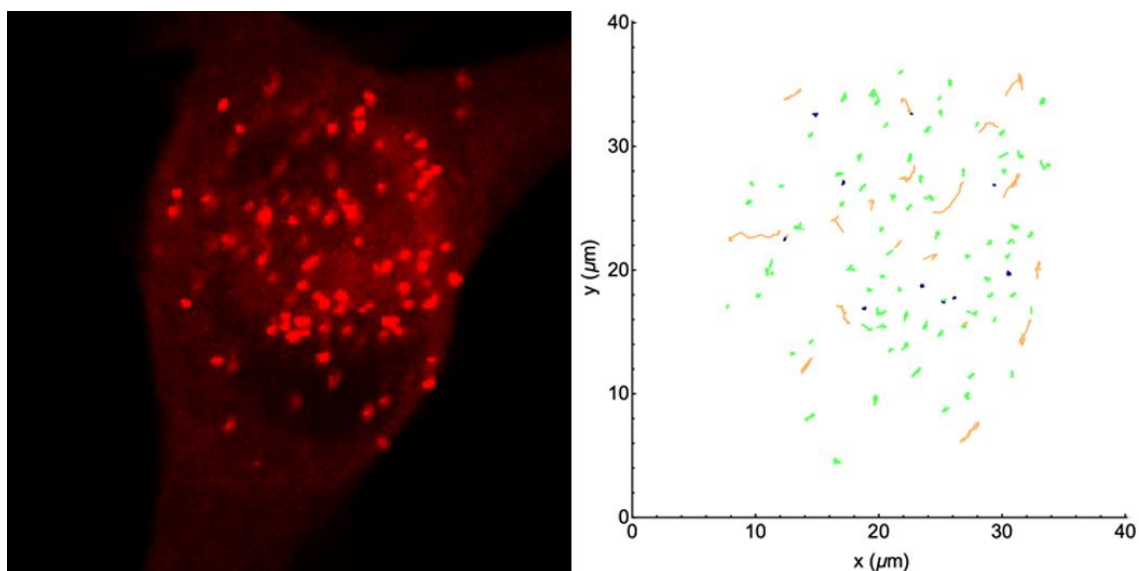
Figure 3.14 Representative cell expressing MamL$_{trunc}$ particle trajectories.

A confocal image of the analyzed cell is shown on the left. Analyzed trajectories are

shown on the right, with stationary particles shown in dark blue, and Brownian motion

and directed motion trajectories represented in green and orange, respectively.
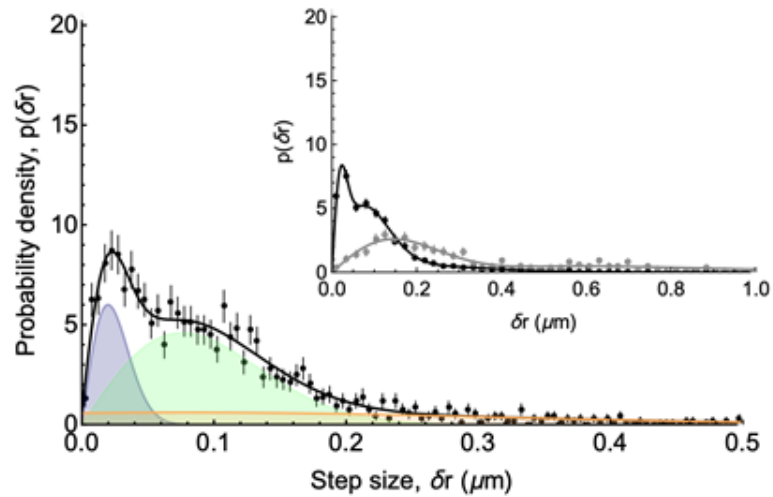
Figure 3.15 Representative distributions of displacements obtained for MamL$_{trunc}$ trajectories of a single cell.

In the main panel the probability density of displacements after t = 1s is shown (black symbols) and fitted assuming two diffusive populations and one directed population (the blue and green shaded peaks represent the contributions of the slow and fast diffusing populations, the orange shaded peak that of the directed population and the black curve shows the sum of these three contributions). The inset shows a comparison between the distribution of displacements after t = 1s (black symbols) and after t = 20 s (grey symbols).

Table 3.5 Summary table of MamL$_{trunc}$ trajectory analysis.

	Number of cells	Number of analyzed trajectories	Percent immobile	Percent Brownian	Percent directed	*Apparent diffusion coefficient (10^{-3} μm^2/s)	*Velocity (μm/s)
Tomato-MamL$_{trunc}$	7	516	14	60	26	1.9 ± 1.1	0.14 ± 0.06

*The apparent diffusion coefficient is measured from particles undergoing Brownian motion. The velocity is measured from particles undergoing directed motion.

3.3.7   Mobility of Tomato-MamL/EGFP-MamI

Tomato-MamL particles not only retain their mobility when co-expressed with EGFP-MamI, the latter appear to be recruited to the same mobile complex. These mobile particles, consisting of co-localized protein, also display both directed and Brownian motion. A visual representation of the detected MamL+MamI particles is shown in Figure 3.16, and their displacement distribution is shown in Figure 3.17. In-depth analysis of the MamL+MamI trajectories revealed that 21% of MamL+MamI particles were immobile, 45% were undergoing Brownian motion, and 32% underwent directed motion at some point in their trajectories (Table 3.6). The average apparent diffusion coefficient of MamL+MamI particles undergoing Brownian motion is 3.2 ± 2.5 x 10^{-3} μm^2/s. The average velocity of MamL+MamI particles undergoing directed motion is 0.23 ± 0.09 μm/s.
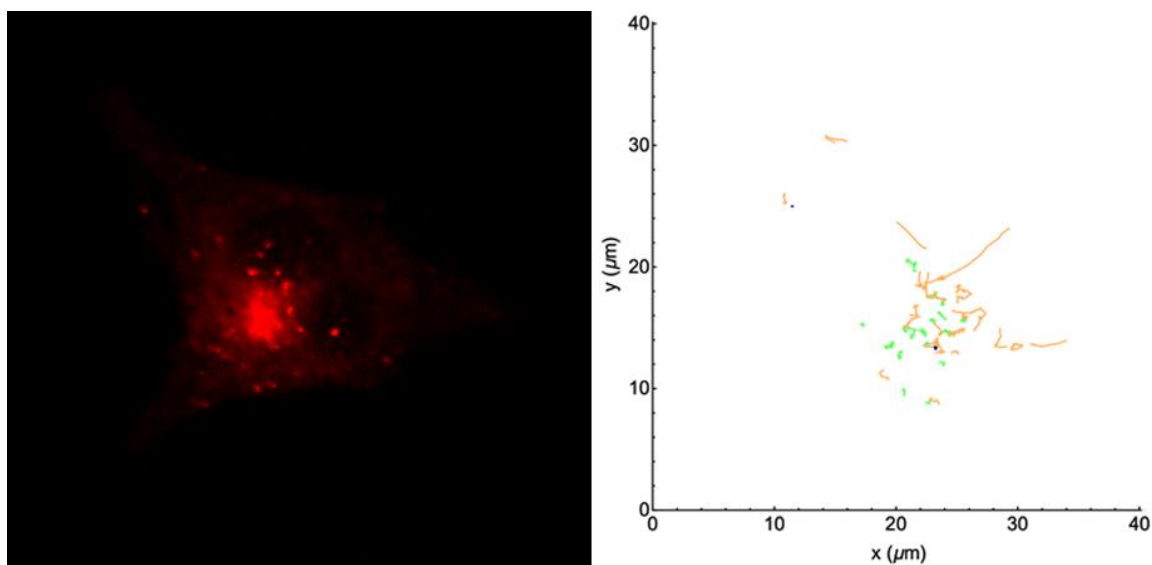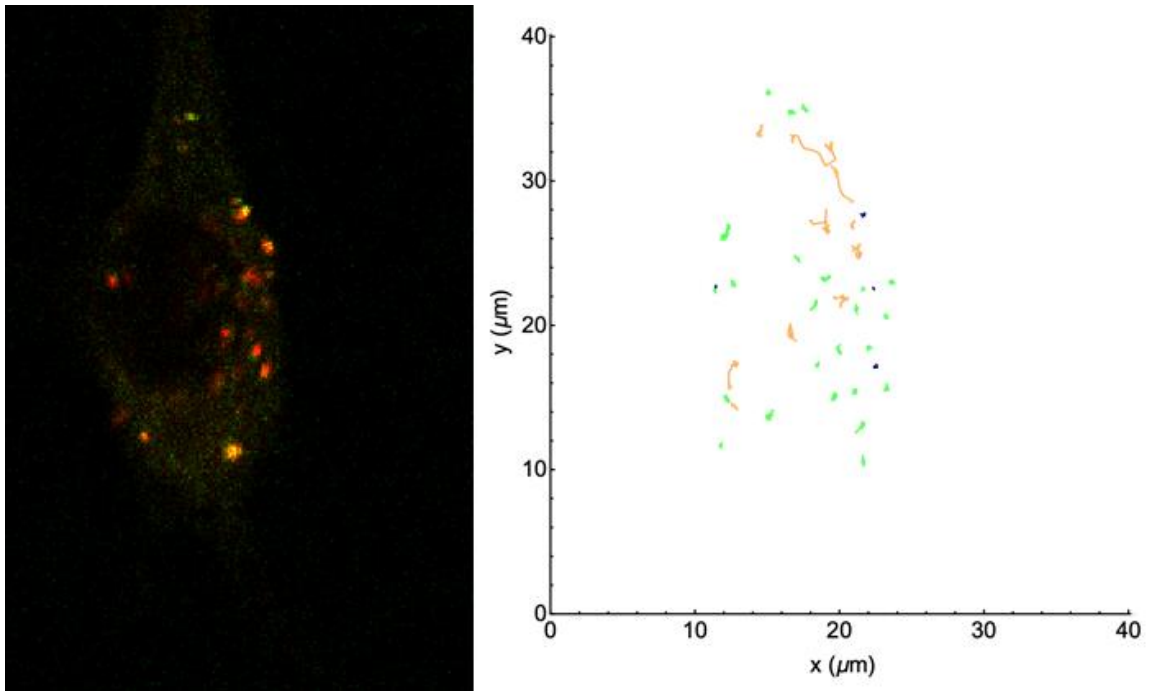
Figure 3.16 Representative cell expressing MamL+MamI particle trajectories.

A confocal image of the analyzed cell is shown on the left. Analyzed trajectories are

shown on the right, with stationary particles shown in dark blue, and Brownian motion

and directed motion trajectories represented in green and orange, respectively.
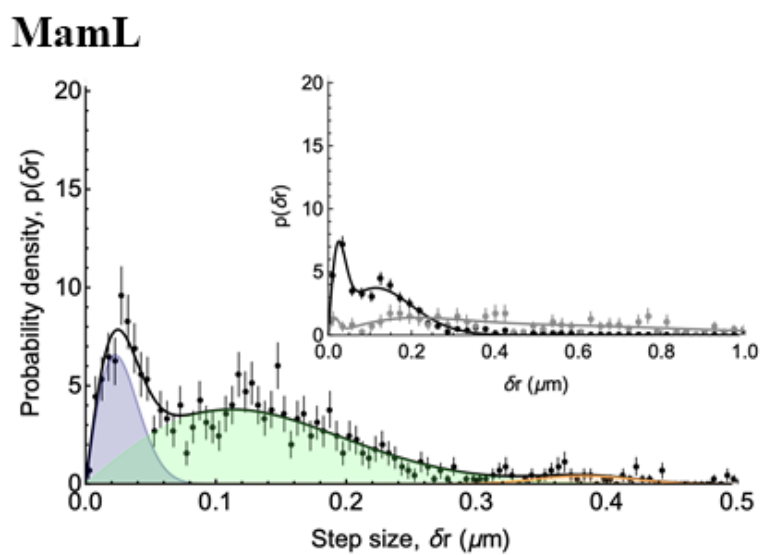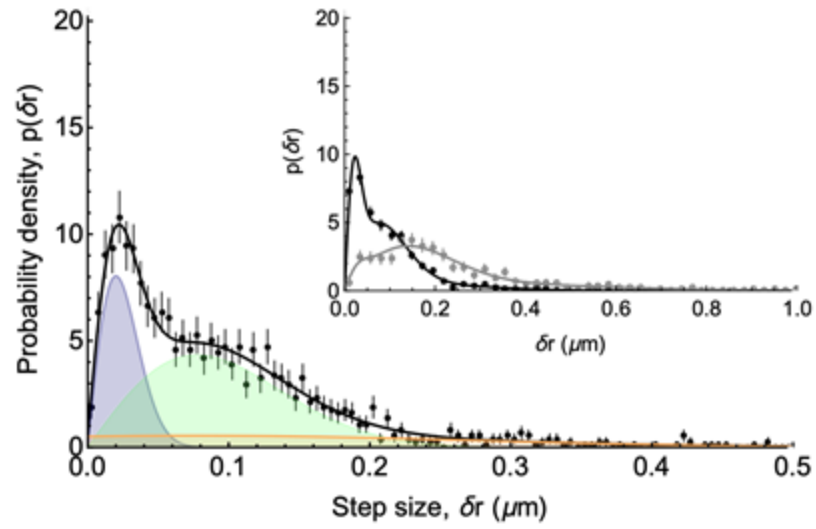
Figure 3.17 Representative distributions of displacements obtained for MamL+MamI trajectories of a single cell.

In the main panel the probability density of displacements after t = 1s is shown (black symbols) and fitted assuming two diffusive populations and one directed population (the blue and green shaded peaks represent the contributions of the slow and fast diffusing populations, the orange shaded peak that of the directed population and the black curve shows the sum of these three contributions). The inset shows a comparison between the distribution of displacements after t = 1s (black symbols) and after t = 20 s (grey symbols).

Table 3.6 Summary table of MamL+MamI trajectory analysis.

	Number of cells	Number of analyzed trajectories	Percent immobile	Percent Brownian	Percent directed	*Apparent diffusion coefficient $(10^{-3}\,\mu m^2/s)$	*Velocity $(\mu m/s)$
Tomato-MamL + EGFP-MamI	4	225	21	45	32	3.2 ± 2.5	0.23 ± 0.09

*The apparent diffusion coefficient is measured from particles undergoing Brownian motion. The velocity is measured from particles undergoing directed motion.

3.3.8   Mobility of FLAG-MamL/EGFP-MamI

The FLAG-MamL/EGFP-MamI co-expression system was created as both an improvement to the Tomato-MamL/EGFP-MamI system and to enable downstream applications (as explained in chapter 2.2.10). To compare the movement of Tomato-MamL/EGFP-MamI particles with FLAG-MamL/EGFP-MamI, the latter particles were analyzed for their trajectories. A visual representation of the detected FLAG-MamL+MamI particles is shown in Figure 3.18, and their displacement distribution is shown in Figure 3.19. In-depth analysis of the FLAG-MamL+MamI trajectories revealed that 21% of FLAG-MamL+MamI particles were immobile, 45% were undergoing

Brownian motion, and 32% underwent directed motion at some point in their trajectories (Table 3.7). The average apparent diffusion coefficient of FLAG-MamL+MamI particles undergoing Brownian motion is $5.0 \pm 0.9 \times 10^{-3}\,\mu m^2/s$. The average velocity of FLAG-MamL+MamI particles undergoing directed motion is $0.23 \pm 0.09\,\mu m/s$.
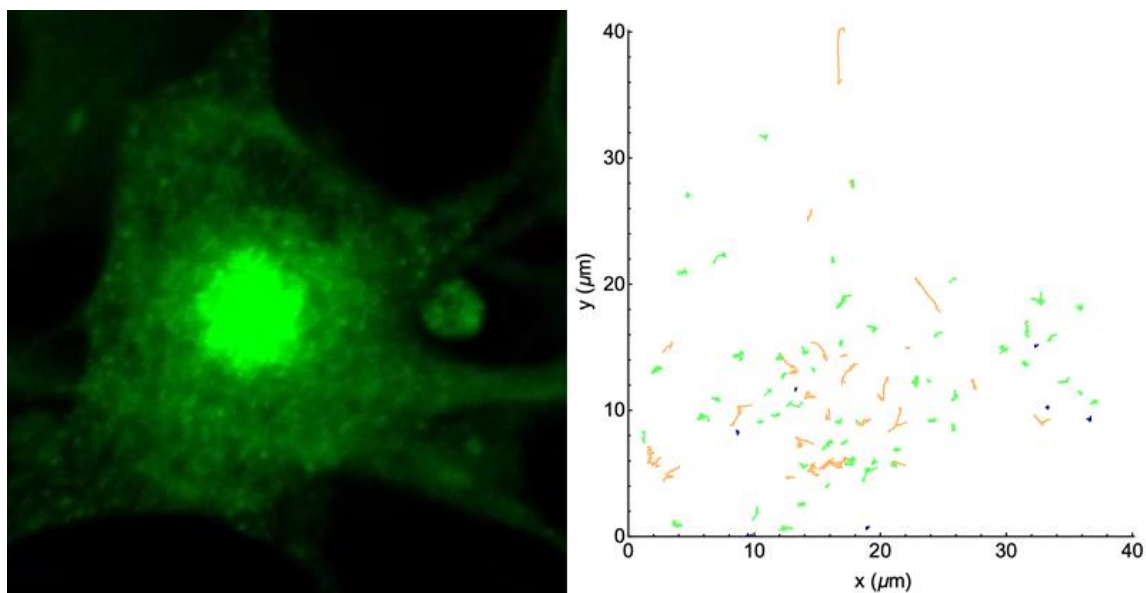
Figure 3.18 Representative cell expressing FLAG-MamL+MamI particle trajectories.

A confocal image of the analyzed cell is shown on the left. Analyzed trajectories are shown on the right, with stationary particles shown in dark blue, and Brownian motion and directed motion trajectories represented in green and orange, respectively.
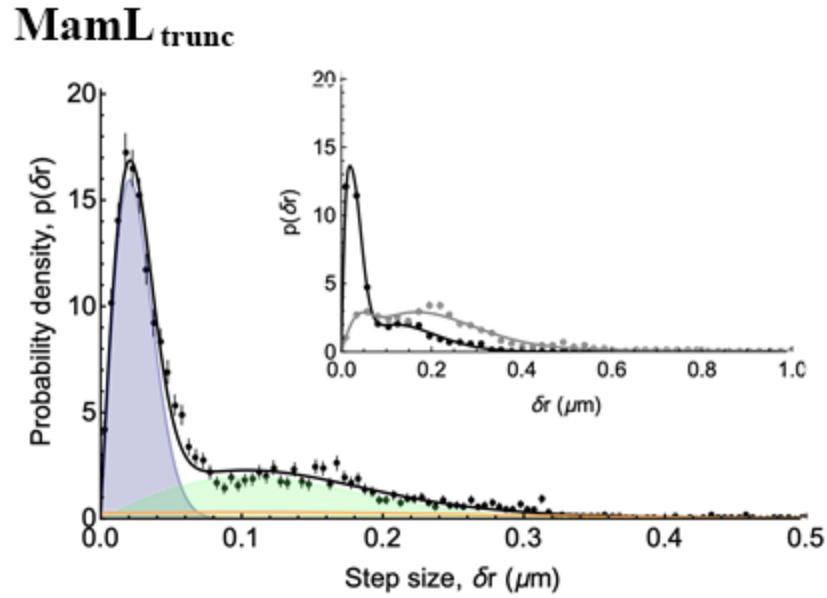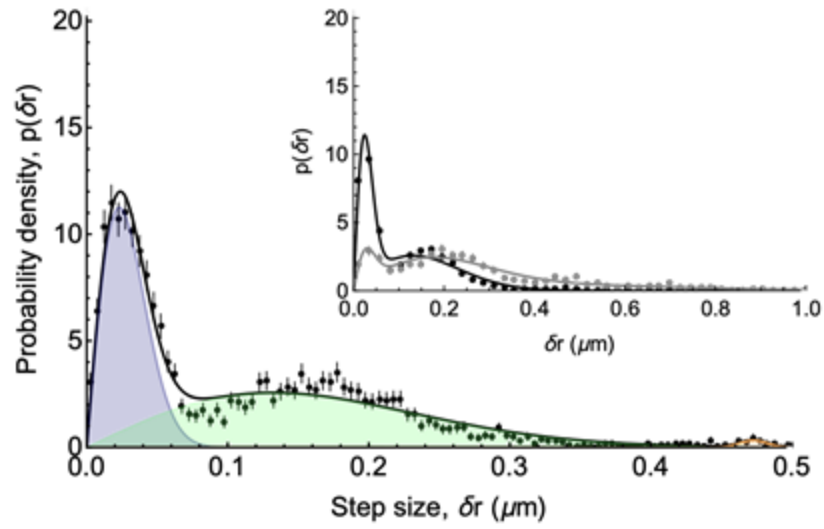
Figure 3.19 Representative distributions of displacements obtained for FLAG-MamL+MamI trajectories of a single cell.

In the main panel the probability density of displacements after t = 1s is shown (black symbols) and fitted assuming two diffusive populations and one directed population (the blue and green shaded peaks represent the contributions of the slow and fast diffusing populations, the orange shaded peak that of the directed population and the black curve shows the sum of these three contributions). The inset shows a comparison between the distribution of displacements after t = 1s (black symbols) and after t = 20 s (grey symbols).

Table 3.7 Summary table of different parameters obtained from FLAG-MamL+MamI trajectory analysis.

	Number of cells	Number of analyzed trajectories	Percent immobile	Percent Brownian	Percent directed	*Apparent diffusion coefficient ($10^{-3}\,\mu m^2/s$)	*Velocity ($\mu m/s$)
FLAG-MamL + EGFP-MamI	5	520	8	60	22	5.0 ± 0.9	0.14 ± 0.05

*The apparent diffusion coefficient is measured from particles undergoing Brownian motion. The velocity is measured from particles undergoing directed motion.

3.4 Discussion

This chapter reports the first instance of the individual expression of magnetosome proteins MamE and MamB in mammalian cells. Cells expressing MamE or MamB appeared healthy and displayed stellate morphology. Both proteins displayed intracellular, punctate fluorescence patterns, much similar to the expression pattern of MamL (chapter 2.3.1), although MamE and MamB expression patterns were not as distinct or uniform as MamL. EGFP-MamE-expressing cells often displayed diffuse green fluorescence throughout the cell and had punctate MamE structures near the nucleus. MamB-expressing cells also displayed diffuse fluorescence, with 30% of the cells displaying no punctate fluorescence.

The focus of this chapter was to analyze the intracellular mobility of the puncta formed by magnetosome proteins. For all magnetosome proteins analyzed (MamL, MamL$_{trunc}$, MamB, and MamE), three types of particle movement were observed for the puncta: confined trajectories, Brownian trajectories, and trajectories with stretches of directed motion.

Trajectories undergoing Brownian motion have apparent diffusion coefficients between 2 and 5 x 10^{-3} μm^2/s (Table 3.8). This diffusion coefficient is very slow compared to that of a soluble protein in the cytoplasm of mammalian cells, which is on the order of 10 μm^2/s (16). Since magnetosome proteins MamI, MamL, MamE, and MamB are all membrane-associated proteins, the diffusion coefficients measured in this chapter confirms that these proteins are not soluble in the cytoplasm, but instead are part of a rather large, membranous structure. Since this structure cannot be resolved (since they appear punctate in confocal microscope images), it must be smaller than the resolution of the microscope (ie. ~100 nm in radius or less). Likely possibilities are that they either localize to the membrane of already existing lipid vesicles (17), or promote the formation of new lipid vesicles on which they then localize. The confined trajectories may then correspond to particles localized in immobilized vesicles.

Particles that undergo active directed motion have a maximum velocity from 0.1 to 0.3 μm/s (Table 3.9). These particles usually also undergo stretches of Brownian motion or immobility. These particles may be localized in vesicles that are attached to molecular motors and/or the magnetosome proteins themselves are interacting with these molecular motors, and these molecular motors transiently walk along protein filaments.

3.4.1 Brownian motion of magnetosome proteins particles

Table 3.8 Summary of apparent diffusion coefficient and anomalous exponent values for magnetosome proteins particles undergoing Brownian motion.

Magnetosome protein	% Particles undergoing Brownian motion	*Apparent diffusion coefficient (10^{-3} μm^2/s)	α value
EGFP-MamE	62	0.8 ± 0.1 [†, §]	0.15 ± 0.04
Tomato-MamB	57	4.0 ± 1.0 [§]	0.54 ± 0.08
Tomato-MamL	56	5.1 ± 1.7 [†, ‡]	0.43 ± 0.17
Tomato-MamL$_{trunc}$	60	1.9 ± 1.1 [‡]	0.52 ± 0.11
Tomato-MamL + EGFP-MamI	45	3.2 ± 2.5	0.42 ± 0.11
FLAG-MamL + EGFP-MamI	60	5.0 ± 0.9	0.41 ± 0.11

* Data are the mean ±standard deviation   [†, ‡] $p < 0.001$ [§] $p < 0.05$

MamE particles are mostly immobile (26%) or undergoing some form of Brownian motion (62%), however several clues point towards a very restricted type of Brownian motion. First, Brownian MamE particles have an apparent diffusion coefficient of $1.9 \pm 0.4 \times 10^{-3}$ $\mu m^2/s$, which is significantly lower compared to the diffusion of MamL and MamB particles (Table 3.14). This shows that MamE is localized in different structures than MamL and MamB, with more restricted mobility. Additionally, Brownian MamE particles have trajectories characterized by an extremely low anomalous exponent of 0.15 ± 0.04, which is the lowest α value out of all expression systems. An α value below 1 points to constrained or restricted diffusion (i.e. diffusion in the presence of obstacles), and a value below 0.5 further points towards caged diffusion (18, 19). Taken together, the low diffusion coefficient of MamE particles, extremely low value of the anomalous exponent α, and the high occurrence of stationary MamE particles suggest that this protein is the most constrained out of the proteins studied.

In contrast to MamE, Brownian MamL and MamB particle have a noticeably larger diffusion coefficient (on the order of $4-5 \times 10^{-3}$ $\mu m^2/s$), and a larger anomalous exponent α (on the order of 0.4 to 0.5). These values are consistent with the proteins localizing on particles (e.g. lipid vesicles) 10s to 100s of nm in size and undergoing restricted diffusion (17). MamL$_{trunc}$ particles, which diffuse at $1.9 \pm 1.1 \times 10^{-3}$ $\mu m^2/s$, diffuse significantly slower than MamL particles. Perhaps the removal of the MamL C-terminal tail causes the protein to localize in different (more confined) structures than full-length MamL. It is also possible that the MamL C-terminal confers some mobility to the structures to which the protein is localized, for example by binding molecular motors that would be able to get past some obstacles.

When MamL is co-expressed with MamI, Tomato-MamL/EGFP-MamI particles do not have significantly different diffusion coefficient than MamL alone particles (3.2 ± 2.5 vs. 5.1 ± 1.7 x 10^{-3} µm^2/s). This confirms that MamL and MamI are localized within the same structures/particles, and more specifically that MamI is recruited to the same structure as MamL when they interact. This is further supported by the FLAG-MamL/EGFP-MamI expression system. FLAG-MamL/EGFP-MamI particles diffuse at 5.0 ± 0.9 x 10^{-3} µm^2/s, which is neither significantly different from the diffusion coefficient of Tomato-MamL/EGFP-MamI particles nor of Tomato-MamL alone particles. Furthermore, the α value of Tomato-MamL alone, Tomato-MamL/EGFP-MamI, and FLAG-MamL/EGFP-MamI particles are all comparable (Table 3.14).

3.4.2 Directed motion of magnetosome proteins

Although the magnetosome proteins studied undergo directed motion to a different extent (ie. variability in the percentage of detected particles that display directed motion and in the average value of the α exponent for these directed trajectories), similar velocities (around 0.2 µm/s) were measured for all particles (Table 3.15), and except for MamE particles, the aspect of these directed trajectories (which very often are accompanied by period of intermittent Brownian motion) is similar for all studied proteins (Fig. 3.20).

Table 3.9 Summary of velocity of magnetosome proteins undergoing directed motion.

Magnetosome protein	% Particles undergoing directed motion	* Velocity (µm/s)	α value
EGFP-MamE	13	0.17 ± 0.03	0.26 ± 0.32
Tomato-MamB	28	0.24 ± 0.01	1.24 ± 0.04
Tomato-MamL	25	0.19 ± 0.05	1.01 ± 0.18
Tomato-MamL$_{trunc}$	26	0.14 ± 0.06	0.88 ± 0.31
Tomato-MamL + EGFP-MamI	32	0.23 ± 0.09	0.66 ± 0.10
FLAG-MamL + EGFP-MamI	22	0.14 ± 0.05	0.95 ± 0.33

* Data are the mean ± standard deviation.
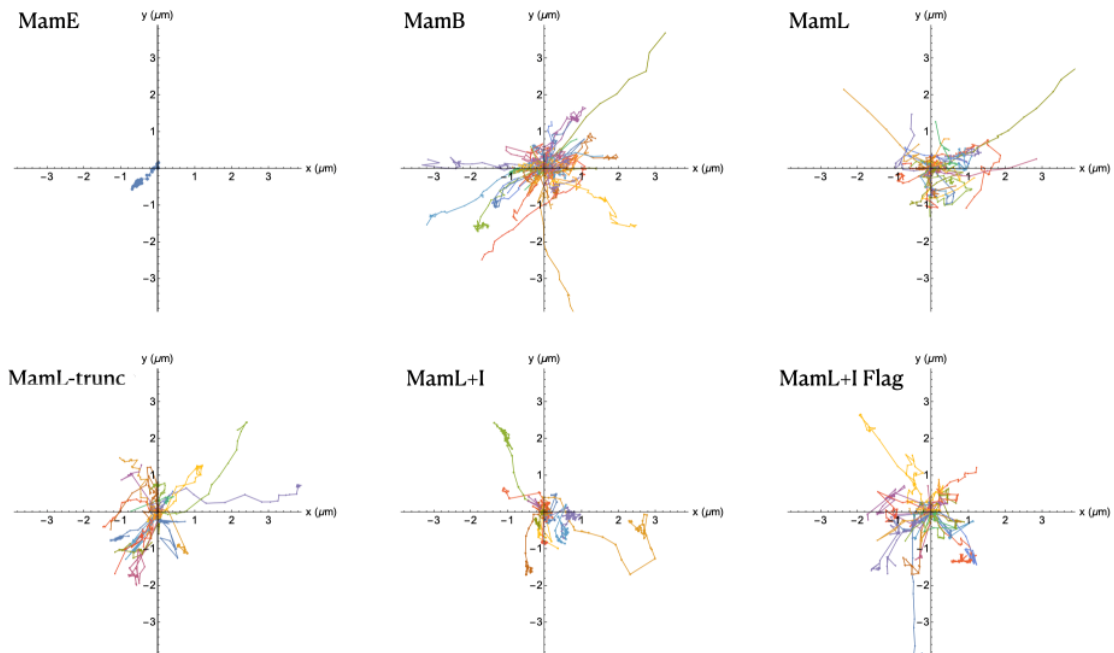
Figure 3.20 Representative directed trajectories of magnetosome proteins.

Each panel shows all the directed trajectories detected in a single representative cell, for each of the different expression systems under study. All trajectories have been plotted by placing the first point of the trajectory at the point with coordinates x = y = 0.

The directed motion observed suggest that the detected particles interact with some kind of linear molecular motor present in the cell, for example a type of myosin motor. In mammalian cells, myosin motors are a group of molecular motor proteins responsible for directed movement of intracellular cargo. These structures, specifically myosin IB, myosin II, and myosin V, all move at a velocity of 0.2 µm/s (20). The speeds observed for the detected particles are therefore consistent with interactions with myosin. Molecular motors with a negative charge, or that associate with cargo adaptor proteins that are negatively charged, can interact with positively-charged proteins in the cell (10).

MamE stands out from other magnetosome proteins studied here in that much fewer MamE particles are undergoing directed motion and/or they spend less time undergoing active directed motion (Fig. 3.20). This is further indicated by the low α exponent of 0.26 ± 0.32. As mentioned in section 3.2.6.3, particles undergoing directed motion should have α exponents close to 2; however, a lower exponent can also indicate that the directed motion alternates with either Brownian motion or immobilized motion, as is the case in fact with all the particles detected here, but especially with MamE particles. When undergoing directed motion, MamE particles move at a velocity of 0.17 μm/s. From protein structure analysis in results section 1.1.2.4, the cytoplasmic tail of MamE is short and has only 2 positively-charged amino acids (Fig. 1.10); therefore, MamE most likely does not bind to molecular motors strongly or frequently due to its negligible positive charge. Alternatively, MamE may be located in a vesicle that does not interact often with molecular motors. This may explain why MamE is not undergoing directed motion as often and why the protein seems mostly immobile while observed under a confocal fluorescence microscope.

MamB particles undergoing active directed motion travel at 0.24 μm/s. From protein structure analysis in results section 1.1.2.3, the cytoplasmic domain of MamB is quite large and almost 20% of its amino acids have positive charges (Fig. 1.7). These positive charges, therefore, have opportunities to interact with negatively-charged molecular motors in the mammalian cytoplasm. We can thus infer that MamB either interacts directly with molecular motors or is located in a vesicle that interacts with molecular motors.

MamL particles undergoing active directed motion move at approximately 0.2 µm/s, and thus is expected to also be interacting with molecular motors (ie. myosin). Although the cationic amino acid residues of the MamB and MamL cytoplasmic domains are not arranged in a similar pattern, we can speculate that these two proteins may be interacting with similar molecular motors since they move at similar velocities. MamL$_{trunc}$ particles that are undergoing active directed motion travel at 0.15 µm/s, which is not significantly different from the velocity of full-length MamL particles. It is notable to point out that the α exponent of MamL$_{trunc}$ particles is smaller than that of MamL particles (0.88 ± 0.31 vs. 1.01 ± 0.18). This result aligns with what is seen with the confocal microscope: that MamL$_{trunc}$ particles do not undergo directed motion as frequently as full-length MamL particles (chapter 2).

Tomato-MamL/EGFP-MamI and FLAG-MamL/EGFP-MamI particles undergoing active directed motion move at similar velocities as Tomato-MamL alone (0.23 µm/s vs. 0.14 µm/s vs. 0.20 µm/s, respectively). This suggests that Tomato-MamL alone, Tomato-MamL/EGFP-MamI, and FLAG-MamL/EGFP-MamI particles interact with the same molecular motors. Based on predicted protein structures of MamL and MamI, MamI has no cytoplasmic tail or domain and thus has no opportunity to interact with molecular motors (21). Whether expressed alone or together with MamI, MamL is the protein that likely interacts with molecular motors.

3.5   Conclusion

This is the first report of the mobility of magnetosome proteins MamL, MamB, and MamE in a mammalian system and their possible interaction with mammalian molecular motors. The pattern of motion of the structures to which these proteins localize is consistent with the motion of lipid vesicles (endosomes, lysosomes) observed in mammalian cells, namely a mixture of Brownian motion (with very small diffusion coefficient on the order of 10^{-3} to $10^{-2}\,\mu m^2/s$) and directed motion (with velocity on the order of 0.1 to 1 µm/s) (22, 23). MamL, MamB, and MamE all move at similar velocities when undergoing active directed motion. This suggests that, when these proteins are expressed in mammalian cells, they may be interacting with the same type of molecular motor or are localized in vesicles that interact with the same type of molecular motor.

When co-expressed, MamI and MamL localize to the same intracellular compartment and co-localize in punctate, mobile structures. Importantly, MamI+L particles undergoing directed motion move at the same velocity as MamL, suggesting they interact with the same molecular motors, and MamI+L particles diffuse slower than MamL alone particles consistent with the expected slower diffusion of larger structures relative to smaller ones.

Taken together, our trajectory analysis supports the evidence that MamL and MamI interact. Looking back on the working model of magnetosome assembly in the mammalian cell (chapter 1; Fig. 1.1); trajectory analysis supports that these essential magnetosome proteins are localized on an intracellular membrane in the mammalian cell. The co-localization and interaction of MamI and MamL is further demonstrated in this chapter through the analysis and comparison of the mobility of MamL alone and

MamL+MamI particles. This study is thus consistent with our hypothesis that these magnetosome proteins will interact in a membranous compartment when expressed in mammalian cells.

3.6   References

1.   Goldhawk DE, Gelman N, Thompson RT, Prato FS. Forming Magnetosome-Like Nanoparticles in Mammalian Cells for Molecular MRI. In: Bulte JWM, Modo MMJ, editors. Design and Applications of Nanoparticles in Biomedical Imaging. Cham: Springer International Publishing; 2017. p. 187-203.

2.   Komeili A. Molecular mechanisms of compartmentalization and biomineralization in magnetotactic bacteria. FEMS Microbiol Rev. 2012;36(1):232-55.

3.   Uebe R, Schüler D. Magnetosome biogenesis in magnetotactic bacteria. Nat Rev Microbiol. 2016;14(10):621-37.

4.   Lefèvre CT, Trubitsyn D, Abreu F, Kolinko S, Jogler C, de Almeida LG, et al. Comparative genomic analysis of magnetotactic bacteria from the Deltaproteobacteria provides new insights into magnetite and greigite magnetosome genes required for magnetotaxis. Environ Microbiol. 2013;15(10):2712-35.

5.   Murat D, Quinlan A, Vali H, Komeili A. Comprehensive genetic dissection of the magnetosome gene island reveals the step-wise assembly of a prokaryotic organelle. Proc Natl Acad Sci U S A. 2010;107(12):5593-8.

6.   Raschdorf O, Forstner Y, Kolinko I, Uebe R, Plitzko JM, Schüler D. Genetic and Ultrastructural Analysis Reveals the Key Players and Initial Steps of Bacterial Magnetosome Membrane Biogenesis. PLoS Genet. 2016;12(6):e1006101.

7.   Uebe R, Junge K, Henn V, Poxleitner G, Katzmann E, Plitzko JM, et al. The cation diffusion facilitator proteins MamB and MamM of Magnetospirillum gryphiswaldense have distinct and complex functions, and are involved in magnetite biomineralization and magnetosome membrane assembly. Mol Microbiol. 2011;82(4):818-35.

8.   Uebe R, Keren-Khadmy N, Zeytuni N, Katzmann E, Navon Y, Davidov G, et al. The dual role of MamB in magnetosome membrane assembly and magnetite biomineralization. Molecular Microbiology. 2018;107(4):542-57.

9.   Quinlan A, Murat D, Vali H, Komeili A. The HtrA/DegP family protease MamE is a bifunctional protein with roles in magnetosome protein localization and magnetite biomineralization. Mol Microbiol. 2011;80(4):1075-87.

10.   Schmidt N, Mishra A, Lai GH, Wong GC. Arginine-rich cell-penetrating peptides. FEBS Lett. 2010;584(9):1806-13.

11.   Rohani R, Figueredo R, Bureau Y, Koropatnick J, Foster P, Thompson RT, et al. Imaging tumor growth non-invasively using expression of MagA or modified ferritin subunits to augment intracellular contrast for repetitive MRI. Mol Imaging Biol. 2014;16(1):63-73.

12.   Smith P, Krohn R, Hermanson G, Mallia A, Gartner F, Provenzano M, et al. Measurement of protein using bicinchoninic acid. Anal Biochem. 1985;150:76-85.

13.   Sbalzarini IF, Koumoutsakos P. Feature point tracking and trajectory analysis for video imaging in cell biology. J Struct Biol. 2005;151(2):182-95.

14.   Schneider CA, Rasband WS, Eliceiri KW. NIH Image to ImageJ: 25 years of image analysis. Nat Methods. 2012;9(7):671-5.

15.   Hershey DM, Browne PJ, Iavarone AT, Teyra J, Lee EH, Sidhu SS, et al. Magnetite Biomineralization in Magnetospirillum magneticum Is Regulated by a Switch-like Behavior in the HtrA Protease MamE. J Biol Chem. 2016;291(34):17941-52.

16.   Wachsmuth M, Waldeck W, Langowski J. Anomalous diffusion of fluorescent

probes inside living cell nuclei investigated by spatially-resolved fluorescence correlation spectroscopy. J Mol Biol. 2000;298(4):677-89.

17.   Bandyopadhyay D, Cyphersmith A, Zapata JA, Kim YJ, Payne CK. Lysosome transport as a function of lysosome diameter. PLoS One. 2014;9(1):e86847.

18.   Weeks ER, Weitz DA. Subdiffusion and the cage effect studied near the colloidal glass transition. Chemical Physics. 2002;284(1):361-7.

19.   Kapanidis AN, Uphoff S, Stracy M. Understanding Protein Mobility in Bacteria by Tracking Single Molecules. J Mol Biol. 2018;430(22):4443-55.

20.   Howard J. Mechanics of Motor Proteins and the Cytoskeleton Sunderland. 552001.

21.   Nudelman H, Zarivach R. Structure prediction of magnetosome-associated proteins. Front Microbiol. 2014;5:9.

22.   Matteoni R, Kreis TE. Translocation and clustering of endosomes and lysosomes depends on microtubules. J Cell Biol. 1987;105(3):1253-65.

23.   Cordonnier MN, Dauzonne D, Louvard D, Coudrier E. Actin filaments and myosin I alpha cooperate with microtubules for the movement of lysosomes. Mol Biol Cell. 2001;12(12):4013-29.

Chapter 4

4 Magnetic resonance parameters and cellular iron content of magnetosome proteins expressed in mammalian cells

To evaluate whether magnetosome genes *mamI, mamL, mamB,* and *mamE* are suitable as gene-based contrast agents, we determined their effect(s) on cellular magnetic resonance (MR) parameters and cellular iron content.

Chapter 4 describes the effect of these genes, when expressed in cultured mammalian cells grown in the presence and absence of iron supplementation, on both the transverse and longitudinal MR relaxation rates and on total cellular elemental iron.

This chapter will be submitted for publication with the tentative author list: Sun Q, Vivekanantha P, Gelman N, Thompson RT, Prato FS, and Goldhawk DE.

4.1 Introduction

Molecular imaging has been used for the detection of biological processes (1) and provides monitoring of diseases from diagnosis through therapy. Molecular probes in the form of contrast agents have been developed as molecular imaging tools for modalities such as computed optical imaging, positron emission tomography (PET), and magnetic resonance imaging (MRI) (2). Among these, MRI is an ideal candidate due to its superb ability to discern anatomic detail at any tissue depth (3, 4) over optical. However, MRI lacks the sensitivity and specificity needed to effectively detect and track cellular and molecular activities. To account for this need, gene-based MR contrast agents are currently being developed in the molecular imaging field (5). Since these endogenous contrast agents originate from the cell and remain throughout its life cycle, they provide many advantages for long term, repetitive tracking of disease progression.

To improve molecular imaging techniques for MRI, we are developing MRI reporter gene expression based on the magnetosome. In magnetotactic bacteria (MTB), magnetosome formation compartmentalizes iron biominerals in membrane-enclosed vesicles (6). This technology not only provides a genetically-controlled iron biomineral, but also prevents iron cytotoxicity by virtue of the lipid bilayer barrier. Magnetosome formation is a stepwise, protein-directed process that begins with vesicle formation and culminates with iron biomineralization (7). While the entire process is regulated by approximately 30 genes, the majority of which are located on a magnetosome genomic island (6, 7), in some cases select genes have been successfully used to enhance the cellular MRI signal. For example, *mms6*, a gene involved in promoting uniform magnetite crystal morphology, has been expressed in human mesenchymal stem cells to

enhance their MRI detection (8). In addition, expression of *magA*, a putative iron transporter, enhances MRI contrast and cellular iron content, and is compatible with a mammalian model of tumour growth (9, 10, 11, 12).

To improve the localization and compartmentalization of a rudimentary magnetosome-like particle in mammalian cells, we are introducing select genes deemed essential for the initial stages of magnetosome formation. The targeted genes, *mamI, mamL, mamB* and *mamE*, are clustered on the *mamAB* operon and are highly conserved in several species of MTB (6, 13). The putative roles of *mamI*, *mamL*, and *mamB* are necessary for initial stages of magnetosome vesicle formation (7, 14), and may even provide docking site(s) for additional protein(s) (15), like MamE, that facilitates iron biomineralization (16, 17). The mutated form of MamL, MamL$_{trunc}$, was also investigated in this study to gain further knowledge of the effect of different domains of the MamL protein on cellular MR relaxation and iron content.

We are introducing these magnetosome genes in a mammalian system by expressing them in the human melanoma tumor cell line MDA-MB-435. These cells are a model of the cancer stem cell phenotype and demonstrate metastatic behavior (9, 18). In the present study, we evaluated the behaviour and interactions of magnetosome genes *mamI, mamL, mamB,* and *mamE* in the MDA-MB-435 cell line and assessed their effect(s) on cellular MR relaxation rates and total cellular iron content.

4.2   Materials and Methods

4.2.1 Molecular Cloning

Magnetosome genes *mamI* and *mamL* were amplified by PCR from the genomic

DNA of *Magnetospirillum magneticum* strain AMB-1 (ATCC 700264) using custom

primers (Table 2.1). The *mamI* and *mamL* amplicons were purified using a PCR clean-up

kit (Invitrogen, Life Technologies, Burlington, Canada); digested with appropriate

restriction enzymes (Table 2.1); and purified once more with the PCR clean-up kit, prior

to insertion in the molecular cloning vectors pEGFP-C1 (Clontech; Fig. 2.1) and

ptdTomato-C1 (Clontech; Fig. 2.2), respectively. Sequencing information for *mamI* and

mamL is available in Appendix A.1 and A.2, respectively. After propagation in

Escherichia coli strain XL10GOLD, the vector-insert plasmid constructs were purified

and used for mammalian cell transfection.

For cloning of Tomato-MamL$_{trunc}$, the last 15 amino acids from the C-terminus of

MamL were removed by PCR site-directed mutagenesis. Briefly, primers were designed

that included a stop codon 45 nucleotides upstream from the end of *mamL* (Table 2.2).

These primers were then used in PCR amplification of the truncated *mamL* gene, which

was then inserted into the ptdTomato-C1 vector with restriction enzymes EcoRI and

BglII (Fig. 2.3). Sequencing information is available in Appendix A.3.

For cloning of FLAG-MamL, primers flanking *mamL* in ptdTomato-*mamL* were

designed to include a FLAG tag for immunodetection. The FLAG-*mamL* insert was

amplified using PCR; purified using a PCR clean-up kit (Invitrogen, Life Technologies,

Burlington, Canada); and restriction digested using SacI and EcoRI (Table 2.3). FLAG-*mamL* was then inserted into the pSF-EMCV-*FLuc* vector and propagated in *Escherichia coli* strain XL10GOLD (Fig. 2.4). Sequencing information is available in Appendix A.4.

For cloning of Tomato-MamB, the *mamB* gene was amplified by PCR from AMB-1 genomic DNA using custom primers (Table 3.1). The amplicon was purified with a PCR clean-up kit; digested with restriction enzymes (Table 3.1); purified once more; and inserted into the ptdTomato-C1 vector (Clontech; Fig 3.1). The vector-insert construct was propagated in *E. coli* strain XL10GOLD; purified; and then used for mammalian cell transfection. Sequencing information is available in Appendix A.5.

For cloning of Tomato-MamE, the *mamE* gene was amplified by PCR from AMB-1 genomic DNA using custom primers (Table 3.1). The amplicon was purified with a PCR clean-up kit; digested with restriction enzymes (Table 3.1); purified once more; and inserted into the pEGFP-C1 vector (Clontech; Fig 3.2). The vector-insert construct was propagated in *E. coli* strain XL10GOLD; purified; and then used for mammalian cell transfection. Sequencing information is available in Appendix A.6.

4.2.2 Cell Culture

MDA-MB-435 cells (ATCC HTB-129; derived from an adult female and characterized as a melanoma cell line) are a model of aggressive tumorigenesis (9). Cells were cultured in 100 mm polystyrene-coated cell culture dishes (CELLSTAR, VWR International, Mississauga, Canada) with Dulbecco's Modified Eagle Medium (DMEM) containing 1 g/L glucose (Gibco, Life Technologies, Burlington, Canada), 10% fetal

bovine serum (FBS; Gibco), 4 U/mL penicillin, and 4 µg/mL streptomycin at 37°C with 5% CO_2.

To create cell lines expressing the enhanced green fluorescent protein (EGFP)-MamI fusion protein or the red fluorescent protein tdTomato (Tomato)-MamL fusion protein, cells were grown to 60-70% confluency on a 100 mm dish and transfected using Lipofectamine 2000 (Invitrogen), according to company protocol, using 8 µg of pEGFP-*mamI* or ptdTomato-*mamL*, respectively.

For co-expression of both pEGFP-*mamI* and ptdTomato-*mamL,* cells stably expressing Tomato-MamL were transfected with 8 µg of pEGFP-*mamI*. After 16 hours transfections were stopped, and cells were placed in complete medium for 48 hours before commencing antibiotic selection. For co-expression with the pSF-FLAG-*mamL*-EMCV-*FLuc* construct, cells stably expressing EGFP-MamI were grown to 60-70% confluency on a 100 mm dish and transfected using Lipofectamine 2000 (Invitrogen), according to company protocol, using 8 µg of pSF-FLAG-*mamL*-EMCV-*FLuc*. After 16 hours transfection was stopped, and cells were placed in complete medium for 48 hours before commencing antibiotic selection. To select for stable cell lines, cells were grown in the presence of 500 µg/mL Geneticin (G418; Gibco) and 0.5 µg/mL Puromycin (Gibco).

To create the Tomato-MamB or EGFP-MamE cell line, parental MDA-MB-435 cells were grown to 60-70% confluency on a 100 mm dish and transfected using Lipofectamine 2000 (Invitrogen), according to company protocol, using 8 µg of ptdTomato-*mamB* or 4 µg of pEGFP-*mamE*, respectively. After 16 hours cells were

placed in complete medium for 48 hours before commencing antibiotic selection. To select stable cell lines, transfected cells were grown in the presence of 500 µg/mL Geneticin (G418; Gibco).

4.2.3 Cell Harvest and Phantom Preparation

A spherical MR phantom was constructed using two 9 cm plastic hemispherical molds (Fig. 4.1). One hemisphere was filled with 4% gelatin (porcine type A)/Phosphate Buffered Saline (PBS; 137 mM NaCl, 2.7 mM KCl, 8 mM Na_2HPO_4, 2 mM KH_2PO_4) (approximately 420 mL), and the other is half-filled with 4% gelatin/PBS (approximately 200 mL).

To prepare cell samples, MDA-MB-435 cells expressing MamI, MamL, MamB, MamE, MamI+L, or $MamL_{trunc}$ were cultured, with or without the presence of 250 µM ferric nitrate $(Fe(NO_3)_3)$ (19), in forty 150 mm cell culture dishes (approximately 800 million cells total). Cells were harvested by first washing each plate twice with 10 mL of PBS, then incubating the cells in 5 mL of 0.05% trypsin-Ethylenediamine Tetraacetic Acid (EDTA) (Gibco) at room temperature for 60-90 seconds. The trypsin-EDTA was then carefully aspirated, and 5 mL of DMEM low glucose media was added to each plate. Cells were then gently removed from the bottom of each plate by trituration and loaded into a 50 mL conical tube.

After cells from all plates have been harvested, tubes containing the cells were centrifuged at 400 x g at 15°C for 5 minutes. Cells were then washed by resuspending the cell pellet in 35 mL of PBS, then centrifuged again. The pellet was then resuspended and washed in 10 mL of PBS, and the cell slurry was transferred to a 15 mL conical tube.

Tubes were once again centrifuged, washed in 10 mL of PBS, and centrifuged one last time. Approximately 140 µL of cell slurry was then loaded into a custom made Ultem well (inner diameter 4mm, height 10 mm; Lawson Imaging Prototype Lab) to fully fill the well.

Each cell phantom experiment contains four Ultem wells filled with cells of one expression system. These Ultem wells were then mounted on the half-filled 4% gelatin/PBS hemisphere (Fig. 4.2). The hemisphere was then fully filled with approximately 200 mL of 4% gelatin/PBS and was left at room temperature overnight to solidify.
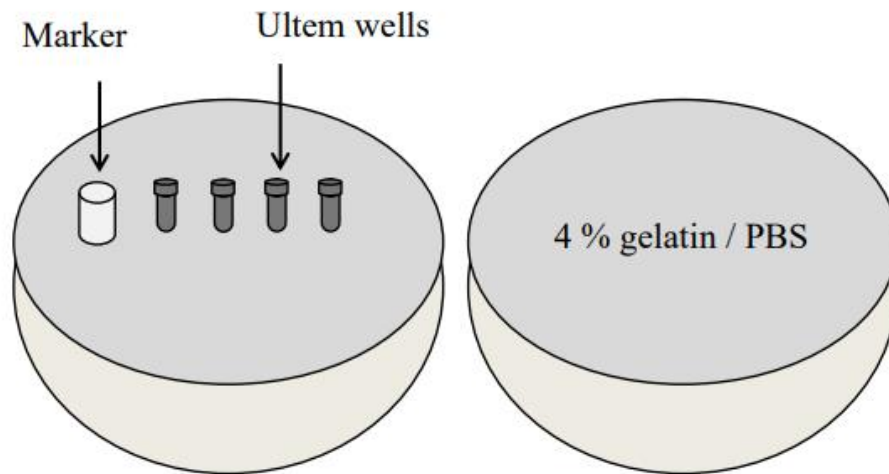
Figure 4.1 MRI cell phantom layout.

Hemispherical phantom moulds (9 cm diameter) are filled with 4% gelatin/PBS. Cells are loaded into Ultem wells that are mounted into one hemisphere (19, 20).
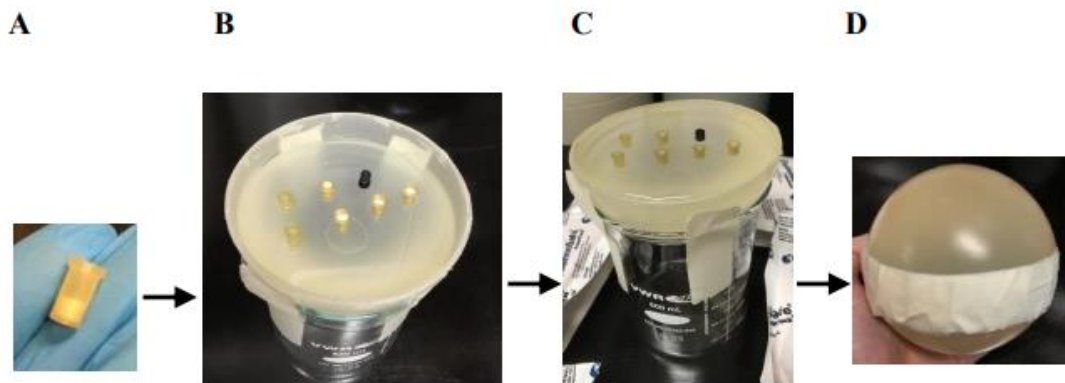
Figure 4.2 Experimental flow chart of MRI phantom preparation.

A. Cells are loaded into Ultem wells using centrifugation to create a compact pellet. **B.** Fully filled Ultem wells are mounted on a solidified, half-filled 4% gelatin/PBS phantom hemisphere. **C.** The half-filled hemisphere is completely overlaid with 4% gelatin/PBS and left to solidify. **D.** The full spherical phantom is assembled by taping both hemispheres together (19, 20).

Before the scheduled MRI scan, the phantom hemispheres are moved to the fridge to ensure that gelatin has solidified. One hour prior to the scan, the phantom hemispheres are taken out of the fridge, taped together to form a sphere, and left at room temperature until scanned.

4.2.4 MRI Sequences

The phantom was scanned at 3 Tesla (T) on a Biograph mMR (Siemens AG, Erlangen, Germany) using previously developed sequences to acquire longitudinal and transverse relaxation rates (19). All image acquisitions used for relaxation measurement

had a slice thickness of 3 mm and field of view of 120 x120 mm^2 (locator image, Fig. 4.3).
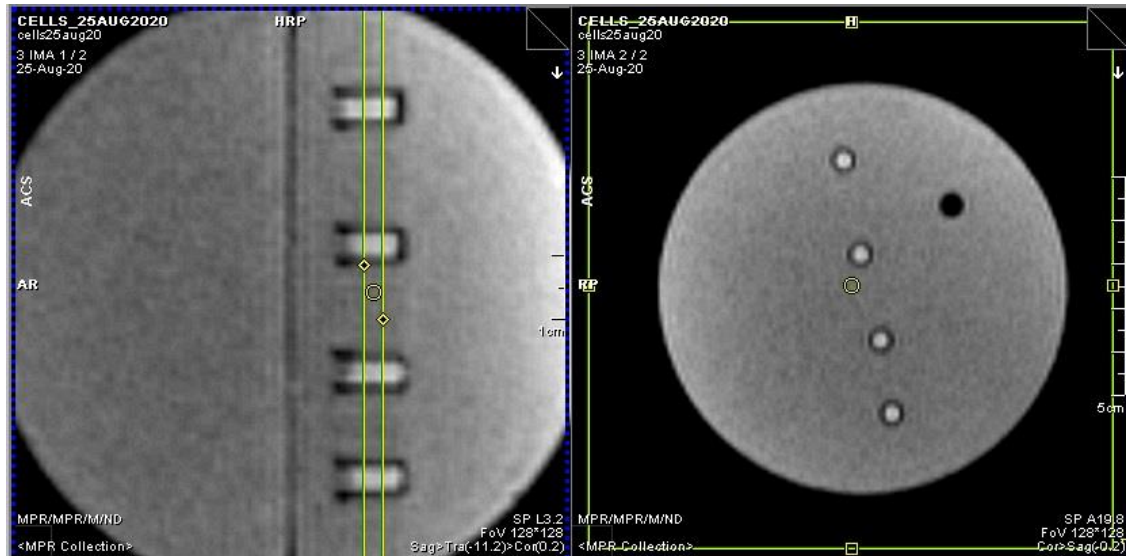
Figure 4.3 Representative locator image of MRI phantom experiment of cells stably-expressing EGFP-MamI.

The 3 mm slice (indicated by yellow lines, left panel) was positioned perpendicular to the wells and within the cell pellet volume in each Ultem well. The right panel shows a cross-section top view of the phantom and shows the layout of the four Ultem wells (white circles) and the position marker (black circle).

To measure R1 longitudinal relaxation rates, a magnitude reconstruction inversion recovery (IR) spin echo sequence was used (19). The matrix resolution was 128×128 mm^2 and voxel size was $3.0 \times 0.9 \times 0.9$ mm^3. Repetition time (TR) was 4000 ms, excitation flip angle was 90˚, and inversion times were 22, 200, 500, 1000, 2000 and 3900 ms.

For acquisition of R2 transverse relaxation rates, a single-echo (SE) spin echo sequence was used with matrix resolution of 192 x 192 mm^2 and voxel size 3.0 x 0.6 x 0.6 mm^3. Echo times (TE) were 13, 20, 25, 30, 40, 60, 80, 100, 150, and 200 ms. TR was 2200 ms and excitation flip angle was 90°.

For acquisition of R2* transverse relaxation rates, a multi-echo gradient echo (GRE) sequence was used with matrix resolution of 192 x 192 mm^2 and voxel size 3.0 x 0.6 x 0.6 mm^3. TE were 6.12, 14.64, 23.16, 31.68, 40.2, 50, 60, 70 and 79.9 ms; TR was 2000 ms; and flip angle was 60˚.

4.2.5 Protein Assay

Cells remaining after the preparation of MRI cell phantoms were mixed with 850 µL of RIPA and 150 µL of Complete Mini protease inhibitor cocktail (Roche Diagnostic Systems, Laval, Canada). Cells were lysed by sonication using three 12-second bursts of a Sonic Dismembrator (model 500, Thermo Fischer Scientific, Ottawa, Canada) at an amplitude of 30%. Total amount of protein was quantified using the bicinchoninic acid (BCA) assay (21).

4.2.6 Preparation of ICP-MS

For elemental iron and zinc analysis, a minimum of 2.5 mL of each sample containing 2 mg/mL of protein were prepared. Each sample represents the cell population mounted in a single well of the MR phantom. Samples were stored at -20°C until transported to the inductively-coupled plasma mass spectrometry (ICP-MS) facility

(Biotron Analytical Services, Western University). This data is reported as total cellular iron content normalized to total amount of protein.

4.2.7 MR Data Analysis

Longitudinal relaxation rates of samples were determined using Matlab 7.9.0 (R2010b). This software was used to select a 9-voxel circular region of interest (ROI) corresponding to 22 mm^3 that encompasses the area containing cells without including the wall of the Ultem wells. The average signal intensity within the ROI was determined at each TI and recorded in an Excel spreadsheet with a set layout (Appendix D.1). This spreadsheet was then entered in a Matlab script (developed by Neil Gelman, Prushoth Vivekanantha, Moiez Ahmed, and Salvan Hassan, 2021) to determine R1 values. R1 curve fitting was determined using the standard inversion recovery equation for magnitude signals:

$$S = |k\rho \left(1 - 2e^{\frac{-TI}{T_1}} + e^{\frac{-TR}{T_1}} \right)|$$

The R1 values will appear under the entered signal intensity values on the spreadsheet (Appendix D.1).

Transverse relaxation rates (both R2* and R2) of samples were determined using custom software developed in Matlab 7.9.0 (R2010b). This software was used to select a 21-voxel circular ROI corresponding to 23 mm^3 that encompasses the area of the cells without including the wall of the Ultem wells. The average signal intensity within the ROI was determined at each TE, and these values were plotted using GraphPad Prism software version 8.0.1. A mono-exponential nonlinear fit was applied to determine R2*

or R2' values. R2' was calculated by subtraction (R2* - R2 = R2') (22). Relaxation rates of

replicate samples were reported as the mean +/- standard error of the mean (SEM) using

GraphPad Prism software. All transverse relaxation rates collected are listed in the

Appendix.

4.2.8 Statistical Analysis

All statistical tests were performed using GraphPad Prism version 8.0.1. An

unpaired t-test was used to identify any significant difference between iron supplemented

cells and those without iron supplement (Parental vs. Parental + Fe, MamI vs. MamI +

Fe, MamL vs. MamL + Fe, MamB vs. MamB + Fe, and MamE vs. MamE + Fe) for

transverse relaxation rates (R2*, R2, R2′) and longitudinal relaxation rates (R1). For

cellular iron content, an unpaired t-test was also used to identify any significant

difference caused by iron supplementation (Parental vs. Parental + Fe, MamI vs. MamI +

Fe, MamL vs. MamL + Fe, MamB vs. MamB + Fe, and MamE vs. MamE + Fe).

4.3   Results

4.3.1 Effect of individually expressed magnetosome proteins on R2*

relaxation

In the absence of iron supplementation, MDA-MB-435 cells expressing MamI, MamL, MamB, or MamE exhibit R2* comparable to the untransfected parental control (15.02 ± 2.5, 17.87 ± 1.0, 18.70 ± 4.9, and 14.00 ± 1.4, respectively, vs. 15.81 ± 2.7; Fig. 4.4). In the presence of iron supplementation, MDA-MB-435 cells expressing MamI, MamL, or MamB display a significant increase in R2* compared to when unsupplemented (30.38 ± 2.8 vs. 15.02 ± 2.5, 37.07 ± 5.6 vs. 17.87 ± 1.0, and 35.35 ± 5.2 vs. 18.70 ± 4.9, respectively). Representative monoexponential decay curves are shown in Figure 4.5 for MamB-expressing cells and show the difference of iron supplementation. Cells expressing $MamL_{trunc}$ grown in the presence of an iron supplement exhibited an R2* comparable to full-length MamL (39.84 ± 5.7 vs. 37.07 ± 5.6, Fig. 4.4). Interestingly however, cells expressing MamE did not display any difference in R2* between iron-supplemented and non-supplemented samples (16.52 ± 0.9 vs. 14.00 ± 1.4). This cell type produced R2* values that were no different than the parental control.

Figure 4.4 R2* of cells stably expressing magnetosome proteins.

Bar graphs show R2* transverse relaxation rates of parental MDA-MB-435 cells (gray) and those cells stably expressing either MamI (green), MamL (red), $MamL_{trunc}$ (maroon), MamB (blue) or MamE (pink). Hashed bars represent cells grown in the presence of iron supplement whereas solid bars are those grown in the absence of iron supplement. Significant differences are indicated by * ($p < 0.05$) and *** ($p < 0.001$). Sample numbers are indicated within each bar (N = 4 – 12). Data is presented as mean $\pm$ SEM.

Figure 4.5 Representative R2* decay curves of mammalian cells expressing MamB.

Changes in signal intensity reflect a monoexponential signal decay for cells grown in the presence (A and B, red circles and squares) and absence (C and D, black triangles and inverted triangles) of iron supplement. Data is presented as mean ± SEM. N = 4 for all samples.

4.3.2 Effect of individually expressed magnetosome proteins on R2 relaxation

In the absence of iron supplementation, MDA-MB-435 cells expressing MamI, MamL, MamB, or MamE exhibit R2 values that are comparable to those of the parental cell type (12.40 ± 1.0, 12.23 ± 0.7, 12.76 ± 0.8, and 10.31 ± 1.2, respectively, vs. 12.45 ± 0.7; Fig. 4.6). Relative to non-supplemented cells, iron-supplemented MDA-MB-435 cells expressing MamI, MamL, or MamB display significant increases in R2 (19.12 ± 2.6, 23.38 ± 4.4, and 23.64 ± 3.7 respectively). However, as for R2* measures, MamE-

expressing cells showed no change in R2 whether or not they were grown in the presence

or absence of iron supplementation (10.31 ± 1.2 vs. 10.22 ± 1.4, respectively).

Representative monoexponential decay curves are shown in Figure 4.7 for MamB-

expressing cells.

Figure 4.6 R2 values of cells stably expressing magnetosome proteins.

R2 transverse relaxation rates of parental MDA-MB-435 cells (gray), MDA-MB-435

cells stably expressing MamI (green), MamL (red), MamL$_{trunc}$ (maroon), MamB (blue)

and MamE (pink) are displayed in this graph. Hashed bars represent cells grown in the

presence of iron supplement. Solid bars represent cells grown in the absence of iron

supplement. Significant data is indicated by * ($p<0.05$) or ** ($p<0.01$). Sample numbers

are indicated within each bar ($N = 4 – 9$). Data is presented as mean $\pm$ SEM.
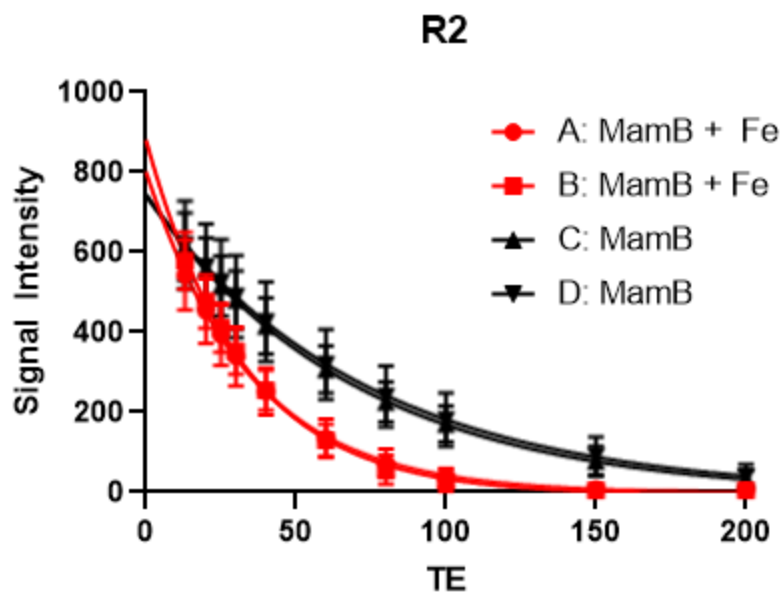
Figure 4.7 Representative R2 decay curves of mammalian cells expressing MamB.

Cells grown in iron supplement (red) and cells grown without iron supplement (black) are shown. A and B are replicates of samples of cells expressing iron-supplemented MamB, and C and D are replicates of samples of cells expressing nonsupplemented MamB. Data is presented as mean ± SEM. N = 4 for all samples.

4.3.3 Effect of individually expressed magnetosome proteins on R2' relaxation

Without iron supplementation, MDA-MB-435 cells expressing MamI, MamL, MamB, or MamE have comparable R2' to the parental control (2.70 ± 1.0, 7.04 ± 2.2, 7.64 ± 2.8, and 3.69 ± 0.8, respectively, vs. 3.37 ± 0.4; Fig. 4.8). When grown in the presence of iron supplement, MDA-MB-435 cells expressing MamI or MamL have significantly increased R2' compared to when they are unsupplemented (11.26 ± 1.8 vs. 2.70 ± 1.0 and 13.69 ± 1.5 vs. 7.04 ± 2.2 respectively) while cells expressing MamB or

MamE showed no changes in R2' values whether or not they were grown in the presence

of iron supplementation (7.64 ± 2.8 vs. 11.72 ± 1.8 and 3.69 ± 0.8 vs. 6.29 ± 1.8,

respectively). Iron-supplemented cells expressing MamL$_{trunc}$ showed no changes in R2'

compared to iron-supplemented MamL (21.14 ± 2.6 vs. 13.69 ± 1.5, respectively; Fig.

4.8); however, is it notable that MamL$_{trunc}$ has the largest R2' signal out of all the
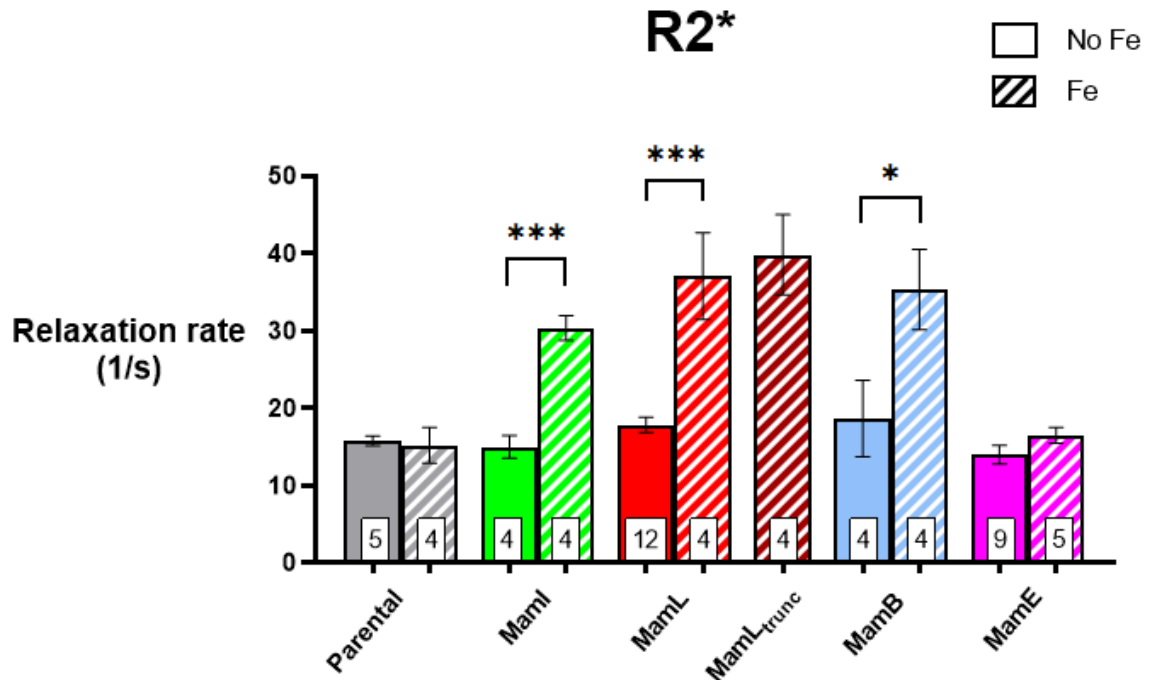
magnetosome protein expression systems studied.

Figure 4.8 R2' values of cells stably expressing magnetosome proteins.

R2' transverse relaxation rates of parental MDA-MB-435 cells (gray), MDA-MB-435

cells stably expressing MamI (green), MamL (red), MamL$_{trunc}$ (maroon), MamB (blue)

and MamE (pink) are displayed in this graph. Hashed bars represent cells grown in the

presence of an iron supplement. Solid bars represent cells grown in the absence of iron

supplement. Significant data is indicated by ** $p<0.01$. Sample numbers are indicated within each bar (N = 4 – 9). Data is presented as mean ± SEM.

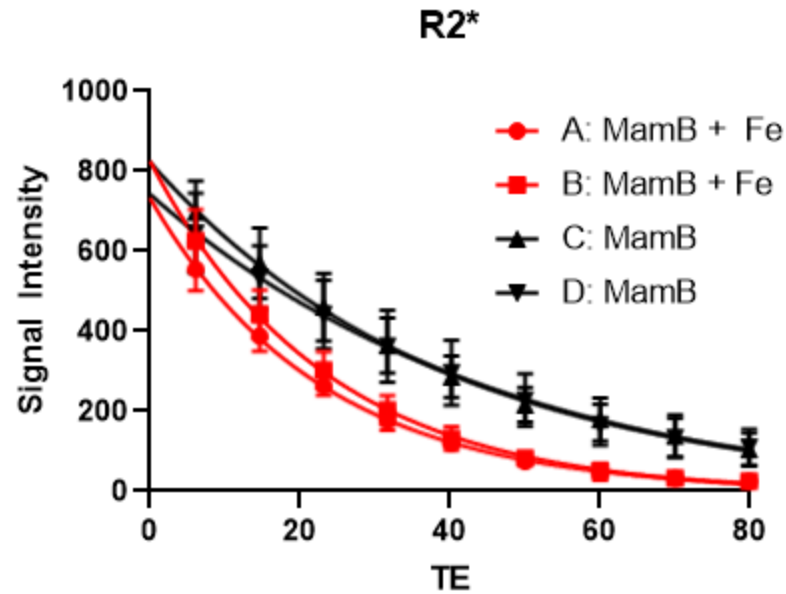## 4.3.4 Effect of co-expressed magnetosome proteins on R2* relaxation

As expected, in the presence of iron supplementation, MDA-MB-435 cells co-expressing EGFP-MamI with either Tomato-MamL or FLAG-MamL have comparable R2* (25.36 ± 3.0 vs. 18.58 ± 2.5, respectively; Fig. 4.9); however, these values are significantly higher than the R2* of the parental control (15.81 ± 2.7). Furthermore, irrespective of iron supplement, co-expression of FLAG-MamL/EGFP-MamI resulted in no changes to R2* values (14.32 ± 2.1 unsupplemented vs. 18.58 ± 2.5 supplemented). Compared to single expression systems, the interaction of MamI and MamL downregulates the R2* signal, although not significantly.
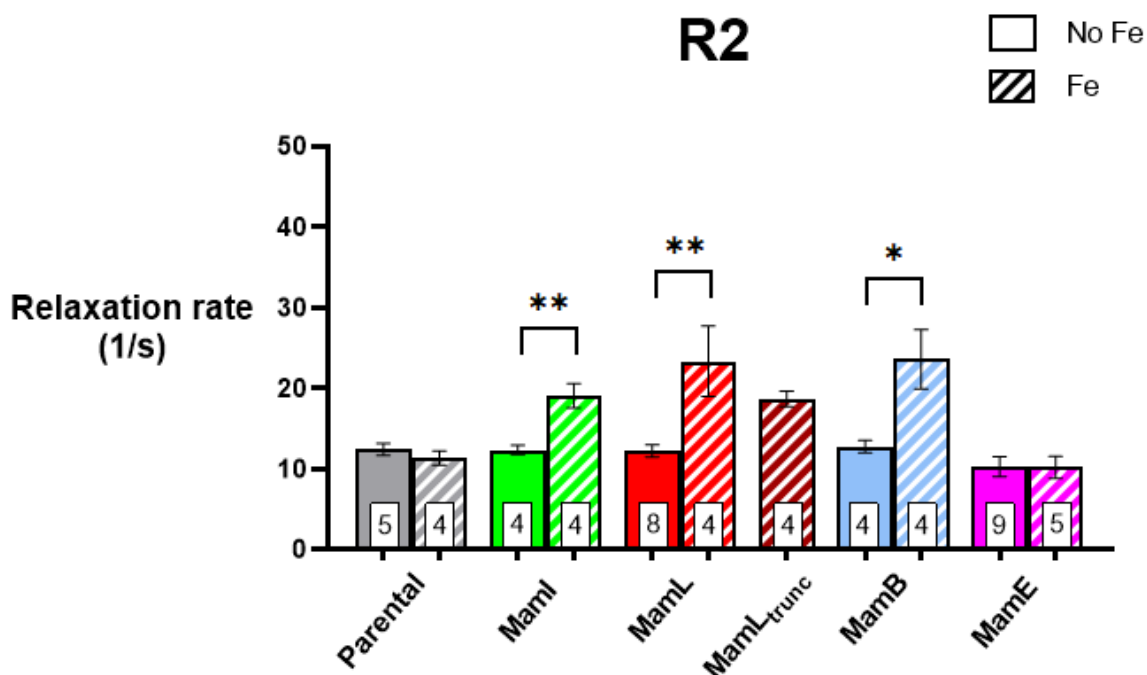
R2*
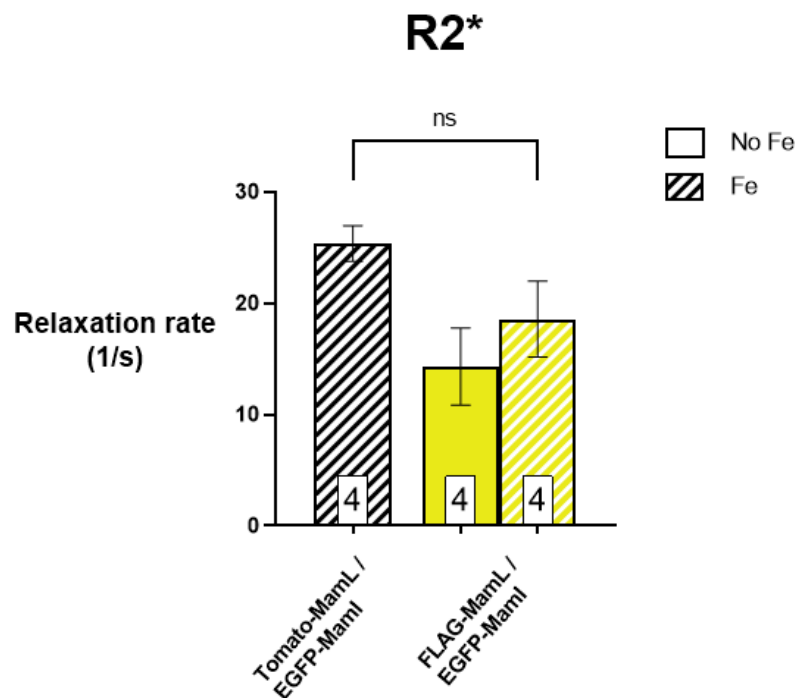
Figure 4.9 R2* values of cells stably co-expressing magnetosome proteins.

R2* transverse relaxation rates of MDA-MB-435 cells stably co-expressing Tomato-MamL/EGFP-MamI (black) or FLAG-MamL/EGFP-MamI (yellow) are displayed in this graph. Hashed bars represent cells grown in the presence of iron supplement. The solid bar represents cells grown in the absence of iron supplement. Sample numbers are indicated within each bar (N = 4). Data is presented as mean ± SEM. ns = p ≥ 0.05. Statistical analyses include the student's t-test.

4.3.5 Effect of co-expressed magnetosome proteins on R2 relaxation

In the presence of iron, MDA-MB-435 cells co-expressing Tomato-MamL/EGFP-MamI or FLAG-MamL/EGFP-MamI have comparable R2 (17.85 ± 1.2 vs. 15.00 ± 0.9, respectively; Fig. 4.10). MDA-MB-435 cells co-expressing FLAG-MamI/EGFP-MamI

did not have any significant changes to R2 values whether or not they were grown in the

presence of iron (14.32 ± 0.3 unsupplemented vs. 15.00 ± 0.9 supplemented).
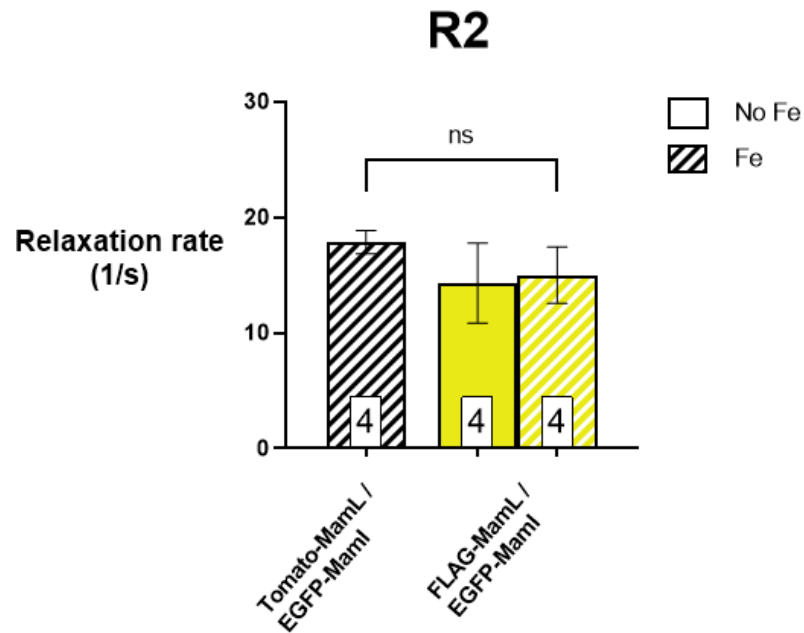
Figure 4.10 R2 values of cells stably co-expressing magnetosome proteins.

R2 transverse relaxation rates of MDA-MB-435 cells stably co-expressing Tomato-

MamL/EGFP-MamI (black) or FLAG-MamL/EGFP-MamI (yellow) are displayed in this

graph. Hashed bars represent cells grown in the presence of iron supplement. The solid

bar represents cells grown in the absence of iron supplement. Sample numbers are

indicated within each bar (N = 4). Data is presented as mean $\pm$ SEM. ns = p $\geq$ 0.05.

Statistical analyses include the student's t-test.

4.3.6 Effect of co-expressed magnetosome proteins on R2' relaxation

In the presence of iron, MDA-MB-435 cells co-expressing Tomato-MamL/EGFP-MamI or FLAG-MamL/EGFP-MamI have comparable R2' (7.51 ± 1.2 vs. 4.58 ± 0.5, respectively; Fig. 4.11). MDA-MB-435 cells co-expressing FLAG-MamL/EGFP-MamI did not have any significant changes to R2' values whether or not they were grown in the presence of iron (2.53 ± 0.2 unsupplemented vs. 4.58 ± 0.5 supplemented).
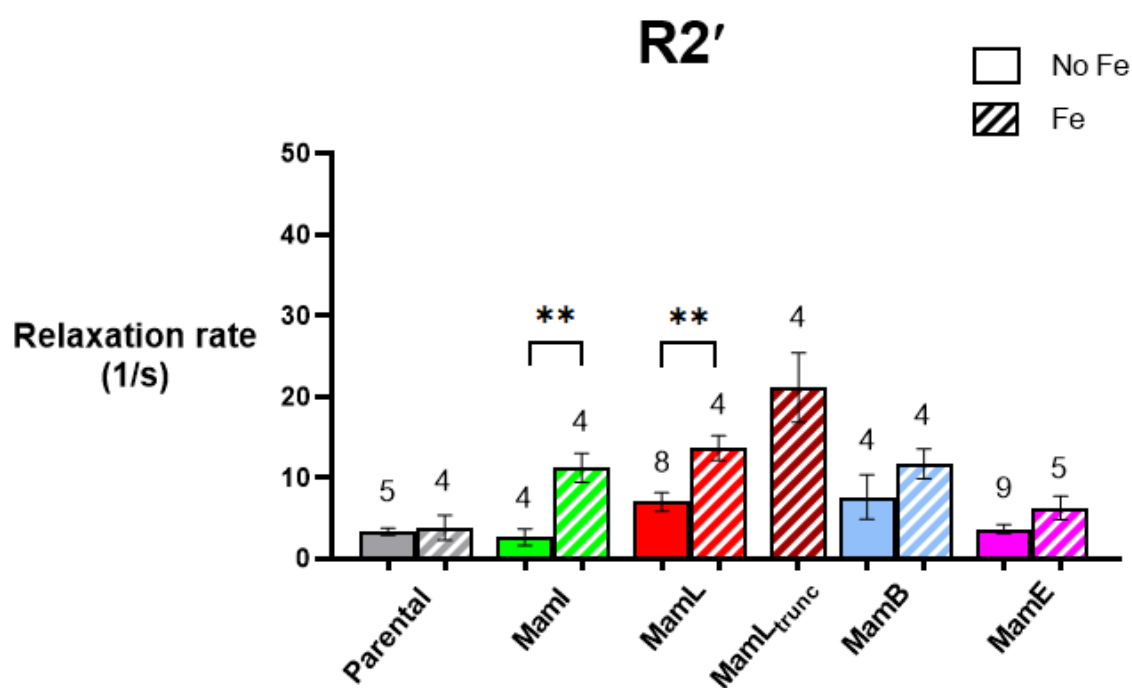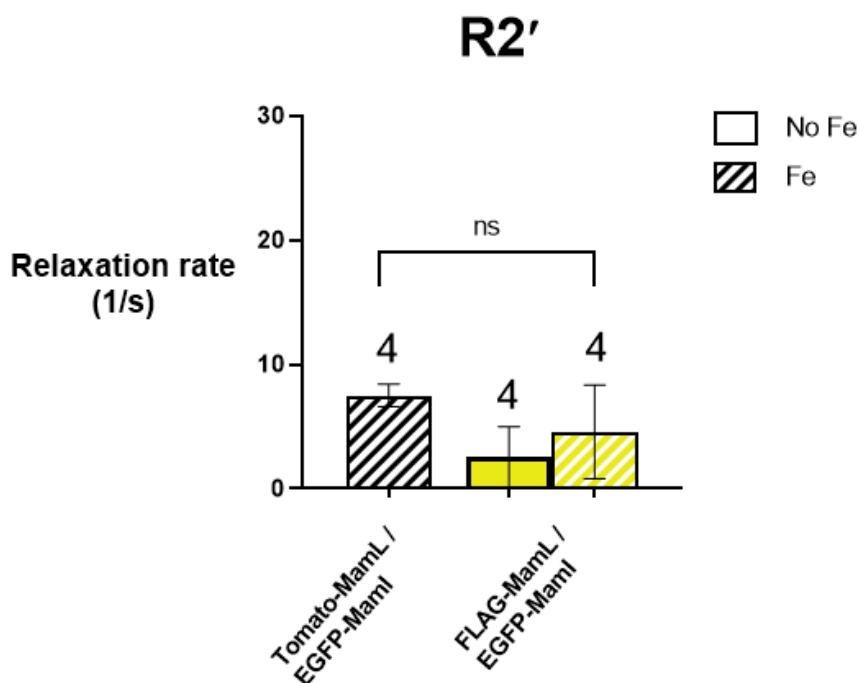

Figure 4.11 R2' values of cells stably co-expressing magnetosome proteins.

R2' transverse relaxation rates of MDA-MB-435 cells stably co-expressing Tomato-MamL/EGFP-MamI (black) or FLAG-MamL/EGFP-MamI (yellow) are displayed in this graph. Hashed bars represent cells grown in the presence of iron supplement. The solid

bar represents cells grown in the absence of iron supplement. Sample numbers are

indicated within each bar (N = 4). Data is presented as mean ± SEM. ns = p ≥ 0.05.

Statistical analyses include the student's t-test.

4.3.7 Effect of magnetosome proteins on R1 relaxation

Without iron supplementation, MDA-MB-435 cells expressing MamI, MamL,

MamI+L, MamB, or MamE have comparable R1 to parental MDA-MB-435 cells (0.91 ±

0.02, 0.88 ± 0.05, 0.90 ± 0.12, 0.97 ± 0.15, and 0.98 ± 0.32, respectively, vs. 0.90 ± 0.02;

Fig. 4.12). In the presence of iron supplementation, MDA-MB-435 cells expressing

MamI, MamL, or MamI+L display small but significant increases in R1 (0.91 ± 0.02 vs.

1.08 ± 0.03, 0.88 ± 0.05 vs. 1.18 ± 0.07, and 0.90 ± 0.12 vs. 0.97 ± 0.05, respectively).

MDA-MB-435 cells expressing MamB or MamE showed no changes in R1 whether or

not they were grown in the presence of iron supplementation (0.97 ± 0.15 vs. 1.28 ± 0.11

and 0.98 ± 0.32 vs. 1.12 ± 0.35, respectively). Cells expressing MamL$_{trunc}$ grown in the

presence of iron did not have significantly different R1 compared to full-length MamL

(1.18 ± 0.02 vs. 1.18 ± 0.07, respectively).
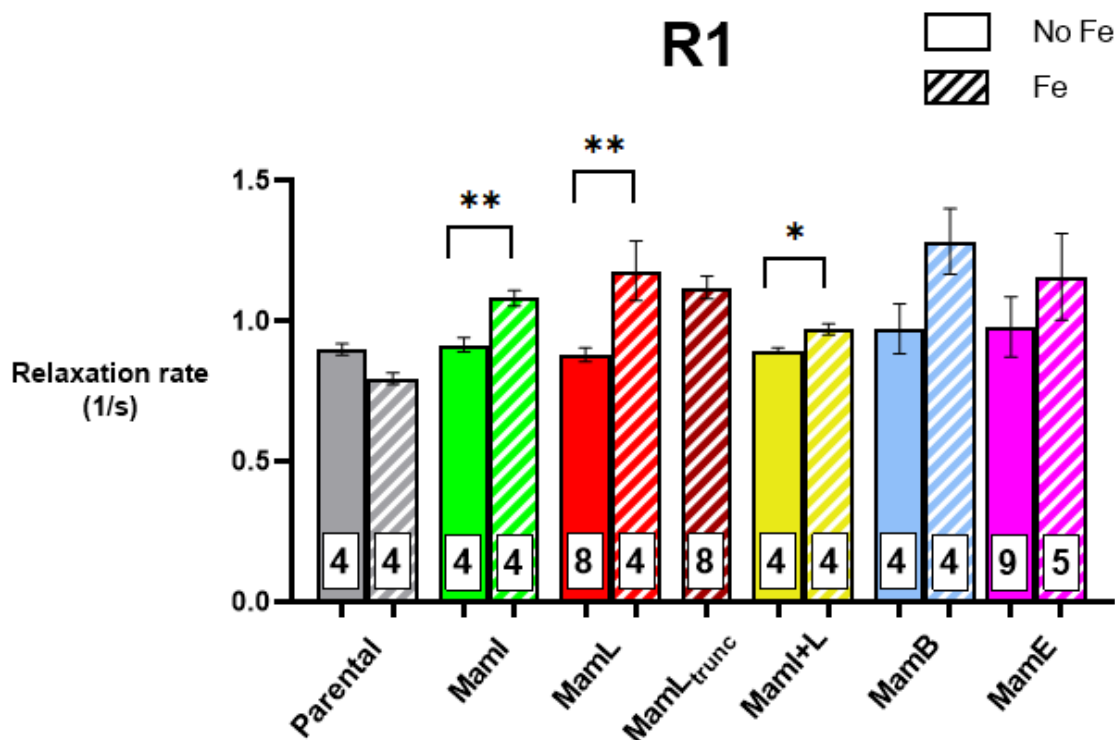
Figure 4.12 R1 values of cells stably expressing or co-expressing magnetosome proteins.

R1 relaxation rates of parental MDA-MB-435 cells (gray), MDA-MB-435 cells stably expressing MamI (green), MamL (red), MamL$_{trunc}$ (maroon), MamB (blue) and MamE (pink) are displayed in this graph. Hashed bars represent cells grown in the presence of iron supplement. Solid bars represent cells grown in the absence of iron supplement. Sample numbers are indicated within each bar (N = 4 – 9). Significance is indicated by * (p<0.05) or ** (p<0.01).

4.3.8 Effect of magnetosome proteins on cellular iron content

Without iron supplementation, MDA-MB-435 cells expressing MamI, MamL, MamB, MamE, or MamI+L (here all ICP-MS data of I+L co-expression are derived from

FLAG-MamL/EGFP-MamI) have cellular iron content comparable to the parental cell line (0.04 ± 0.001, 0.08 ± 0.01, 0.08 ± 0.01, 0.07 ± 0.02, and 0.15 ± 0.13 µg Fe/mg protein, respectively, vs. 0.05 ± 0.02 µg Fe/mg protein; Fig. 4.13). In the presence of iron supplementation, cells expressing MamI, MamL, MamB, or MamE display increased cellular iron content compared to when unsupplemented (1.12 ± 0.11, 1.11 ± 0.45, 1.48 ± 0.09, and 0.94 ± 0.34 µg Fe/mg protein respectively). Cells expressing $MamL_{trunc}$ grown in the presence of an iron supplement displayed cellular iron content comparable to full-length MamL (0.93 ± 0.18 vs. 1.11 ± 0.45 µg Fe/mg protein). Surprisingly, cells expressing MamE grown in the presence of iron supplement had cellular iron content comparable to cells expressing MamI, L, or B even though MamE, grown in the presence of iron, did not affect MR relaxation rates. In contrast, iron-supplemented cells expressing MamI+L have a decrease in transverse relaxation rates commensurate with the decrease in total cellular iron content compared to their individual expression.
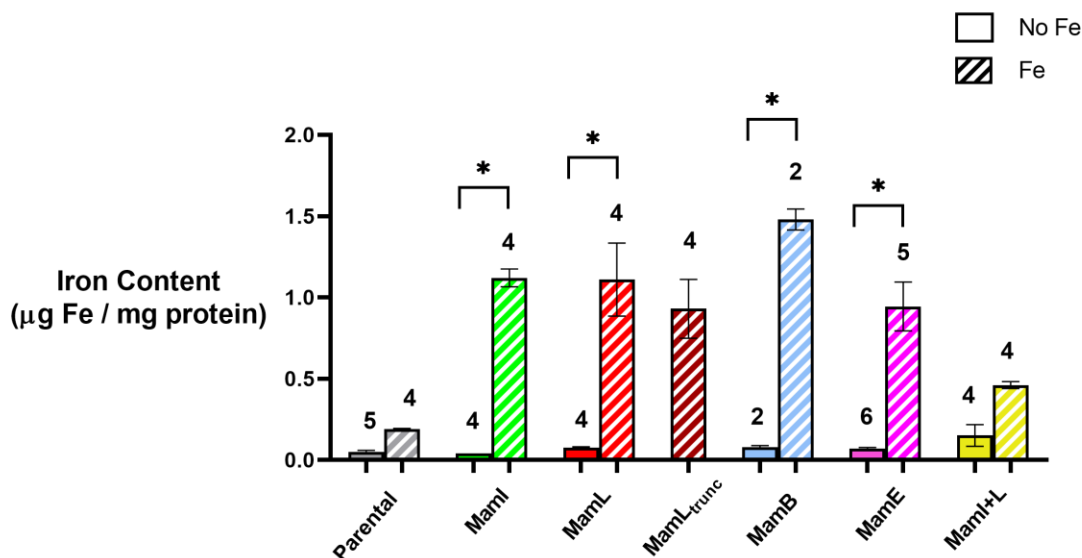
Figure 4.13 Total cellular iron values of cells stably expressing or co-expressing magnetosome proteins.

Cellular iron content of parental MDA-MB-435 cells (gray), MDA-MB-435 cells stably expressing MamI (green), MamL (red), MamL$_{trunc}$ (maroon), MamB (blue), MamE (pink), or co-expressing FLAG-MamL/EGFP-MamI (yellow) are displayed in this graph. Hashed bars represent cells grown in the presence of iron supplement. Solid bars represent cells grown in the absence of iron supplement. Sample numbers are indicated above each bar (N = 2 – 5). Significant differences are indicated by an asterisk with p<0.05.

4.3.9 Correlation between relaxation rate and cellular iron content

To assess the correlation between transverse relaxation rates and total cellular iron content, corresponding data from parental cells and cells expressing magnetosome protein(s) was analyzed using a linear regression (Fig. 4.14). When MamE is removed

from the equation (due to the protein having seemingly no effect on cellular iron content), the correlation between R2*, R2, and R2′ and cellular iron content is $r^2 = 0.61, 0.32$, and 0.48, respectively. It is notable that the iron-sensitive component R2' has a stronger correlation to elemental iron content than R2.
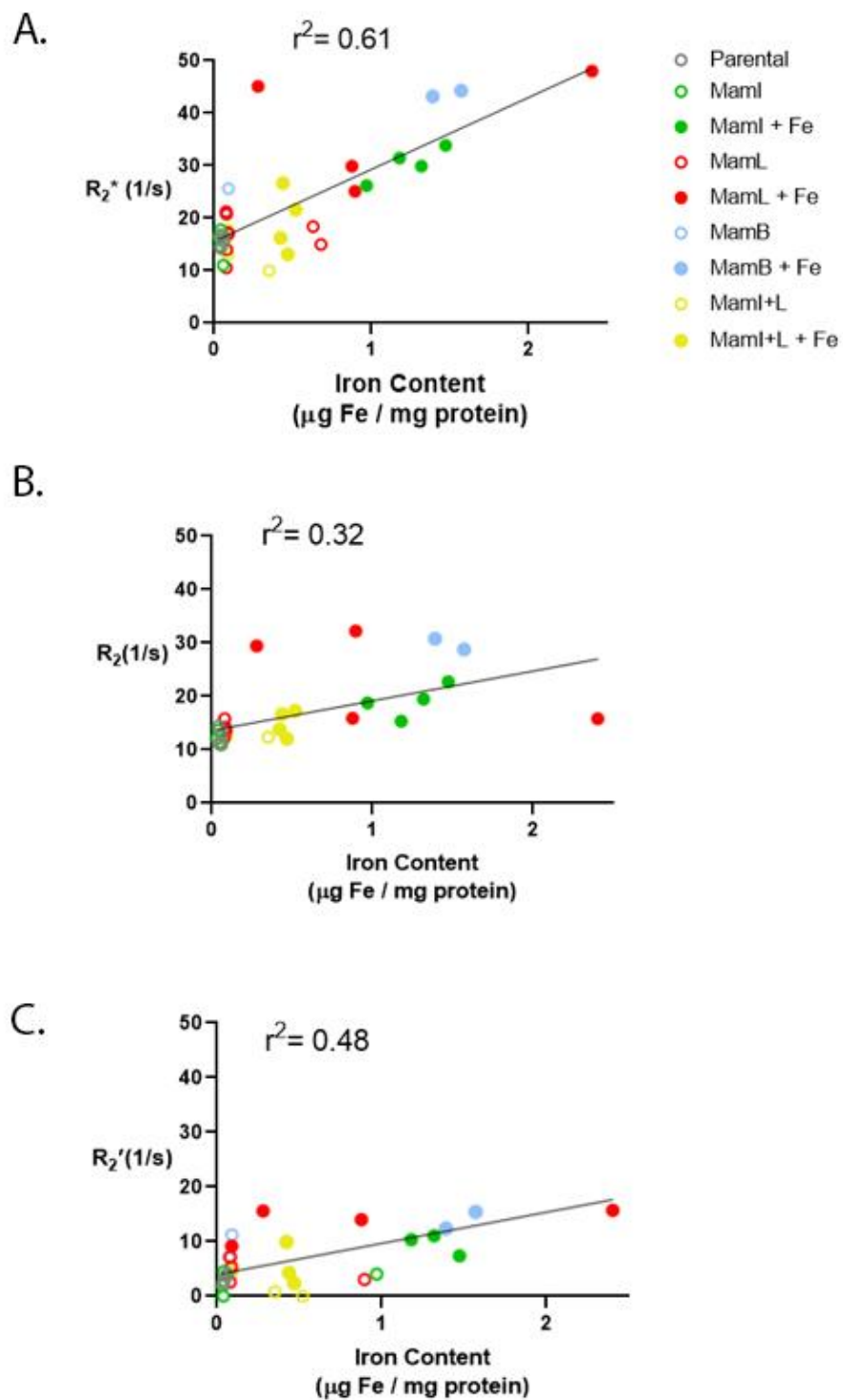
Figure 4.14 Correlation between transverse relaxation and cellular iron content of cells stably expressing and co-expressing magnetosome proteins.

Correlation between cellular iron content and R2* (A), R2 (B), and R2' (C) of parental

MDA-MB-435 cells or MDA-MB-435 cells stably expressing MamI, MamL, FLAG-

MamL/EGFP-MamI, or MamB. Open circles represent cells grown without iron

supplement, while closed circles represent cells grown in the presence of iron

supplement.

To assess the correlation between longitudinal relaxation rates and total cellular

iron content, corresponding data from parental cells and cells expressing magnetosome

protein(s) was analyzed using a linear regression (Fig. 4.15). There is a weak correlation

($r^2 = 0.19$) between R1 and cellular iron content.
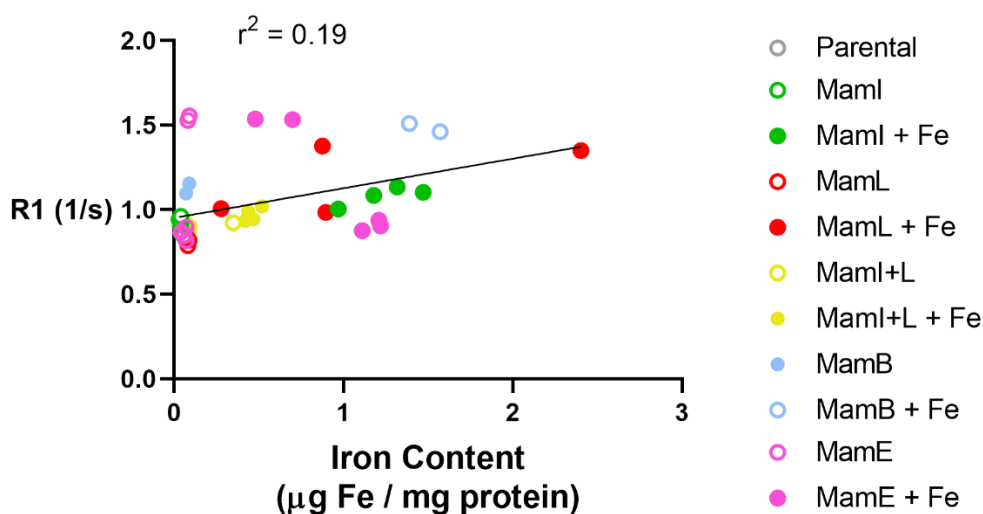
Figure 4.15 Correlation between longitudinal relaxation and cellular iron content of cells stably expressing and co-expressing magnetosome proteins.

Correlation between cellular iron content and R1 of parental MDA-MB-435 cells or

MDA-MB-435 cells stably expressing MamI, MamL, FLAG-MamL/EGFP-MamI,

MamB, or MamE. Open circles represent cells grown without iron supplement, while closed circles represent cells grown in the presence of iron supplement.

4.4 Discussion

In this study, the effect of magnetosome proteins MamI, MamL, MamB, and MamE on mammalian cellular MR parameters and cellular iron content were investigated (Appendix D.2). Here we report that, when expressed in cells grown in iron-supplemented media, magnetosome proteins MamI, MamL, and MamB significantly affected R2* and R2 relaxation rates, which is unexpected. In the AMB-1 species, *mamI* and *mamL* have function(s) related to invagination of the magnetosome membrane (6) and do not have any reported interactions with iron. However, in the MTB species *Magnetospirillum gryphiswaldense* (MSR-1), *mamI* has a putative role in magnetite nucleation (23). Currently, there are no known reports of *mamL* in MTB having any interactions or roles involving iron.

The gene *mamB* has an essential role in magnetosome membrane formation (6) but it has been speculated, especially in MSR-1, that *mamB* also has an essential role in iron biomineralization (24). MamB is a member of the cation diffusion facilitator (CDF) protein family which export divalent metal cations from the cytoplasm into intracellular compartments (24, 25). Based on these reports, MamB may affect the cellular MR signal by sequestering iron in an intracellular vesicle on which it is localized and thus increasing MR relaxation rates.

4.4.1 Effect of MamE on R2 relaxation

The role of *mamE* in iron biomineralization and crystal maturation is reported in multiple MTB species (6). Based on its interactions with iron in MTB, we predicted that *mamE* would affect the cellular MR signal by increasing elemental iron content and thus increasing MR relaxation rates. However, as shown here, this was not the case. It is speculated that perhaps the interaction of MamE with iron is dependent upon the established interaction of MamE with other magnetosome proteins such as MamI, MamL, and/or MamB. MamE is a bifunctional protein in AMB-1 (16), with a role in both protein localization and biomineralization (16). Deletion studies of MamE report that localization of both soluble proteins (ie. MamC and MamF) and membrane-bound protein (MamI) were disrupted (16). Since magnetosome formation is a stepwise process, the biomineralization function of MamE is potentially not activated unless the MamE protein has successfully interacted with other magnetosome proteins.

4.4.2 Effect of MamE on total cellular iron

Iron-supplemented mammalian cells expressing MamE had total cellular iron levels similar to iron-supplemented cells expressing MamI, MamL, or MamB. This is a surprising result considering that MamE did not significantly alter cellular MR relaxation rates. This raises the possibility that MamE interacts with iron in an MR silent manner. Models of MamE expression in MTB predict an intracellular protein with one transmembrane domain (amino acids 22-42) and a large domain in the magnetosome vesicle lumen (amino acids 43-728) (17, 26) . Within the luminal domain there are two heme binding domains containing iron binding sites (16, 27). Using AlphaFold software,

the location of these binding sites is predicted to lie deep in the large luminal protein domain of MamE (Fig. 4.16), which may result in protein shielding of bound iron and a reduction in proton-electron interactions detected by MRI. Contrast agents associated with larger protein structures have decreased MR detection and thus MR signal due to the presence of a larger diffusive barrier, resulting in limited water exchange and slower electron relaxation (28, 29, 30). This diffusive barrier could be further extended due to the presence of the lipid membrane of the vesicle in which MamE is located, causing further limitation in water exchange.

Figure 4.16 Two iron binding sites are shown in the AlphaFold of magnetosome protein MamE.

The full predicted MamE protein structure is shown in the center. Iron binding sites are located at histidine 396 (top; highlighted in pink) and histidine 442 (bottom; highlighted in pink), both of which are located within the protein's heme binding groups. The figure was adapted from AlphaFold protein structure predictions (31, 32).

Another explanation for the MR-silent nature of MamE-expressing cells is that the protein is not in its active form when expressed in the mammalian cell. MamE is a trypsin-like protease and autoproteolysis is required for biomineralization function (17). AMB-1 cells with a catalytically inactive MamE show a phenotype in which biomineralization is altered and smaller magnetite crystals are produced (17). When detecting the presence of MamE protein in lysed cells, we detect the presence of full-length MamE protein (Chapter 3; Fig. 3.5). This suggests that inactive, unprocessed MamE protein is present in MDA-MB-435 cells, and is unable to perform its full function (ie. have a significant effect on the cellular MR signal). Further studies on the function of cleaved, active MamE are required.

4.4.3 Effect of magnetosome proteins on R1 relaxation

Although some magnetosome expression systems (MamI, MamL, MamI+L) have significantly different R1 values when comparing iron-supplemented to non-supplemented cells, these differences are small compared to differences in their R2 relaxation rates. Due to the relatively consistent R1 values between magnetosome expression systems, the longitudinal relaxation rates are unlikely to be useful as indicators of cellular iron contrast.

4.4.4 Effect of co-expressed magnetosome proteins on R2 relaxation

MamI and MamL expression increased both transverse and longitudinal relaxation rates as well as total cellular iron content when individually expressed in mammalian cells, cultured in the presence of an iron supplement. However, their co-

expression did not have a similar effect. The interaction of MamI and MamL reduced transverse relaxation rates and total cellular iron content, consistent with a role in regulating the iron-handling capability of mammalian cells. This form of iron regulation may serve a protective role as magnetosome components assemble in the designated intracellular compartment. Prior to iron biomineralization on any scale, the interaction between essential magnetosome proteins should sufficiently define the magnetosome-like vesicle to avoid cytotoxicity before sequestering cellular iron. Future work will indicate the degree to which MamI and MamL rely on MamB and/or MamE to upregulate MR relaxation rates through manipulation of cellular iron.

4.4.5 Comparison of magnetosome gene-based contrast agents

When compared with MR relaxation rates obtained from cells expressing MagA, a non-essential magnetosome protein putatively involved in iron transport, cells expressing essential magnetosome genes MamI, MamL, and MamB show comparable transverse and longitudinal relaxation rates. Phantom experiments conducted previously in our lab show that iron-supplemented mammalian cells expressing MagA have R1 values between 0.72-0.91 s^{-1} (19), while our expression systems examined havein have R1 values between 0.88-1.28 s^{-1} . R2*, R2, and R2′ values of iron-supplemented cells expressing MagA are 26.46 ± 8.69, 17.37 ± 4.80, and 9.09 ± 4.12 s^{-1}, respectively (18), which are comparable to R2*, R2, and R2′ values of MamI, MamL, and MamB expression systems.

Another magnetosome protein, Mms6, has been studied in the field of molecular imaging for its potential as an MR contrast agent (8). *mms6* belongs in a cluster of genes

on the magnetosome gene island (MAI) and plays a dominant role in defining the magnetite crystal size; specifically, it encodes an iron binding protein that is responsible for initiating magnetite nucleation (8). In an *in vitro* experiment of *mms6*-expressing tumor cells (8), the R2 relaxation rate measured at 3T in cell pellets consisting of 10 million cells supplemented with 200 µM ferric citrate was approximately 10 s^{-1}. Our study on the effects of essential magnetosome proteins MamI, MamL, MamB, and MamE further encourages the development of a rudimentary magnetosome-like nanoparticle as an MRI contrast agent. We speculate that synergistic effects on the MR signal of all four proteins expressed together will be greater than their individual effects. The positive influence of MagA and Mms6 on MR relaxation rates raises the possibility of adding nonessential MTB proteins in future optimization of a rudimentary magnetosome-like nanoparticle.

Although Mms6 is a cytosolic protein and MagA is a membrane protein, their cellular MR signals are comparable. Thus, the localization of magnetosome proteins MamI, MamL, MamB, and MamE cannot currently be distinguished by their effects on the cellular MR signal. Although experiments have not been conducted to determine the specific location of these magnetosome proteins and the iron they sequester in the cells, results from Chapters 2 and 3 strongly suggest protein localization in a lipid membrane. One method to determine such localization of iron is by coupling ICP-MS with differential fractionation, in which different compartments of the cell can be separated by centrifugation and analyzed for elemental iron content.

4.4.6 Correlation between relaxation rates and cellular iron content

With the exclusion of MamE, correlation of R2*, R2, and R2′ and iron content of cells expressing magnetosome proteins is r^2 = 0.61, 0.32, and 0.48, respectively. In MDA-MB-435 cells expressing MagA, the correlation between R2′ and iron content is high, at r^2 = 0.96 (33). This suggests that MagA has more specific and robust interactions with iron, although the correlation of individual essential magnetosome proteins has not yet been investigated. The correlation could also be influenced by the presence of other proteins that interact with iron, such as hepcidin (34).

4.5 Conclusion

In conclusion, essential AMB-1 magnetosome genes *mamI*, *mamL*, *mamB*, and *mamE* are compatible with mammalian cell systems. This is the first study investigating the effect of these essential genes on MR relaxation rates in mammalian cells. *mamI*, *mamL*, and *mamB* affect mammalian MR relaxation rates while all four genes increase cellular iron content when expressed in cells grown in an iron supplement. Based on these results, we conclude that *mamI*, *mamL*, and *mamB*, genes initially thought to only be involved in magnetosome membrane formation, interact with iron. With the unexpected result that *mamE* alone interacts with iron but does not affect cellular MR relaxation, we examined the predicted MamE protein structure. The bulky luminal domain of MamE may interfere with proton exchange between the aqueous environment and iron particles that bind to MamE. With MamE being MR silent, we also suggest that this result further implies the importance of the step-wise development of the

magnetosome (6), since the MR signal of MamE-expressing cells may be dependent on protein interaction(s) with the other magnetosome components.

Future studies will involve co-expressing multiple magnetosome genes, in particular *mamI*, *mamL*, and *mamE*, and *mamI, mamL,* and *mamB,* to investigate whether the collective presence of these genes will render an increase in MR measures. The combined expression of all four magnetosome genes, which we anticipate will create a rudimentary magnetosome-like nanoparticle, will also be investigated. The combination of these essential genes is expected to improve cellular MR detection and open paths to developing gene-based MR contrast technologies that can noninvasively monitor, identify, and track expression of cellular and molecular biomarkers.

4.6 References

1.   Massoud TF, Gambhir SS. Molecular imaging in living subjects: seeing fundamental biological processes in a new light. Genes Dev. 2003;17(5):545-80.
2.   James ML, Gambhir SS. A molecular imaging primer: modalities, imaging agents, and applications. Physiol Rev. 2012;92(2):897-965.
3.   Burtea C, Laurent S, Vander Elst L, Muller RN. Contrast agents: magnetic resonance. Handb Exp Pharmacol. 2008(185 Pt 1):135-65.
4.   Goldhawk D, Gelman N, Thompson R, Prato F. Forming Magnetosome-Like Nanoparticles in Mammalian Cells for Molecular MRI. 2017. p. 187-203.
5.   Geraldes CF, Laurent S. Classification and basic properties of contrast agents for magnetic resonance imaging. Contrast Media Mol Imaging. 2009;4(1):1-23.
6.   Uebe R, Schüler D. Magnetosome biogenesis in magnetotactic bacteria. Nat Rev Microbiol. 2016;14(10):621-37.
7.   Komeili A. Molecular mechanisms of compartmentalization and biomineralization in magnetotactic bacteria. FEMS Microbiol Rev. 2012;36(1):232-55.
8.   Zhang X-Y, Robledo BN, Harris SS, Hu XP. A bacterial gene, mms6, as a new reporter gene for magnetic resonance imaging of mammalian cells. Molecular imaging. 2014;13.
9.   Rohani R, Figueredo R, Bureau Y, Koropatnick J, Foster P, Thompson RT, et al. Imaging tumor growth non-invasively using expression of MagA or modified ferritin subunits to augment intracellular contrast for repetitive MRI. Mol Imaging Biol. 2014;16(1):63-73.
10.   Liu LS, Alizadeh K, Donnelly SC, Dassanayake P, Hou TT, McGirr R, et al. MagA expression attenuates iron export activity in undifferentiated multipotent P19 cells. Plos One. 2019;14(6).
11.   Goldhawk DE, Lemaire C, McCreary CR, McGirr R, Dhanvantari S, Thompson RT, et al. Magnetic Resonance Imaging of Cells Overexpressing MagA, an Endogenous Contrast Agent for Live Cell Imaging. Molecular Imaging. 2009;8(3):129.
12.   Zurkiya O, Chan AWS, Hu XP. MagA is sufficient for producing magnetic nanoparticles in mammalian cells, making it an MRI reporter. Magnetic Resonance in Medicine. 2008;59(6):1225-31.
13.   Lefèvre CT, Trubitsyn D, Abreu F, Kolinko S, Jogler C, de Almeida LG, et al. Comparative genomic analysis of magnetotactic bacteria from the Deltaproteobacteria provides new insights into magnetite and greigite magnetosome genes required for magnetotaxis. Environ Microbiol. 2013;15(10):2712-35.
14.   Murat D, Quinlan A, Vali H, Komeili A. Comprehensive genetic dissection of the magnetosome gene island reveals the step-wise assembly of a prokaryotic organelle. Proc Natl Acad Sci U S A. 2010;107(12):5593-8.
15.   Goldhawk DE, Gelman N, Thompson RT, Prato FS. Forming Magnetosome-Like Nanoparticles in Mammalian Cells for Molecular MRI. In: Bulte JWM, Modo MMJ, editors. Design and Applications of Nanoparticles in Biomedical Imaging. Cham: Springer International Publishing; 2017. p. 187-203.
16.   Quinlan A, Murat D, Vali H, Komeili A. The HtrA/DegP family protease MamE is a bifunctional protein with roles in magnetosome protein localization and magnetite biomineralization. Mol Microbiol. 2011;80(4):1075-87.

17.   Hershey DM, Browne PJ, Iavarone AT, Teyra J, Lee EH, Sidhu SS, et al. Magnetite Biomineralization in Magnetospirillum magneticum Is Regulated by a Switch-like Behavior in the HtrA Protease MamE. J Biol Chem. 2016;291(34):17941-52.

18.   Croker AK, Goodale D, Chu J, Postenka C, Hedley BD, Hess DA, et al. High aldehyde dehydrogenase and expression of cancer stem cell markers selects for breast cancer cells with enhanced malignant and metastatic ability. J Cell Mol Med. 2009;13(8B):2236-52.

19.   Sengupta A, Quiaoit K, Thompson RT, Prato FS, Gelman N, Goldhawk DE. Biophysical features of MagA expression in mammalian cells: implications for MRI contrast. Front Microbiol. 2014;5:29.

20.   Donnelly SC. The development of bacterial magnetic resonance imaging for microbiota analyses. London, Ontario, Canada: Western University; 2020.

21.   Smith PK, Krohn RI, Hermanson GT, Mallia AK, Gartner FH, Provenzano MD, et al. Measurement of protein using bicinchoninic acid. Anal Biochem. 1985;150(1):76-85.

22.   Lee CY, Thompson RT, Prato FS, Goldhawk DE, Gelman N. Investigating the Relationship between Transverse Relaxation Rate (R2) and Interecho Time in MagA-Expressing, Iron-Labeled Cells. Mol Imaging. 2015;14(12):551-60.

23.   Bereczk-Tompa E, Posfai M, Toth B, Vonderviszt F. Magnetite-Binding Flagellar Filaments Displaying the MamI Loop Motif. Chembiochem. 2016;17(21):2075-82.

24.   Uebe R, Keren-Khadmy N, Zeytuni N, Katzmann E, Navon Y, Davidov G, et al. The dual role of MamB in magnetosome membrane assembly and magnetite biomineralization. Molecular Microbiology. 2018;107(4):542-57.

25.   Uebe R, Junge K, Henn V, Poxleitner G, Katzmann E, Plitzko JM, et al. The cation diffusion facilitator proteins MamB and MamM of Magnetospirillum gryphiswaldense have distinct and complex functions, and are involved in magnetite biomineralization and magnetosome membrane assembly. Mol Microbiol. 2011;82(4):818-35.

26.   Nudelman H, Zarivach R. Structure prediction of magnetosome-associated proteins. Front Microbiol. 2014;5:9.

27.   Siponen MI, Adryanczyk G, Ginet N, Arnoux P, Pignol D. Magnetochrome: a c-type cytochrome domain specific to magnetotatic bacteria. Biochem Soc Trans. 2012;40(6):1319-23.

28.   Yang JJ, Yang J, Wei L, Zurkiya O, Yang W, Li S, et al. Rational design of protein-based MRI contrast agents. J Am Chem Soc. 2008;130(29):9260-7.

29.   Karfeld-Sulzer LS, Waters EA, Davis NE, Meade TJ, Barron AE. Multivalent protein polymer MRI contrast agents: controlling relaxivity via modulation of amino acid sequence. Biomacromolecules. 2010;11(6):1429-36.

30.   Licciardi G, Rizzo D, Salobehaj M, Massai L, Geri A, Messori L, et al. Large Protein Assemblies for High-Relaxivity Contrast Agents: The Case of Gadolinium-Labeled Asparaginase. Bioconjug Chem. 2022;33(12):2411-9.

31.   Jumper J, Evans R, Pritzel A, Green T, Figurnov M, Ronneberger O, et al. Highly accurate protein structure prediction with AlphaFold. Nature. 2021;596(7873):583-9.

32.   Varadi M, Anyango S, Deshpande M, Nair S, Natassia C, Yordanova G, et al. AlphaFold Protein Structure Database: massively expanding the structural coverage of protein-sequence space with high-accuracy models. Nucleic Acids Res.

2022;50(D1):D439-D44.

33.   Goldhawk DE, Gelman N, Sengupta A, Prato FS. The Interface Between Iron Metabolism and Gene-Based Iron Contrast for MRI. Magnetic Resonance Insights. 2015;8(Suppl 1):9-14.

34.   Alizadeh K, Sun Q, McGuire T, Thompson T, Prato FS, Koropatnick J, et al. Hepcidin-mediated Iron Regulation in P19 Cells is Detectable by Magnetic Resonance Imaging. Sci Rep. 2020;10(1):3163.

Chapter 5

5   Conclusions, limitations, and future directions

In chapters 2, 3, and 4, the expression and interaction(s) of essential magnetosome proteins in a mammalian cell system were described. Each project contributes to the testing of our hypothesis that four essential magnetotactic bacterial genes expressed in mammalian cells would produce a rudimentary magnetosome-like nanoparticle that would significantly improve magnetic resonance imaging (MRI) contrast. Section 5.1 below summarizes key findings and discussions from each chapter. Section 5.2 outlines the limitations of this study. Finally, section 5.3 explores the potential future directions of this work.

5.1   Summary and conclusions

5.1.1 Chapter 2

Chapter 2 focused on the interaction between essential magnetosome proteins MamI and MamL. This chapter also showcased the first instance of MamI and/or MamL expressed in mammalian cells, and confirmed that these proteins are tolerated in a mammalian system. Our hypothesis that essential magnetosome proteins colocalize and interact on an intracellular vesicle (Fig. 5.1) was supported by the fluorescence microscopy, western blot, co-immunoprecipitation, and fluorescence correlation spectroscopy (FCS) data presented. The unique cellular localization patterns of MamI (net-like pattern) and MamL (punctate, mobile pattern) suggests additional roles that have

not been previously recognized in their native magnetotactic bacterial environment. The

co-localization and interaction of these two proteins gives rise to the potential of a

rudimentary magnetosome-like structure assembling and using the proteins as an initial

scaffold. Through the expression and recruitment of other essential magnetosome

proteins that interact with iron, such as MamB and MamE (1, 2), this magnetosome-like

structure can be crafted into a gene-based magnetic resonance (MR) contrast agent.
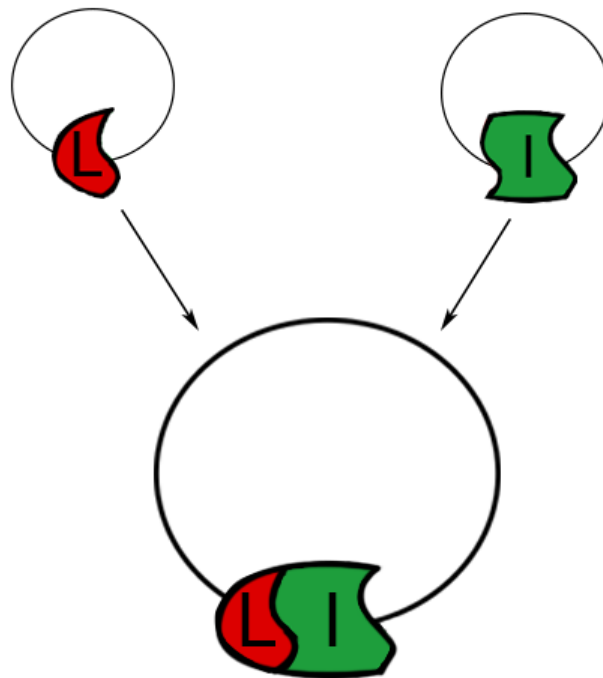
Figure 5.1 Magnetosome proteins MamI and MamL co-localize and interact in the mammalian cell.

MamL (red, top left) and MamI (green, top right) are expressed and sorted to the same

intracellular compartment in the mammalian cell.

5.1.2 Chapter 3

Chapter 3 focused on the mobility of magnetosome proteins, and showcased for the first time the expression of MamB and MamE in a mammalian cell system. MamB showed a punctate, mobile fluorescence pattern, and MamE showed a punctate, seemingly stationary fluorescence pattern. This chapter describes both the Brownian motion and directed motion of magnetosome proteins by analyzing the movement trajectories of each protein. Data presented in this chapter further supports the hypothesis that magnetosome proteins interact, specifically showing that MamL retains mobility when interacting with MamI. This chapter also reveals the potential interaction between magnetosome proteins and mammalian molecular motors. MamL (and MamL$_{trunc}$), MamI+L, MamB, and MamE all undergo directed motion at a velocity similar to the velocity that myosin V travel in mammalian cells and thus are predicted to interact and move along with them (Fig. 5.2). Additionally, analysis of particle Brownian motion provides insight of the size of particles in live cells in contrast to the cell-free FCS analysis of the size of these proteins provided in chapter 2.
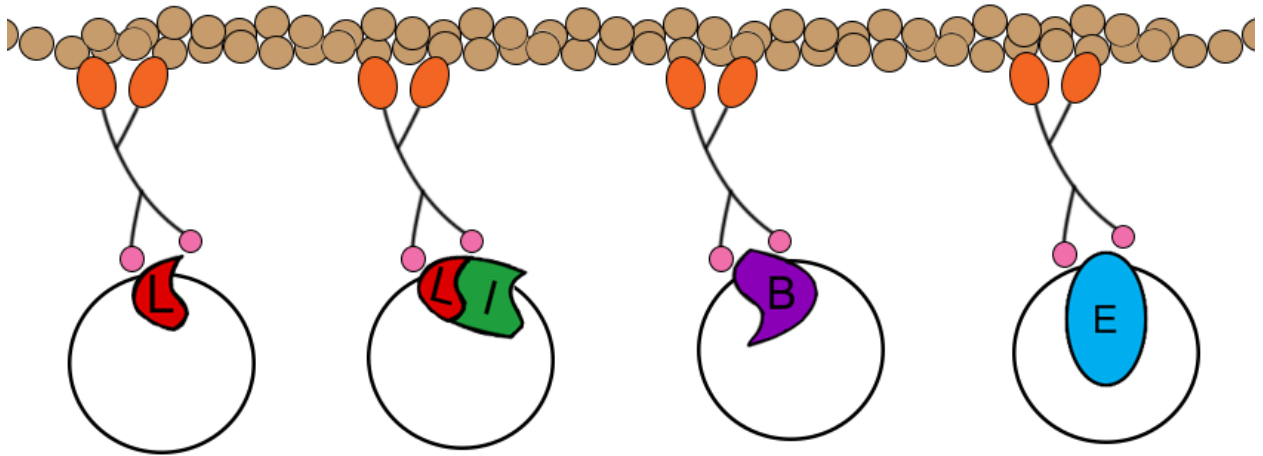
Figure 5.2 Working model of magnetosome proteins interacting with mammalian motor proteins.

Motor proteins (ie. Myosin V) are attached to filaments (ie. actin) (brown spheres) via their motor domain (orange ellipses) and bind magnetosome proteins MamL (red), MamI+L (green and red), MamB (purple) and MamE (cyan) via the cargo-binding domain (pink spheres). Adaptor proteins (not shown), which coat the exterior of cargo vesicles (ie. clathrin-coated vesicles), facilitate interaction between the cargo-binding domain and the vesicle (3).

5.1.3   Chapter 4

Chapter 4 focused on the effects of essential magnetosome proteins on the MR relaxation rates and iron content of mammalian cells. Surprising and unexpected results were revealed throughout this chapter, the first being that MamI and MamL affect mammalian MR relaxation rates when individually expressed (Fig. 5.3A). These proteins

were described in literature to function in invagination of the magnetosome membrane (1, 4) and did not have any known interactions with iron, thus this study reveals new roles for these proteins. The second unexpected result revealed that, although MamI and MamL individually increase cellular MR relaxation rates, this increase does not occur when the two proteins are co-expressed and interact (Fig. 5.3B). We speculate that the interaction between MamI and MamL impose a dampening of the MR signal and require the presence of additional magnetosome proteins, such as MamB or MamE, to lift that inhibition. The third unexpected result was that MamE, a protein that has reported interactions with iron in the magnetotactic bacteria (5, 6), did not seem to affect mammalian MR relaxation rates (Fig. 5.3C). However, all 4 magnetosome proteins that we investigated, including MamE, had an effect on the total cellular iron content. We speculate that MamE may only alter MR relaxation rates after the protein interacts with other essential magnetosome proteins. This further accentuates the importance of the step-wise assembly of the magnetosome (1, 4).

This hypothesis that a rudimentary nanoparticle can be created by appropriate interaction of the four essential proteins now needs to be further tested. Success will be contingent on achieving regulation, subcellular localization, timing of nanoparticle assembly and disassembly, and regulation of iron biomineralization. Specifically the extent to which the size, the shape, and the composition of the iron crystal can be controlled is unknown. It is possible that such control on the nanoparticle will require additional genes. All these factors may influence cellular MRI, and may contribute to the improvement of cellular and molecular MRI.
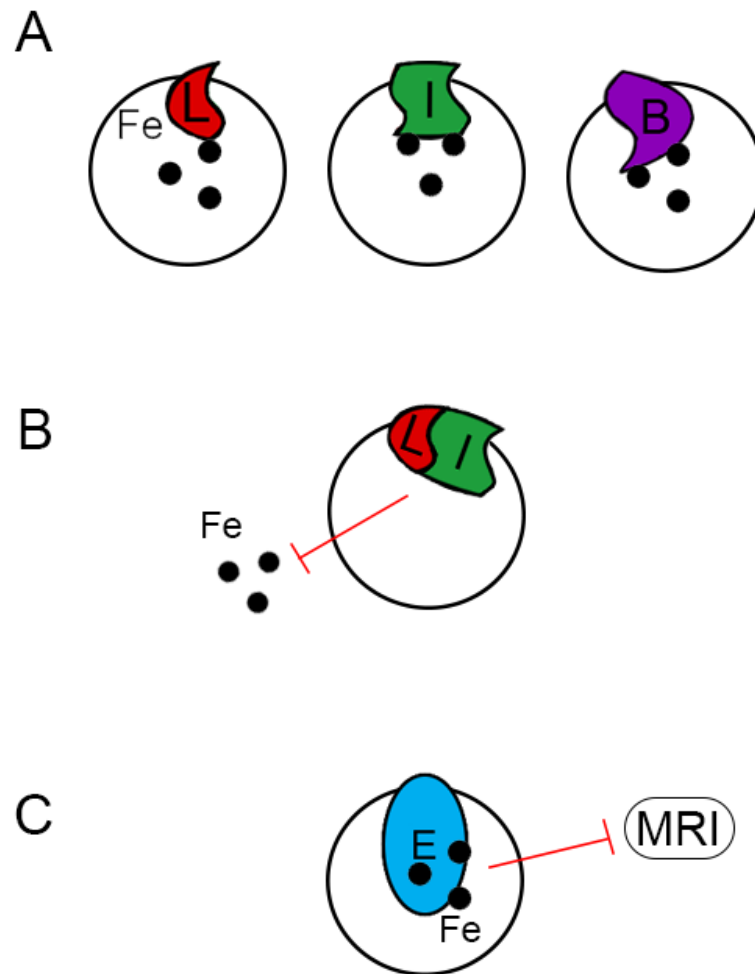
Figure 5.3 Interaction between cellular iron and essential magnetosome proteins.

A. Magnetosome proteins MamL (red), MamI (green), and MamB (purple) interact with iron and affect MR relaxation rates when individually expressed. B. When MamL (red) and MamI (green) are co-expressed, the interaction between the two proteins prevents their individual interaction(s) with iron. C. MamE (blue) interacts with iron but remains MR silent.

5.2   Limitations

The "elephant in the room" is the hypothesis that a rudimentary magnetosome-like nanoparticle of sufficient iron concentration and of approximately 40 nm in diameter will be formed if the identified four essential magnetosome genes are successfully expressed in mammalian cells. Of course this has been demonstrated in magnetotactic bacteria but not in mammalian cells. It may be that additional genes will be needed which could be added if necessary. Regardless, we have demonstrated that magnetotactic bacterial genes can be successfully introduced and integrated into mammalian cells. This has laid the foundation for future work even if additional genes are needed for further improvement of the nanoparticle.

5.2.1 Molecular cloning

The use of plasmids in the transfer and introduction of DNA across species has been used in scientific research and applications since the 1990s (7). Plasmids have been popularized in research due to their low cost, their easy production and storage, and their long-lasting shelf-life (8). However, plasmids do have notable limitations. Plasmids are generally inefficient at introducing foreign DNA into a host cell compared to other techniques such as viral transduction (8). Larger plasmids with a significant bacterial backbone have decreased uptake in the host cell and are more likely to be targeted by the mammalian immune system (8). Although our plasmids are currently not large since the genes we work with are relatively small (200 bp – 2 kb), alternative cloning strategies, such as the use of DNA minicircles (9, 10), might be needed once we work with additional genes.

Since protein targeting sequences are often present at the N terminal of proteins, the presence of the N-terminal fluorescent proteins may prevent correct sorting of the magnetosome proteins in the mammalian cell. A previous study that expressed magnetosome protein MagA in mammalian cells showed localization in the Golgi apparatus (11). Additionally, the net-like localization pattern of EGFP-MamI is similar to the pattern of peripheral endoplasmic reticulum tubules (12). When expressed with a FLAG peptide (small, 8 amino acid immunotag), FLAG-MamL+EGFP-MamI has the same co-expression pattern as Tomato-MamL+EGFP-MamI (Chapter 2). However, the FLAG tag is still located at the N-terminus of MamL. To determine if the fluorescent protein affects protein sorting, future experiments may examine expression of essential magnetosome proteins with a C-terminal protein tag.

Although experiments determining the specific localization of magnetosome proteins in the mammalian cell have not yet been performed, our study, especially experiments detailing the diffusion of these magnetosome proteins in Chapter 3, is consistent with the possible expression of these proteins in a mammalian, intracellular lipid membrane. Future experiments that reveal intracellular location of magnetosome proteins MamI, MamL, MamB, and MamE include immunocytochemistry, in which different compartments in the cell can be immunostained to determine protein co-localization. Further experiments with fluorescence correlation spectroscopy (FCS) and fluorescence cross-correlation spectroscopy (FCCS), techniques described in Chapter 2, can reveal the interaction of magnetosome proteins with membranes or lipid rafts, or the stoichiometry and oligomerization of the proteins, respectively, in a cell-free system.

5.2.2 Cell culture

Although cell culture has been an inexpensive, established, and useful tool in modern scientific research, the technique has its limitations. Firstly, researchers must be familiar with the specific characteristics and phenotypes of the cell line they are utilizing in order to accurately interpret any results (13). Additionally, different cell lines have very different phenotypes. For example, the human melanoma cell line MDA-MB-435, an adherent cell line with cells having a stellate morphology (14), is very different from the human monocyte cell line THP-1, a suspension cell line with cells having a rounded morphology (15). Secondly, the obtained results cannot easily be extrapolated or related to human or other multicellular organisms (13). Results obtained from cell culture are generally limited to the cell line experimented on and to cell lines with similar phenotypes. In a multicellular organism, different types of cells cross-talk with each other and interact with the extracellular matrix and the host immune system (16, 17). Although co-culture models exist in cell culture, many are difficult to set up, expensive, and cannot replicate the extensive and complicated cellular environment of a multicellular organism (18). Lastly, cell culture requires proper and careful handling and time to become a viable model. For example, the MDA-MB-435 cell line requires approximately 2 weeks to be fully established in culture from thawing, and cells divide approximately once every 24 hours. Experiments that require large-scale cell culture (MRI phantom experiments) take careful planning and require 2-3 weeks of cell growth.

5.2.3 Fluorescence microscopy

Fluorescence microscopy is a popular and powerful imaging tool used to collect spatial and functional information from labeled cells and structures (19), and has been a major technique used in this study. Although the technique offers many advantages, such as live cell imaging and high specificity as the cells emit their own signal, there are limitations to fluorescence microscopy. One drawback is that the sample needs to be compatible with fluorescent probes or immunofluorescent labeling (19). If no antibody exists for the specific structure of interest, other processes such as the creation of hybrid fluorescent proteins will need to be followed. These techniques need to be carefully planned and assessed, as the introduction of the fluorescent gene near the gene of interest may affect its expression, synthesis, sorting, and function (20). Furthermore, the large size of fluorescent proteins (~25 kDa for EGFP, ~54 kDa for tdTomato) may alter the function of the protein they are attached to (20). Additionally, results from fluorescence microscopy can be confounding due to autofluorescence of cells if they are not interpreted by an experienced individual. Autofluorescence can be reduced by the use of confocal microscopy, which has pinpoint accuracy due to elimination of light above and below the focal plane. However, photobleaching of the fluorescent signal still occurs during long periods of imaging, especially in cells expressing weaker signals (20). This makes data harder to analyze for time-lapses and z-stacks that have longer data acquisition times, as the signal intensity decreases with time. Although confocal fluorescence microscopy has improved resolution compared to conventional fluorescence microscopy, the resolution is still limited by fluorophore brightness, size, and numerical aperture of the objective according to the Ernst Abbe equation:

$$Resolution\ (r) = \frac{\lambda}{2NA}$$

Where r is the resolution, or smallest distance resolvable by the microscope between two objects, λ is the imaging wavelength, and NA is the numerical aperture of the microscope. Thus, with a numerical aperture of 0.75 (which is the numerical aperture on our 20X objective) and using green fluorescent protein (GFP) which has an emission wavelength of ~510 nm, our resolution limit is 340 nm. Any particles that are less than 340 nm apart, or are smaller than 340 nm in diameter, will be harder to resolve and will have a less accurate size estimation.

5.2.4 MRI phantom

Phantoms containing tissue mimicking material (ie. gelatin) have been used for decades in scientific research and imaging and therapeutic applications (21). Gelatin-based phantoms are made to resemble fatty-like tissues and soft tissues (21, 22). However, gelatin does not mimic the complex, multicellular aspects of tissues, and lacks the capability to withstand temperature change (23). Gelatin phantoms are prone to melting and thus causing artifacts in the subsequent MR images. Another limitation of the gelatin phantom is the presence of microbial or fungal growth on or within the phantom (24). This can be avoided by pouring a fresh gelatin phantom prior to each experiment.

5.3 Future work

Future studies will involve expressing multiple magnetosome proteins in the mammalian cell, starting with triple expression systems. I have done preliminary work

toward this expression system that will allow future students in the Goldhawk/Prato lab to easily continue the work. Firstly, MamI, MamL, and MamE will be expressed together in the cell. This triple expression system will investigate whether MamE will have an effect on mammalian MR relaxation rates in the presence of MamI and MamL. As discussed in chapter 4, we predict that MamE requires interaction with other magnetosome proteins (ie. MamI and/or MamL) to activate iron-interacting functions that are MR visible. To develop this expression system, MamI and MamL have been cloned into the same plasmid (pSF-FLAG-MamL-T2A-EGFP-MamI). This plasmid will express both MamL and MamI, and the proteins will be cleaved into their separate protein via the T2A sequence. MamE was cloned into ptdTomato-C1 to form tdTomato-MamE. pSF-FLAG-MamL-T2A-EGFP-MamI and tdTomato-MamE will be co-expressed in MDA-MB-435 cells, selection of stable cell line will be done with both G418 and puromycin, and cells will be observed using the confocal fluorescence microscope. With this method, instances of triple expression will be indicated by punctate, yellow fluorescence.

Furthermore, the MamE expression system will be investigated for the presence of MamE protein that has gone through autoproteolysis. This is important since the MamE protein has to be cleaved in order to be fully functional (25). This will be evaluated by measuring trypsin activity with methods described by Hershey *et al* (25). Interactions between MamE and iron, specifically the labile iron pool (LIP), will also be investigated to evaluate whether the protein regulates iron homeostasis in the mammalian cell. This will be evaluated using CALB-AM (calcein blue and their acetomethoxies) epifluorescence analysis according to methods described by Glickstein *et al* (26). These

protocols have been thoroughly investigated and will be performed by a current fourth-year project undergraduate student in the Goldhawk lab.

The triple expression system including MamI, MamL, and MamB will also be developed to investigate whether these proteins work together to increase MR relaxation rates and cellular iron content further than when they are expressed alone in the cell. pSF-FLAG-MamL-T2A-EGFP-MamI will be co-expressed with tdTomato-MamB in MDA-MB-435 cells.

Finally, the quaternary expression system including MamI, MamL, MamB, and MamE will be developed to assess the potentially synergistic effect of these proteins on cellular MR relaxation rates and iron content. MamB and MamE will be cloned into the same plasmid with a T2A sequence, and will be co-expressed with pSF-FLAG-MamL-T2A-EGFP-MamI. The combination of these essential genes, and thus the development of a rudimentary magnetosome-like nanoparticle, is expected to improve cellular MR detection and open paths to developing gene-based MR contrast technologies that can noninvasively monitor, identify, and track expression of cellular and molecular biomarkers.

5.4   References

1.   Uebe R, Schüler D. Magnetosome biogenesis in magnetotactic bacteria. Nat Rev Microbiol. 2016;14(10):621-37.

2.   Uebe R, Keren-Khadmy N, Zeytuni N, Katzmann E, Navon Y, Davidov G, et al. The dual role of MamB in magnetosome membrane assembly and magnetite biomineralization. Molecular Microbiology. 2018;107(4):542-57.

3.   Akhmanova A, Hammer JA. Linking molecular motors to membrane cargo. Curr Opin Cell Biol. 2010;22(4):479-487.

4.   Komeili A. Molecular mechanisms of compartmentalization and biomineralization in magnetotactic bacteria. FEMS Microbiol Rev. 2012;36(1):232-55.

5.   Murat D, Quinlan A, Vali H, Komeili A. Comprehensive genetic dissection of the magnetosome gene island reveals the step-wise assembly of a prokaryotic organelle. Proc Natl Acad Sci U S A. 2010;107(12):5593-8.

6.   Quinlan A, Murat D, Vali H, Komeili A. The HtrA/DegP family protease MamE is a bifunctional protein with roles in magnetosome protein localization and magnetite biomineralization. Mol Microbiol. 2011;80(4):1075-87.

7.   Wolff JA, Malone RW, Williams P, Chong W, Acsadi G, Jani A, et al. Direct gene transfer into mouse muscle in vivo. Science. 1990;247(4949 Pt 1):1465-8.

8.   Hardee CL, Arévalo-Soliz LM, Hornstein BD, Zechiedrich L. Advances in Non-Viral DNA Vectors for Gene Therapy. Genes (Basel). 2017;8(2).

9.   Dietz WM, Skinner NE, Hamilton SE, Jund MD, Heitfeld SM, Litterman AJ, et al. Minicircle DNA is superior to plasmid DNA in eliciting antigen-specific CD8+ T-cell responses. Mol Ther. 2013;21(8):1526-35.

10.   Wang T, Chen Y, Goodale D, Allan AL, Ronald JA. A survivin-driven, tumor-activatable minicircle system for prostate cancer theranostics. Mol Ther Oncolytics. 2021;20:209-19.

11.   Liu L. Characterization of MagA Expression and Iron Uptake in P19 Cells: Implications for Use as a Gene-Based Contrast Agent. London, Ontario, Canada: University of Western Ontario: 2015.

12.   Gao G, Zhu C, Liu E, Nabi IR. Reticulon and CLIMP-63 Regulate Nanodomain Organization of Peripheral ER Tubules. PLOS Biol. 2019;17(8).

13.   Balon K, Wiatrak B. PC12 and THP-1 Cell Lines as Neuronal and Microglia Model in Neurobiological Research. Applied Sciences. 2021;11.

14.   Sun Q, Fradin C, Tahir M, Thompson RT, Prato FS, Goldhawk DE. Interaction of Essential Magnetosome Genes in Mammalian Cells. Magnetotactic Bacteria: 6th International Meeting, Kanazawa, Japan. 2018.

15.   Dassanayake P. Monocyte MRI Relaxation Rates are Regulated by Extracellular Iron and Hepcidin. London, Ontario, Canada: University of Western Ontario; 2019.

16.   Hodgkin PD, Rush J, Gett AV, Bartell G, Hasbold J. The logic of intercellular communication in the immune system. Immunol Cell Biol. 1998;76(5):448-53.

17.   Bogdanowicz DR, Lu HH. Multifunction co-culture model for evaluating cell-cell interactions. Methods Mol Biol. 2014;1202:29-36.

18.   Whiteley JT, Fernandes S, Sharma A, Mendes APD, Racha V, Benassi SK, et al. Reaching into the toolbox: Stem cell models to study neuropsychiatric disorders. Stem

Cell Reports. 2022;17(2):187-210.

19.   Jensen EC. Types of imaging, Part 2: an overview of fluorescence microscopy. Anat Rec (Hoboken). 2012;295(10):1621-7.

20.   Wiedenmann J, Oswald F, Nienhaus GU. Fluorescent proteins for live cell imaging: opportunities, limitations, and challenges. IUBMB Life. 2009;61(11):1029-42.

21.   McGarry CK, Grattan LJ, Ivory AM, Leek F, Liney GP, Liu Y, et al. Tissue mimicking materials for imaging and therapy phantoms: a review. Phys Med Biol. 2020;65(23).

22.   Steinmann A, Stafford RJ, Sawakuchi G, Wen Z, Court L, Fuller CD, et al. Developing and characterizing MR/CT-visible materials used in QA phantoms for MRgRT systems. Med Phys. 2018;45(2):773-82.

23.   Antoniou A, Georgiou L, Christodoulou T, Panayiotou N, Ioannides C, Zamboglou N, et al. MR relaxation times of agar-based tissue-mimicking phantoms. J Appl Clin Med Phys. 2022;23(5):e13533.

24.   Rathbun KM, Harryman CF, Re AT. Prolonging the Shelf Life of Homemade Gelatin Ultrasound Phantoms. J Med Ultrasound. 2022;30(2):130-4.

25.   Hershey DM, Browne PJ, Iavarone AT, Teyra J, Lee EH, Sidhu SS, et al. Magnetite Biomineralization in Magnetospirillum magneticum Is Regulated by a Switch-like Behavior in the HtrA Protease MamE. J Biol Chem. 2016;291(34):17941-52.

26.   Glickstein H, El RB, Shvartsman M, Cabantchik ZI. Intracellular labile iron pools as direct targets of iron chelators: a fluorescence study of chelator action in living cells. Blood. 2005;106(9):3242-50.

APPENDIX A – Sequencing

Appendix A.1: *mamI* **sequence information.** The *mamI* gene (pink) is shown downstream and in frame with EGFP (green). Restriction sites used in the cloning of *mamI* are labeled and boxed in red.

Appendix A.2: *mamL* sequence information.

The *mamL* gene (blue) is shown downstream and in frame with Tomato (red). Restriction

sites used in the cloning of *mamL* are labeled and boxed in green.
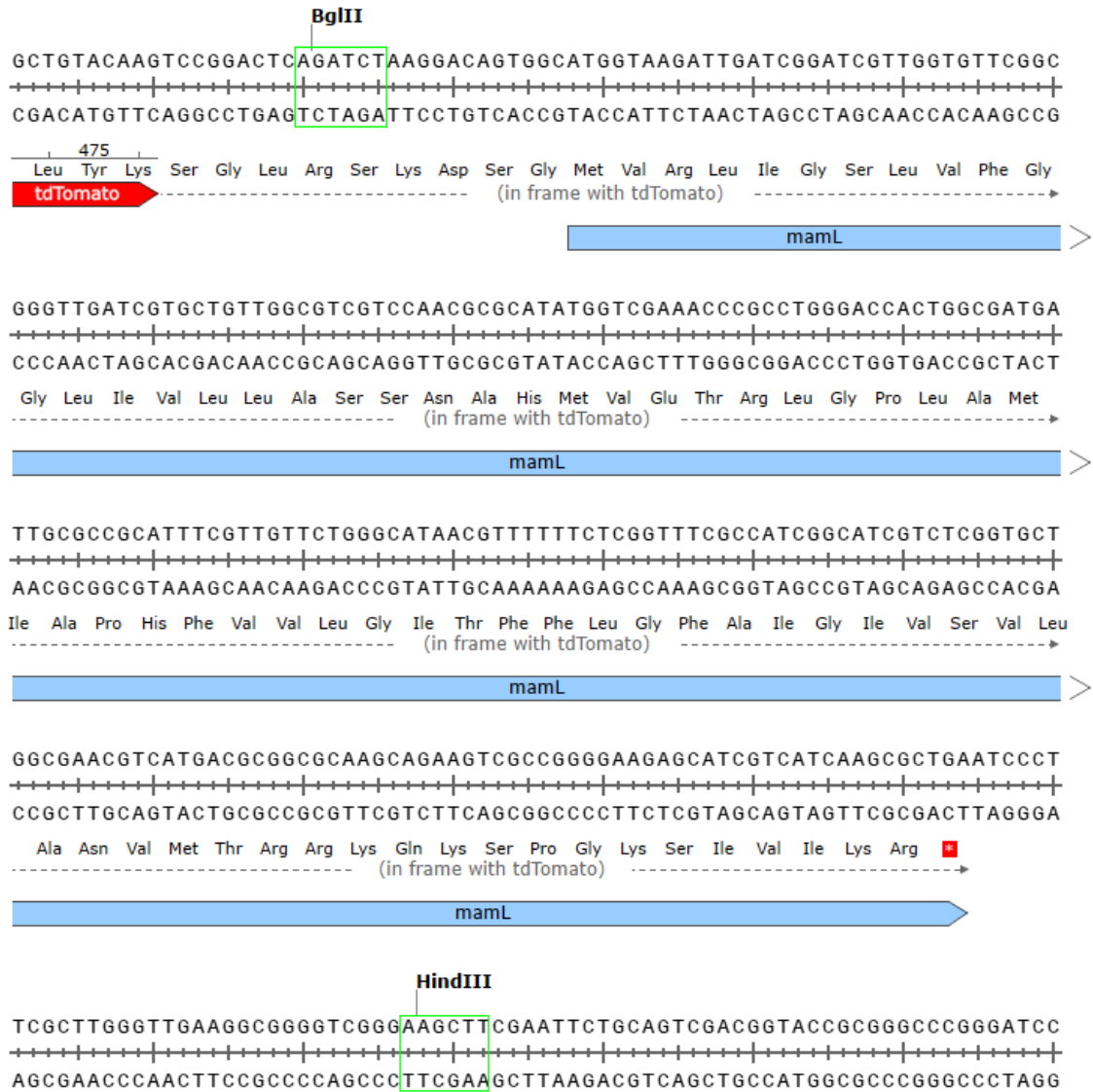
Appendix A.3: *mamL_trunc* sequence information. The *mamL_trunc* gene (light green) is shown downstream and in frame with Tomato (red). The stop codon introduced to truncate *mamL* is shown in black. Restriction sites used in the cloning of *mamL_trunc* are labeled and boxed in pink.
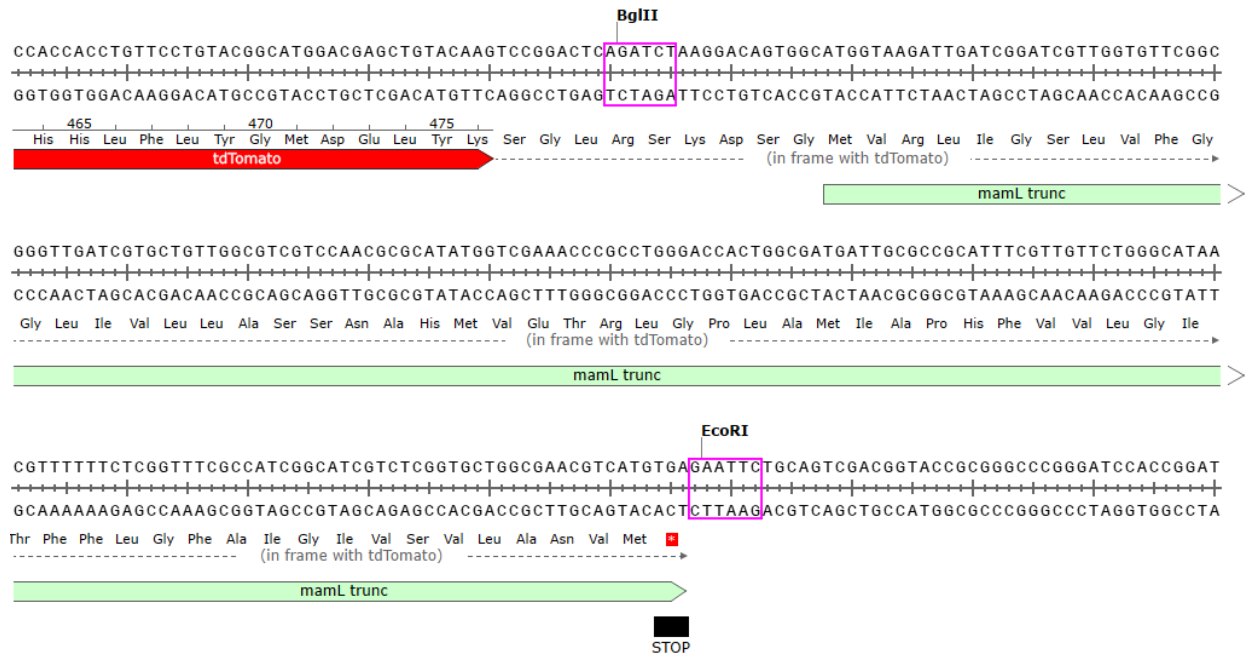
Appendix A.4: *FLAG-mamL* sequence information. The *mamL* gene (blue) is shown

downstream and in frame with FLAG (lavender). Restriction sites used in the cloning of

FLAG-mamL are labeled and boxed in red.

Appendix A.5: *mamB* sequence information. The *mamB* gene (cyan) is shown

downstream and in frame with Tomato (red). Restriction sites used in the cloning of

mamB are labeled and boxed in green.

```
GGAGGAAATCCCCCACGCCCGCGACATCCGCCTGTTCGTCAGCCCGGCACCCGCCGCCGCGGCACGGGCCTGAGCGAGAGAGGGGCGGCGTCATGGACAT
++++++++++|++++++++++|++++++++++|++++++++++|++++++++++|++++++++++|++++++++++|++++++++++|++++++++++|++++++++++|
CCTCCTTTAGGGGGTGCGGGCGCTGTAGGCGGACAAGCAGTCGGGCCGTGGGCGGCGGCGCCGTGCCCGGACTCGCTCTCTCCCCGCCGCAGTACCTGTA
```
```
            275        280        285        290        295
        Glu Glu Ile Pro His Ala Arg Asp Ile Arg Leu Phe Val Ser Pro Ala Pro Ala Ala Ala Ala Arg Ala ▪
```
```
mamB
```

```
SmaI
```
```
CCCGGGATCCACCGGATCTAGATAACTGATCATAATCAGCCATACCACATTTGTAGAGGTTTTACTTGCTTTAAAAAAACCTCCCACACCTCCCCCTGAAC
++++++++++|++++++++++|++++++++++|++++++++++|++++++++++|++++++++++|++++++++++|++++++++++|++++++++++|++++++++++|
GGGCCCTAGGTGGCCTAGATCTATTGACTAGTATTAGTCGGTATGGTGTAAACATCTCCAAAATGAACGAAATTTTTTGGAGGGTGTGGAGGGGGACTTG
```

Appendix A.6: *mamE* **sequence information.** The *mamE* gene (purple) is shown downstream and in frame with EGFP (green). MamE (G49S, T641S) mutations are labeled in orange and MamE (T317A) mutation is labeled in pink. Restriction sites used in the cloning of *mamE* are labeled and boxed in red.
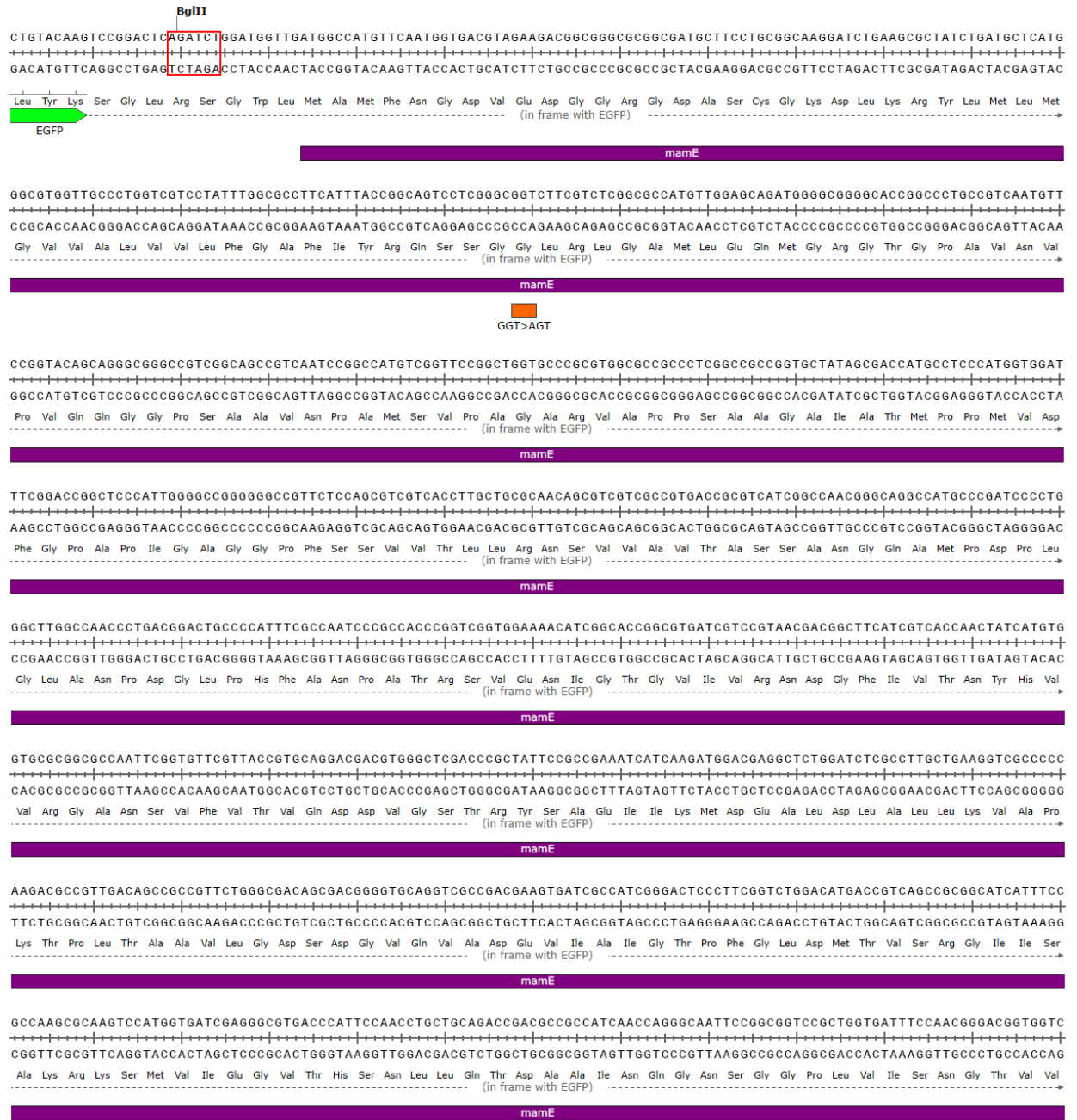
```
GGCATCAATACCGCCATCTACACCCCCAACGGCGCCTTTGCCGGAATAGGCTTCGCCGTGCCCAGCAATCAGGCCCGCCTGTTCATCTTGGATGAAGTGGGCTGGCTGCCGACCTCCACC
CCGTAGTTATGGCGGTAGATGTGGGGGTTGCCGCGGAAACGGCCTTATCCGAAGCGGCACGGGTCGTTAGTCCGGGCGGACAAGTAGAACCTACTTCACCCGACCGACGGCTGGAGGTGG
Gly Ile Asn Thr Ala Ile Tyr Thr Pro Asn Gly Ala Phe Ala Gly Ile Gly Phe Ala Val Pro Ser Asn Gln Ala Arg Leu Phe Ile Leu Asp Glu Val Gly Trp Leu Pro Thr Ser Thr
(in frame with EGFP)
mamE
ACC>GCC
```

```
GCCGAGGGGGCCTCCATGGGCCTGGTGGCCATGCAGCGCCCCATGGGCGGCGGCGTGGGCGCGGCGGGTCCGGCCATTTTCGCCGGGACTAGGGCGCCCCACACCGATGGCCGCCAGAAC
CGGCTCCCCCGGAGGTACCCGGACCACCGGTACGTCGCGGGGTACCCGCCGCCGCACCCGCGCCGCCCAGGCCGGTAAAAGCGGCCCTGATCCCGCGGGGTGTGGCTACCGGCGGTCTTG
Ala Glu Gly Ala Ser Met Gly Leu Val Ala Met Gln Arg Pro Met Gly Gly Gly Val Gly Ala Ala Gly Pro Ala Ile Phe Ala Gly Thr Arg Ala Pro His Thr Asp Gly Arg Gln Asn
(in frame with EGFP)
mamE
```

```
ATGGATTGCACCACCTGCCACGATCTGATTCCGGCCGGAAACGGGCGGCCCGCGCCGATGATGCCCATCGCCGCCCCGATTCCGCCGCCGCCGATTCCCATGGGCGCCGTCTCGCCCCAT
TACCTAACGTGGTGGACGGTGCTAGACTAAGGCCGGCCTTTGCCCGCCGGGCGCGGCTACTACGGGTAGCGGCGGGGCTAAGGGTACCCGCGGCAGAGCGGGGTA
Met Asp Cys Thr Thr Cys His Asp Leu Ile Pro Ala Gly Asn Gly Arg Pro Ala Pro Met Met Pro Ile Ala Ala Pro Ile Pro Pro Pro Pro Ile Pro Met Gly Ala Val Ser Pro His
(in frame with EGFP)
mamE
```

```
ACCGACGGCCGTCAGAACATGAACTGCGCCAATTGCCATCAGATGCTGGGCGGTGCCGCGCCCATCGCCGCACCGGGACTCGGCGGGGGGGGCTTACCGCTTCGCGCAGCCGCCGGGAAGC
TGGCTGCCGGCAGTCTTGTACTTGACGCGGTTAACGGTAGTCTACGACCCGCCACGGCGCGGGTAGCGGCGTGGCCCTGAGCCGCCCCCCCGAATGGCGAAGCGCGTCGGCGGCCCTTCG
Thr Asp Gly Arg Gln Asn Met Asn Cys Ala Asn Cys His Gln Met Leu Gly Gly Ala Ala Pro Ile Ala Ala Pro Gly Leu Gly Gly Gly Ala Tyr Arg Phe Ala Gln Pro Pro Gly Ser
(in frame with EGFP)
mamE
```

```
CTGGCCATCAATATTCAGGGGCCGCGCGGCGGGCAGTCGACCGCCGCCGGGAACCGGCCGGGTCACGCTTTTGGGCGCCGCCTTGACTCCCATGTCGCAGCGCCTTGGCGCCCAGACCGGC
GACCGGTAGTTATAAGTCCCCGGCGCGCCGCCCGTCAGCTGGCGGCGGCCCTTGGCCGGCCCAGTGCGAAAACCCGCGGCGGAACTGAGGGTACAGCGTCGCGGAACCGCGGGTCTGGCCG
Leu Ala Ile Asn Ile Gln Gly Pro Arg Gly Gly Gln Ser Thr Ala Ala Gly Thr Gly Arg Val Thr Leu Leu Gly Ala Ala Leu Thr Pro Met Ser Gln Arg Leu Gly Ala Gln Thr Gly
(in frame with EGFP)
mamE
```

```
GAAGAAGTCTCCGCCATCATGGTCGAGATGCATGCCGGACGGTCGGTGCGGCTCGGCGTCCTGCGCGATGGCGATGTGCGCAACATGACCCTGGTCGCGGGACCCGCCGGTCTGGCCGCC
CTTCTTCAGAGGCGGTAGTACCAGCTCTACGTACGGCCTGCCAGCCACGCCGAGCCGCAGGACGCGCTACCGCTACACGCGTTGTACTGGGACCAGCGCCCTGGGCGGCCAGACCGGCGG
Glu Glu Val Ser Ala Ile Met Val Glu Met His Ala Gly Arg Ser Val Arg Leu Gly Val Leu Arg Asp Gly Asp Val Arg Asn Met Thr Leu Val Ala Gly Pro Ala Gly Leu Ala Ala
(in frame with EGFP)
mamE
```

```
GCAGCGGTCCAGGCTCCGGCCATTGCCGACATGGCGCAGCCGCCCATGGGCGGCATGGCCCCCACTGCACCCGGCATGGTCGCGGTTCCCGGTGGTCCGGCCGTCATGCCGAAGCCTCCG
CGTCGCCAGGTCCGAGGCCGGTAACGGCTGTACCGCGTCGGCGGGTACCCGCCGTACCGGGGGTGACGTGGGCCGTACCAGCGCCAAGGGCCACCAGGCCGGCAGTACGGCTTCGGAGGC
Ala Ala Val Gln Ala Pro Ala Ile Ala Asp Met Ala Gln Pro Pro Met Gly Gly Met Ala Pro Thr Ala Pro Gly Met Val Ala Val Pro Gly Gly Pro Ala Val Met Pro Lys Pro Pro
(in frame with EGFP)
mamE
```

```
ACCGAGTTCAACTGGCTGGGCATGGAGATCGAAACCTTCCAGGCGCCGCGTCCGATCACCGGTGTGCCGGGCGCCGTTCCGGTTCCCGGAGCCAAGGGTGCCCAGGTGGCCGAGGTTCTG
TGGCTCAAGTTGACCGACCCGTACCTCTAGCTTTGGAAGGTCCGCGGCGCAGGCTAGTGGCCACACGGCCCGCGGCAAGGCCAAGGGCCTCGGTTCCCACGGGTCCACCGGCTCCAAGAC
Thr Glu Phe Asn Trp Leu Gly Met Glu Ile Glu Thr Phe Gln Ala Pro Arg Pro Ile Thr Gly Val Pro Gly Ala Val Pro Val Pro Gly Ala Lys Gly Ala Gln Val Ala Glu Val Leu
(in frame with EGFP)
mamE
ACC>TCC
```

```
GTCGGGTCCCGGGCCGCCGTGGCGGGGCTCCAGGCCAATGACCTCATCCTCGAGGTCAATAATCGGCCGGTGGCCGGTCCGGCTCGTCTCGACGCCGCCATTAAGGGGGCGACGAATGCC
CAGCCCAGGGCCCGGCGGCACCGCCCCGAGGTCCGGTTACTGGAGTAGGAGCTCCAGTTATTAGCCGGCCACCGGCCAGGCCGAGCAGAGCTGCGGCGGTAATTCCCCCGCTGCTTACGG
Val Gly Ser Arg Ala Ala Val Ala Gly Leu Gln Ala Asn Asp Leu Ile Leu Glu Val Asn Asn Arg Pro Val Ala Gly Pro Ala Arg Leu Asp Ala Ala Ile Lys Gly Ala Thr Asn Ala
(in frame with EGFP)
mamE
```

```
                                                                                                 SacI
GGGCAGCAGATTTTGCTGAAGGTCAACCGCAATGGCCAAGAGTTCTGGATTGTCCTTTGATGGTG GAGCTC AAGCTTCGAATTCTGCAGTCGACGGTACCGCGGGCCCGGGATCCACCGG
CCCGTCGTCTAAAACGACTTCCAGTTGGCGTTACCGGTTCTCAAGACCTAACAGGAAACTACCAC CTCGAG TTCGAAGCTTAAGACGTCAGCTGCCATGGCGCCCGGGCCCTAGGTGGCC
Gly Gln Gln Ile Leu Leu Lys Val Asn Arg Asn Gly Gln Glu Phe Trp Ile Val Leu *
(in frame with EGFP)
mamE
```

APPENDIX B – Western blot

Appendix B.1: Immunoblots of total cellular protein from mammalian cells expressing EGFP-MamI, Tomato-MamL, or co-expressing EGFP-MamI/Tomato-MamL. Total cellular protein from MDA-MB-435 cells stably expressing EGFP, EGFP-MamI, and co-expressing EGFP-MamI/Tomato-MamL were examined with mouse α-EGFP (left). Total cellular protein from cells stably expressing Tomato, Tomato-MamL, and co-expressing EGFP-MamI/Tomato-MamL were examined with α-Tomato (right). Full-length western blots are displayed.
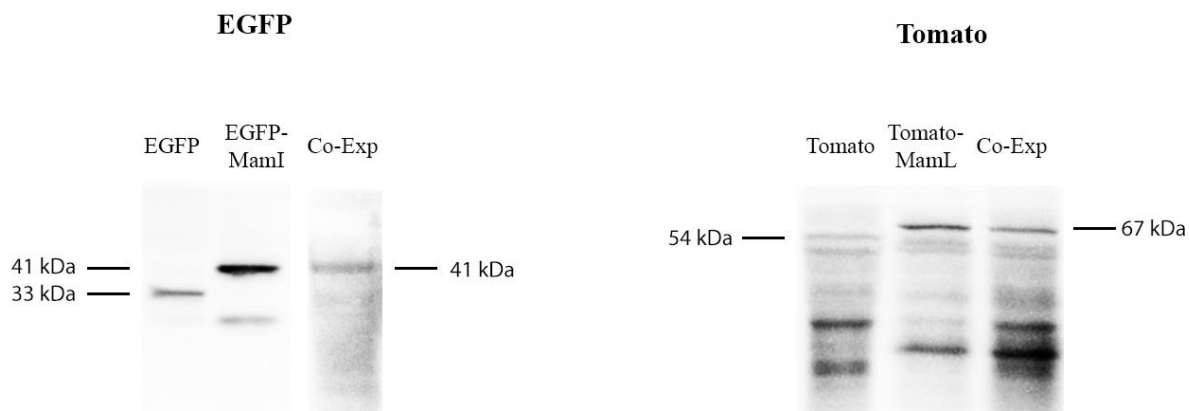
Appendix B.2: Immunoblots of total cellular protein from mammalian cells expressing Tomato-MamL$_{trunc}$ or co-expressing Tomato-MamL$_{trunc}$/EGFP-MamI .

Total cellular protein from MDA-MB-435 cells stably expressing Tomato, Tomato-MamL, Tomato-MamL$_{trunc}$, and co-expressing Tomato-MamL$_{trunc}$/EGFP-MamI were examined with rabbit α-Tomato or mouse α-EGFP (far right lane). Full-length western blots are displayed.
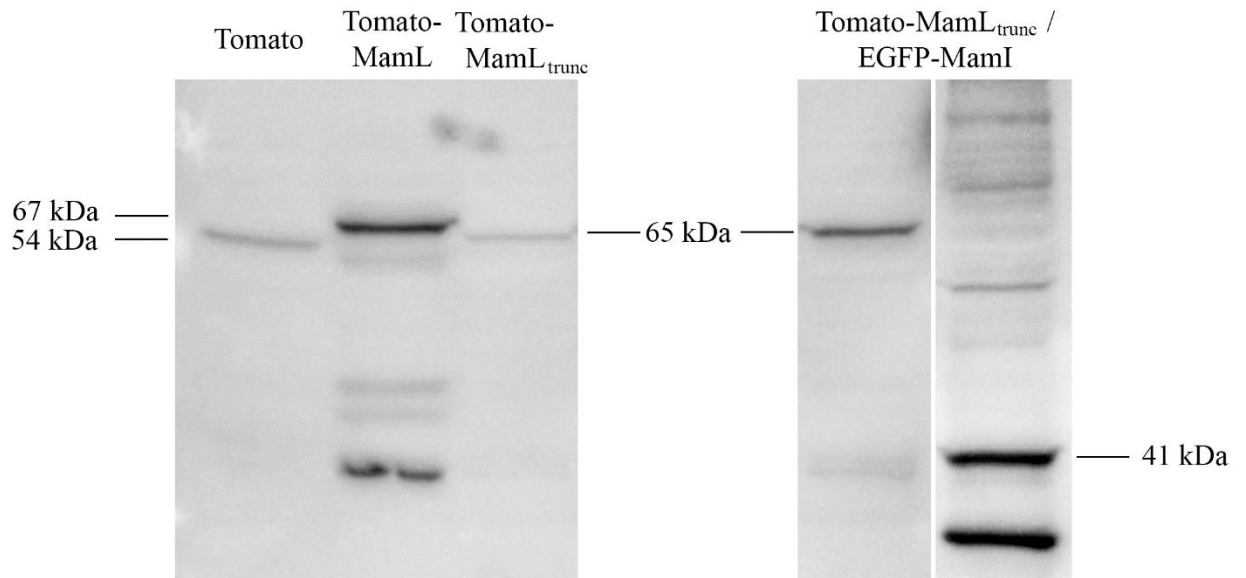
Appendix B.3: Immunoblots of total cellular protein from mammalian cells co-expressing FLAG-MamL/EGFP-MamI. Total cellular protein from MDA-MB-435 cells stably expressing FLAG-MamL was examined with mouse α-FLAG (left) or stably expressing EGFP-MamI was examined with mouse α-EGFP (right). Full-length western blots are displayed.
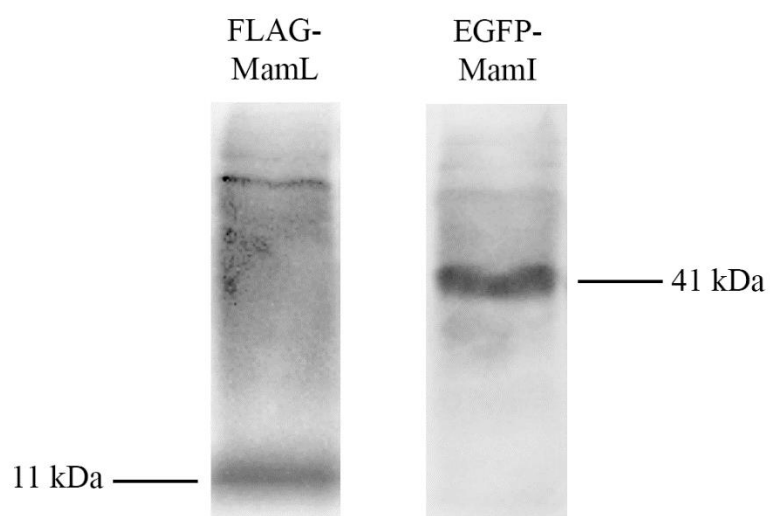
Appendix B.4: Immunoblot of total cellular protein from mammalian cells

expressing EGFP-MamE. Total cellular protein from MDA-MB-435 cells stably

expressing EGFP-MamE was examined with mouse α-EGFP. The full-length western

blot is displayed.
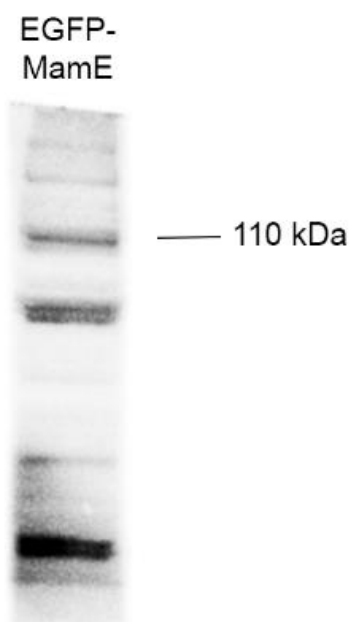
Appendix B.5: Immunoblot of total cellular protein from mammalian cells expressing Tomato-MamB. Total cellular protein from MDA-MB-435 cells stably expressing Tomato-MamB was examined with rabbit α-Tomato. The full-length western blot is displayed.
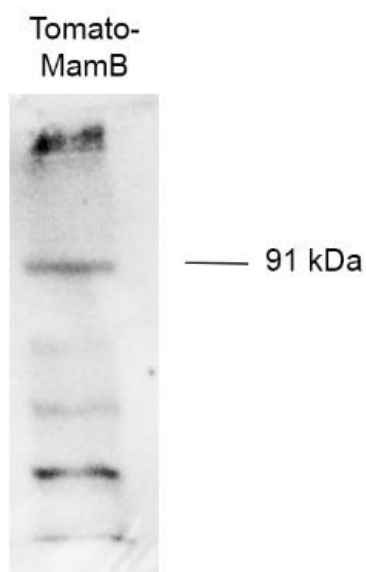
APPENDIX C – Simple Trajectory Analysis

Appendix C.1: Velocity and diffusion coefficient of EGFP-MamE particles in mammalian cells.

	Directed Motion			Brownian Motion		
Cell Sample	Number of Particles per Cell	*Velocity (µm/s)	†Average Velocity (µm/s)	Number of Particles per Cell	‡Diffusion Coefficient (µm²/s)	†Average Diffusion Coefficient (µm²/s)
1	0	N/A	N/A	3	0.0076	0.0053 ± 0.0029
2	0	N/A		1	0.0019	
3	0	N/A		2	0.0054	
4	0	N/A		1	0.0015	

*Particles undergoing directed motion are determined as any particle with a mean-squared displacement that is non-linear in time, and proportional to t^{α} and $\alpha > 1.2$.

†Average velocity and average diffusion coefficient are the weighted mean $\pm$ standard deviation.

‡Particles undergoing Brownian motion are determined as any particle with a mean-squared displacement close to linear in time, i.e., proportional to t^{α} and $0.7 < \alpha < 1.1$.

Appendix C.2: Velocity and diffusion coefficient of Tomato-MamB particles in mammalian cells.

	Directed Motion			Brownian Motion		
Cell Sample	Number of Particles per Cell	*Velocity (μm/s)	†Average Velocity (μm/s)	Number of Particles per Cell	‡Diffusion Coefficient (μm²/s)	†Average Diffusion Coefficient (μm²/s)
1	46	0.17		38	0.0070	
2	251	0.17		163	0.0074	
3	62	0.15	0.17 ± 0.015	48	0.0047	0.0066 ± 0.0012
4	55	0.18		23	0.0049	
5	52	0.19		35	0.0066	

*Particles undergoing directed motion are determined as any particle with a mean-squared displacement that is non-linear in time, and proportional to t^α and $\alpha > 1.2$.

†Average velocity and diffusion coefficient are the weighted mean ± standard deviation.

‡Particles undergoing Brownian motion are determined as any particle with a mean-squared displacement close to linear in time, i.e. proportional to t^α and $0.7 < \alpha < 1.1$.

Appendix C.3: Velocity and diffusion coefficient of Tomato-MamL particles in mammalian cells.

Cell Sample	Directed Motion			Brownian Motion		
	Number of Particles per Cell	[*]Velocity (μm/s)	[†]Average Velocity (μm/s)	Number of Particles per Cell	[‡]Diffusion Coefficient (μm²/s)	[†]Average Diffusion Coefficient (10^{-3} μm²/s)
1	23	0.15		50	0.0022	
2	34	0.20		48	0.0033	
3	65	0.16	0.18 ± 0.061	79	0.0020	2.7 ± 0.073
4	17	0.30		17	0.0031	
5	21	0.17		46	0.0037	

[*]Particles undergoing directed motion are determined as any particle with a mean-squared displacement that is non-linear in time, and proportional to t^{α} and $\alpha > 1.2$.

[†]Average velocity and diffusion coefficient are the weighted mean ± standard deviation.

[‡]Particles undergoing Brownian motion are determined as any particle with a mean-squared displacement close to linear in time, i.e. proportional to t^{α} and $0.7 < \alpha < 1.1$.

Appendix C.4: Velocity and diffusion coefficient of Tomato-MamL$_{trunc}$ particles in mammalian cells.

Cell Sample	Directed Motion			Brownian Motion		
	Number of Particles per Cell	*Velocity (µm/s)	†Average Velocity (µm/s)	Number of Particles per Cell	‡Diffusion Coefficient (µm²/s)	†Average Diffusion Coefficient (µm²/s)
1	188	0.13		91	0.0050	
2	36	0.14		41	0.0017	
			0.14 ± 0.037			0.0038 ± 0.0022
3	32	0.17		35	0.0055	
4	63	0.14		48	0.0028	
5	8	0.07		12	0.00027	

*Particles undergoing directed motion are determined as any particle with a mean-squared displacement that is non-linear in time, and proportional to t^{α} and $\alpha > 1.2$.

†Average velocity and diffusion coefficient are the weighted mean ± standard deviation.

‡Particles undergoing Brownian motion are determined as any particle with a mean-squared displacement close to linear in time, i.e. proportional to t^{α} and $0.7 < \alpha < 1.1$.

Appendix C.5: Velocity and diffusion coefficient of Tomato-MamL/EGFP-MamI particles in mammalian cells.

Cell Sample	Number of Particles per Cell	*Velocity (µm/s)	†Average Velocity (µm/s)	Number of Particles per Cell	‡Diffusion Coefficient (µm²/s)	†Average Diffusion Coefficient (µm²/s)
	Directed Motion			**Brownian Motion**		
1	79	0.43		72	0.028	
2	50	0.45	0.47 ± 0.17	23	0.041	0.038 ± 0.031
3	40	0.78		23	0.100	
4	20	0.36		27	0.033	
5	70	0.40		47	0.023	

*Particles undergoing directed motion are determined as any particle with mean-squared displacement non-linear in time, and proportional to t^α and $\alpha>1.2$.

†Average velocity and diffusion coefficient are the weighted mean ± standard deviation.

‡Particles undergoing Brownian motion are determined as any particle with mean-squared displacement close to linear in time, i.e. proportional to t^α and $0.7<\alpha<1.1$.

Appendix C.6: Velocity and diffusion coefficient of FLAG-MamL/EGFP-MamI particles in mammalian cells.

Cell Sample	Directed Motion			Brownian Motion		
	Number of Particles per Cell	*Velocity (μm/s)	†Average Velocity (μm/s)	Number of Particles per Cell	‡Diffusion Coefficient (μm²/s)	†Average Diffusion Coefficient (μm²/s)
1	95	0.19		94	0.011	
2	22	0.15	0.19 ± 0.03	19	0.0066	0.012 ± 0.004
3	94	0.22		62	0.016	
4	83	0.16		39	0.015	
5	108	0.19		47	0.010	

*Particles undergoing directed motion are determined as any particle with mean-squared displacement non-linear in time, and proportional to t^{α} and $\alpha > 1.2$.

†Average velocity and diffusion coefficient are the weighted mean ± standard deviation.

‡Particles undergoing Brownian motion are determined as any particle with mean-squared displacement close to linear in time, i.e. proportional to t^{α} and $0.7 < \alpha < 1.1$.

APPENDIX D – MRI Supplementary Data

Appendix D.1: Example T1 results generated from Matlab script. Generated values are in the black box. The first row represents the R1 values, the second row represents uncertainty with R1, the third row represents percentage uncertainty, and the last row represents the coefficient of non-determination.

TI	A	B	C	D
22	472.33	513.56	554	616.11
200	219	224.33	323.56	371.33
500	4.11	4.11	64.22	86.56
1000	267.89	314.67	205.89	205.33
2000	492.11	548.11	500.78	534.67
3900	539.78	591.89	613.67	682.44
	1.460737	1.509206	1.154108	1.096474
	0.1272	0.1552	0.0693	0.0667
	8.7103	10.2812	6.0045	6.0833
	0.0143	0.0195	0.0083	0.0086

Appendix D.2: MRI (R2*, R2, R2′, R1) and elemental iron analysis data for all magnetosome expression systems.

Protein	No iron supplement				
	R2*	R2	R2′	R1	Fe
EGFP-MamI	15.02 ± 2.5	12.40 ± 1.0	2.70 ± 1.0	0.91 ± 0.02	0.04 ± 0.001
Tomato-MamL	17.87 ± 1.0	12.23 ± 0.7	7.04 ± 2.2	0.88 ± 0.05	0.08 ± 0.01
Tomato-MamL$_{trunc}$	N/A	N/A	N/A	N/A	N/A
Tomato-MamL/ EGFP-MamI	N/A	N/A	N/A	N/A	N/A
FLAG-MamL/ EGFP-MamI	14.32 ± 2.1	14.32 ± 0.3	2.53 ± 0.2	0.90 ± 0.12	0.15 ± 0.13
Tomato-MamB	18.70 ± 4.9	12.76 ± 0.8	7.64 ± 2.8	0.97 ± 0.15	0.08 ± 0.01
EGFP-MamE	14.00 ± 1.4	10.22 ± 1.4	3.69 ± 0.8	0.98 ± 0.32	0.07 ± 0.02

Protein	With iron supplement				
	R2*	R2	R2′	R1	Fe
EGFP-MamI	30.38 ± 2.8	19.12 ± 2.6	11.26 ± 1.8	1.08 ± 0.03	1.12 ± 0.11
Tomato-MamL	37.07 ± 5.6	23.38 ± 4.4	13.69 ± 1.5	1.18 ± 0.07	1.11 ± 0.45
Tomato-MamL$_{trunc}$	39.84 ± 5.7	18.71 ± 2.0	21.14 ± 2.6	1.18 ± 0.02	0.93 ± 0.18
Tomato-MamL/ EGFP-MamI	25.36 ± 3.0	17.85 ± 1.2	7.51 ± 1.2	N/A	N/A
FLAG-MamL/ EGFP-MamI	18.58 ± 2.5	15.00 ± 0.9	4.58 ± 0.5	0.97 ± 0.05	0.46 ± 0.04
Tomato-MamB	35.35 ± 5.2	23.64 ± 3.7	11.72 ± 1.8	1.28 ± 0.11	1.48 ± 0.09
EGFP-MamE	16.52 ± 0.9	10.31 ± 1.2	6.29 ± 1.8	1.12 ± 0.35	0.94 ± 0.34

Curriculum Vitae

Name: Qin (Daisy) Sun

Post-secondary **Bachelor of Medical Sciences with Honors: Interdisciplinary**
Education and **Medical Sciences**
Degrees: The University of Western Ontario
       London, Ontario, Canada
       2012-2017

       Doctor of Philosophy in Medical Biophysics
       The University of Western Ontario
       London, Ontario, Canada
       2017-2023

Honours and   **The Western Scholarship of Excellence**
Awards: University of Western Ontario
       2012

       Dean's Honor List
       University of Western Ontario
       2013-2017

       Ontario Graduate Scholarship
       Council of Ontario Universities
       2017-2018, 2021-2022

       Western Graduate Research Scholarship
       University of Western Ontario - Medical Biophysics Department
       2017-2022

       Cancer Research and Technology Transfer Scholarship
       University of Western Ontario
       2017-2018

       Poster Award for Imaging Network of Ontario
       Imaging Network of Ontario (ImNO)
       2018

       Poster Award for Cancer Research and Technology Transfer
       Cancer Research and Technology Transfer (CaRTT)
       2018

       Alan Groom Award – Junior Graduate Seminar
       University of Western Ontario – Medical Biophysics Department
       2019

Youth Investigator Award
World Molecular Imaging Society – Molecular Imaging in
Nanotechnology and Theranostics (WMIS – MINT)
2020

Poster Award for London Imaging and Discovery Day
University of Western Ontario
2022

Related Work Experience	**Graduate Teaching Assistant** The University of Western Ontario 2018-2022
	Graduate Research Assistant Lawson Health Research Institute 2020-present

Publications:

Sun Q, Prato FS, and Goldhawk DE. (2020). Optimizing Reporter Gene Expression for Molecular Magnetic Imaging: Lessons from the Magnetosome. In: Ueno S, editor. Bioimaging: Imaging by Light and Electromagnetics in Medicine and Biology. CRC Press Taylor & Francis Group.

Alizadeh K, **Sun Q,** McGuire T, Thompson RT, Prato FS, Koropatnick J, Gelman N, and Goldhawk DE. (2020). Hepcidin-mediated Iron Regulation in P19 Cells is Detectable by Magnetic Resonance Imaging. *Scientific Reports 10: 3163.*

Sun Q, Yu L, Donnelly SC, Fradin C, Thompson RT, Prato FS, and Goldhawk DE. (2022). Essential iron biomineralization proteins MamI and MamL from Magnetotactic bacteria interact in mammalian cells. *Journal of Biological Chemistry.* In submission.